

**THE MOTT TRANSITION
IN STRONGLY FRUSTRATED LATTICES**

By
NYAYABANTA SWAIN
PHYS08200905003

Harish-Chandra Research Institute, Allahabad

*A thesis submitted to the
Board of Studies in Physical Sciences
In partial fulfillment of requirements
for the Degree of
DOCTOR OF PHILOSOPHY
of
HOMI BHABHA NATIONAL INSTITUTE*



March, 2017

Homi Bhabha National Institute¹

Recommendations of the Viva Voce Committee

As members of the Viva Voce Committee, we certify that we have read the dissertation prepared by Nyayabanta Swain entitled "The Mott Transition in Strongly Frustrated Lattices" and recommend that it may be accepted as fulfilling the thesis requirement for the award of Degree of Doctor of Philosophy.

Chairman - Prof. Sumathi Rao

Date:



3/8/17

Guide / Convener - Prof. Pinaki Majumdar

Date:



3/8/17

Co-guide -

Date:



Examiner - Prof. Vijay B. Shenoy

Date: Aug 3, 2017

Member 1- Prof. G. V. Pai

Date:



03-08-2017

Member 2- Prof. Aditi Sen (De) 

Date: 03.08.17

Member 3- Prof. Satchitananda Naik 

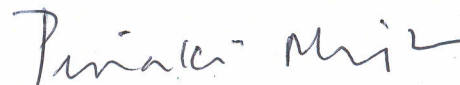
Date: 3/8/17.

Final approval and acceptance of this thesis is contingent upon the candidate's submission of the final copies of the thesis to HBNI.

I/We hereby certify that I/we have read this thesis prepared under my/our direction and recommend that it may be accepted as fulfilling the thesis requirement.

Date: 03/08/2017

Place: Allahabad



Prof. Pinaki Majumdar

¹ This page is to be included only for final submission after successful completion of viva voce.

STATEMENT BY AUTHOR

This dissertation has been submitted in partial fulfillment of requirements for an advanced degree at Homi Bhabha National Institute (HBNI) and is deposited in the Library to be made available to borrowers under rules of the HBNI.

Brief quotations from this dissertation are allowable without special permission, provided that accurate acknowledgement of source is made. Requests for permission for extended quotation from or reproduction of this manuscript in whole or in part may be granted by the Competent Authority of HBNI when in his or her judgment the proposed use of the material is in the interests of scholarship. In all other instances, however, permission must be obtained from the author.

Nyayabanta Swain

Nyayabanta Swain

DECLARATION

I, hereby declare that the investigation presented in the thesis has been carried out by me. The work is original and has not been submitted earlier as a whole or in part for a degree / diploma at this or any other Institution / University.

Nyayabanta Swain

Nyayabanta Swain

List of Publications arising from the thesis

Journal

1. “Mott-Hubbard Transition and Spin Liquid State on the Pyrochlore Lattice”, Nyayabanta Swain, Rajarshi Tiwari and Pinaki Majumdar, *Phys. Rev. B*, **2015**, *94*, 155119-155129.
2. “Magnetic Order and Mott Transition on the Checkerboard Lattice”, Nyayabanta Swain and Pinaki Majumdar, *J. Phys. Condens. Matter*, **2017**, *29*, 85603-85613.

Communicated

1. “Mott Transition and Anomalous Resistive State in the Pyrochlore Molybdates”, Nyayabanta Swain and Pinaki Majumdar, arXiv:1606.06277 (2016)
2. “Ground State of the Two Orbital Hubbard Model on the Pyrochlore Lattice with Competing Double Exchange and Superexchange Interactions”, Nyayabanta Swain and Pinaki Majumdar, arXiv:1610.00695 (2016)

Nyayabanta Swain

Nyayabanta Swain

DEDICATIONS

*To my parents
and
teachers.*

ACKNOWLEDGEMENTS

First and foremost, I would like to thank my adviser Prof. Pinaki Majumdar for all his guidance and support. He has always been a constant source of encouragement during my thesis work, not only for his physics intuition and ingenuity, but also for his unbiased nature towards everyone and incredulous patience. I will always be indebted to him for all the training I have received from him.

During my Ph.D. work, I have a wonderful time at HRI, thanks to my friends, seniors and juniors. I can't name all of them here as the list is huge! However, I thank them for the numerous physics discussions that I have with them, and for making life enjoyable and enriched. Also I would like to thank the HRI faculty, administration, residents and support staff for being extremely helpful at all times. I would always be grateful for the many beautiful memories at HRI, and feel fortunate to have come here for my Ph.D.

I would like to thank my family and friends for always being supportive to me.

Finally, there are so many people who have touched my life through their own lives, words and actions. I would like to thank all of them from my heart, for it is because of them I am what I am today.

CONTENTS

Synopsis	2
List of Figures	7
List of Tables	8
1 Introduction	9
1.1 Geometric frustration	9
1.1.1 General overview	9
1.1.2 Experimental relevance	11
1.1.3 Theoretical understanding	15
1.2 Correlated electron systems	21
1.2.1 General overview	21
1.2.2 Experimental relevance	22
1.2.3 Theoretical understanding	24
1.3 Interplay of frustration and correlation	26
1.3.1 General overview	27
1.3.2 Experimental relevance	28
1.3.3 Theoretical understanding	33
1.4 Agenda of the thesis	37
2 Theoretical tools	39
2.1 The Hubbard model	39
2.2 The static path approximation	40
2.3 Numerical methods	43
2.3.1 Real space Monte Carlo	43
2.3.2 Variational calculation at $T = 0$	45
2.4 Equilibrium properties	46
2.4.1 Auxiliary field correlations	46
2.4.2 Electronic correlation functions	47
2.5 Methodological issues	47
2.5.1 The static approximation	47
2.5.2 System size dependence	48
2.5.3 Annealing time dependence	48
2.5.4 Cluster based update	49

3	Mott transition on the pyrochlore lattice	51
3.1	Introduction	51
3.2	Previous work	52
3.2.1	Pyrochlore Heisenberg model	53
3.2.2	Pyrochlore Hubbard model	54
3.3	Results of our study	55
3.3.1	The ground state	55
3.3.2	Thermal phase diagram	57
3.3.3	Density of states	57
3.3.4	Transport and optics	58
3.4	Discussion	60
3.4.1	Overall scenario	60
3.4.2	Effective models in limiting cases	61
3.4.3	Detailed magnetic structure	63
3.4.4	Variational check	64
3.5	Conclusion	65
4	Mott transition on the checkerboard lattice	67
4.1	Introduction	67
4.2	Results of our study	70
4.2.1	Ground state	70
4.2.2	Finite temperature correlations	71
4.2.3	Local moment distribution	73
4.2.4	Insulator-metal transition	74
4.3	Discussion	76
4.3.1	Origin of the magnetic phases	76
4.3.2	Magnetic impact on electrons	80
4.4	Conclusion	82
5	Mott physics in the pyrochlore molybdates	83
5.1	Introduction	83
5.2	Model for the molybdates	84
5.2.1	Method	87
5.2.2	Observables	88
5.3	Model Hamiltonian study	89
5.3.1	Ground state results	89
5.3.2	Finite temperature results	99
5.3.3	Summary of the model study	119
5.4	Comparing to molybdate experiments	121
5.4.1	Parameter calibration	121
5.4.2	Results	122
5.4.3	Discussion	127
5.4.4	Conclusion	128

6	Mott physics in the pyrochlore iridates	129
6.1	Introduction	129
6.2	Model for the iridates	132
6.2.1	Method	134
6.2.2	Observables	135
6.3	Model Hamiltonian study	136
6.3.1	Ground state results	136
6.3.2	Finite temperature	137
6.3.3	Discussion	143
6.3.4	Conclusion	144
6.4	Comparing to iridate experiments	144
	Concluding Remarks	148
	Appendix	150
A	Effective spin models via perturbation expansion	150
A.1	Weak coupling	151
A.2	Strong coupling	152
A.2.1	Some Results	153
A.2.2	Effective spin model for the pyrochlore molybdates	157
A.2.3	Effective spin model for the pyrochlore iridates	157
	References	158

SYNOPSIS

The Mott metal-insulator transition (MIT), driven by electron-electron interaction, is a fundamental problem in correlated electron physics. It requires a framework that can describe the dual character of the electron - simultaneously itinerant and localized. The two limits of fully itinerant and strongly localized behaviour are well understood but the transition region poses a problem due to the absence of any obvious small parameter controlling the theory.

Geometric frustration, in the magnetic context, arises when the arrangement of spins on a lattice cannot minimise all interactions simultaneously. Geometrically frustrated magnets are different from both unfrustrated and disordered magnets (spin glasses). They typically have a huge number of degenerate minima in their classical energy landscape, leading to a macroscopic ground state degeneracy. Sometimes thermal effects lead to ordering via an entropic ‘order-by-disorder’ effect. In some frustrated geometries, with triangular motifs, the ratio, α , of the Curie constant to T_c is large but finite. There are lattices, however, the pyrochlore being a notable example, where no ordering is observed at any temperature, and $\alpha \rightarrow \infty$. These define the strong frustration limit.

How are the two phenomena above related? Correlated systems involve metals with *itinerant* electrons, while traditional frustrated systems are insulating magnets with *localised* electrons. These two ends are connected by varying interaction strength in a Hubbard like model, and via pressure variation in real materials. The following is a sampling of the new physics that arises as the frustrated magnet in the deep Mott regime is driven towards the insulator-metal transition (IMT):

- The ‘virtual hopping’ of the electrons mediate long range and multispin coupling, and
- The *magnitude* of the local moments weaken as the system is pushed towards the IMT.

The first effect can lift the degeneracy of the short range model and promote an ordered state while the second tends to destroy the magnetic state altogether. The outcome of this interplay is lattice specific, of relevance to several real life materials, and requires tools beyond those usually applied in frustrated magnetism.

We address the interplay of correlation effects and geometric frustration in pyrochlore based lattices in this thesis. The thesis consists of six chapters as detailed below.

Chapter 1: Introduction - We provide a quick review of the experimental observation of Mott transition in real life pyrochlores, the rare earth molybdates and iridates, and a summary of the theory situation. In the pyrochlore oxides $R_2Mo_2O_7$ and $R_2Ir_2O_7$, where R is a rare earth or Y, the Mo and Ir ions live on a pyrochlore lattice while the R inhabit an interpenetrating pyrochlore structure. These materials allow variation of the correlation strength via application of pressure, or change of ionic radius, or an applied magnetic field, driving an insulator-metal transition (IMT).

The molybdates exhibit an IMT with increasing rare earth ionic radius r_A [1–3]. Materials with larger r_A are ferromagnetic (FM) metals, those with small r_A are spin glass (SG) insulators, and there is a SG metal phase near the MIT [4]. Pressure and magnetic field can drive an IMT in materials like $Gd_2Mo_2O_7$ which is weakly insulating [5]. An anomalous Hall effect (AHE) has been observed [6,7] in $Nd_2Mo_2O_7$ and is ascribed to non vanishing spin chirality.

The iridates also show an IMT with increasing r_A , but in this case the transition is accompanied by a magnetic transition from a paramagnetic to an antiferromagnetic ‘all-in-all-out’ (AIAO) ordering [8,9]. While the magnetic character differs distinctly from molybdates, iridates also show a pressure driven insulator-metal transitions, via unusually resistive ground states [10,11], and spin chirality driven AHE in materials like $Pr_2Ir_2O_7$ [12,13].

In contrast to 3d electron based systems which are dominated by the Hubbard U , the molybdates involve 4d electrons - where the Hund’s coupling J_H is also important, while the iridates involve 5d electrons - with spin-orbit coupling playing a vital role. This chapter discusses the phenomenology of these materials and the basic theory results in the field.

Chapter 2: Theoretical tools - We study the single band Hubbard model, with nearest neighbour hopping, on the pyrochlore lattice:

$$H = \sum_{ij,\sigma} (t_{ij} - \mu\delta_{ij}) c_{i\sigma}^\dagger c_{j\sigma} + U \sum_i n_{i\uparrow} n_{i\downarrow} \quad (1)$$

where $t_{ij} = -t$ for nearest neighbour hopping on the pyrochlore lattice and $U > 0$ is the Hubbard repulsion. We will set $t = 1$. The chemical potential μ is varied to

maintain the density at $n = 1$ as the interaction and temperature T are varied.

We use a Hubbard-Stratonovich (HS) transformation that introduces a vector field $\mathbf{m}_i(\tau)$ and a scalar field $\phi_i(\tau)$ at each site to decouple the interaction [14]. This decomposition retains the rotation invariance of the Hubbard model, and hence the correct low energy excitations, and reproduces unrestricted Hartree-Fock theory at $T = 0$.

We treat the \mathbf{m}_i and ϕ_i as classical fields, *i.e.*, neglect their time dependence, but completely retain the *thermal fluctuations* in \mathbf{m}_i . ϕ_i is treated at the saddle point level, *i.e.*, $\phi_i \rightarrow \langle \phi_i \rangle = (U/2)\langle \langle n_i \rangle \rangle = U/2$ at half-filling, since charge fluctuations would be penalised at temperatures $T \ll U$. Retaining the spatial fluctuations of \mathbf{m}_i allows us to estimate T_c scales, and access the crucial thermal effects on transport. In the literature the overall scheme is known as the ‘static path approximation’ (SPA) to the functional integral for the partition function. Within this approach the half-filled Hubbard problem is mapped on to electrons coupled to the field \mathbf{m}_i , which itself follows a distribution function $P\{\mathbf{m}_i\}$.

$$\begin{aligned}
 H_{eff} &= \sum_{ij,\sigma} (t_{ij} - \mu\delta_{ij}) c_{i\sigma}^\dagger c_{j\sigma} - \frac{U}{2} \sum_i \mathbf{m}_i \cdot \vec{\sigma}_i + \frac{U}{4} \sum_i \mathbf{m}_i^2 \\
 P\{\mathbf{m}_i\} &\propto \text{Tr}_{cc^\dagger} e^{-\beta H_{eff}}
 \end{aligned} \tag{2}$$

where the chemical potential μ is replaced by $\tilde{\mu} = \mu - \frac{U}{2}$. H_{eff} can be seen as comprising of an electronic Hamiltonian, H_{el} (the first three terms) and the classical ‘stiffness’ $H_{cl} = \frac{U}{4} \sum_i \mathbf{m}_i^2$. In an exact calculation, where the dynamics of \mathbf{m}_i and ϕ_i are retained, H_{eff} would be replaced by an effective action while P would be replaced by a fermion determinant in the $\{\mathbf{m}, \phi\}$ background. Within SPA H_{eff} and $P\{\mathbf{m}_i\}$ define a coupled fermion-local moment problem.

The method of choice in these situations is a combination of Monte Carlo (MC) for updating the \mathbf{m}_i with exact diagonalisation (ED) of the fermion Hamiltonian for computing the Metropolis update cost. To access large sizes within limited time, we use a cluster algorithm for estimating the update cost [15]. The energy cost of updating the variable \mathbf{m}_i is computed by diagonalizing a cluster (of size N_c , say) constructed around the site \mathbf{R}_i .

Chapter 3: Mott transition on the pyrochlore lattice - The pyrochlore lattice involves corner sharing tetrahedra and the resulting geometric frustration is believed to suppress any antiferromagnetic order for Mott insulators on this structure [16–18]. There are nevertheless short range correlations which could be vital

near the Mott-Hubbard insulator-metal transition. We use a static auxiliary field based Monte Carlo to study this problem in real space on reasonably large lattices. The method reduces to unrestricted Hartree-Fock at zero temperature but captures the key magnetic fluctuations at finite temperature. Our results reveal that increasing interaction drives the non magnetic (semi) metal to a ‘spin disordered’ metal with small local moments, at some critical coupling, and then, through a small pseudogap window, to a large moment, gapped, Mott insulating phase at a larger coupling. The spin disordered metal has a finite residual resistivity which grows with interaction strength, diverging at the upper coupling. We present the resistivity, optical conductivity, and density of states across the metal-insulator transition and for varying temperature. These results set the stage for the more complex cases of Mott transition in the pyrochlore iridates and molybdates.

Chapter 4: Mott transition on the checkerboard lattice - The checkerboard lattice, with alternating ‘crossed’ plaquettes, serves as the two dimensional analog of the pyrochlore lattice. The corner sharing plaquette structure leads to a hugely degenerate ground state, and no magnetic order, for classical spins with short range antiferromagnetic interaction. For the half-filled Hubbard model on this structure, however, we find that the Mott insulating phase involves virtual electronic processes that generate longer range and multispin couplings. These couplings lift the degeneracy, selecting a ‘flux like’ state in the Mott insulator. Increasing temperature leads, strangely, to a sharp crossover from this state to a ‘120 degree’ correlated state and then a paramagnet. Decrease in the Hubbard repulsion drives the system towards an insulator-metal transition - the moments reduce, and a spin disordered state wins over the flux state. Near the insulator-metal transition the electron system displays a pseudogap extending over a large temperature window.

Chapter 5: Mott physics in the molybdates - The rare earth based pyrochlore molybdates involve orbitally degenerate electrons Hund’s coupled to local moments. The large Hund’s coupling promotes ferromagnetism, the superexchange between the local moments prefers antiferromagnetism, and Hubbard repulsion tries to open a Mott gap. The phase competition is tuned by the rare earth ionic radius, decreasing which leads to change from a ferromagnetic metal to a spin disordered highly resistive ground state, and ultimately an ‘Anderson-Mott’ insulator. We attempt a quantitative theory of the molybdates by studying their minimal model [19] on a pyrochlore geometry, using a static auxiliary field based Monte Carlo. We establish a thermal phase diagram that closely corresponds to the experiments, predict

the hitherto unexplored orbital correlations, quantify and explain the origin of the anomalous resistivity, and present dynamical properties across the metal-insulator transition.

Chapter 6: Mott physics in the iridates - The iridate ($R_2Ir_2O_7$) structure consists of two interpenetrating pyrochlore lattices, one formed by Ir cations and the other by R. We ignore the orbitals on R and oxygen, focusing instead on the orbitals on Ir. The Ir atom has octahedral oxygen coordination, resulting a crystal field environment which splits the tenfold degenerate (considering both orbital and spin degeneracy) Ir 5d states into fourfold degenerate e_g and sixfold degenerate t_{2g} manifolds. Strong spin-orbit coupling (SOC) of Ir splits the t_{2g} levels further into an effective total angular momentum $J_{eff} = 1/2$ doublet and $J_{eff} = 3/2$ quartet levels. The Ir cation is nominally tetravalent (Ir^{4+}) and has five electrons on average. The deeper $J_{eff} = 3/2$ quartet levels get one electron each, and the single electron in the $J_{eff} = 1/2$ doublet levels is the ‘itinerant’ degree of freedom [20]. The e_g states remains unoccupied. Thus the iridates have one itinerant electron in two degenerate $J_{eff} = 1/2$ levels, making it an effectively half-filled $J_{eff} = 1/2$ single band system. Hubbard repulsion on this narrow bands opens a Mott gap, making it a $J_{eff} = 1/2$ Mott insulator.

To study the Mott transition in the iridates, we use the one band Hubbard model with a spin-orbit coupling as the minimal model. This model is studied via a Monte-Carlo sampling. We discover that

- the low temperature state is a paramagnetic metal at weak interaction, but a Mott insulator with all-in-all-out order at intermediate and strong interaction.
- there is a narrow pseudogap window near the insulator-metal boundary.

We make qualitative comparisons of our transport results with that of the iridates. We have established the overall phase diagram in terms of correlation strength, SOC and temperature. We delineate the metal, semi-metal, and insulator phases, their topological character, the nature of magnetic order and the finite temperature charge dynamics.

LIST OF FIGURES

1.1	Three Ising spins on a triangle	10
1.2	Different lattices in 2D and 3D	10
1.3	$J_1 - J_2$ antiferromagnet on a square lattice geometry	11
1.4	Spinel system- AB_2O_4	13
1.5	Hyper-kagome system - $Na_4Ir_3O_8$	14
1.6	Characteristic behaviour of a geometrically frustrated antiferromagnet	15
1.7	Ground state of a frustrated plaquette with four Heisenberg spins . .	16
1.8	Ground state of Heisenberg spins on Kagome lattice	18
1.9	Phase space of frustrated antiferromagnets	19
1.10	Fluctuations away from ground state configurations for a plaquette of four spins	19
1.11	Phase space of frustrated magnets - Order by disorder	20
1.12	Mott physics in V_2O_3	22
1.13	Mott physics in high T_c cuprates	23
1.14	Schematic picture of the Mott transition	26
1.15	Interpenetrating pyrochlore lattice structures of rare earth oxides . .	28
1.16	Illustration of the MIT based on rare earth ionic size	29
1.17	MIT in molybdates - experimental indicators	30
1.18	MIT in iridates - experimental indicators	32
1.19	MIT in molybdates - theory study	35
1.20	MIT in iridates - theory study	37
2.1	Visualisation of the our cluster based update scheme	44
2.2	Benchmarking - System size dependence	49
2.3	Benchmarking - Annealing time dependence	49
2.4	Benchmarking - Cluster based update	50

3.1	Pyrochlore lattice structure	52
3.2	Pinch-points in the pyrochlore lattice	53
3.3	Pyrochlore results - ground state behaviour	55
3.4	Pyrochlore results - phase diagram	56
3.5	Pyrochlore results - density of states	58
3.6	Pyrochlore results - resistivity	59
3.7	Pyrochlore results - optical conductivity	60
3.8	Pyrochlore results - magnetic susceptibility	62
3.9	Pyrochlore results - distribution of local moments	64
3.10	Pyrochlore results - magnetic structure factor	65
3.11	Pyrochlore results - variational calculation for average moment value	66
4.1	Checkerboard lattice structure	68
4.2	Checkerboard results - magnetic structure factor	71
4.3	Checkerboard results - phase diagram	72
4.4	Checkerboard results - temperature dependence of structure factor peak	73
4.5	Checkerboard results - average local moment and it's distribution	74
4.6	Checkerboard results - density of states	75
4.7	Checkerboard results - Free energy comparison	76
4.8	Checkerboard results - magnetic susceptibility	79
4.9	Checkerboard results - DOS for ideal confurations	81
5.1	Mo 4d level split in the molybdates	85
5.2	Schematic of relevant interactions and hopping processes in the molybdates.	86
5.3	Ground state results of molybdate model - phase diagram	89
5.4	Ground state results of molybdate model - effective ferromagnetic exchange	90
5.5	Ground state results of molybdate model - magnetisation and orbital moment	91
5.6	Ground state results of molybdate model - magnetic structure factor	93
5.7	Ground state results of molybdate model - orbital moment distribution	94
5.8	Ground state results of molybdate model - orbital structure factor	94
5.9	Ground state results of molybdate model - density of states	95
5.10	Ground state results of molybdate model - optical conductivity	96
5.11	Ground state results of molybdate model - comparison of optical gap with spectral gap	97

5.12	Ground state results of molybdate model - inverse participation ratio	98
5.13	Ground state results of molybdate model - IPR and rescaled gaps . .	99
5.14	Finite temperature results of molybdate model - overall phase diagram	100
5.15	Finite temperature MIT in the double exchange dominated region . .	102
5.16	Temperature dependence of magnetic structure factor in the double exchange dominated region	103
5.17	Average orbital moment distribution in the double exchange domi- nated region	104
5.18	Temperature dependence of orbital structure factor in the double ex- change dominated region	104
5.19	Temperature dependence of DOS and optics in the double exchange dominated region	105
5.20	Temperature dependence of resistivity in the double exchange domi- nated region	107
5.21	Finite temperature MIT in the competing phase region	109
5.22	Temperature dependence of magnetic structure factor in the phase competing region	110
5.23	Average orbital moment distribution in the competing phase region .	111
5.24	Temperature dependence of orbital structure factor in the competing phase region	111
5.25	Temperature dependence of DOS and optics in the competing phase region	112
5.26	Temperature dependence of resistivity in the competing phase region	113
5.27	Finite temperature MIT in the superexchange dominated region . . .	115
5.28	Temperature dependence of magnetic structure factor in the superex- change dominated region	116
5.29	Average orbital moment distribution in the superexchange dominated region	117
5.30	Temperature dependence of orbital structure factor in the superex- change dominated region	117
5.31	Temperature dependence of DOS and optics in the superexchange dominated region	118
5.32	Temperature dependence of resistivity in the superexchange domi- nated region	119
5.33	Calibration of the theory gap with the experiments	122
5.34	Experiment versus theory comparison - phase diagrams	123

5.35	Experiment versus theory comparison - resistivity	124
5.36	Experiment versus theory comparison - effective carrier density	125
5.37	Prediction from our theory results - density of states	126
5.38	Experiment versus theory comparison - phase diagrams	127
6.1	MIT in iridates under application of hydrostatic pressure	130
6.2	MIT in iridates by applying an external magnetic field	130
6.3	MIT in iridates - theoretical understanding	131
6.4	Ir 5d level splitting in the pyrochlore iridates	132
6.5	Schematics of the Mott transition in the iridates.	133
6.6	Nearest-neighbour Dzyaloshinski-Moriya vectors on the pyrochlore lattice	134
6.7	Results of iridate model - phase diagram in the non-interacting limit .	136
6.8	Results of iridate model - average moment and spectral gap in the ground state	137
6.9	Results of iridate model - thermal phase diagram	138
6.10	Results of iridate model - magnetic structure factor	139
6.11	Results of iridate model - temperature dependence of magnetic structure factor peak	140
6.12	Results of iridate model - resistivity	141
6.13	Results of iridate model - temperature dependence of optics and DOS	142
6.14	Results of iridate model - effect of spin-orbit coupling on phase diagram and resistivity	143
6.15	Theory and experiment comparison - thermal phase diagram	145
6.16	Theory and experiment comparison - resistivity	146

LIST OF TABLES

1.1	Some characteristic quantities of the frustrated spinel materials. . . .	12
1.2	Comparison of the ground states and magnetic entropy in the ground state for Ising spins on different lattices.	17
1.3	The magnetic ground states for different classes of spins on several frustrated lattices.	21
5.1	Changing physical properties, as one moves from DE dominated to phase competing to the SE dominated regimes.	120

INTRODUCTION

In any solid the spin, charge, and the lattice degrees of freedom are all coupled together. However there are situations where the low energy physics is primarily governed by only one of the degrees of freedom. For example in a magnetic insulator, where the charge gap is sufficiently large, the low energy physics is primarily governed by the excitations of magnetic nature. Such systems can safely be investigated using an effective ‘spin-only’ description. In these problems the lattice geometry plays an important role, with several interesting effects arising purely due to the geometry.

1.1 Geometric frustration

1.1.1 General overview

The study of geometrically frustrated antiferromagnets is mainly concerned with what happens when lattice geometry inhibits the formation of an ordered low-temperature magnetic configuration [21–24]. These systems present greater experimental and theoretical challenges than those posed by simple antiferromagnets. The origin of the complex behaviour in such a magnet can simply be illustrated by considering just three antiferromagnetically coupled Ising spins on a triangular structure (Fig.1.1). Once two of the spins on the triangle are aligned antiparallel to satisfy their antiferromagnetic interaction, the third one can no longer point in a direction opposite to both of them. On the triangle not all interactions can be minimised simultaneously.

Now consider lattices with this kind of ‘frustrating’ motifs. The existence of a unique ground state for a lattice, with all pairwise antiferromagnetic interactions satisfied, is possible only when the lattice sites can be divided into two sub-lattices.

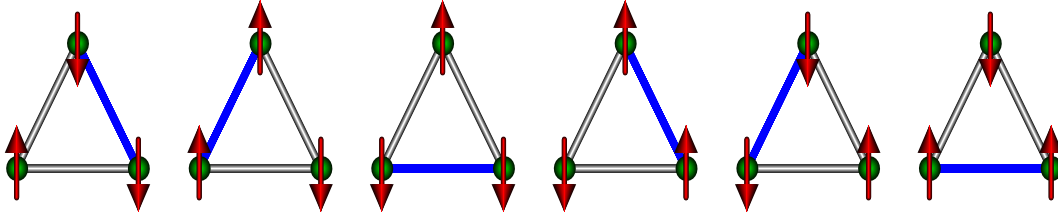


Figure 1.1: Demonstration of possible antiparallel spin arrangements for three spins on an elementary triangle. Each configuration has two bonds with antiparallel arrangement satisfied (denoted by a grey line) and one bond unsatisfied (denoted by a blue line).

This is the case of a bipartite lattice resulting in the antiferromagnetic Neel state. It can occur, for example, on a square lattice (Fig.1.2(a)), and a simple cubic lattice. However, for the triangular lattice (Fig.1.2(b)), such a division of the lattice into two sub-lattices, does not work. This lattice is non-bipartite. Other lattices belonging to this class are the face centered cubic (FCC) lattice (Fig.1.2(c)) and the pyrochlore lattice (Fig.1.2(d)). On such a lattice it is geometrically impossible to satisfy all the pairwise interactions simultaneously, i.e., to have a Neel state. These are *frustrated* antiferromagnets. Based on this nomenclature, antiferromagnets with square or simple cubic lattice geometries are referred as *unfrustrated* antiferromagnets. One reason for studying frustrated antiferromagnets is that they escape Neel order, and the resulting correlated low temperature state would have novel features.

Though evading Neel order is a characteristic of geometrically frustrated antiferromagnets, there exists situations where Neel order can be avoided even on a bipartite lattice due to the presence of competing interactions which make contributions to the energy that cannot be minimised simultaneously. As an example, consider the

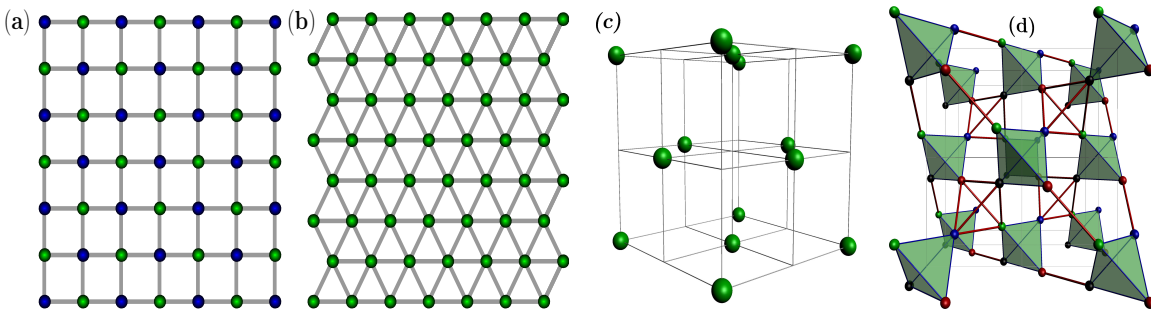


Figure 1.2: (a) The square lattice is bipartite as we can divide it into two sub-lattices, say blue and green, where neighbours of blue are only green (and vice versa). (b) In the triangular lattice such division is not possible. The same is true for the FCC and the pyrochlore lattices ((c) and (d)).

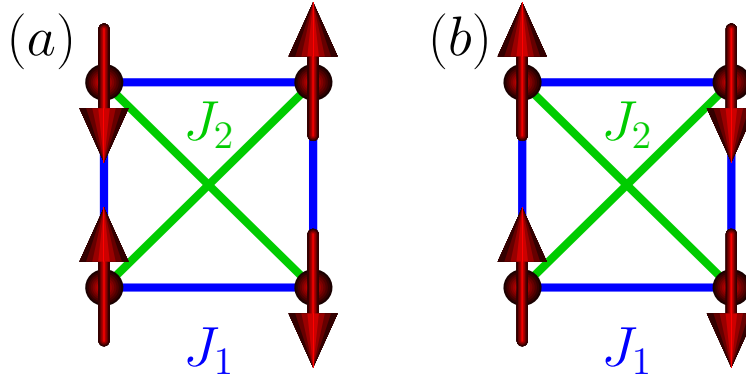


Figure 1.3: The antiferromagnetic $J_1 - J_2$ model on a square lattice geometry, showing ground state spin configurations for : (a) $J_1 > 2J_2$, (b) $J_1 < 2J_2$.

antiferromagnetic $J_1 - J_2$ model (both $J_1 > 0$ and $J_2 > 0$) on the square lattice [25] (Fig. 1.3). The classical ground state of this model depends on the ratio of nearest neighbour and further neighbour interaction, J_1/J_2 . For $J_1 > 2J_2$, all nearest neighbour spins are antiparallel. This enforces ferromagnetic arrangements of second neighbours and results in the frustration of the J_2 interaction. In the regime, $J_1 < 2J_2$, second neighbours are antiferromagnetically aligned. This occurs at the expense of frustration of half of the J_1 interactions. At $J_1 = 2J_2$, these classical states are degenerate. While this model provides an attractive point for theoretical work, such models are difficult to realise experimentally (due to the fine-tuning of interaction required). From this perspective, the existence of *frustrated magnets which destabilise Neel order, with only nearest neighbour interactions and solely due to the geometry of the underlying lattice* is very important.

1.1.2 Experimental relevance

The spinel AB_2O_4 with the A site occupied by a nonmagnetic ion (such as Zn or Cd or Hg), and the B site occupied by Cr^{3+} ions with spin $S = 3/2$ on a pyrochlore lattice (see figure 1.4) is a prototypical frustrated system. In table 1.1, we have listed out some of the characteristic quantities of the frustrated spinel materials. The presence of strong frustration is clear from the temperature dependence of the magnetic susceptibility $\chi(T)$, and magnetic specific heat $C_m(T)$ [26, 27]. There is no signal of any magnetic transition for $T \sim |\Theta_{CW}|$, where the Curie-Weiss constant, Θ_{CW} , characterises the sign (negative for an antiferromagnet) and strength of interactions. $ZnCr_2O_4$ which has a Curie-Weiss scale of 390 K, does not show any evidence of magnetic ordering until it's cooled down to 12.5 K. Similarly $CdCr_2O_4$ and $HgCr_2O_4$

Compound	S	Θ_{CW} (K)	T_N (K)	f	References
ZnCr ₂ O ₄	3/2	-390.0	12.5	31.2	[26–28]
CdCr ₂ O ₄	3/2	-70.0	7.8	9.0	[26, 29]
HgCr ₂ O ₄	3/2	-32.0	5.8	5.5	[26, 30]

Table 1.1: Some characteristic quantities of the frustrated spinel materials. S denotes the spin quantum number, T_N is the Neel ordering temperature, Θ_{CW} is the Curie-Weiss scale (negative for antiferromagnetism) extracted from susceptibility measurements, and f denotes the degree of frustration, computed as $f = \frac{|\Theta_{CW}|}{T_N}$.

show no sign of magnetic ordering until $T \sim 10$ K, despite the Curie-Weiss scales being 70K and 32K respectively. The phase in the regime $T_N < T < |\Theta_{CW}|$ is a spin-liquid. In this regime, a large magnetic entropy $S_m(T)$ is associated with the system, indicating the presence of high density of low energy spin excitations. Inelastic neutron scattering measurements of ZnCr₂O₄ at low energy transfer show a strong signal above $T_N = 12.5$ K (see figure 1.4.(e)) over a broad wave number window [28]. This temperature window corresponds to the cooperative paramagnetic regime. For $T < T_N$, the low energy spectral weight concentrates into a constant energy mode. The frustrated pyrochlore lattice structure of the Cr sublattice is mainly attributed to these behaviours in the spinels.

Another spinel compound, Na₄Ir₃O₈, has a hyper-kagome lattice structure [31]. The B sites of this spinel are occupied by $S = 1/2$ Ir⁴⁺ and nonmagnetic Na⁺ ions, such that each tetrahedron has three Ir⁴⁺ ions and one Na⁺ ion. The Ir⁴⁺ ions form corner-sharing triangles, with little twisting, and the structure is known as “hyper-kagome” lattice. Magnetic susceptibility measurements have estimated $\Theta_{CW} \sim -650$ K. Despite this large Curie-Weiss scale, no signature of magnetic order has so far been observed in the magnetic susceptibility or the specific heat, or neutron diffraction studies down to 2K [31]. Thus, geometrical frustration seems to be very strong in this system. It is believed that the ground state of this three-dimensional $S = 1/2$ hyper-kagome system is a quantum spin liquid [31].

The following general inferences can be made based on the behaviour of the above mentioned frustrated magnets.

(i) The characteristic signature of a frustrated magnet is the dependence of its magnetic susceptibility on temperature T . At high temperature, the inverse susceptibility has the linear form $\chi^{-1} \propto T - \Theta_{CW}$. In unfrustrated systems, a magnetic order, signalled by a cusp in χ , appears at the Neel temperature T_N , which is a

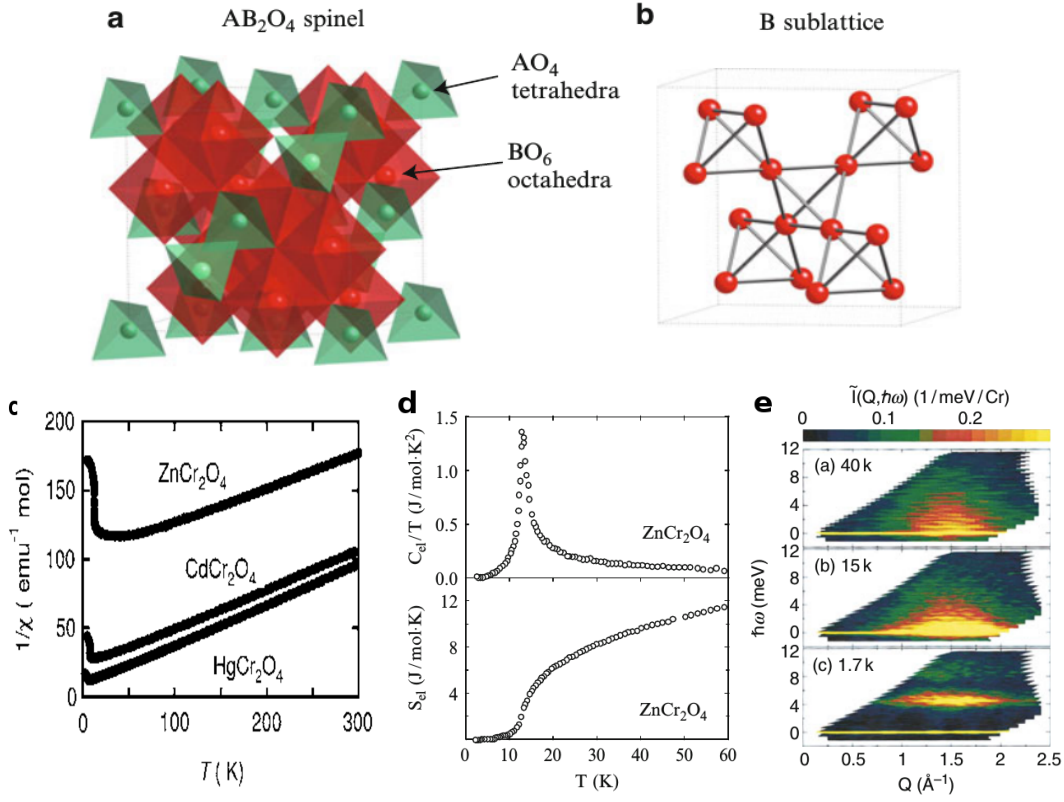


Figure 1.4: (Taken from [26–28]) (a) The spinel structure, with the two basic structural units of AO_4 tetrahedra and BO_6 octahedra. (b) The B sublattice of the spinels, forming a pyrochlore lattice. (c) Behaviour of inverse magnetic susceptibility $1/\chi$ with temperature. (d) Variation of magnetic specific heat $C_m(T)$ and magnetic entropy $S_m(T)$ with temperature for $ZnCr_2O_4$. (e) Contour plot of magnetic neutron scattering intensity in the plane of energy transfer $\hbar\omega$ and wave number Q for $ZnCr_2O_4$ for indicated temperatures.

fraction of the Curie-Weiss scale. In geometrically frustrated systems nothing sharp is observed at the temperature scale $T \sim |\Theta_{CW}|$; instead, the paramagnetic phase extends to temperatures $T \ll \Theta_{CW}$ and in some cases to zero temperature. At a lower temperature, T_c , spin freezing or a frustration-relieving structural transition might appear. This behaviour is illustrated schematically in figure 1.6. A simple measure of the degree of frustration was introduced by Ramirez [21], as the ratio $f \equiv \frac{|\Theta_{CW}|}{T_c}$. The state of the system in the temperature range $T_c < T \ll \Theta_{CW}$, where spins are highly correlated and strongly fluctuating, was termed by Villain, a *cooperative paramagnet* [32]. This is also identified as a classical spin liquid state.

(ii) Another important feature of frustrated magnets is their finite residual entropy for $T \ll |\Theta_{CW}|$. At very high temperature, the entropy per spin of a $S = 1/2$ system is $S = k_B \ln 2$. With decreasing temperature, correlations develop between

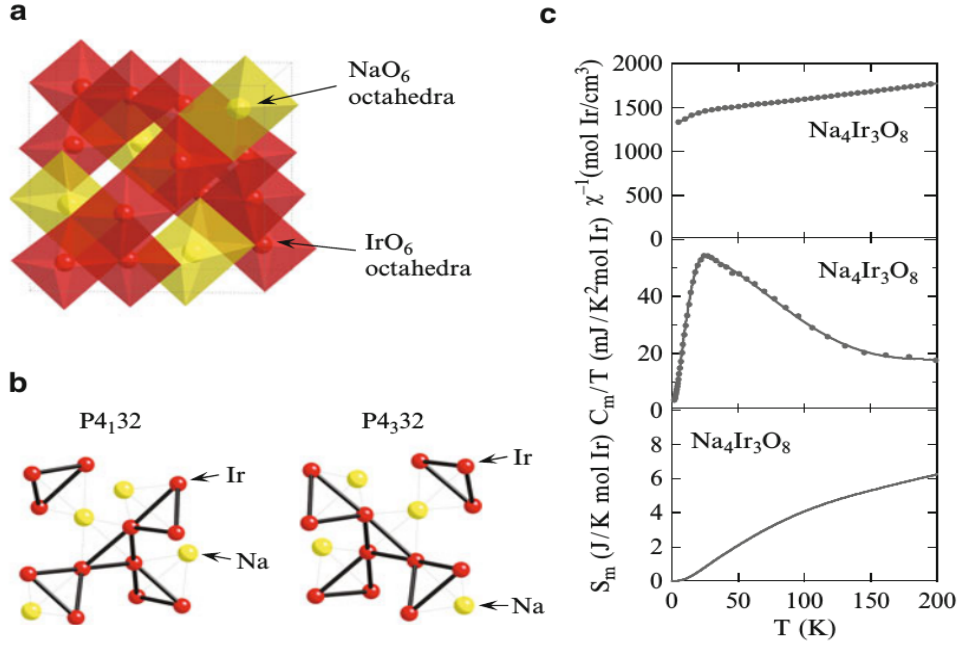


Figure 1.5: (Taken from [31]) (a) Crystal structure of $\text{Na}_4\text{Ir}_3\text{O}_8$ showing the NaO_6 and IrO_6 octahedra. (b) Two types of Ir_3Na sublattice with different chirality. The Ir ions form a hyper-kagome lattice. (c) Inverse magnetic susceptibility $1/\chi$, magnetic specific heat $C_m(T)$, and magnetic entropy $S_m(T)$ for the hyper-kagome system $\text{Na}_4\text{Ir}_3\text{O}_8$.

the spins. An unfrustrated system will order below a critical temperature, having zero entropy. However, a frustrated system may not order owing to finite entropy even for $T \ll |\Theta_{CW}|$. This finite residual entropy of the frustrated magnets are attributed to the existence of large ground state degeneracy.

(iii) Detailed information on the low temperature behaviour of geometrically frustrated magnets is provided by magnetic neutron scattering. The structure factor $S(\mathbf{Q})$ shows a broad peak at finite wavevector \mathbf{Q} (see Fig. 1.6). This suggests that the spin correlations are predominantly short-ranged. The width of this peak indicates a correlation length of the order of the lattice spacing, while the small value of the elastic scattering cross-section for $\mathbf{Q} \rightarrow \mathbf{0}$ shows that correlations suppress long wavelength fluctuations in magnetisation density. This is in contrast both to that in unfrustrated antiferromagnets, where Neel order leads to magnetic Bragg peaks, and to that in systems with short-range ferromagnetic correlations, where the structure factor is peaked at $\mathbf{Q} = \mathbf{0}$.

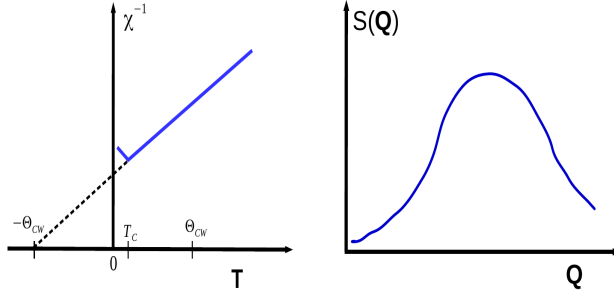


Figure 1.6: Characteristic behaviour of a geometrically frustrated antiferromagnet. (Left) Sketch of χ^{-1} vs T . (Right) Sketch of $S(Q)$ vs Q .

1.1.3 Theoretical understanding

1.1.3.1 Ground state degeneracy

An essential feature of any highly frustrated system is the existence of extensive classical ground state degeneracy. This degeneracy suggests that within the ground state manifold there are local fluctuations which take place independently in different parts of a large system. However, the counting of the classical ground state degeneracy depends on whether we treat the spin variables as discrete variables (e.g. Ising spins) or continuous variables (e.g. classical Heisenberg spins). Some of the most important lattices for the study of geometrically frustrated magnets can be constructed as corner-sharing arrangements of their frustrated units (plaquettes). For such lattices constructed out of corner-sharing arrangements of frustrated plaquettes, with local magnetic moments at the vertices of each plaquette and exchange interactions of equal strength J between all moments in each plaquette, the Hamiltonian has the form

$$H = J \sum_{\langle ij \rangle} \mathbf{S}_i \cdot \mathbf{S}_j \equiv \frac{J}{2} \sum_p |\mathbf{S}_p|^2 + c \quad (1.1)$$

where $\mathbf{S}_p = \sum_{i \in p} \mathbf{S}_i$. The ground state has spin configurations such that the total spin on each plaquette is zero.

Let us count the ground state degeneracy for the pyrochlore lattice. We begin by examining a single tetrahedral plaquette of four spins, with the Hamiltonian $H_p = \frac{J}{2} |\mathbf{S}_p|^2 + \tilde{c}$, where $\mathbf{S}_p = \mathbf{S}_1 + \mathbf{S}_2 + \mathbf{S}_3 + \mathbf{S}_4$. We see that the ground states are those with $\mathbf{S}_p = \mathbf{0}$. For the discrete Ising spins, in a single plaquette, out of a total of $2^4 = 16$ states, 6 states form the ground state manifold. In a pyrochlore lattice, made up of N_p plaquettes (tetrahedra), we have in total $N_s = 2N_p$ spins (each spin is corner-shared between two tetrahedra) and a total of 2^{2N_p} states. The number of ground

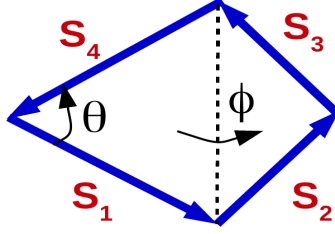


Figure 1.7: A ground state configuration for a frustrated plaquette of four classical Heisenberg spins

states for the Ising spins on the pyrochlore lattice (assuming that the restrictions to ground states are independent on each tetrahedron) is estimated as $-2^{2N_p} \times (\frac{6}{16})^{N_p} = (\frac{3}{2})^{N_p} = (\frac{3}{2})^{N_s/2}$, which is an extensive quantity. The residual entropy per spin, $S = 1/2 \ln(3/2)$, calculated this way turns out to be very close to the measured entropies in some of the spin-ice compounds [33]. For the classical Heisenberg spins (continuous spin degrees of freedom), the ground states on a plaquette have two internal degrees of freedom – the angles θ and ϕ (see Fig. 1.7), in addition to the degeneracies under global rotations which are expected from the symmetry of H_p .

To understand how this accidental ground state degeneracy extends from a single plaquette to a periodic lattice the Maxwellian counting argument has been used [34]. This counting principle compares F , the number of degrees of freedom in the system with K , the number of constraints that must be satisfied in ground states. The central point is that if all constraints are independent, then the number of ground state degrees of freedom is given by $D = F - K$. For a system of N_s classical Heisenberg spins, $F = 2N_s$, since two angles are required to specify the orientation of each spin. In a system with the Hamiltonian consisting of N_p plaquettes, $K = 3N_p$, since in ground states all three components of \mathbf{S}_p must be zero for every plaquette p (Under the assumptions that all constraints can be satisfied simultaneously, and that they are all linearly independent, we arrive at an estimate for D , the number of ground-state degrees of freedom: $D = F - K$. Taking the example of the pyrochlore lattice, we have $N_s = 2N_p$ (though four spins are associated with each tetrahedron, every spin is shared between two tetrahedra) and hence $D = N_c$, an extensive quantity.

This suggests that the ensemble of states satisfying the plaquette constraint has macroscopic entropy. Thus there are local degrees of freedom which can fluctuate independently without the system leaving its ground state manifold. This also imply that macroscopic degeneracy may prevent long range order at the temperature scale set by interaction strength, Θ_{CW} .

Lattices	Magnetic entropy	Ground state
Triangle	$S \approx 0.34k_B N$	Disordered
Checkerboard	$S \approx 0.216k_B N$	Disordered
Kagome	$S \approx 0.502k_B N$	Disordered
FCC	$S \sim k_B N^{1/3}$	Disordered
Pyrochlore	$S \approx 0.203k_B N$	Disordered

Table 1.2: Comparison of the ground state magnetic entropy (S) and phases for Ising spins on different lattices. N is the system size (number of spins on the lattice).

For any magnetic ordered state, the residual magnetic entropy in the ground state is zero. However, on frustrated lattices the residual magnetic entropy in the ground state may not vanish, rather the residual magnetic entropy dictates the ground state magnetic state in these systems. In table 1.2, we show the residual magnetic entropy in the ground state for Ising spins on various frustrated lattices.

Real materials with more complicated corner-sharing arrangements of frustrated plaquettes are also possible. The results of the Maxwellian counting argument do not depend on the details of the lattice under consideration, but rather on the size of the corner-sharing plaquettes. The Maxwellian counting argument has two possible limitations.

- The counting argument rests on an assumption that all ground state constraints are linearly independent. If this is not the case, we underestimate D . This occurs in the kagome lattice Heisenberg antiferromagnet. In this case the Maxwellian counting yields $D = 0$ since, the kagome lattice is built from corner-sharing triangles, $N_s = \frac{3N_p}{2}$. But by explicit construction, one finds sets of states with special spin arrangements for which $D = \frac{N_s}{9}$. Such an arrangement is illustrated in figure 1.8. But for the pyrochlore Heisenberg antiferromagnet, it is known that corrections to the estimate for D are at most sub-extensive [34].
- There can be frustrated lattices, where no spin configuration satisfy the plaquette constraint condition $\mathbf{S}_p = \mathbf{0}$ for all plaquettes p [34].

The phase space of a classical geometrically frustrated Heisenberg antiferromagnets is given in figure 1.9. In the (high-dimensional) phase space for the system as a whole, the ground states form a manifold with a dimension that is much smaller but nevertheless extensive. At temperatures small compared to the Curie-Weiss constant

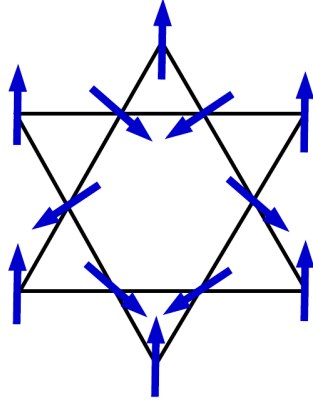


Figure 1.8: Illustration of the ground state degrees of freedom of the Heisenberg spins on the kagome lattice: spins on the central hexagon may be rotated together through any angle about the axis defined by the outer spins, without leaving the ground state.

($k_B T \ll JS^2$), the system is confined to a region of phase space that forms a thin layer around the ground state manifold. Quantum effects can be neglected provided $JS \ll k_B T$, and a strongly correlated, classical window, $JS \ll k_B T \ll JS^2$, opens up for $S \gg 1$.

1.1.3.2 Order by disorder

The extensive ground state degeneracy in the frustrated lattices is not a consequence of the symmetry of the Hamiltonian. So it is expected that the spectrum of fluctuations around each ground state is different. This accidental extensive degeneracy has interesting consequences in the presence of thermal or quantum fluctuations. One possibility is that the ground states with the lowest excitation frequencies are selected out, because the associated entropy at finite temperature is largest resulting in the lowest free energy. On the other hand at zero temperature, these excitations are associated with the lowest zero-point energy. This paradoxical mechanism, by which fluctuations enhance order instead of suppressing it, is termed ‘order by disorder’. Order by disorder in the frustrated magnet can be the result of thermal or quantum fluctuations about a classical ground state.

Effects of thermal fluctuations : To understand the effects of thermal fluctuation on lifting the ground state degeneracy, first consider a plaquette of four spins. Two ground states with fluctuations of contrasting types are illustrated in figure 1.10. For the configuration shown on the left, the total spin of the plaquette has a magnitude $|\mathbf{S}_p|$ that varies with the departure $\delta\theta$ from the ground state as $|\mathbf{S}_p| \propto \delta\theta$. Since the

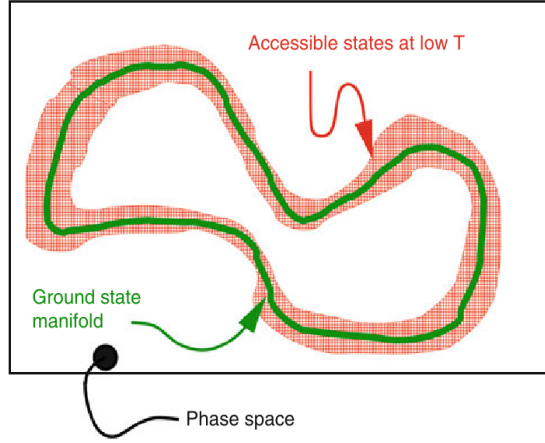


Figure 1.9: (Taken from the chapter-1 of [24]) Schematic view of phase space for a geometrically frustrated magnet.

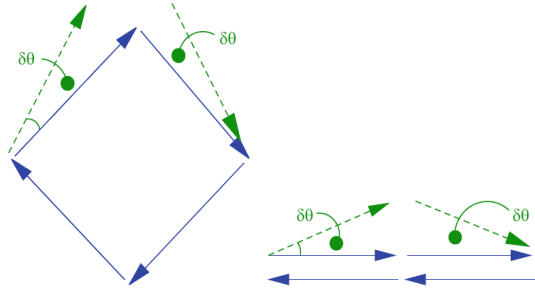


Figure 1.10: (Taken from the chapter-1 of [24]) Fluctuations away from ground state configurations for a plaquette of four spins. Left: a conventional fluctuation; right: a soft mode

excitation energy is proportional to $|\mathbf{S}_p|^2$, it has a conventional, quadratic dependence on $\delta\theta$. By contrast, for the excitation from a collinear ground state shown on the right, $|\mathbf{S}_p| \propto (\delta\theta)^2$. This later mode is therefore soft, with an energy proportional to $(\delta\theta)^4$. The presence of this soft mode prefers almost collinear configurations at low temperature. Through rigorous analytic calculations its shown that on the pyrochlore lattice, order by disorder is absent for Heisenberg spins, but present for XY spins [32].

The case for the lattice can be argued in a similar spirit. In most cases, the ground states with soft modes (see Fig 1.11) are selected by thermal fluctuations. One can explore this aspect by studying the system numerically via Monte Carlo simulations. Such calculations have shown that for the Heisenberg antiferromagnet on the kagome lattice there is coplanar spin ordering at $T \sim 10^{-3}J$ [35], while on the pyrochlore lattice there is no order by disorder.

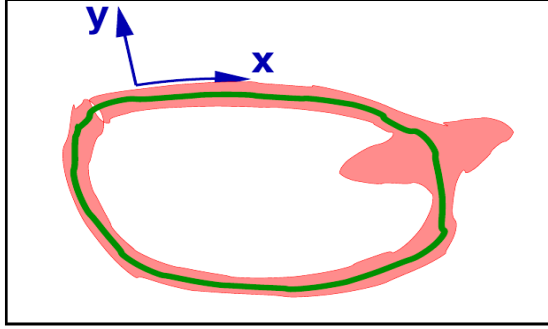


Figure 1.11: (Taken from the chapter-1 of [24]) Schematic view of phase space. The full curve represents the ground state manifold. Coordinates \mathbf{x} and \mathbf{y} are respectively parallel and perpendicular to it. The bulge region represents the points on the ground state manifold at which there are soft modes.

Effects of quantum fluctuations : Like thermal fluctuations, quantum fluctuations can also select out a ground state from the extensively degenerate classical ground state manifold. Using harmonic spin wave theory, the excitations around any point \mathbf{x} on the ground state manifold can be studied. Excitations involving the coordinates \mathbf{y} locally orthogonal to the ground state manifold are conventional modes with non-zero frequencies $\omega_l(\mathbf{x})$. By contrast, fluctuations involving the coordinates \mathbf{x} are, within a harmonic approximation, zero modes. The zero-point energy of the conventional, finite-frequency mode provides an effective Hamiltonian for these remaining degrees of freedom, the classical ground state coordinates. This Hamiltonian takes the form

$$H_{eff}(\mathbf{x}) = \frac{1}{2} \sum_l \hbar \omega_l(\mathbf{x}) \quad (1.2)$$

The ground state is the set of points \mathbf{x} at which $H_{eff}(\mathbf{x})$ is minimised, *i.e.* the ground state wave function, for large S , is peaked at the set of points $\mathbf{x} = \mathbf{x}_{\mathbf{G}}$. In the Heisenberg antiferromagnet model with large S , quantum fluctuations select out coplanar spin configurations on the kagome lattice [36] and collinear spin configurations on the pyrochlore lattice [37].

Difference between the effects of thermal and quantum fluctuations : In the limit $T \ll J$, order by disorder may arise due to thermal fluctuations depending on the nature of the ground state distribution. But in this limit, order by disorder arises due to quantum fluctuations for $S \gg 1$. This is because, for $S \gg 1$, quantum fluctuations around the minimum of $H_{eff}(\mathbf{x}) = \frac{1}{2} \sum_l \hbar \omega_l(\mathbf{x})$ are arbitrarily small. Nevertheless, order by disorder may not occur due to quantum fluctuations if S is sufficiently small (say, for $S = 1/2$), and one may end up having a spin liquid state.

Lattices	Ising	Heisenberg (classical)	Heisenberg ($S = 1/2$)
Triangle	Disordered [38]	Ordered 120-degree [39]	Ordered 120-degree [40]
Checkerboard	Disordered [41]	Classical spin liquid [18]	Valence bond solid [42]
Kagome	Disordered [43]	Coplanar $\sqrt{3} \times \sqrt{3}$ [44]	Quantum spin liquid [45]
FCC	Disordered [46]	Collinear AF [47]	Collinear AF [48]
Pyrochlore	Disordered [41]	Classical spin liquid [18]	Quantum spin liquid [49]

Table 1.3: The magnetic ground states for different classes of spins on several frustrated lattices.

In table 1.3, we compare the ground state magnetic phases of Ising spins with those of Heisenberg spins (classical and quantum).

1.2 Correlated electron systems

1.2.1 General overview

The basic classification of solids in terms of their electronic properties is based on band theory – a theory of the non interacting electrons on a lattice. Band theory predicts that (i) a completely filled or empty band results in insulating behaviour, (ii) partially filled bands lead to a metallic behaviour. This holds true mainly because the Pauli exclusion principle severely limits the phase space for electron collisions [50]. However, it was found that some compounds (e.g., NiO) at half-filling behave as insulators, contradicting the predictions of the band theory [51]. This requires us to widen the conditions under which solids exist as metals or insulators.

Electrons in a solid interact with each other while they move from site to site to gain kinetic energy. In the narrow band solids a tight binding description is reasonable. This is augmented by the inclusion of short range Coulomb repulsion between electrons. This electron electron interaction plays crucial role in determining electronic properties, and producing magnetic moments.

Slater suggested that an insulating state could arise as a result of long-range antiferromagnetic ordering (due to Fermi surface instability), which leads to a lattice period doubling (reduction of the brillouin zone), and opening of a gap at the Fermi level [52]. Later, it was shown by Mott that strong electron-electron interaction could prevent electron delocalisation (leading to an insulating state) if the bandwidth of the material falls below a critical value [53]. Thus, by tuning the electron-electron

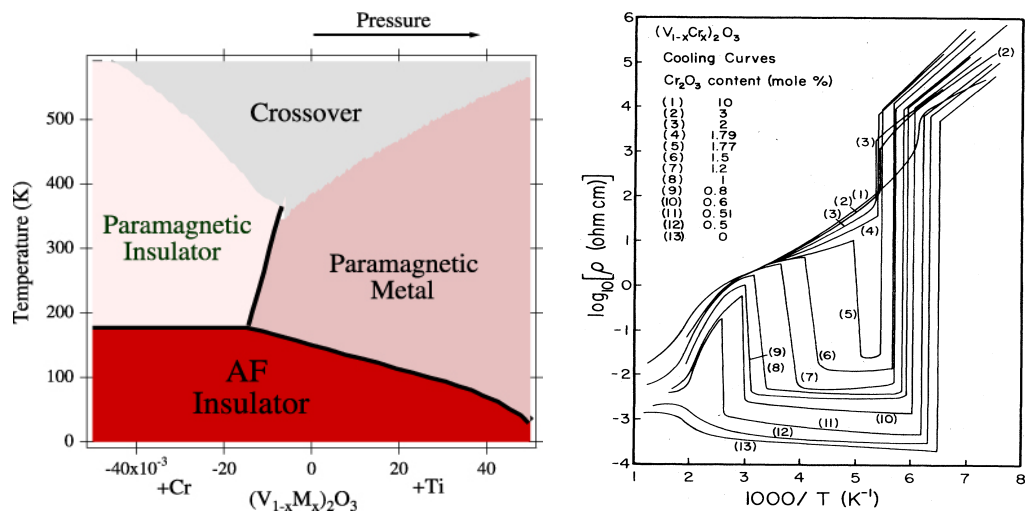


Figure 1.12: (Taken from [64, 65]) (Left) Phase diagram of V_2O_3 showing the Mott transition as a function of alloying with Cr and Ti. (Right) Variation of resistivity of $(V_{1-x}Cr_x)_2O_3$ with inverse temperature for Cr doping.

interaction a half-filled band metallic system can be turned into a Mott-insulator. This scenario is known as the Mott transition.

Detailed theoretical understanding of the Mott transition can be achieved by using the celebrated Hubbard model. The Hubbard model [54–57] describes electron delocalisation in the presence of local repulsion. Originally introduced to address itinerant ferromagnetism [55] in transition metals, its usefulness now extends to describing metal-insulator transitions, antiferromagnetic order, and possibly *d*-wave superconductivity. In several papers [58–62] Hubbard had worked out various limits of this model, giving an approximate description of the Mott transition. We will discuss the theory approaches in a later section.

1.2.2 Experimental relevance

In strongly correlated electron systems the strength of electron-electron interactions is comparable to or larger than the kinetic energy. The main motivations for the study of these systems arise from experiments on transition metal oxides. These show a wide variety of physical phenomena ranging from the Mott metal-insulator transition, high temperature superconductivity in the doped cuprates, itinerant ferromagnetism, and the ‘colossal’ magnetoresistance in the manganites.

Vanadium sesquioxide (V_2O_3) is considered the prototype material for illustrating the Mott transition [63, 64]. Doping Cr or Ti for V only changes the one-electron bandwidth via a slight modification of the lattice. This is analogous to applying

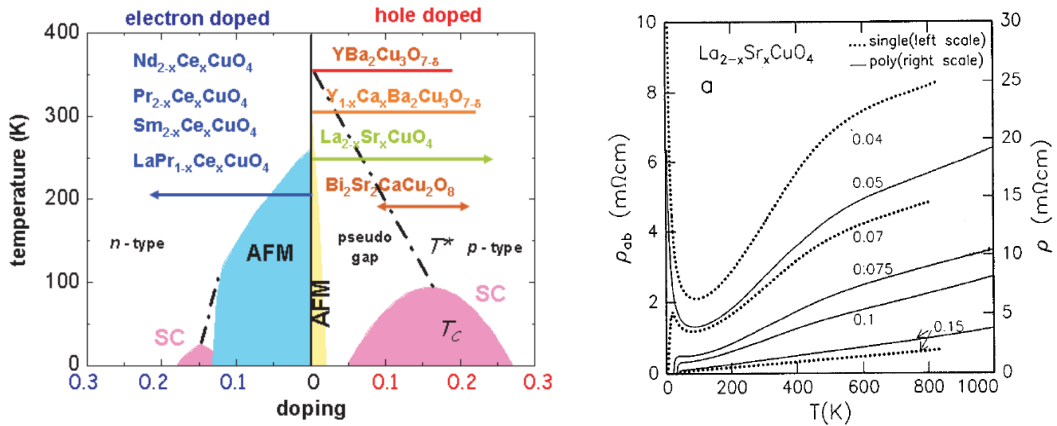


Figure 1.13: (Taken from [69] and [70]) (Left) Phase diagram of the electron and hole doped cuprates as a function of carrier concentration showing superconducting (SC), antiferromagnetic (AF), pseudogap, and normal metal regions. $doping = 0$ corresponds to the half-filled Mott insulating phase. This phase diagram shows the accessible regions for the different compounds of the cuprates family. (Right) Temperature dependence of the in-plane resistivity, ρ_{ab} , of the hole doped $La_{2-x}Sr_xCuO_4$ for doping concentrations $0.0 < x \leq 0.15$ (for single and poly crystals samples).

physical pressure and depends only on the size of the dopant ion. As the size of Ti^{3+} is larger than V^{3+} , alloying Ti for V in V_2O_3 can be thought of as applying a positive chemical pressure. The size of Cr^{3+} is smaller than V^{3+} . Alloying Cr for V in V_2O_3 is like applying a negative chemical pressure. The temperature versus alloying phase diagram shows the presence of three main phases: antiferromagnetic insulator (AFI), paramagnetic insulator (PI), and paramagnetic metal (PM). The PI phase is accessed via Cr alloying of V_2O_3 at temperatures higher than the Neel temperature. The high temperature phase above the critical point is a crossover regime between the paramagnetic insulator and paramagnetic metal. In figure 1.12(right panel), we show the resistivity of $(V_{1-x}Cr_x)_2O_3$ for $0 < x < 0.1$ [65]. The resistivity shows a metal-insulator transition (characterised by the sign change of $d\rho/dT$) at $T \sim 150K$ for $0 < x < 0.005$. This temperature scale coincides with the onset of antiferromagnetic ordering. For $0.005 < x < 0.018$ the resistivity shows insulating behaviour at low temperature, metallic behaviour at intermediate temperatures, and again an insulating behaviour at higher temperature. For $0.018 < x < 0.1$ the resistivity shows insulating behaviour at low and intermediate temperatures, but metallic at high temperatures.

In the cuprates, the undoped parent compound is a Mott insulator with antiferromagnetic order (see figure 1.13). Upon doping this Mott insulator, antiferromagnetism is destroyed, and above a critical doping superconductivity shows up with

$d_{x^2-y^2}$ pairing symmetry [66–68]. Figure 1.13 shows the accessible regions for the different compounds of the cuprates family and the temperature dependence of resistivity of hole doped cuprate, $\text{La}_{2-x}\text{Sr}_x\text{CuO}_4$, with doping. For $0.0 < x \leq 0.05$, we see a resistivity upturn as $T \rightarrow 0$, indicating an insulating state. For $0.05 < x \leq 0.15$, the resistivity vanishes as $T \rightarrow 0$, signalling the occurrence of superconductivity. Also a linear-T behaviour of the in-plane resistivity, ρ_{ab} over a wide temperature window is seen. This is a characteristic feature of the charge dynamics of the cuprates [70].

1.2.3 Theoretical understanding

Theoretical progress in the field of correlated electron systems has been impeded by the difficulty in dealing with even the simplest model Hamiltonians appropriate for these systems. The one-dimensional Hubbard model can be studied systematically. However there are no exact methods or controlled approximations to study the two and three-dimensional cases. This is mainly due to the non-perturbative nature of the problem, and reflects the presence of several competing physical mechanisms for even the simplest model.

Numerous approximate schemes have been employed to overcome these difficulties. In some cases an extreme limit of the model is considered where the problem simplifies and can be solved in a controlled manner. It is often easier to identify which of the physical aspects of the problem will be addressed by a specific limit, and thus to choose that specific limit best adapted to the physical phenomenon under consideration. In favourable cases, the physical ingredients that have been left out can be reintroduced by expanding around the starting point.

In recent times, with the dramatic increase in computational power a direct numerical solution of these models using exact diagonalisation and quantum Monte Carlo methods is possible. However, the exact diagonalisation technique is limited by the exponential growth of computation time with system size, while the quantum Monte Carlo method is often restricted to rather high temperatures by the sign problem.

In order to study the Mott transition and associated phenomena in real materials, one needs methods to solve the Hubbard model and its extended versions. Those models include parameters that are to be determined so as to reproduce experimentally measured physical properties of real systems as closely as possible. In order to check the validity of theoretical ideas through comparison with experiments, it is often desirable not only to adjust the model parameters but also to have independent estimates of those parameters a priori. Once we know the parameter values,

especially how they change when the chemical composition of materials is changed, we are able to predict to some extent the physical properties of those materials using the parameter values as an input to theoretical calculations. The development of powerful tools like dynamical mean field theory (DMFT) and its combination with *ab initio* methods has greatly served this purpose and have clarified many aspects of correlation physics over the last two decades [71].

One of the most drastic simplification in the Hubbard model is to consider only electrons in a single band. In contrast, the experimental systems – transition-metal compounds (d-electron systems) have large orbital degeneracy, which is an important source of complicated behaviour. In addition strong spin fluctuations, effects of orbital fluctuations and orbital symmetry breaking play important roles in many d-electron systems. The orbital correlations are frequently strongly coupled with spin correlations through the usual relativistic spin-orbit coupling as well as through orbital-dependent exchange interactions (e.g. manganites).

1.2.3.1 Basic features of the Mott transition

Correlated electronic systems [66, 71–73] involve strong short-range repulsion. At integer filling, the primary effect of correlation is the emergence of an insulating state where band theory predicts a metal. This insulating state is very different from the band insulator and involves non trivial magnetic correlations.

The physics of Mott transition can be studied by the single band Hubbard model.

$$H = \sum_{ij,\sigma} \left[t_{ij} c_{i\sigma}^\dagger c_{j\sigma} + \text{h.c.} \right] + U \sum_i n_{i\uparrow} n_{i\downarrow} \quad (1.3)$$

The first term in equation (1.3) denotes the kinetic energy involving the hopping amplitudes t_{ij} . On a given lattice the choices of t_{ij} define the density of states and bandwidth of the non-interacting systems. The second term in equation (1.3) represents the interaction between electrons on the same site. Whether the model has a metallic or insulating ground state depends on the relative strength of interaction U/t , the electron density, and the nature of the lattice.

The Mott transition can manifest itself in the following two ways (see Fig. 1.14),

- Staying at large, fixed, U/t but tuning the electron density across half-filling ($n = 1$), which is know as the filling controlled Mott transition.
- Staying at half-filling ($n = 1$), but tuning the strength of interaction U/t , which is known as the bandwidth controlled Mott transition

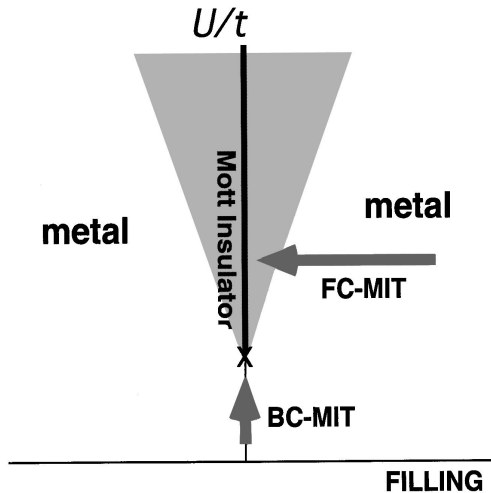


Figure 1.14: (Taken from [73]) Schematic picture of the Mott metal insulator transition, showing the filling controlled (FC) transition and the bandwidth controlled (BC) transition. We will focus on the BC scenario in this thesis.

While it is the strength of electron-electron interaction U/t that is responsible for the Mott transition, the detailed physics depends crucially on the symmetry of the underlying lattice, and the hopping parameters t_{ij} . This is because weak coupling magnetic instabilities depend on nesting features of the Fermi surface, and the magnetism in the Mott phase depends on the lattice geometry.

On bipartite lattices the Mott transition is well understood in terms of magnetic ordering and transport properties. However, this is not the case for a frustrated lattice, due the presence of triangular or tetrahedral motifs in the lattice, which disfavour long range antiferromagnetic order and promote complex electronic states with non-trivial magnetic character [23, 24]. Their nature and impact on the Mott transition remain outstanding problems.

1.3 Interplay of frustration and correlation

The presence of geometric frustration disfavours long-range antiferromagnetic order and promotes a complex magnetic state in insulating magnets with short-range interaction [21–24]. Two complications arise in magnetic insulators close to a Mott insulator-metal transition (IMT): (i) the ‘virtual hopping’ of the electrons mediate long-range and multi-spin coupling, and (ii) the *magnitude* of the local moments weaken as the system is pushed towards the IMT. The first effect can lift the degeneracy of the short range model and promote an ordered state while the second tends

to destroy the magnetic state altogether. The outcome of this interplay is lattice specific, of relevance to several real life materials, and requires tools beyond those usually applied in frustrated magnetism.

The pyrochlore lattice is a fascinating structure (see figure 1.2(d)) to explore the interplay of electron itinerancy and geometric frustration. In the deep Mott state on a pyrochlore lattice, where one expects only nearest neighbour antiferromagnetic coupling, the effective model can be written as a sum, over the tetrahedra, of squares of the total moment in each tetrahedron [34, 74]. The minimum of this is infinitely degenerate since the four spins at the vertices of each tetrahedron just need to satisfy a zero vector sum. The appearance of longer range couplings as the electron-electron Hubbard repulsion is reduced (or the bandwidth is increased) can, potentially, lift the degeneracy and promote some ordered state. Whether it does so is not known. In the tight binding limit, the pyrochlore lattice has two dispersive and two flat bands. At half-filling, which corresponds to the full occupation of the two dispersive bands, a sharply suppressed density of states at the Fermi level is observed. This is the semi-metallic state.

The transport and spectral character between the spin liquid Mott insulator and the band semimetal is also not known. The possibilities in charge transport are also interesting. While the large moment, gapped, Mott phase is insulating, the strong suppression of the moment near the IMT, and possible orientational randomness due to frustration, can generate a ‘bad metal’ state on the disordered magnetic background. Such a state can involve a pseudogap, an unusually large low temperature resistivity, and, possibly, an anomalous Hall response if the moments organise in a non coplanar manner.

1.3.1 General overview

Traditional Mott materials involve a strong on-site Coulomb interaction that, beyond a critical value, and at integer filling, inhibits electron motion [53]. This, in a clean material, leads to an abrupt change in the zero temperature state from perfectly conducting to non conducting. The non conducting state typically has strong antiferromagnetic (AF) correlations, if not long range order, since that lowers the kinetic energy.

The most commonly studied Mott problem involves the single band Hubbard model on a bipartite lattice [72]. In such a model, typically, nesting features drive a transition to an antiferromagnetic insulating state at arbitrarily weak interaction – masking the ‘Mott’ effect. One can certainly study frustrated lattices, which

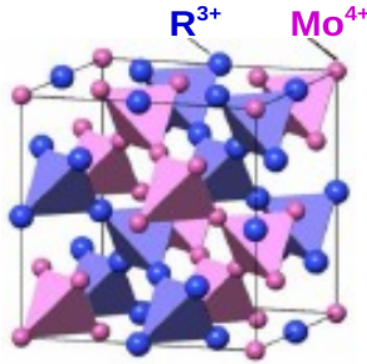


Figure 1.15: (Taken from [4]) Interpenetrating pyrochlore lattice structures of R^{3+} and Mo^{4+} ions in the molybdates. The iridates have a similar structure of R^{3+} and Ir^{4+} ions.

suppress magnetic order. There is much work on the triangular lattice [75–80], the Kagome [81, 82] in two dimensions (2D) and the FCC [83, 84] and pyrochlore lattices [85–87] in three dimensions (3D). These are all harder problems than the square (or cubic) lattice since there is no longer any obvious magnetic order to simplify the correlated problem. Overall, these lattices provide interesting variation from the bipartite case because,

- the MIT could occur in the background of short-range magnetic correlation,
- the deep Mott insulating state itself could be a spin liquid.

1.3.2 Experimental relevance

It would be vital to have experimental realisations to test out the predictions of the frustrated Mott studies. While there is significant effort in analysing the quasi 2D κ -BEDT organics [88–91] in terms of the triangular lattice, 3D realisations of ‘Hubbard physics’ on a frustrated structure are rare. Materials like the manganites [92, 93] do involve strong correlation effects (and much else) but are on a bipartite structure - with relatively simple magnetic order. In this situation the discovery of the rare-earth (R) based pyrochlores – the molybdates [1, 2, 94–96] with chemical formula $R_2Mo_2O_7$, and the iridates [8–10, 97] with chemical formula $R_2Ir_2O_7$, provided a breakthrough.

The molybdate/iridate family of compounds are composed of two pyrochlore sublattices of R site and Mo/Ir site. The O atoms form an octahedron cage around the R and the Mo/Ir sites. These sublattices are structurally identical, but are displaced by half a lattice constant from each other (see figure 1.15). Both these fam-

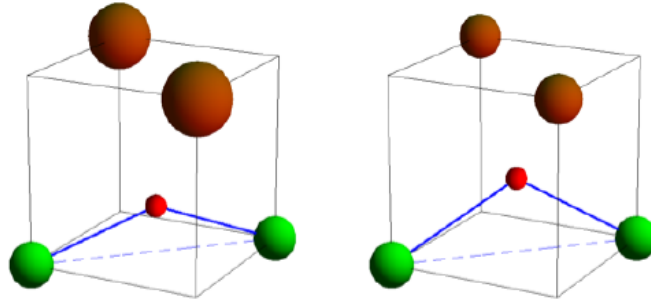


Figure 1.16: (Taken from [98]) The R^{3+} , Mo^{4+} and O^{2-} ions are represented by dark, green and red spheres respectively. (Left) The larger R^{3+} pushes the O^{2-} closer to the Mo^{4+} ions, thereby increasing the $Mo-O-Mo$ bond angle and the hopping amplitude. (Right) When R^{3+} is smaller, the pushing of the O^{2-} towards the Mo^{4+} ions becomes less effective. As a result the $Mo-O-Mo$ bond angle and the hopping amplitude decrease.

ilies show a metal-insulator transition as the rare-earth ionic radius, r_R , is changed [8, 9, 95, 96]. The rare-earth samples with larger r_R , are more metallic in nature. A qualitative understanding of this can be argued in a simple way [98] (see figure 1.16). Consider a scenario with a larger r_R in the molybdates. The larger R^{3+} pushes the O^{2-} closer to the Mo^{4+} ions, thereby increasing the $Mo-O-Mo$ bond angle and the hopping amplitude. As a result the bandwidth of the system increases and it behaves as a metallic system. Considering the other scenario, where the r_R is small, the pushing of the O^{2-} towards the Mo^{4+} ions becomes less effective. This leads to lower hopping amplitude and reduced bandwidth, and the system behaving as less metallic. A similar argument for the iridates also holds true.

The pyrochlore molybdates and iridates have become the hot spots of current research in the electron correlation driven metal insulator transition. In these compounds both the rare-earth and the Mo/Ir sublattice have the pyrochlore structure, but it is the electrons of Mo/Ir atoms that are mainly responsible for exhibiting the Mott phenomena. However, the role of the electrons of the rare-earth atom can not be completely ignored, especially regarding the studies of anomalous Hall effect. Though these two families exhibit several similarities, a closer look reveals differences too. Some key differences are in terms of

- degrees of freedom and couplings (with respect to the Hubbard model)
- the magnetic state that emerges

We will now briefly highlight the important features of the Mott transition in the molybdates and iridates.

1.3.2.1 Mott transition in the pyrochlore molybdates

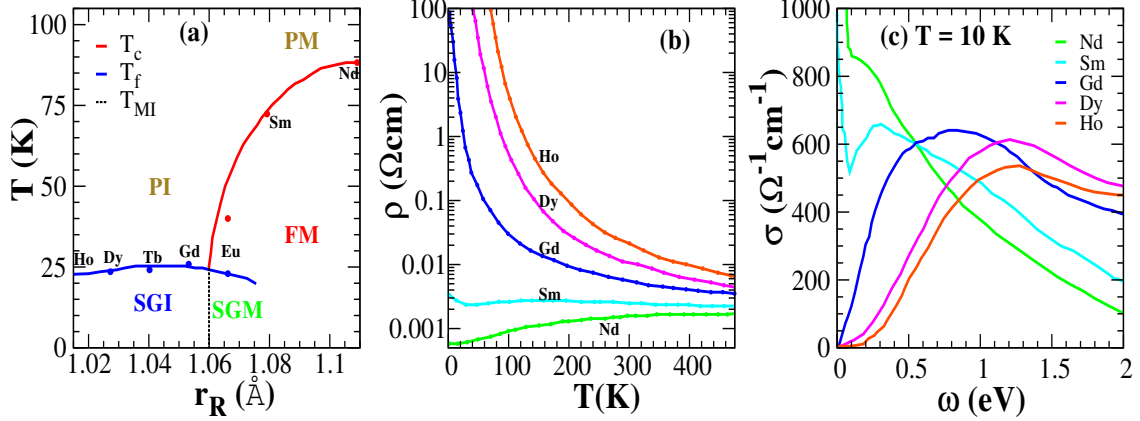


Figure 1.17: (Adapted from [4] and [102]) Left: Phase diagram of the pyrochlore molybdate family ($R_2\text{Mo}_2\text{O}_7$) showing the Mott transition with changing ionic radius of the rare-earth atom. The different phases are ferromagnetic metal (FM), spin-glass metal (SGM), spin-glass insulator (SGI), paramagnetic metal (PM) and a paramagnetic insulator (PI). Middle: Variation of the d.c. resistivity of the $R_2\text{Mo}_2\text{O}_7$ family with temperature. Right: Optical conductivity spectra of the molybdate family at $T = 10\text{K}$.

Rare-earth pyrochlore molybdates ($R_2\text{Mo}_2\text{O}_7$) undergo a Mott transition by changing the rare-earth atom. Some noteworthy features of the Mott transition in the this family are,

- *Metal-insulator transition:* MIT is governed by changing the rare-earth atom (R). Nd and Sm based molybdates with relatively larger ionic radius, r_R , are ferromagnetic metals (FM) in the ground state, where as Ho, Dy, Tb and Gd based molybdates with relatively smaller ionic radius are spin-glass Mott insulators (SGI) [95,96].
- *Magnetic phases:* The Mott insulating phase has a disordered spin-glass phase below the antiferromagnetic (AF) spin-glass freezing temperature. Magnetic properties of spin-glass phase have been investigated by neutron-scattering study [1,99,100] as well as muon spin rotation studies [101]. The magnetic ground state is controlled by the competition between double-exchange driven ferromagnetic metal and superexchange mediated antiferromagnetic correlations.
- *Simultaneity of the magnetic and metal-insulator transition:* The SG-FM transition does not coincide with the MIT. Ferromagnetism survives in the insulat-

ing phase beyond the MIT phase boundary, as in the case of $\text{Gd}_2\text{Mo}_2\text{O}_7$ [102]. Thus, it can be said that ferromagnetism and metallicity are not so strongly coupled in pyrochlore molybdates.

- *Resistivity:* Measurements of d.c. resistivity shows that Ho, Dy, and Gd based molybdates are insulators with decreasing charge gap in that order, whereas Sm and Nd based molybdates exhibit bad metallic behaviour [102]. The residual resistivity $\rho(T = 0)$ of the metallic molybdates are very close to the Ioffe-Regel limit ($\rho_{IR} \approx 0.5m\Omega cm$) corresponding to one conduction electron per Mo site. Irrespective of the ground-state behaviour, the resistivity curves tend to converge towards high temperature. This suggest that at high-temperature the screening of the Coulomb interaction become ineffective.
- *Optics:* Optical conductivity measurements show that the charge gap of $\text{Gd}_2\text{Mo}_2\text{O}_7$ is very small ($\Delta/U \sim 0.03$). The linear dependence of low temperature optical gap, $\Delta(T = 10K)$ with $r_{R=Gd} - r_R$ shows that the charge gap closes continuously. From this, it has been inferred that $\text{Gd}_2\text{Mo}_2\text{O}_7$ lies very close to the MIT boundary. On this basis, it has been concluded that the molybdates show a second-order MIT [103].
- *Effect of an external magnetic field:* $\text{Gd}_2\text{Mo}_2\text{O}_7$ which lies in the vicinity of the MIT, shows the Anderson-Mott transition with the application of an external magnetic field [5]. In the absence of any magnetic field, it is a Mott insulator with a disordered SG phase. The magnetic field controls directly the magnitude of the random potential in this disordered phase and thereby leads to the insulator-metal transition. Such a phenomenon with huge magnetoresistance in moderate magnetic field is very rare in solid state materials.
- *Anomalous Hall response:* The anomalous Hall coefficient in ferromagnetic pyrochlores is finite at low temperatures [6, 7]. This behaviour is reported to be due to finite spin chirality of the ground state, which originates from geometric frustration of the pyrochlore lattice.
- *Degrees of freedom:* The magnetic and transport properties arise from the electrons populating the t_{2g} subspace of Mo $4d$ levels as is pointed out by photoemission experiments [104]. The relevant degrees of freedom are two orbitals per site and a $S = 1/2$ moment.

1.3.2.2 Mott transition in the pyrochlore iridates

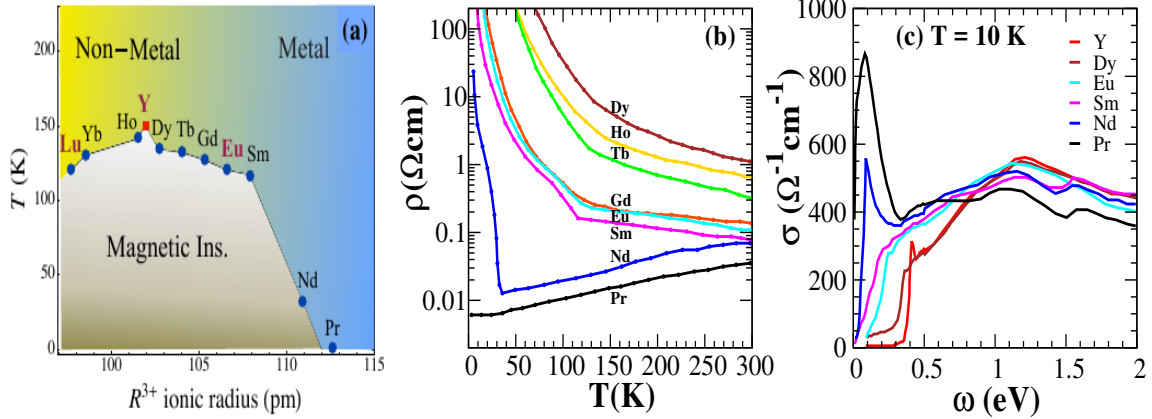


Figure 1.18: (Adapted from [105], [9] and [109]) Left: Phase diagram of the pyrochlore iridate family showing the Mott transition with changing ionic radius of the rare-earth atom. The distinguished phases are a metal and a Mott insulating phase. The Mott insulating phase has AIAO magnetic ordering below the antiferromagnetic transition temperature. Middle: Variation of the d.c. resistivity of the iridate family with temperature. Right: Optical conductivity spectra of the $R_2Ir_2O_7$ family at $T = 10K$.

Rare-earth pyrochlore iridates ($R_2Ir_2O_7$) too undergo a Mott transition by changing the rare-earth atom. Some noteworthy features of this Mott transition are,

- *Metal-insulator transition:* MIT is governed by changing the rare-earth atom (R). Pr based iridate with relatively larger ionic radius, r_R , is a paramagnetic metal (PM) in the ground state, whereas Nd, Eu, Gd, Dy and Ho based iridates with relatively smaller ionic radius are antiferromagnetic Mott insulators [8,9].
- *Magnetic phases:* Magnetic properties of these compounds have been investigated by neutron-scattering study [106] and muon spin rotation studies [107, 108]. It has been observed that the Mott insulating phase has a non collinear all-in-all-out (AIAO) ordered phase below the antiferromagnetic (AF) Neel temperature. However $Pr_2Ir_2O_7$ doesn't show any magnetic ordering down to the lowest measured temperature [13]. The magnetic ground state is controlled by not only the superexchange interaction dependent on the kinetic energy and Coulomb repulsion, but also on the Dzyaloshinskii-Moriya interaction dependent on the kinetic energy and the strength of SOC.
- *Simultaneity of magnetic and metal-insulator transition:* The paramagnetic to AIAO AF transition coincides with the MIT [8,9]. Thus, it can be said

that antiferromagnetism and Mott insulating phases are strongly coupled in pyrochlore iridates.

- *Resistivity:* d.c. resistivity measurements show Ho, Dy, Gd, Eu and Nd based iridates are insulators with decreasing charge gap in that order, whereas Pr based iridate exhibiting bad metallic behaviour [8, 9]. The residual resistivity $\rho(T = 0)$ of Pr iridate is very close to the Ioffe-Regel limit ($\rho_{IR} \approx 0.5m\Omega cm$) corresponding to one conduction electron per Ir site [109]. Irrespective of the ground-state behaviour, the resistivity curves tend to converge towards high temperature. This suggest that at high-temperature the screening of the Coulomb interaction become ineffective.
- *Optics:* Optical conductivity measurements show that the charge gap of $Nd_2Ir_2O_7$ is very small [11]. In the iridates, the antiferromagnetic AIAO order gives rise to a dramatic suppression of low-energy optical conductivity, leading to a gapped spectrum [109]. It is observed that this magnetic order promotes the metal-insulator transition in the iridates.
- *Effect of an external magnetic field:* Magnetic field driven metal-insulator transitions for $(Nd_{1-x}Pr_x)_2Ir_2O_7$ has been observed [110]. It is expected that this MIT is accompanied by a change in the magnetic ordering due to the applied magnetic field. By applying a 10 Tesla magnetic field, it has been observed that $Nd_2Ir_2O_7$ undergoes a transition from a magnetic insulator to a metallic phase [111].
- *Anomalous Hall response:* Though $Pr_2Ir_2O_7$ doesn't show any magnetic ordering down to the lowest measured temperature, it displays a large anomalous Hall effect even in zero field [12].
- *Degrees of freedom:* The magnetic and transport properties arise from the electrons populating the t_{2g} subspace of Ir $5d$ levels. Spin-orbit coupling (SOC) plays a very significant role in these family of materials. The relevant degrees of freedom includes effectively one orbital per site.

1.3.3 Theoretical understanding

At the outset the behaviour of the pyrochlore molybdates and iridates may seem complicated, involving several orbitals and multiple interactions (spin-orbit coupling, Hund's coupling, superexchange interaction, etc.) determining the low temperature

behaviour. However, first principle studies have provided crucial inputs in this matter. The magnetic and transport properties of these family of materials can be studied with effective single band Hubbard models with minimal additional interaction terms. We will quickly discuss the findings of the first principle studies, and then briefly review the model based studies.

1.3.3.1 Pyrochlore molybdates

Following points have been discovered.

- A first-principle based band structure calculation has suggested that the t_{2g} electrons of the Mo play an important role [112]. Further a trigonal lattice distortion along the [111] direction splits the t_{2g} levels to a higher energy e'_g doublet and a lower energy a_{1g} state. Strong on-site Coulomb interaction leads to one localised electron (spin) at the a_{1g} level and another at the e'_g levels. The electron at the e'_g levels behaves as localised or itinerant depending on the strength of electron correlation. The interaction between the neighbouring Mo spins (a_{1g} electrons) is antiferromagnetic (AF) due to superexchange (SE) interaction. The interaction between the e'_g electrons on a given site is ferromagnetic (FM) due to strong Hund's coupling and mediated via the double-exchange (DE) mechanism. The ferromagnetic metallic phase is stabilised by the DE interaction, while the transition to spin-glass insulator is governed by the Coulomb repulsion between the Mo 4d electrons [112]. The resulting FM or SG phase in the $R_2Mo_2O_7$ family is determined by this competition.
- The competition between DE and SE has been investigated with a Monte Carlo study [113] arriving at a phase diagram 1.19. Further bringing the Coulomb repulsion into account it has been predicted that there are competitions between the spin, orbital and electronic phases in the molybdate family [19] (see figure 1.19).

Though the magnetic phase competition between the various interactions in the molybdates have been explored, following aspects are still unsettled.

- There are few attempts at addressing the impact of the magnetic phase competition on the electronic properties (like transport and optics).
- There is no clear understanding if the magnetic and the metal-insulator transitions should be necessarily simultaneous.

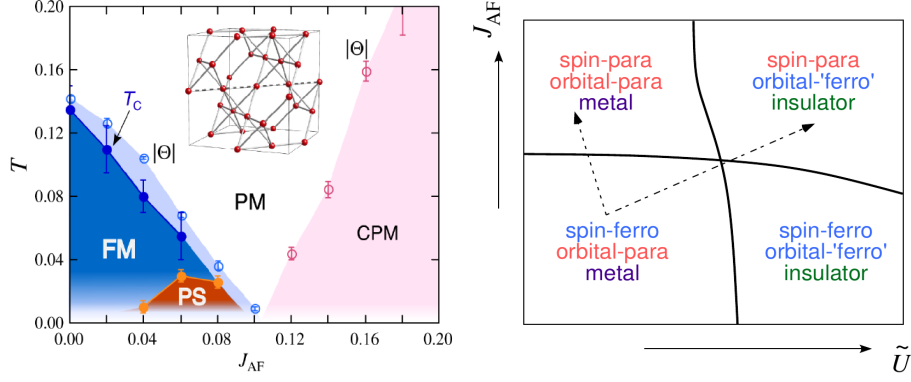


Figure 1.19: (Taken from [113] and [19]) Left: Phase diagram highlighting the competition between DE and SE on the pyrochlore lattice at quarter filling. Right: Illustration of the ground state phase diagram with competition between DE, SE and Coulomb repulsion (represented by \tilde{U}). The dotted and dashed arrows in the figure indicate the tuning of relevant parameters which mimic the changing of the physical and chemical pressure respectively, in the pyrochlore molybdates.

- No detailed understanding of the huge magnetoresistance due to an external applied field.
- The origin of the anomalous Hall response.

1.3.3.2 Pyrochlore iridates

The physics of the pyrochlore iridates is mainly dictated by the 5d electrons of Ir, which has strong spin-orbit coupling (SOC) and moderate Hubbard repulsion U (due to large spatial extent of 5d orbitals). The Ir atom has octahedral oxygen coordination (IrO_6), and the resulting crystal field splits the fivefold degenerate Ir 5d states into doubly degenerate e_g and triply degenerate t_{2g} manifolds. As a result, the $L = 2$ orbital angular momentum of the d orbitals is projected down to an effective angular momentum $l = 1$ (with a minus sign) in the t_{2g} manifold. SOC splits the t_{2g} orbitals with spin into a $j = 1/2$ doublet and $j = 3/2$ quadruplet. Strong SOC, thus, not only lifts the orbital degeneracy of 5d electrons, but also reduces the bandwidth. In the iridates, SOC leads to an effective single band description in terms of pseudo-spin $j_{eff} = 1/2$ states. The $j_{eff} = 1/2$ states are given by

$$\begin{aligned}
 |J_{eff} = 1/2, +1/2\rangle &= \frac{1}{\sqrt{3}}(|xy, \uparrow\rangle + |yz, \downarrow\rangle + i|zx, \downarrow\rangle) \\
 |J_{eff} = 1/2, -1/2\rangle &= \frac{1}{\sqrt{3}}(|xy, \downarrow\rangle - |yz, \uparrow\rangle - i|zx, \uparrow\rangle)
 \end{aligned}$$

There have been attempts to understand the behaviour of the iridates within a single band Hubbard model. Following details have been established.

- In the absence of interaction, the ground state is a semimetal or topological insulator depending on the ratio of spin-orbit coupling and the hopping amplitude [114]. This picture remains roughly unchanged for weak electron interaction, but for strong interactions, the system becomes an AIAO magnetic insulator [114].
- Hartree-Fock mean-field theory (MFT) calculation shows that near the magnetic transition, a topological Weyl semimetal phase shows up [115].
- A cluster dynamical mean-field theory (CDMFT) calculation confirms this scenario, and in addition finds an axion-insulator phase near the MIT point [116]. A more elaborate LDA+CDMFT study shows a first order MIT from a paramagnetic metal to an antiferromagnetic AIAO ordered insulating phase by taking into consideration a three-band description of the Iridates [117].

Despite some success, there are important features of the iridate Mott transition that are yet to be understood. We list those out here.

- While the MFT captures the correct AIAO ordering, its prediction that T_N would keep increasing with U at all interaction window is clearly opposite to what has been observed in the experiments.
- The LDA+CDMFT study has captured this physics correctly. However, due to ignoring the long-range spatial fluctuations, the maximum T_N scale it gives is roughly 3-times that of the experimentally observed T_N values. Thus, an approach retaining the spatial fluctuations seems more appealing.
- Also there are very limited attempts to study the transport and optical behaviour systematically for these family of compounds. While experiments have provided a wealth of data, the above mentioned techniques are not able to uncover the detailed transport, optics and spectral features.
- Further it would be interesting to study the magnetic field driven MIT and the anomalous Hall effect in the iridates.

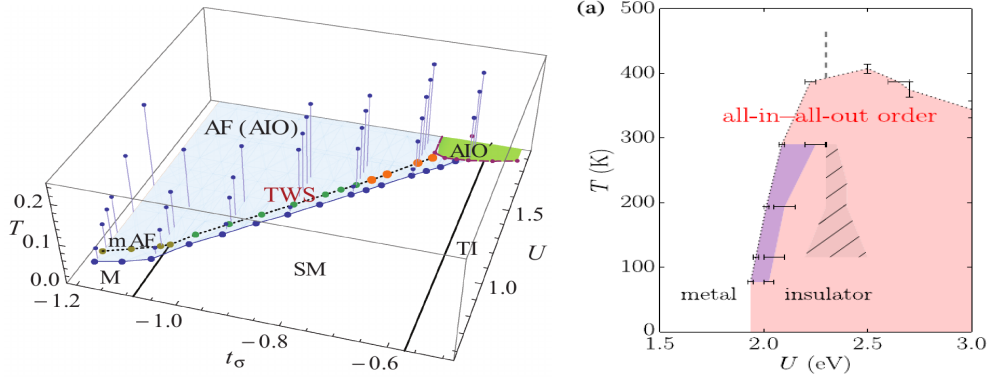


Figure 1.20: (Taken from [115] and [117]) Left: $U - T$ mean-field phase diagram of the pyrochlore Hubbard model with small next nearest-neighbour hopping. The out-of-plane fibres along the T -axis represent the antiferromagnetic (AF) T_N for the continuous transition at which this magnetic order melts. The two shaded regions correspond to AF phases: either the all-in-all-out (shown as AIO here) or AIO' phase, a type related to the AIO by a $\pi/2$ rotations. The solid/dashed lines denote second- and first-order quantum phase transitions, whereas, the dotted lines in the AIO phase denote a gap closing signalling a Lifshitz transition out of the topological Weyl semimetal (TWS) or metallic AF (mAF). Right: $U - T$ phase diagram of the pyrochlore Hubbard model at half filling studied with a LDA+CDMFT scheme with appropriate parameter choices for the iridates. There is a first-order transition between the all-in-all-out magnetic insulator and the paramagnetic metal at low T and small U . The blue shaded region denotes the hysteresis region associated with this transition. The error bars reflect the uncertainty caused by the finite number of parameter values considered. The metal-insulator crossover in the high- T paramagnetic phase is shown by a broken line. The hashed region represents the first-order Mott transition and its hysteresis region in paramagnetic DMFT calculations.

1.4 Agenda of the thesis

As shown by the various experiments, the pyrochlore molybdates and iridates show unusual magnetic ordering. These magnetic states would lead to distinct transport, optical and spectral features. Our aim is to explore the possible magnetic ground state on these family of materials, their impact on the electronic properties of the materials and to uncover the effect of thermal fluctuations with increased temperature.

We would follow a real space approach which captures the spatial fluctuations, describes a fully disordered phase, and effect of temperature. This approach can be thought of as a complementary approach to the dynamical mean-field theory (and its cluster versions). Within this approach, we would provide a detailed study of the Mott transition in the pyrochlore molybdates and iridates.

We first focus on the role of the Hubbard interaction on the half filled pyrochlore lattice and the checkerboard lattice. Next we study the more realistic but complex models capturing the details of the Mott transition in the pyrochlore molybdates and iridates.

We address the following broad questions:

- What is the nature of the magnetic state as one moves towards weaker interaction in the Mott insulator?
- What are the magnetic correlations near the Mott transition boundary?
- What is the impact of these magnetic correlations on electron physics (resistivity, optics, spectral features) near the IMT?

THEORETICAL TOOLS

We study our Mott transition problems within the framework of the Hubbard model [53]. In this chapter we first discuss the approximations we use to set up a tractable computational approach to the Hubbard model. We then discuss the implementation of the numerical scheme and the benchmarks against which we have tested our results.

2.1 The Hubbard model

The Hubbard model minimally accounts for both the quantum mechanical motion of electrons and the short range repulsion between them. While too simple to capture all materials details it is often a useful starting point. In spite of its rather simple look the model exhibits various phenomena including metal-insulator transition, antiferromagnetism, ferromagnetism, and superconductivity.

The Hubbard model is defined as:

$$H = H_{hop} + H_{int} = \sum_{\langle ij \rangle \sigma} t_{ij} \left[c_{i\sigma}^\dagger c_{j\sigma} + \text{h.c.} \right] + U \sum_i \hat{n}_{i\uparrow} \hat{n}_{i\downarrow} \quad (2.1)$$

where H_{hop} describes the quantum mechanical hopping of electrons, and H_{int} describes the short ranged repulsive (Coulomb) interaction U between the electrons at the same site [118]. t_{ij} is the hopping amplitude between states localised [54] at positions \vec{R}_i and \vec{R}_j . The eigenstates of H_{hop} are ‘wave like’, while H_{int} would prefer localised, ‘particle like’, behaviour to minimise interaction between electrons. Though H_{hop} and H_{int} individually do not have any ordering tendency their sum can generate ordering.

The parameters of the model are the ratio U/t (where t is the nearest neighbour hopping), the density n (or chemical potential μ), and the temperature T . The degree of magnetic frustration which is controlled by the lattice structure and the hoppings t_{ij} also implicitly affects the physics.

The solution of the Hubbard model has been a central problem in condensed matter physics. No exact solution exists in more than one dimensions [119]. The limit of ‘infinite dimensionality’ yields a computationally tractable problem. In this limit [120] one redefines the hopping matrix elements as $t_{ij} = (1/\sqrt{d})^{|i-j|}$, with $|i-j|$ the minimum number of links that one has to traverse on the lattice in order to connect the sites i and j , as $d \rightarrow \infty$. In this limit the *kinetic energy* (not individual hopping) and the interaction energy per site are still of the same order and the problem remains physically non trivial.

The simplest approach to the Hubbard model is mean-field theory. Numerically exact approaches include quantum Monte Carlo (QMC) and exact diagonalisation (ED). Approximate schemes like dynamical mean-field theory (DMFT) [71] also ultimately resort to QMC or ED. Despite the enormous increase in computing power over the last two decades the QMC and ED methods are still seriously size limited.

We use a new approach, discussed in the next section, which focuses on spatial order and its fluctuations, and allows us to access large lattice sizes. It is approximate in nature, and maps the Hubbard problem at half filling to an effective Kondo lattice like problem.

2.2 The static path approximation

In what follows we discuss the most general single band Hubbard model, written in terms of the pseudo-spins variables - α, β as

$$H = \sum_{\langle ij \rangle, \alpha\beta} t_{ij}^{\alpha\beta} c_{i\alpha}^\dagger c_{j\beta} + U \sum_{i, \alpha \neq \beta} n_{i\alpha} n_{i\beta} - \mu \sum_i n_i \quad (2.2)$$

where α, β could be spin, orbital, or mixed spin-orbital variables. μ is the chemical potential to maintain the electron density at half-filling ($n = 1$) as the interaction and temperature are varied. We handle the problem in real space as follows:

- The partition function is originally a functional integral over Grassmann fields $\psi_{i\alpha}(\tau)$ and $\bar{\psi}_{i\alpha}(\tau)$:

$$Z = \int \mathcal{D}\psi \mathcal{D}\bar{\psi} e^{-\int_0^\beta d\tau \mathcal{L}(\tau)}$$

$$\mathcal{L}(\tau) = \sum_{\langle ij \rangle, \alpha\beta} \{ \bar{\psi}_{i\alpha} ((\partial_\tau - \mu)\delta_{ij}\delta_{\alpha\beta} + t_{ij}^{\alpha\beta}) \psi_{j\beta} \} + U \sum_{i, \alpha \neq \beta} \bar{\psi}_{i\alpha} \psi_{i\alpha} \bar{\psi}_{i\beta} \psi_{i\beta}$$

- We use a Hubbard-Stratonovich (HS) transformation [14, 121, 122] that decouples $U n_{i\alpha} n_{i\beta}$ in terms of an auxiliary variable $\mathbf{\Gamma}_i(\tau)$, coupling to the electronic ‘local moment’ $\mathbf{O}_i = \sum_{\mu\nu} c_{i\mu}^\dagger \vec{\sigma}_{\mu\nu} c_{i\nu}$, and a scalar field $\Phi_i(\tau)$ coupling to the electronic density n_i at each site. i, τ refer to spatial coordinate and imaginary time, respectively. The Fourier transformed, Matsubara frequency, versions of these fields are $\mathbf{\Gamma}_{i,n}$ and $\Phi_{i,n}$, where $\Omega_n = 2\pi nT$ is a bosonic frequency (T is the temperature). The interaction term takes the form:

$$e^{U \bar{\psi}_{i\alpha} \psi_{i\alpha} \bar{\psi}_{i\beta} \psi_{i\beta}} = \int \frac{d\Phi_i d\mathbf{\Gamma}_i}{4\pi^2 U} e^{(i\Phi_i n_i - \mathbf{\Gamma}_i \cdot \mathbf{O}_i + \frac{\Phi_i^2}{U} + \frac{\mathbf{\Gamma}_i^2}{U})}$$

- This leads to:

$$\begin{aligned} Z &= \int \mathcal{D}\psi \mathcal{D}\bar{\psi} \prod_i \frac{d\Phi_i d\mathbf{\Gamma}_i}{4\pi^2 U} e^{-\int_0^\beta d\tau \mathcal{L}(\tau)} \\ \mathcal{L}(\tau) &= \mathcal{L}_0(\tau) + \mathcal{L}_{int}(\tau) + \mathcal{L}_{cl}(\tau) \\ \mathcal{L}_0(\tau) &= \sum_{\langle ij \rangle, \alpha\beta} \{ \bar{\psi}_{i\alpha} ((\partial_\tau - \mu)\delta_{ij}\delta_{\alpha\beta} + t_{ij}^{\alpha\beta}) \psi_{j\beta} \} \\ \mathcal{L}_{int}(\tau) &= \sum_{i, \alpha\beta} \{ i\Phi_i \bar{\psi}_{i\alpha} \psi_{i\beta} \delta_{\alpha\beta} - \mathbf{\Gamma}_i \cdot \bar{\psi}_{i\alpha} \vec{\sigma}_i \psi_{i\beta} \} \\ \mathcal{L}_{cl}(\tau) &= \sum_i \left\{ \frac{\Phi_i^2}{U} + \frac{\mathbf{\Gamma}_i^2}{U} \right\} \end{aligned}$$

- Since the fermions are now quadratic, the $\int \mathcal{D}\Psi \mathcal{D}\bar{\psi}$ integrals can be formally performed to generate the effective action for the background fields:

$$\begin{aligned} Z &= \int \mathcal{D}\Phi \mathcal{D}\mathbf{\Gamma} e^{-S_{eff}\{\Phi, \mathbf{\Gamma}\}} \\ S_{eff} &= \log \text{Det}[\mathcal{G}^{-1}\{\Phi, \mathbf{\Gamma}\}] + \int_0^\beta d\tau \mathcal{L}_{cl}(\tau) \end{aligned}$$

In the expression above \mathcal{G} is the electron Green’s function in a $\{\Phi, \mathbf{\Gamma}\}$ background.

Now there are various options.

- Quantum Monte Carlo would proceed by using S_{eff} as the ‘weight’ for the background configurations, and compute electron properties on these after equilibration.
- Mean field theory would assume the fields to be time independent, replace them by their mean values, and minimise the free energy.
- A *static path approximation* (SPA) to Z again assumes the fields to be time independent, but samples over spatial fluctuations.

We adopt the last option as our preferred method. This is computationally simpler than QMC, but much more sophisticated than MFT at finite temperature. So we

- neglect the imaginary time dependence of Φ_i and Γ_i , *i.e.*, retain only the zero Matsubara frequency modes of these fields, and
- replace Φ_i by its saddle point value, $\Phi_i \rightarrow \langle \Phi_i \rangle = (U/2)\langle n_i \rangle = U/2$, since the important low energy fluctuations arise from the Γ_i .

Within this scheme the electron is subject to *static* background fields $\{\Phi, \Gamma\}$. The Φ_i is frozen and the Γ_i follow an effective ‘Hamiltonian’

$$H_{eff}\{\Gamma_i\} = -\frac{1}{\beta} \log \text{Tr} e^{-\beta H_{el}} + \frac{1}{U} \sum_i \Gamma_i^2$$

$$H_{el} = \sum_{ij}^{\alpha\beta} t_{ij}^{\alpha\beta} c_{i\alpha}^\dagger c_{j\beta} - \tilde{\mu} \sum_i n_i - \sum_i \Gamma_i \cdot \mathbf{O}_i$$

with $\tilde{\mu} = \mu - U/2$. For convenience we redefine $\Gamma_i \rightarrow \frac{U}{2}\Gamma_i$, so that the Γ_i is dimensionless. This leads to:

$$H_{el} = \sum_{ij}^{\alpha\beta} t_{ij}^{\alpha\beta} c_{i\alpha}^\dagger c_{j\beta} - \tilde{\mu} \sum_i n_i - \frac{U}{2} \sum_i \Gamma_i \cdot \mathbf{O}_i$$

and

$$H_{eff}\{\Gamma_i\} = -\frac{1}{\beta} \log \text{Tr} e^{-\beta H_{el}} + \frac{U}{4} \sum_i \Gamma_i^2$$

The localised moment configurations follow the distribution

$$P\{\Gamma_i\} \propto \text{Tr}_{cc^\dagger} e^{-\beta H_{eff}}$$

Within SPA H_{eff} and $P\{\Gamma_i\}$ define a coupled fermion-local moment problem. If the moments are large and random the electronic problem requires numerical diagonalisation. Similarly, the $P\{\Gamma_i\}$ cannot be written down in closed form since the fermion free-energy is not known for arbitrary $\{\Gamma_i\}$ background. The method of choice in these situations is a combination of Monte Carlo (MC) for updating the Γ_i with exact diagonalisation of the quadratic fermion Hamiltonian for computing the Metropolis update cost. This overall approach has been used in the nuclear many body problem [123, 124], superconductivity [125, 126], *etc*, and by us in other studies of the Mott problem [87, 127, 128].

There are regimes where some analytic progress can be made, as we discuss later, but most of our results are based on a numerical solution of the Hubbard model. For the Hubbard model our approximate scheme allows:

- Access to non trivial magnetic states and captures their T_c scales accurately.
- Access to spectral and transport properties without any need for analytic continuation.
- Description of electronic phases without any long range order.

2.3 Numerical methods

We obtain a solution of the Hubbard model via a Monte Carlo by generating the equilibrium configuration for the $\{\Gamma_i\}$ through iterative diagonalisation of H_{eff} . We start with reasonable high temperature, $T \sim t$, higher than any transition temperature in the problem, and reduce it to $T \sim 10^{-3}t$ to access ground state properties. At $T = 0$ our method reduces to unrestricted Hartree-Fock. Traditionally, Hartree-Fock calculations impose a certain pattern on the order parameter and minimise with respect to the amplitude. On a frustrated geometry it is not clear what pattern to impose so our approach samples the entire space of $\{\Gamma_i\}$ via thermal annealing.

2.3.1 Real space Monte Carlo

We set up the electronic Hamiltonian in real space basis for a given lattice size, for an initial configuration of the auxiliary fields and attempt to ‘update’ this configuration. The energy cost of this update is computed through the free energy change of the system. The transition probability between configurations is $\propto \exp(-\beta(F' - F))$,

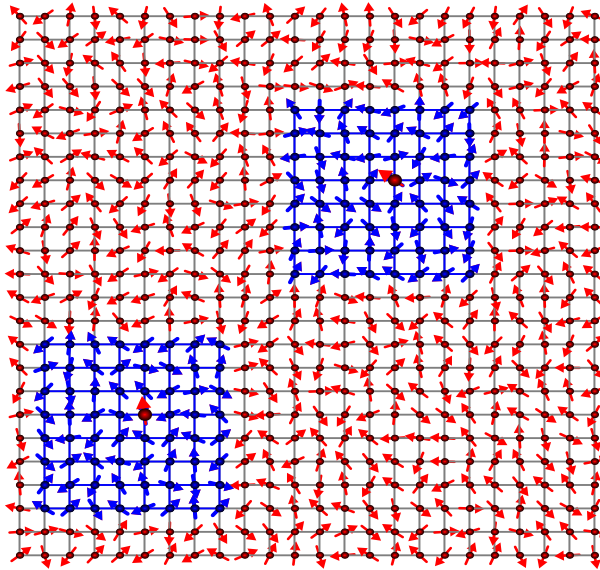


Figure 2.1: Visualisation of the our cluster based update scheme. Local moments of the cluster (size 8×8) are drawn as blue vectors, whereas the local moments of the lattice (size 24×24) are drawn as red vectors. The energy cost of updating the variable Γ_i (local moment drawn in red within the cluster) is computed by diagonalising the cluster of size 8×8 , constructed around that site rather than diagonalising H_{el} for the full lattice of size 24×24 . Such update attempts at each site of the lattice (on average) would constitute one MC sweep.

where F' and F are free energy in the attempted and initial configuration respectively. Computing $F' - F$ requires diagonalising H_{el} . This involves an $\mathcal{O}(N^3)$ computational cost per update, *i.e.*, the cost per MC sweep would be N^4 . This limits the accessible lattice size to $N \sim 100$.

To access larger sizes within reasonable time we use a cluster algorithm (TCA) [15] for estimating the update cost. According to this scheme, the energy cost of updating the variable Γ_i is computed by diagonalising a cluster (of size N_c , say) constructed around the site \mathbf{r}_i , rather than diagonalising H_{el} for the full lattice. This scheme has been extensively benchmarked [15] and works reasonably unless we are attempting to recover states with a large spatial period. A cartoon of the cluster scheme is shown in figure 2.1. With this choice of MC update, the computational cost now scales as NN_c^3 , which is linear in lattice size N . This lets us access large lattice sizes $N \sim 1000$.

Once equilibrium is attained within the Monte Carlo scheme at a given temperature, we use the MC configurations to calculate various physical observables of interest. Below we list some of the key observables that we track in our calculation.

We start with high temperature, $\sim t$, higher than any transition temperature in the problem, and reduce it to $T = 0.001t$ in 30-50 steps of temperature to access the ground state properties. Our typical MC run lengths are 10^4 steps per temperature. Our studies on the three dimensional (3D) pyrochlore lattice are done with system sizes of $6 \times 6 \times 6$ unit cells ~ 800 atoms (the pyrochlore has 4 atoms per unit cell) and $8 \times 8 \times 8$ unit cells ~ 2000 atoms with the choice of a $3 \times 3 \times 3$ unit cells cluster. For two dimensional (2D) lattice calculation, we choose 24×24 and 32×32 systems sizes with a 8×8 cluster.

2.3.2 Variational calculation at $T = 0$

When the Monte Carlo suggests that the system is heading towards a state with periodic spatial behaviour, a simple way to access the possible ground state is to try a family of variational configurations. For simple enough configurations (discussed further on) the electronic model may be analytically solvable. Even when that is not possible, the numerical cost of diagonalising a system of size N for N_{trial} configurations is $\sim N_{trial}N^3$, compared to the $N_{tempr}N_{sweep}N^4$ cost involved in the MC. N_{tempr} is the number of temperature points and N_{sweep} is the number of MC sweeps per temperature.

Taking our representation of the effective Hamiltonian H_{eff} and assuming a set of periodic configurations Γ_i defined as

$$\Gamma_i = \Gamma(\cos \mathbf{q} \cdot \mathbf{x}_i, \sin \mathbf{q} \cdot \mathbf{x}_i, 0) \quad (2.3)$$

we have

$$H_{el} = \sum_{\mathbf{x}, \vec{\delta}, \sigma} t_{\vec{\delta}} \left[c_{\mathbf{x}, \sigma}^\dagger c_{\mathbf{x} + \vec{\delta}, \sigma} + \text{h.c.} \right] - \frac{U\Gamma}{2} \sum_{\mathbf{x}} \left(e^{-i\mathbf{q} \cdot \mathbf{x}} c_{\mathbf{x}\uparrow}^\dagger c_{\mathbf{x}\downarrow} + e^{i\mathbf{q} \cdot \mathbf{x}} c_{\mathbf{x}\downarrow}^\dagger c_{\mathbf{x}\uparrow} \right) \quad (2.4)$$

This can be simplified by doing Fourier transformation to

$$H = \sum_{\mathbf{k}} \begin{pmatrix} c_{\mathbf{k}, \uparrow}^\dagger & c_{\mathbf{k}-\mathbf{q}, \downarrow}^\dagger \end{pmatrix} \begin{pmatrix} \epsilon_{\mathbf{k}} & -\frac{U\Gamma}{2} \\ -\frac{U\Gamma}{2} & \epsilon_{\mathbf{k}-\mathbf{q}} \end{pmatrix} \begin{pmatrix} c_{\mathbf{k}, \uparrow} \\ c_{\mathbf{k}-\mathbf{q}, \downarrow} \end{pmatrix} \quad (2.5)$$

Where $\epsilon_{\mathbf{k}}$ is the tight binding dispersion for the lattice. The eigenvalues can be readily obtained, and one gets

$$\epsilon_{\pm, \mathbf{k}} = \frac{1}{2} \left[\epsilon_{\mathbf{k}} + \epsilon_{\mathbf{k}-\mathbf{q}} \pm \sqrt{(\epsilon_{\mathbf{k}} - \epsilon_{\mathbf{k}-\mathbf{q}})^2 + U^2\Gamma^2} \right] \quad (2.6)$$

Once we get the dispersion, the total energy is

$$E(\Gamma, \mathbf{q}) = \sum_{\mathbf{k}, \alpha=\pm} \theta(\mu - \epsilon_{\alpha, \mathbf{k}}) \epsilon_{\alpha, \mathbf{k}} + \frac{U}{4} N \Gamma^2 \quad (2.7)$$

To get the ground state, we minimise the total energy $E(\Gamma, \mathbf{q})$ with respect to the magnitude ‘ Γ ’ and vector \mathbf{q} . On a two dimensional $L \times L$ lattice, \mathbf{q} can take L^2 values, as $\mathbf{q} = \frac{2\pi}{L}(q_x, q_y)$, where q_x, q_y are integers ranging from 0 to $L - 1$. We discretise Γ between $[0, 1]$ into ~ 100 intervals. As we will see in the solution of the checkerboard Hubbard model this provides some intuition into the nature of possible magnetic ordering.

2.4 Equilibrium properties

From the equilibrium configurations obtained at the end of annealing we calculate the following auxiliary field and electronic properties. The angular brackets represent thermal average over MC configurations.

2.4.1 Auxiliary field correlations

- The average magnitude of the auxiliary fields Γ_{avg} is computed as

$$\Gamma_{avg} = \frac{1}{N} \sum_i \langle |\Gamma_i| \rangle$$

The sum is over all the lattice sites.

- The size distribution of the auxiliary fields $P(\Gamma)$ is computed as

$$P(\Gamma) = \frac{1}{N} \sum_i \langle \delta(\Gamma - |\Gamma_i|) \rangle$$

- The angular correlation is accessed via the structure factor $S(\mathbf{q})$ computed as

$$S(\mathbf{q}) = \frac{1}{N^2} \sum_{ij} \langle \Gamma_i \cdot \Gamma_j \rangle e^{i\mathbf{q} \cdot (\mathbf{r}_i - \mathbf{r}_j)}$$

The onset of rapid growth in $S(\mathbf{q})$ at some $\mathbf{q} = \mathbf{Q}$, say, indicates a magnetic transition.

2.4.2 Electronic correlation functions

- The electronic density of states (DOS) is,

$$N(\omega) = \frac{1}{N} \sum_n \langle \delta(\omega - \epsilon_n) \rangle$$

where ϵ_n are single particle eigenvalues in an equilibrium configuration.

- The optical conductivity is calculated by using the Kubo formula as:

$$\sigma_{xx}(\omega) = \frac{\sigma_0}{N} \left\langle \sum_{n,m} \frac{f(\epsilon_n) - f(\epsilon_m)}{\epsilon_m - \epsilon_n} |J_x^{nm}|^2 \delta(\omega - E_{mn}) \right\rangle$$

where J_x^{nm} is $\langle n | J_x | m \rangle$ and the current operator is given by

$$J_x = -i \sum_{i,\alpha\beta} \left[(t_{i,i+\hat{x}}^{\alpha\beta} c_{i,\alpha}^\dagger c_{i+\hat{x},\beta} - \text{hc}) \right]$$

$E_{mn} = \epsilon_m - \epsilon_n$, $f(\epsilon_n)$ is the Fermi function, ϵ_n and $|n\rangle$ are the single particle eigenvalues and eigenstates of H_{el} respectively. The conductivity is in units of $\sigma_0 = e^2/(\hbar a_0)$, where a_0 is the lattice constant.

- The d.c. conductivity is obtained as a low frequency average of the optical conductivity over a window $\Omega = 0.05t$.

$$\sigma_{dc} = \frac{1}{\Omega} \int_0^\Omega d\omega \sigma_{xx}(\omega)$$

and the resistivity $\rho = 1/\sigma_{dc}$.

2.5 Methodological issues

In this section we discuss some methodological issues and selected computational checks for our results obtained with Monte Carlo. We specifically choose to show the results of our two-orbital Hubbard model with additional Hund's and superexchange interactions (relevant for the molybdates).

2.5.1 The static approximation

In principle both spatial and temporal fluctuations of the auxiliary field could be important near the Mott transition. However, fully handling the temporal fluctuations

of the Γ_i and ϕ_i fields requires a quantum Monte Carlo scheme. The absence of such results is probably due to the sign problem for fermions in the frustrated geometry. We have retained only the zero Matsubara frequency, $\Omega_n = 0$, mode of the auxiliary fields, exactly.

The neglect of quantum dynamics of the auxiliary fields results in the missing of the correlation effects in the ground state of the metal, overestimating its energy and underestimating the critical U/t for metal-insulator transition. It is possible, but non trivial, to set up a Gaussian expansion for the finite Ω_n modes of Γ_i and ϕ_i , while retaining and treating the $\Omega_n = 0$ mode exactly as we have. This is a project for the future. In the absence of such a calculation we can only make the following conjectures.

- Local moments would remain well defined in the insulating phase, due to the Mott gap. The magnetic state might get affected by quantum fluctuations. However, on strongly frustrated lattices, which does not allow any magnetic order, at any U or temperature, we do not expect additional quantum fluctuations to qualitatively modify the magnetic state.
- A possible *qualitative consequence* of quantum fluctuations could be making the metallic state perfectly conducting at $T = 0$. However, we believe that above a small coherence temperature, one would see the signature of a highly resistive metal for the strongly frustrated systems.

2.5.2 System size dependence

In order to check the finite size effects on the Monte Carlo results, we have compared our $6 \times 6 \times 6$ lattice (864 sites) calculation with that on a $8 \times 8 \times 8$ lattice (2048 sites). In Fig.2.2 we compare the ground state magnetisation, average orbital moment and the ferromagnetic critical temperature for these two sizes. The results indicate that by the time $N \sim 1000$ the finite size effect on thermodynamic properties is negligible.

2.5.3 Annealing time dependence

We compare results obtained for two different Monte Carlo ‘annealing time’ in Fig.2.3. We show results on the ground state magnetisation, average orbital moment and temperature dependence of the $\mathbf{q} = (0, 0, 0)$ magnetic structure factor for a 2500 MC sweeps/temperature run and a 5000 MC sweeps/temperature run. The temperature discretisation is $0.005t$. The 5000 MCS run takes about 10 days. Our

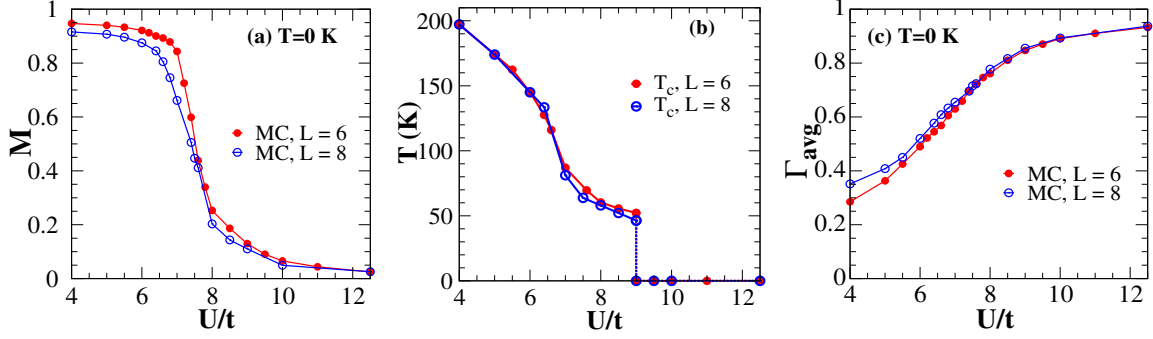


Figure 2.2: Comparison of (a) $T = 0$ magnetisation, (b) ferromagnetic critical temperature, and (c) average orbital moment, calculated on $6 \times 6 \times 6$ and $8 \times 8 \times 8$ pyrochlore lattices. The overall system volumes differ by about 3, but the difference in physical properties is negligible.

results show that annealing time doesn't alter the results significantly once the run time is $\gtrsim 10^3$ MCS/temperature.

The checks above will allow us to focus on the physics that emerges from our calculation without having to check for finite size artefacts frequently.

2.5.4 Cluster based update

Our Metropolis update involves a small cluster rather than diagonalisation of the full Hamiltonian. This is well controlled in the large U/t limit when the 'range' of electron excursion is limited but less reliable near the Mott transition. For that purpose we use variational calculation results, that use the Monte Carlo result as an ansatz and checks the stability of such a state on large system size (up to $10^3 \times 4$ lattices) for the ground state. We show one such result, (see figure 2.4) for the

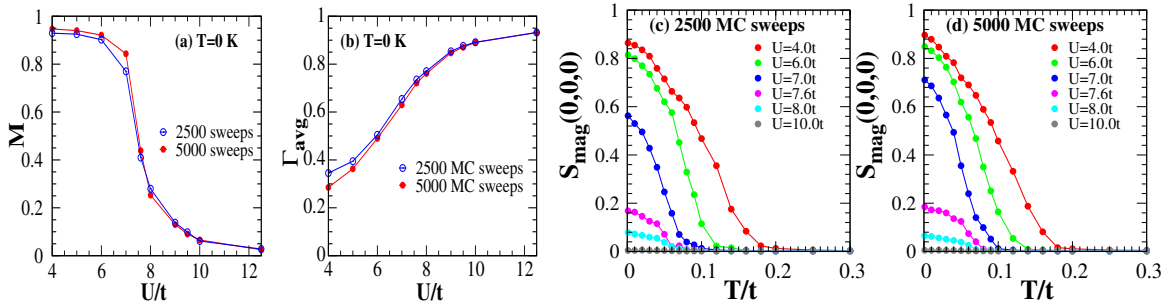


Figure 2.3: Annealing time dependence. (a) $T = 0$ magnetisation, (b) average orbital moment, and (c)-(d) temperature dependence of $S_{mag}(\mathbf{q} = (0, 0, 0))$. Run-times 2500 and 5000 MC sweeps per temperature, with temperature discretisation $\Delta T = 0.005t$. Size $6 \times 6 \times 6$.

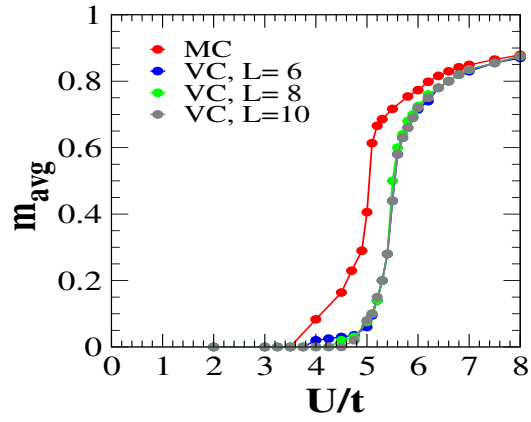


Figure 2.4: Comparison of the average local moment value obtained via Monte Carlo with a cluster based update as $T \rightarrow 0$ with that obtained via a variational minimisation calculation.

pyrochlore Hubbard model - which highlights that the cluster based MC results are consistent with variational calculation results.

MOTT TRANSITION ON THE PYROCHLORE LATTICE

3.1 Introduction

In frustrated magnets the temperature of transition to long range order is strongly suppressed (if finite at all) compared to expectations from mean field theory. This gives rise to a wide cooperative paramagnetic, or ‘spin liquid’, regime extending from the Curie scale, Θ_{CW} , down to the transition temperature, T_c . For some frustrated systems the T_c could be zero, as in the pyrochlore Ising antiferromagnet, already argued in 1956 [41].

The pyrochlore lattice, Fig.3.1, is a fascinating structure to explore the interplay of electron itinerancy and geometric frustration. In the deep Mott state on a pyrochlore lattice one expects only nearest neighbour antiferromagnetic coupling between localised electrons. The effective model can be written as a sum, over the tetrahedra, of squares of the total moment in each tetrahedron [34, 74] (if we treat the spins as classical to start with). The minimum of this is infinitely degenerate since the four spins at the vertices of each tetrahedron just need to satisfy a zero vector sum. The appearance of longer range couplings as the Hubbard repulsion reduces (or the bandwidth increases) can, potentially, lift the degeneracy and promote some ordered state. Whether it does so is not known. The transport and spectral character between the spin liquid Mott insulator and the weak correlation regime is also not known.

In this chapter, we focus on the role of the Hubbard interaction on the half filled pyrochlore lattice. We address two broad questions: (*i*) What is the nature of the

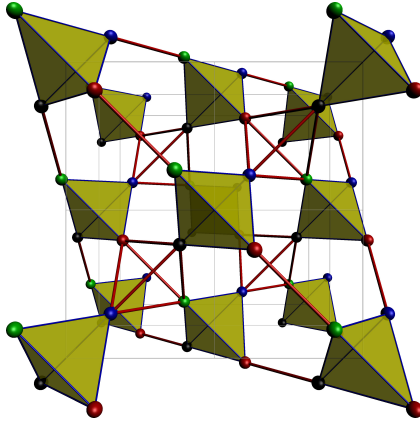


Figure 3.1: The pyrochlore lattice constructed out of corner shared tetrahedra. The interplay of the frustration of the tetrahedral unit cell with the weak connectivity (corner sharing) of the tetrahedra leads to the strongly frustrated nature of this lattice.

magnetic state as one moves towards weaker interaction in the Mott insulator, in particular what are the magnetic correlations near the insulator-metal transition (IMT)? (ii) What is the impact of these magnetic correlations on electron physics (resistivity, optics, spectral features) near the IMT?

The chapter is organized as follows. In the next section we provide a summary of existing results on the pyrochlore structure - in particular the Heisenberg and Hubbard models. This is followed by our results on the phase diagram, density of states, transport, and optics, across the IMT. The final section dwells on effective models that one can derive in limiting cases.

3.2 Previous work

The pyrochlore Heisenberg antiferromagnet, which describes the deep Mott limit, has been well studied in the classical limit. While the Hubbard model at half-filling and large interaction maps on to the $S = 1/2$ Heisenberg antiferromagnet, we provide a discussion of the more general model below.

3.2.1 Pyrochlore Heisenberg model

The nearest-neighbour *classical* Heisenberg antiferromagnet on the pyrochlore lattice can be written as

$$H = J \sum_{\langle ij \rangle} \mathbf{S}_i \cdot \mathbf{S}_j = (J/2) \sum_{\alpha} \mathbf{P}_{\alpha}^2 - JN \quad (3.1)$$

where $J > 0$ is the antiferromagnetic exchange interaction. The sum on $\langle ij \rangle$ runs over all neighbouring pairs of bonds of the lattice and the sum on α runs over the number of tetrahedra making up the lattice. $\mathbf{P}_{\alpha} = \sum_{i=1}^4 \mathbf{S}_i$, where the \mathbf{S}_i 's are spins on the tetrahedron α , with $|\mathbf{S}_i| = 1$. N is the total number of sites of the pyrochlore lattice.

The ground state needs to satisfy the constraint $\mathbf{P}_{\alpha} = 0$ for all α . This results in an infinitely degenerate manifold of possible configurations $\{\mathbf{S}_i\}$. The pyrochlore lattice does not show any magnetic order at zero temperature [34, 74]. Numerical studies based on Monte Carlo simulations suggest that there are no internal energy barriers between the degenerate minima at $T = 0$, and no free-energy barriers at finite T , precluding a freezing transition [34]. However, the absence of long-range order does not mean the physics is trivial at low temperature as the accessible states have nontrivial local constraints on them, leading to a correlated spin structure (cooperative paramagnet). The ‘disordered’ but long-range correlated state generates characteristic features in the magnetic structure factor (see figure 3.2), appearing as “bow-ties” [129] or “pinch-points” [130], indicative of power-law correlations [130, 131].

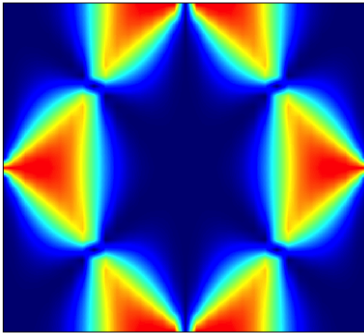


Figure 3.2: Magnetic structure factor of classical Heisenberg spins in the [hhl] plane showing the bow-tie structure with pinch points at their center. The dark-blue regions indicate weak spin correlations, whereas the red regions highlight strong spin correlations. The pinch-points are the locations of discontinuities, rather than divergences.

In the *semiclassical*, $2S \gg 1$, case the classical degeneracy is partially lifted by the zero-point energy of quantum fluctuations at harmonic order, but there remains [132] an infinite manifold of degenerate collinear ground states. Further quantum fluctuations at anharmonic order break the degeneracy between the various harmonic ground states, yet they leave out a massive but nonextensive degeneracy (smaller than the harmonic ground state) [133].

The ground state for $S = 1/2$ is argued to be a quantum spin liquid [49, 134, 135]. This spin-singlet ground state has a finite energy gap for triplet excitations. The spin-spin correlation function decays exponentially with a correlation length shorter than the lattice spacing [49].

3.2.2 Pyrochlore Hubbard model

Heisenberg interactions beyond nearest neighbour induce transitions to various ordered phases (e.g., collinear, nematic and multiple- \mathbf{q} order) [136–138]. Also, easy axis anisotropy, long-range dipolar interaction, *etc.*, lead to multiple- \mathbf{q} ordered phases [139]. It has been argued that beyond the Heisenberg limit the half-filled Hubbard model on the pyrochlore lattice can be expressed as a highly frustrated intratetrahedral spin model with weak intertetrahedral perturbations [135]. This model has an exactly solvable Klein point, about which the ground state is a three-dimensional quantum spin liquid over an extended parameter region. This spin-liquid state hosts massive spinon excitations, which are deconfined and move in all three dimensions within the lattice [135]. For the Hubbard model on the pyrochlore lattice, the only work on the Mott transition, that we know of, suggests a transition from a semimetal to a spin liquid Mott insulator [140]. However, detailed properties near the IMT are not available. A more complicated iridate model has been studied via cluster-dynamic mean field theory [116, 117], and will be discussed in a later chapter 6.

To explore interplay of itinerancy, correlation, and geometric frustration on the pyrochlore lattice, we study the single band Hubbard model with nearest neighbour hopping. We followed the approach mentioned in chapter 2 and present the results here.

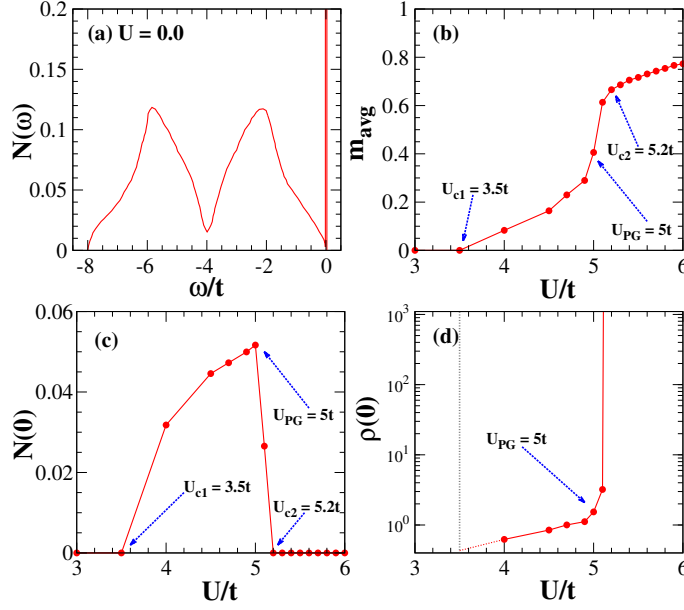


Figure 3.3: (a) Tight binding density of states for the pyrochlore lattice. (b)-(d) Results at $T = 0$ for: (b) variation of the average local moment m_{avg} , (c) the density of states, $N(0)$, at the Fermi level, and (d) the resistivity $\rho(T = 0)$.

3.3 Results of our study

3.3.1 The ground state

As $T \rightarrow 0$ our MC mainly samples configurations that maximise $P\{\mathbf{m}_i\}$, or, alternately, minimise the energy, *i.e.*, $\frac{\delta}{\delta \mathbf{m}_i} \langle H_{eff} \rangle = 0$. This is the same as unrestricted Hartree-Fock in the magnetic channel.

Upto a critical coupling, $U_{c1} \sim 3.5t$, the minimisation yields $m_i = |\mathbf{m}_i| = 0$ at all sites. As a result upto U_{c1} the electronic ground state is essentially tight binding, the density of states for which is shown in Fig.3.3.(a). There is a sharply suppressed DOS at Fermi level characteristic of the pyrochlore band structure, and a flat band right above the Fermi level. For $U < U_{c1}$ the system is a semimetal.

For $U_{c1} < U < U_{PG}$ where $U_{PG} \approx 5t$ we observe a small moment, orientationally disordered, magnetic state. The average moment size is shown in Fig.3.3.(b), and the full distribution later in the chapter. With the disorder caused by these moments breaking the translation invariance of the pyrochlore lattice, the DOS around the Fermi level, $N(0) = (\frac{1}{2\Omega}) \int_{-\Omega}^{\Omega} N(\omega) d\omega$, where $\Omega = 0.05t$, gains weight (Fig.3.3.(c)). In a narrow region around U_{PG} there is rapid increase in the mean magnitude of the moments and, as a result, the DOS at Fermi level gets depressed again. The detailed behaviour of the low energy DOS is shown later. At $U_{c2} \sim 5.2t$ the DOS

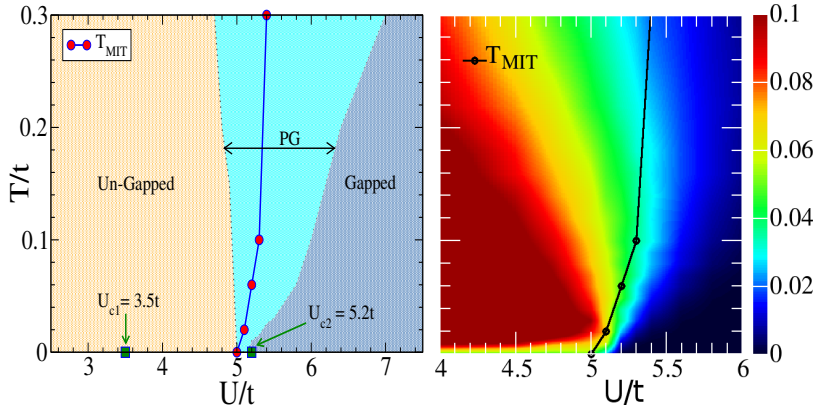


Figure 3.4: Phase diagram (left) and the density of states at the Fermi level (right) for varying U and T . Local moments appear at U_{c1} but the state remains metallic, turning insulating at U_{c2} . PG refers to a pseudogap state and the metal-insulator transition line separates regions with opposite signs of $d\rho/dT$. The right panel highlights the ‘re-entrant’ feature in the low energy DOS with increasing temperature. To avoid clutter we have not marked the U_{PG} scale in the ground state in the left figure.

at the Fermi level vanishes as a Mott gap opens. For $U > U_{c2}$ the moments are large, and saturate to their atomic value, $|\mathbf{m}_i| = 1$, as $U/t \rightarrow \infty$. The coupling of the electrons to the local moments leads to weak scattering and a small resistivity for $U_{c1} < U < U_{PG}$, a rapid growth in resistivity for $U_{PG} < U < U_{c2}$, and zero d.c conductivity for $U > U_{c2}$. This is shown in Fig.3.3.(d). We will discuss the resistivity in much greater detail later, and just wanted to highlight the effect within the $T = 0$ mean-field state here.

A comment about the magnetic state. Since there was no reason to expect that the moments would have any obvious periodic pattern the only way to do the ‘minimisation’ was via simulated annealing employing Monte Carlo. In the $U/t \rightarrow \infty$ limit the half filled Hubbard model leads to a Heisenberg model for the \mathbf{m}_i (classical, in our SPA approximation) and for the pyrochlore Heisenberg antiferromagnet the moments are known to be disordered [34, 74], albeit power law correlated [130, 131]. Our MC minimisation reproduces this state. At lower U/t , both in the Mott phase and the ‘metal’, there are no simple results known - but our results suggest that a ‘disordered’ state persists and correlations reminiscent of a classical spin liquid phase [130] survive down to $U/t \sim 8$.

3.3.2 Thermal phase diagram

Fig.3.4 (left panel) shows the $U - T$ phase diagram in terms of the magnetic, transport, and spectral properties that we observe. The following features emerge:

At finite T thermal fluctuations of local moments on the weak-coupling side ($U < U_{PG}$) lead to a quick low T increase in the low energy DOS, and then a gradual decrease with further increase in T . On the strong-coupling side ($U > U_{c2}$) the angular fluctuations of the local moments result in a slight smearing of the Mott-gap with temperature and an increase in the low energy DOS. However in the Mott-transition neighbourhood, the Mott gap quickly converts to a PG with increasing T , leading to the widening of the PG region shown in Fig.3.4 (left panel).

We demarcate the finite T metal-insulator boundary in terms of the temperature derivative $d\rho/dT$. A state is metallic if $d\rho/dT > 0$ and insulating if $d\rho/dT < 0$. The spectral features and resistivity are discussed in detail further on.

Fig.3.4 (right panel) shows the DOS at the Fermi level varying with U and T . On the Mott insulating side ($U \geq U_{c2}$) we observe the DOS slowly increasing with temperature, which can be understood as the filling of the Mott gap. On the metallic side ($U_{c1} < U < U_{c2}$) we see a non monotonic behaviour. The DOS quickly grows with temperature in the low temperature regime. It then reduces with further increase in temperature, the weight getting transferred to high energy.

3.3.3 Density of states

Fig.3.5 shows the thermal evolution of the DOS in three of the four broad interaction regimes of our phase-diagram.

(i) For $U < U_{c1}$ the ground state is characterized by $m_i = |\mathbf{m}_i| = 0$. The electron model reduces to the usual tight-binding pyrochlore lattice. This is characterised by two flat-bands at the upper band edge and vanishing DOS at the Fermi energy. At finite T , small ‘randomly’ oriented local moments appear in the system broadening the flat bands and leading to a small DOS at the Fermi level. (ii) For $U_{c1} < U < U_{PG}$, the ground state has small disordered local moments. The DOS is gapless and the weight at the Fermi level is nonmonotonic with T , increasing initially and then decreasing as a weak PG forms (see Fig.3.5.(a)). (iii) For $U_{PG} < U < U_{c2}$ the DOS has a PG at $T = 0$. This fills up initially with increasing T , Fig.3.5.(b), but deepens again above a temperature scale that is visible in Fig.3.4 right panel. (iv) For $U \gg U_{c2}$ the ground state has a hard gap. With increase in temperature, the angular fluctuations of the local moments result in a slight smearing of the Mott-

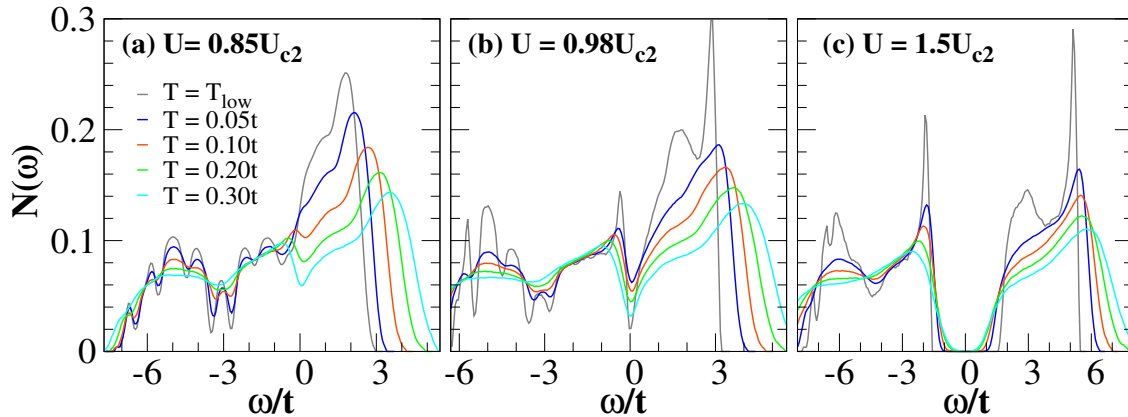


Figure 3.5: Density of states varying with temperature at three representative regimes of our calculation. (a) $U = 0.85U_{c2}$ lies in the gapless metallic side, (b) $U = 0.98U_{c2}$ corresponds to the pseudo-gap (PG) regime with a pronounced dip in the DOS at the Fermi-level. and (c) $U = 1.5U_{c2}$ lies in the gapped Mott-insulating side. $T_{low} = 0.01t$ in panel (a), where as $T_{low} = 0.0$ for panels (b) and (c). In panel (a) the low energy DOS reduces with increasing T , in panel (b) it increases and then reduces with T , and in panel (c) it monotonically increases with T .

gap, and an increase in the low energy DOS Fig.3.5.(c). However, there exists a clear Mott-gap until very high temperature, $T \sim m_{avg}(T)U$.

3.3.4 Transport and optics

Fig.3.6 shows the d.c. resistivity $\rho(T)$ for different U/t . We consider the following regimes. (i) For $U < U_{c1}$ the $T = 0$ phase is a semimetal. Since this lies well below the Mott transition we do not show the T dependence here. (ii) For $U_{c1} < U < U_{PG}$ the residual resistivity $\rho(0)$ is finite with $d\rho/dT > 0$ over the entire T range. The resistivity can be understood in terms of a disorder induced density of states and the scattering of electrons from the small disordered moments. This is the metallic regime. (iii) For $U \gg U_{c2}$ the system has a clear Mott gap at $T = 0$ with $\rho(0) \rightarrow \infty$. In this regime $d\rho/dT < 0$ over the entire temperature window. This is the Mott-insulating regime. (iv) In the neighbourhood of U_{c2} , *i.e.*, $|U - U_{c2}| \ll U_{c2}$, $\rho(T)$ shows a non-monotonic behaviour. We observe $d\rho/dT < 0$ in the low temperature limit, crossing over to $d\rho/dT > 0$ with increasing T . The temperature at which $d\rho/dT$ changes its sign is indicated as the T_{MIT} .

We observe T_{MIT} increasing with U as seen in Fig.3.4. This behaviour can be understood as the scattering of electrons from the background fluctuating local moments. As U increases, the average local moment magnitude $m_{avg}(U)$ also increases,

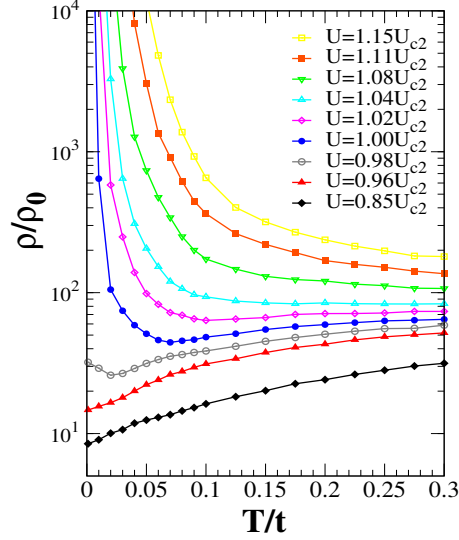


Figure 3.6: Temperature dependence of the resistivity for different U/t near the Mott insulator-metal transition. The normalising scale is $\rho_0 = (\hbar a_0)/e^2$, where a_0 is the lattice spacing.

resulting in the increased scattering of the electrons and a depleting DOS at the Fermi level.

Fig.3.7 shows the optical conductivity from our calculation as we cross the Mott transition. The important points are as follows: (i) $\sigma(\omega)$ for $U < U_{c1}$ is a semimetal at $T = 0$ and does not have a Drude peak. (ii) For $U_{c1} < U < U_{PG}$, $\sigma(\omega)$ shows a response with the peak at a small finite frequency that slowly shifts to higher values with increasing T . (iii) For $U > U_{c2}$ the system has a clear gap $\Delta(T)$ in the DOS. Thus $\sigma(\omega) = 0$ for $\omega < \omega_c \sim \Delta(T)$. With increasing temperature the gap $\Delta(T)$ reduces, resulting in small, but increasing low frequency weight of $\sigma(\omega)$ and the peak position shifts to higher frequency. This Mott-insulating regime of the pyrochlore lattice may have finite spectral weight at $\omega = 0$ in the optical conductivity $\sigma(\omega)$ at high temperatures. (iv) For $U_{PG} < U < U_{c2}$ we have a pseudogap in the DOS. $\sigma(\omega = 0) \rightarrow 0$ in this regime. However with increasing temperature the zero frequency weight increases initially and then decreases in accord with the behaviour of the DOS in this regime.

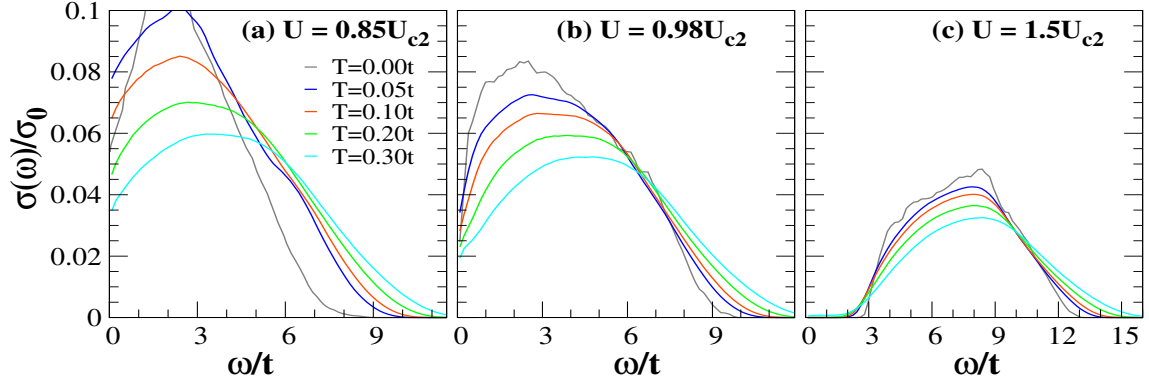


Figure 3.7: Optical conductivity at $U/U_{c2} = 0.85, 0.98$ and 1.5 with varying temperatures. $U = 0.85U_{c2}$ shows a non-Drude like behaviour with peak at small and finite frequency. With increasing U the peak moves to higher frequency and the zero frequency weight decreases continuously and eventually there appears a gap for $U \geq U_{c2}$.

3.4 Discussion

3.4.1 Overall scenario

Within our picture, the interaction effects are encoded in the presence of the ‘local moments’ \mathbf{m}_i . The size m_i of this moment dictates the on site splitting at the site \mathbf{R}_i , and leads to a Mott gap in the overall DOS when $Um_{avg} \gg t$. The spatial correlations of \mathbf{m}_i decide whether the electron spin $\vec{\sigma}_i$ will display any long range order.

Let us correlate the electron physics across the Mott transition to the behaviour of the \mathbf{m}_i , we will then take up the effective models for the \mathbf{m}_i themselves. (i) In the metallic regime, $U \gtrsim U_{c1}$, the m_i ’s are small and the orientations are random. The scattering from these moments leads to a finite broadening, $\tau_{\mathbf{k}}^{-1}$, of the momentum eigenstates. This generates a finite DOS at $\omega = 0$, a non-Drude optical response, and resistivity increasing with temperature (unlike in a semimetal). (ii) In the Mott-insulating regime, $U > U_{c2}$, the m_i ’s are large and show short-range magnetic correlation (discussed next). The large m_i ’s lead to a Mott gap in the DOS and optical conductivity, and a diverging resistivity as $T \rightarrow 0$. (iii) In the pseudogap regime, the m_i ’s are moderately large and orientationally disordered. This results in a strong suppression in the DOS at Fermi energy, but no gap, a large finite residual resistivity and a non-Drude optical response.

We have shown m_{avg} for varying U at $T = 0$ (Fig.3.3(b)). In the next section we discuss the limiting models that dictate the behaviour of \mathbf{m}_i , and in the section after,

we show detailed results on the size distribution of \mathbf{m}_i , and its spatial correlations.

3.4.2 Effective models in limiting cases

We have shown only a formal expression for the effective magnetic Hamiltonian. To get a feel for the magnetic states that arise it is useful to provide the approximate analytic structure in limiting cases. These are (a) weak coupling, when $U \lesssim t$, and (b) strong coupling, when $U \gg t$.

3.4.2.1 Weak coupling

Our effective interaction looks like a ‘Hund’s coupling’, with the electron spin coupled to a background moment through the coupling U . Given the formal similarity with the Hund’s problem we can borrow the form of the weak coupling result [141] from the literature:

$$H_{eff}\{\mathbf{m}_i\} \sim -\frac{U^2}{4} \sum_{ij} (\chi_{ij} - \frac{1}{U} \delta_{ij}) \mathbf{m}_i \cdot \mathbf{m}_j + \frac{U^4}{16} \sum_{ij}^{kl} f(\mathbf{m}_i, \mathbf{m}_j, \mathbf{m}_k, \mathbf{m}_l) + ..$$

The structure of $f(\mathbf{m}_i, \dots, \mathbf{m}_l)$ is complicated, involving two-spin terms such as $\mathbf{m}_i \cdot \mathbf{m}_j$, $(\mathbf{m}_i \cdot \mathbf{m}_j)^2$, three-spin terms such as $(\mathbf{m}_i \cdot \mathbf{m}_j)(\mathbf{m}_i \cdot \mathbf{m}_k)$, and four-spin terms such as $(\mathbf{m}_i \cdot \mathbf{m}_j)(\mathbf{m}_k \cdot \mathbf{m}_l)$. The i, j, k, l can be separated by long distance in the weak-coupling limit.

In contrast to the Hund’s problem, where there were predefined local moments, in our case the moments have to arise from an instability in the electron system. The leading instability involves the vanishing of coefficient of the quadratic term, *i.e.*, $1 - U\chi_0(\mathbf{q}) = 0$. This generates the moment and, if there is a prominent peak at some $\mathbf{q} = \mathbf{Q}$ in χ_0 the moments order with that wavevector. In such a situation the fourth order term can be expanded about \mathbf{Q} . The quartic term decides the magnitude of the order at \mathbf{Q} .

We have computed the $\chi_0(\mathbf{q})$ (see figure 3.8) for the half-filled pyrochlore band, having tested the scheme for the quarter-filled band for which results are available [142]. The $\chi_0(\mathbf{q})$ at half-filling is featureless, suggesting that there is no particular wavevector that would be picked out. In that case the quartic term, whose detailed structure we do not know at half filling, decides not only the magnitude but also the spatial character of the order parameter field. It seems that the nonlinearity creates a bimodal distribution for the m_i , discussed further on, but without any significant spatial correlation.

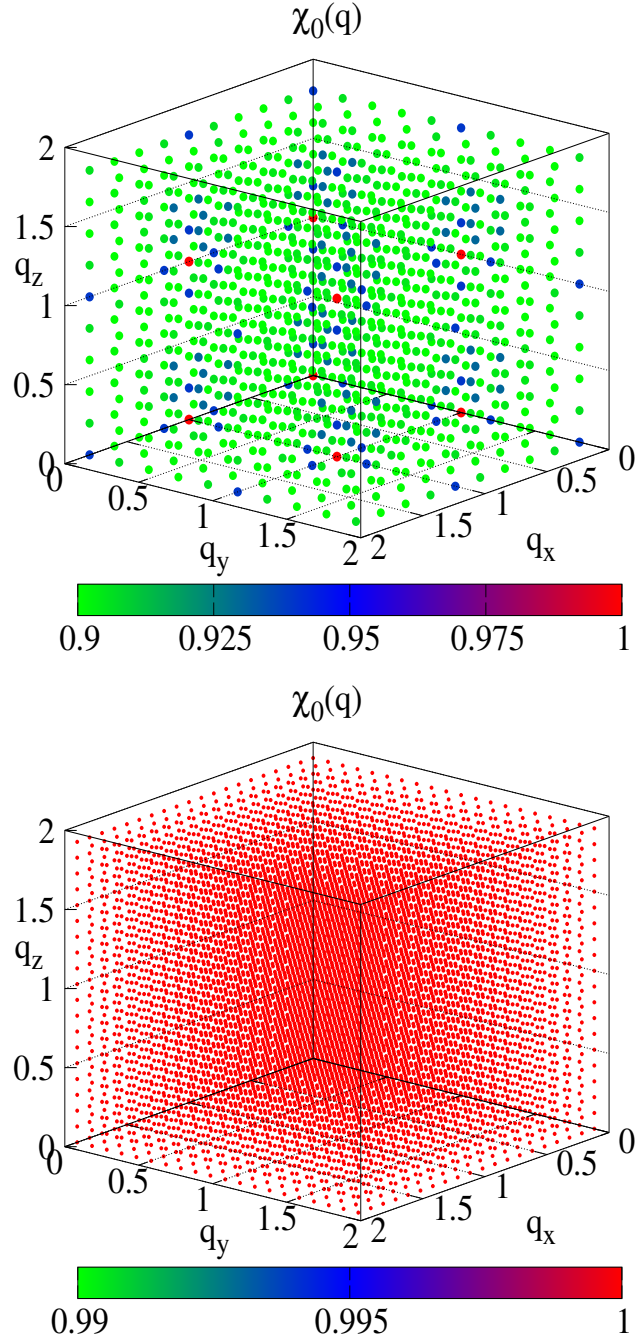


Figure 3.8: $\chi_0(\mathbf{q})$ on the pyrochlore lattice. q_x , q_y and q_z are in the units of π . (Left) For quarter-filling, $\chi_0(\mathbf{q})$ has dominant weight at eight \mathbf{q} points in the Brillouin zone. (Right) At half-filling, however, $\chi_0(\mathbf{q})$ has no dominant weight at any \mathbf{q} , and seems featureless.

3.4.2.2 Strong coupling

For $U \gg t$, one can write an effective magnetic Hamiltonian on the pyrochlore lattice by tracing out fermions order by order in t/U . This gives us

$$\begin{aligned}
 H_{eff}\{\mathbf{m}\} &= H_{tetr}\{\mathbf{m}\} + H_{coup}\{\mathbf{m}\} \\
 H_{tetr}\{\mathbf{m}\} &\sim \sum_{\alpha} (J_0 + J_2 \mathbf{P}_{\alpha}^2 + J_4 \mathbf{P}_{\alpha}^4 + \dots) \\
 H_{coup}\{\mathbf{m}\} &\sim J'_4 \sum_{i \in \alpha, j \in \beta} \mathbf{m}_i \cdot \mathbf{m}_j + J''_4 \sum_{i \in \alpha, j \in \beta}^{k \in \alpha \cap \beta} (\mathbf{m}_i \cdot \mathbf{m}_k)(\mathbf{m}_j \cdot \mathbf{m}_k) \dots
 \end{aligned}$$

where $\mathbf{P}_{\alpha} = \sum_{i=1}^4 \mathbf{m}_i^{\alpha}$ is the total spin on the tetrahedron α , H_{tetr} describes interactions between spins in a tetrahedron while H_{coup} includes the intertetrahedron terms with a common corner shared site. $J_0 = -\frac{8t^2}{U}(1 - \frac{4t^2}{U^2})$, $J_2 = \frac{t^2}{2U}(1 - \frac{24t^2}{U^2})$, $J_4 = \frac{5t^4}{8U^3}$ and $J'_4, J''_4 \sim O(\frac{t^4}{U^3})$.

Deep in the Mott phase, one would drop the J_4 , J'_4 and J''_4 terms and obtain a classical Heisenberg model, which does not show any long-range order or freezing, but power-law correlations at low temperature [130, 131]. The correlations of the electron spins, $\vec{\sigma}_i$, can be computed in response to this. As $U \rightarrow U_{c2}$ the J_4 , J'_4 and J''_4 terms become important. These multi-spin exchange interactions modify the magnetic ground state, but some of the Heisenberg limit features [130] are observable (see next) in the structure factor down to $U \sim 8t$. The expansion in t/U ceases to be useful once the gap closes.

3.4.3 Detailed magnetic structure

Fig.3.9 shows the the amplitude distribution of the magnetic moment $P(m)$ for different temperature and interaction regimes.

Fig.3.9(a) shows $P(m)$ for $U = 0.85U_{c2}$. In the ground state there is a two peak structure, highlighting the presence of amplitude inhomogeneity. We have checked that there is no significant density inhomogeneity, or charge ordering, in the system. With rise in temperature, $P(m)$ shows a broad single peak behaviour with the peak shifting towards large m . This behaviour is seen in the $U_{c1} < U < U_{c2}$ regime. Fig.3.9(b) shows $P(m)$ for $U \sim U_{c2}$, just in the Mott insulating side. The ground state has a narrow single peak feature indicating an amplitude homogeneous Mott state. With rise in temperature this narrow peak broadens, the peak position moves towards higher m . Fig.3.9(c) shows $P(m)$ for $U = 1.5U_{c2}$, well in the Mott regime.

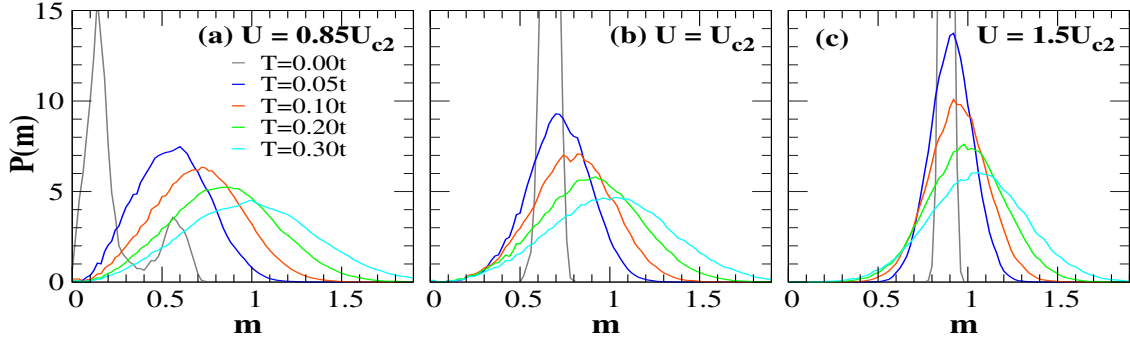


Figure 3.9: Temperature dependence of $P(m)$ for $U = 0.85U_{c2}$, U_{c2} and $1.5U_{c2}$ for indicated temperatures.

$P(m)$ has a single peak feature which broadens with temperature and shifts to higher m . The fluctuations about the mean are weaker in the insulator than in the metallic state.

Fig.3.10 shows the \mathbf{q} dependence of the magnetic structure factor for varying T and U . We observe that even at $T = 0$, $S(\mathbf{q})$ has no ordering peak at any \mathbf{q} 's. The magnetic ground state is disordered. Nevertheless for both $U \sim U_{c2}$ and $U = 1.5U_{c2}$ the weight distribution is not completely homogeneous in \mathbf{q} and have some prominent features. This signature survives to $T \sim 0.03t$. Examination of the classical Heisenberg model has revealed that there are ‘pinch point’ features in scattering, arising from the constrained ground state, that survive [143] to $T \sim 0.1J$, where J is the exchange scale (in our case $J = t^2/U$). Obtaining such a result, indicative of power law correlations, requires larger system size ($\gtrsim 10^3$), much longer annealing ($\gtrsim 10^8$) MC weeps), and a more sophisticated algorithm instead of single spin update. Due to our computational cost and size limitations we only get a hint of this spin liquid state. By the time $T \sim 0.05t$, which is $\sim J/2$ at $U = 1.5U_{c2}$, the \mathbf{q} dependence is completely featureless.

3.4.4 Variational check

Since MC hints that the magnetic ground state involves disordered local moments for $U > U_{c1}$, we tried a simple variational check. We set up trial configurations $\{\mathbf{m}_i\}$ with random orientation, but uniform magnitude m_0 , with m_0 as a variational parameter. This differs from the real situation where the \mathbf{m}_i 's have some amplitude inhomogeneity and also orientational correlation. Energy minimisation confirms the presence of a small moment phase, beyond some U_{low} , with an initial slow growth of $m_0(U)$ and then a rapid crossover to large values at some U_{high} (see Fig.3.11).

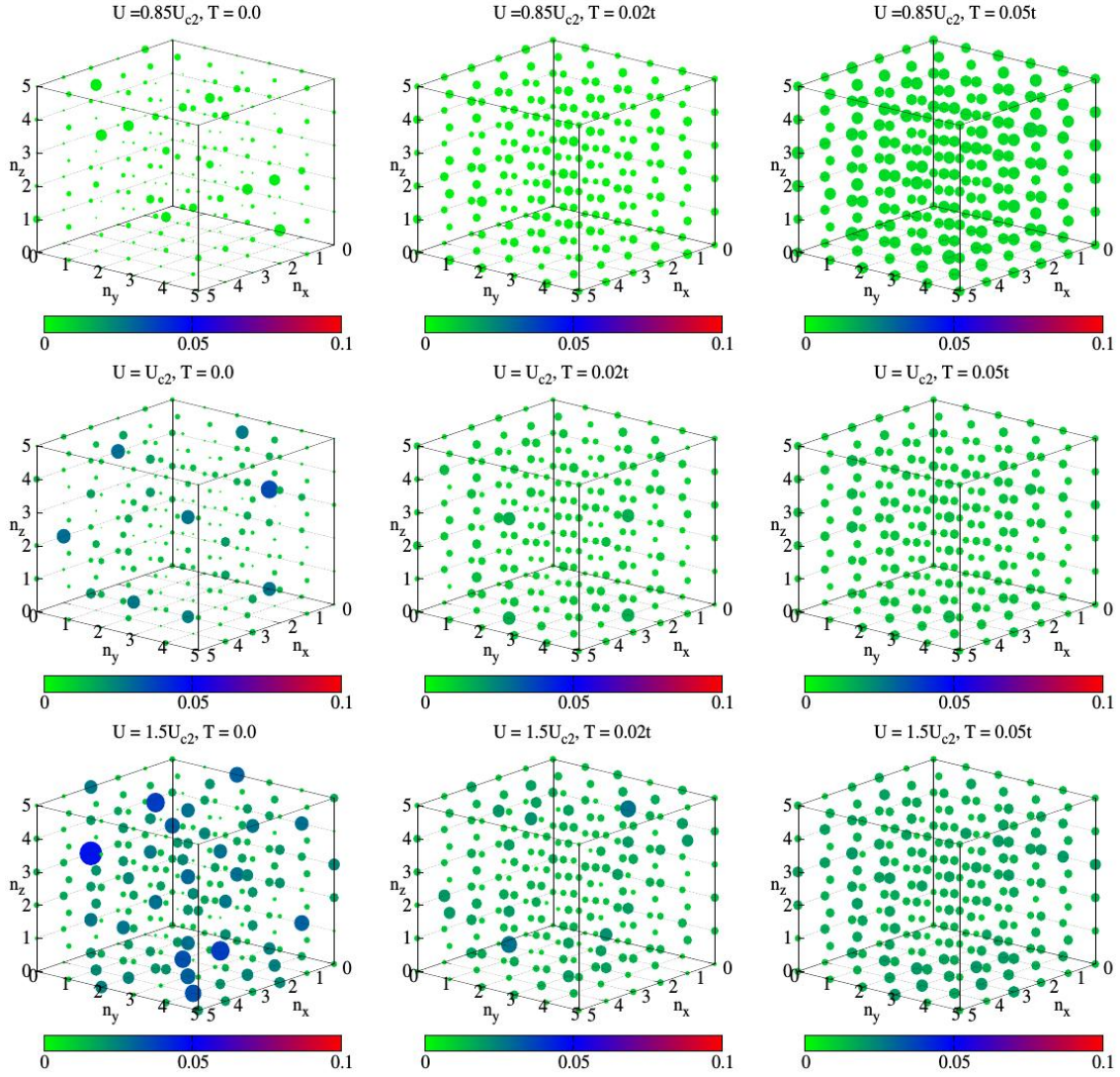


Figure 3.10: The full magnetic structure factor $S(\mathbf{q})$ for $U = 0.85U_{c2}$, U_{c2} , $1.5U_{c2}$ (along column) and $T = 0.0$, $0.02t$ and $0.05t$ (along row). We use the notation $\mathbf{q} = \frac{2\pi}{L}(n_x, n_y, n_z)$, n 's are integers. The size of a dot signifies relative weight at a given \mathbf{q} while its color represents the actual magnitude of $S(\mathbf{q})$.

The U_{low} and U_{high} are about 10% higher than MC estimates and may get reduced if spatial correlations are included.

3.5 Conclusion

We have studied the Mott transition in the half-filled Hubbard model on a pyrochlore lattice. The geometric frustration and the corresponding large magnetic degeneracy prevents the occurrence of any magnetic order in the deep Mott state. This continues

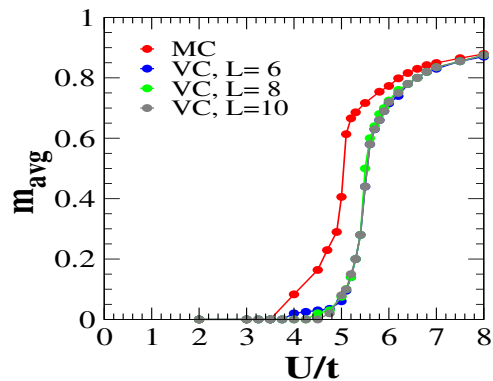


Figure 3.11: Comparison of the variationally obtained average moment value with result from the Monte Carlo as $T \rightarrow 0$.

all the way to the insulator-metal transition. Beyond the insulator-metal transition there is a window with a pseudogap in the density of states, disordered local moments, and a large residual resistivity. At even weaker interaction one recovers the non magnetic band semimetal. Thermal fluctuations destroy the ‘spin-liquid’ correlations in the insulating state, converting the system to an uncorrelated paramagnet. The low energy electronic density of states and the resistivity show a monotonic temperature dependence deep in the metallic and insulating phases, but a non monotonic character near the insulator-metal transition.

Our main results, are the following: (i) Increasing interaction in the ground state leads successively to a small-moment metal, then a narrow insulating pseudogap window, and finally to the gapped Mott insulator. (ii) The resistivity and the low energy density of states have a *strongly non monotonic* temperature dependence near the metal-insulator transition (MIT). (iii) The finite moment phases, from near the MIT to the deep Mott regime, *are all disordered*. Well in the Mott phase they display what seems (within the limits of our system size) to be power law spatial correlations that survive to a small finite temperature.

Though it is expected that additional quantum fluctuations modify qualitatively the underlying magnetic state at low temperature, we don’t expect the local moments to vanish in the insulating phase, due to the presence of finite Mott gap. One possibility is that quantum fluctuations may restore the translation invariance in the ‘small-moment’ metallic phase, making it perfectly conducting at $T = 0$.

MOTT TRANSITION ON THE CHECKERBOARD LATTICE

In chapter 1 we qualitatively described the emergence of a Mott insulating state due to increasing interaction in the half-filled Hubbard model. This chapter discusses the Mott transition on the checkerboard lattice, the two dimensional analog of the pyrochlore lattice. The lattice is shown in the Fig.4.1. In terms of electron hopping it is equivalent to a square lattice with nearest neighbour (NN) hopping t , and next nearest neighbour (NNN) hopping also of amplitude t on alternate plaquettes.

4.1 Introduction

Frustrated magnets arise due to the coupling between electrons localised on non-bipartite lattices [144–146]. The localisation stems from electron correlation, a concrete example being the Mott insulating phase of the half filled Hubbard model. The $U/t \gg 1$ limit in such cases involve virtual hopping of the electrons, and induces antiferromagnetic exchange. With weakening U/t , the electrons ‘delocalise’ over progressively longer distance and mediate longer range couplings [147, 148]. These additional couplings are crucial in deciding the physics when the $U/t \gg 1$ Heisenberg limit involves a macroscopically degenerate ground state. The checkerboard lattice is in this category [18].

Two complications arise with decreasing U/t : (a) the size of the moments diminish as the system heads towards the Mott transition, and (b) the range of electron hops increase and the exchange processes get harder to quantify. Near the insulator-metal transition (IMT) the magnetic correlations, and their impact on electronic

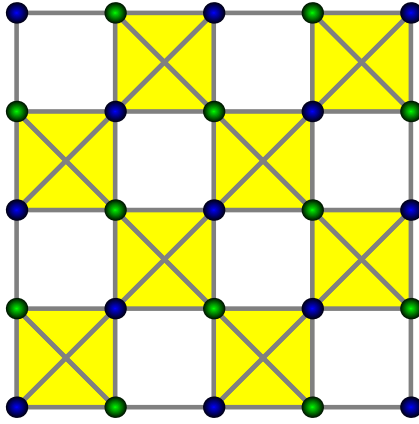


Figure 4.1: The checkerboard lattice with alternating ‘empty’ and crossed plaquettes. All hopping amplitudes (diagonal and axial) are equal. The structural unit cell contains two atoms. Each crossed plaquette, in isolation, can be viewed as a tetrahedron.

properties, have to be worked out self-consistently.

This has indeed been attempted for various frustrated lattices, *e.g.*, the edge-shared triangular [75–80] and FCC [83, 84, 149] lattices, the corner shared kagome [81, 82] and pyrochlore [85, 87] lattices. Surprisingly, very little attention has been given on this direction to the checkerboard lattice. The checkerboard lattice shares similarity with the pyrochlore lattice in having corner shared tetrahedra, but the connectivity is different (all bonds in the pyrochlore tetrahedron are equal, which is not for the case for the checkerboard tetrahedron). So it would be interesting to check if this lowering of the symmetry of the checkerboard lattice allows any magnetic order at low temperature arising due to ‘order by disorder’. In such a case, its impact on the electronic phases would also be worth investigating.

For the checkerboard lattice the Heisenberg antiferromagnet is well understood [18, 42, 150–158]. Like the pyrochlore lattice, the classical ground state on the checkerboard lattice is macroscopically degenerate [18] and there is no order at any temperature. The quantum, $S = 1/2$, case is argued to be a plaquette valence-bond crystal state [42, 150–158] - the product of singlets on the uncrossed plaquettes.

There is limited work on the checkerboard Hubbard model, focused mainly on the ground state. One study [159] suggested that increasing U/t leads to a transition from the semi-metallic band state to a charge-ordered insulator, and then to a magnetically disordered Mott insulator, while another reports a first order transition from the semi-metal to an insulating state with plaquette magnetic order [160].

The varying results, based on different methods [159, 160], leave some questions unanswered:

- What magnetic ground state emerges within a Hartree-Fock (HF) scheme?
- What are the effects of thermal fluctuation on this magnetic state?
- What is the impact of the magnetic order, and fluctuations, on the electronic properties near the IMT?

We address these questions using our approach with a single band Hubbard model on the checkerboard lattice. Our approach, as discussed before, is a combination of Hartree-Fock theory for the ground state and an auxiliary-field-based Monte Carlo to handle thermal fluctuations. We use two approaches to study H_{eff} . (i) At finite T we use a Monte Carlo (MC) approach, using the traveling cluster scheme to generate equilibrium configurations of the \vec{m}_i . We typically use a $N = 24 \times 24$ lattice with 8×8 update clusters. We anneal down from $T = 0.1t$ (since we see no correlations above that temperature) and use 10^4 MC sweeps per temperature, going down to $T = 10^{-4}t$. Physical properties are averaged over ~ 100 configurations at each T . (ii) At $T = 0$ we use a variational scheme, trying out a family of periodic \vec{m}_i configurations (both planar and non-planar) and cross check our results with the Monte Carlo based annealing of the \vec{m}_i .

To characterise the magnetic state we calculate the following indicators with the equilibrium MC configurations.

$$\begin{aligned}
 S(\vec{q}) &= \frac{1}{N^2} \sum_{ij} \langle \vec{m}_i \cdot \vec{m}_j \rangle e^{i\vec{q} \cdot (\vec{R}_i - \vec{R}_j)} \\
 \tau_{avg} &= \frac{1}{N} \sum_i \int_0^{t_{max}} dt' \langle \vec{m}_i(0) \cdot \vec{m}_i(t') \rangle \\
 P(m) &= \frac{1}{N} \sum_i \langle \delta(m - |\vec{m}_i|) \rangle
 \end{aligned}$$

In the expressions above N is the system size and the angular brackets stand for thermal average. In sequence, (i) $S(\vec{q})$ is the thermally averaged magnetic structure factor. The onset of rapid growth in $S(\vec{q})$ at some wavevector \vec{Q} indicates magnetic ordering. In the thermodynamic limit, there would be no ‘true’ long-range magnetic ordering at finite temperature in two dimensions (2D). Our ‘magnetic order’ refers to magnetic correlation length growing to system size. We have checked the size dependence of the various temperature scales associated with these crossovers within the MC. Our MC runs on 16×16 , 24×24 and 32×32 lattices show that the characteristic temperature scales reduce very slowly with increasing size. (ii) To consider the possibility of freezing without long range order we compute a MC based

‘relaxation time’ [161] τ_{avg} where $t_{max} \sim 10^4$ steps and t' is the MC ‘time’. If on lowering the temperature, the system undergoes a magnetic ordering transition, then there is a rapid growth in τ_{avg} accompanied by a growth in the structure-factor at the wavevector \vec{Q} . The case where one observes a rapid growth in τ_{avg} but not in the structure-factor at any \vec{Q} , suggests a glass transition [161]. (iii) The distribution of the magnitude of the auxiliary moments is given by $P(m)$. Since the presence of a gap in the electronic density of states depends on the typical size of the \vec{m}_i , $P(m)$ is an important input in inferring transport. The mean moment $m_{avg} = \int mP(m)dm$.

In the next section we present our results, followed by a detailed discussion on the magnetic behaviour and its impact on the electronic properties.

4.2 Results of our study

4.2.1 Ground state

Let us focus on the low temperature result, at $T \sim 10^{-4}t$, obtained via a MC on lowering T . We label this as $T = 0$ in the lowest row in Fig.4.2, which shows the structure factor versus q_x and q_y . The leftmost panel, typical of the window $3t < U < 5.3t$, show no prominent features in the structure factor. It is suggestive of local moments with weak and short range correlations. We will need to look at the local moment magnitudes to fully characterise this window. For $U \geq 5.3t$ the structure factor shows distinct peaks at $\vec{Q}_{F_1} = (\pi, 0)$ and $\vec{Q}_{F_2} = (0, \pi)$ with the weight at peak position increasing initially with U/t and saturating for $U/t \geq 10$. We call this the ‘flux’ phase. The real space arrangement of the spins in the ‘flux’ phase is shown in the lower panel in Fig.4.3.

In our MC runs, we obtain the ‘flux’ state at the lowest temperature only in a small window of interaction strength, $U = [5.3t, 5.7t]$, near the IMT. The system encounters a ‘120 degree’ spin arrangement when cooled from high temperature, and does not manage to transit to the flux state, despite the flux state having the lowest ground state energy for all $U/t \geq 5.3$. On heating up from the flux state the order survives to a low finite T and then the system enters the 120 degree phase. We will discuss the results of the variational approach and its consistency with the MC results further on.

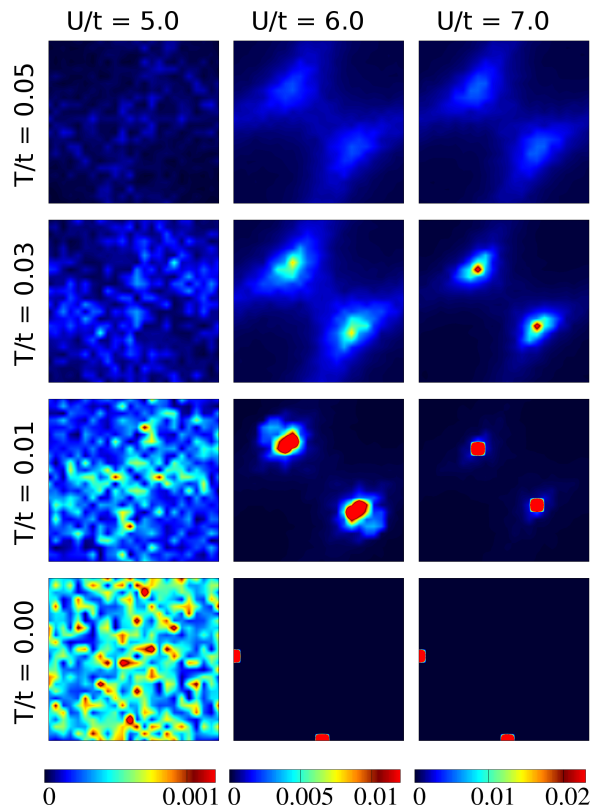


Figure 4.2: Magnetic structure factor $S(\vec{q})$ over $q_x, q_y \in [0, 2\pi]$ for different temperature and interaction strengths. The value of $S(\vec{q})$ follows the colour code. The left column, at $U = 5t$ has no prominent peaks at any temperature, indicating a short range correlated state. The middle and right columns have distinct peaks at $T = 0$, at locations corresponding to flux-like state, but the peak location shifts to that of a 120 degree correlated state at a small finite temperature.

4.2.2 Finite temperature correlations

There are four broad coupling regimes in terms of temperature effects. The data in Fig.4.2 is for the two central regimes, but we discuss all the four regimes below.

(i) At very weak coupling, $U < 3t$, there are no local moments in the ground state. Increasing temperature *generates* small moments but there are no significant spatial correlations between them. Since this state is fairly obvious we have not included the result for this regime in Fig.4.2.

(ii) At somewhat larger couplings, $3t < U < 5.3t$, there are disordered moments in the ground state. These moments seem to be frozen on the basis of τ_{avg} estimates and the frozen state survives to a ‘spin-glass temperature’ T_{SG} . The left column in Fig.4.2 shows the T dependence of magnetic structure factor $S(\vec{q})$ in this coupling window. It is clearly seen that $S(\vec{q})$ is featureless in this regime.

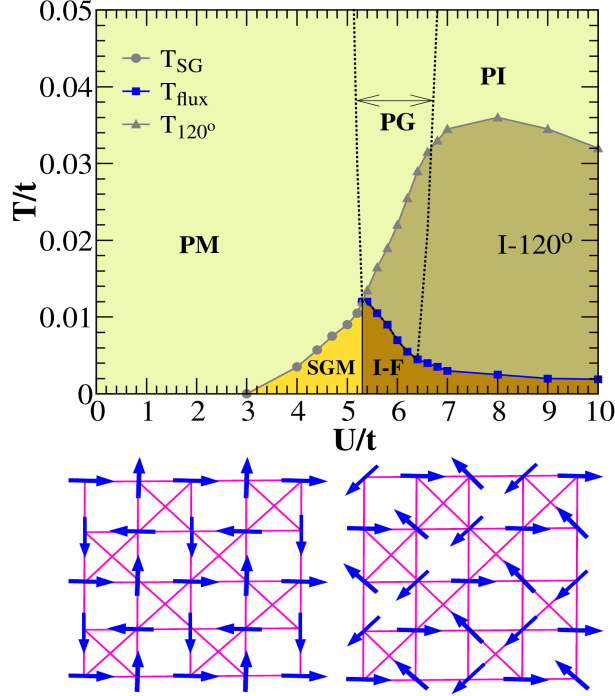


Figure 4.3: Top: The phase diagram of the checkerboard Hubbard model at half-filling. The ground state is a paramagnetic metal (PM) for $U \leq 3t$, a spin glass metal (SGM) for $3t < U < 5.3t$, and an insulator with ‘flux’ like correlations (I-F) for $U \geq 5.3t$. With increase in temperature, the ‘flux’ correlated phase transforms to a 120 degree correlated state (I-120°) and then to the paramagnet (PI). The 120 degree phase is gapped, except for $5.3t \leq U \leq 6.5t$, near the insulator-metal transition, where it shows a pseudogap (PG). The different temperature scales shown in this panel correspond to magnetic correlation length growing beyond system size. These temperature scales are crossover scales from one magnetic phase to another. T_{SG} represents a crossover from a PM to a SGM phase, T_{flux} represents a crossover from flux phase to 120 degree phase and T_{120° refers to a crossover from 120 degree state to a paramagnet. Bottom: A schematic of the ‘flux’ phase (left) and the 120 degree phase (right) on the checkerboard lattice.

(iii) For larger interaction strength, $U \sim [5.3t, 8t]$, $S(\vec{q})$ shows peaks at wavevectors $\vec{Q}_{F_1} = (\pi, 0)$ and $\vec{Q}_{F_2} = (0, \pi)$ in the ground state. We call this the ‘flux’ phase. The amplitude at these wavevectors decrease with increasing T and beyond a scale $T = T_{flux}$ new peaks appear at $\vec{Q}_{T_1} = (\pi/3, 2\pi/3)$ and $\vec{Q}_{T_2} = (2\pi/3, \pi/3)$. These peaks correspond to a 120 degree arrangement of the moments. This is visible in the middle and right columns in Fig.4.2. The weights at the \vec{Q}_T increase quickly with temperature, reach a maximum, and then decrease - vanishing at $T = T_{120^\circ}$. For $T > T_{120^\circ}$ there is no peak in $S(\vec{q})$ for any \vec{q} , indicating the paramagnetic regime. In this U/t window T_{120° increases with increasing U .

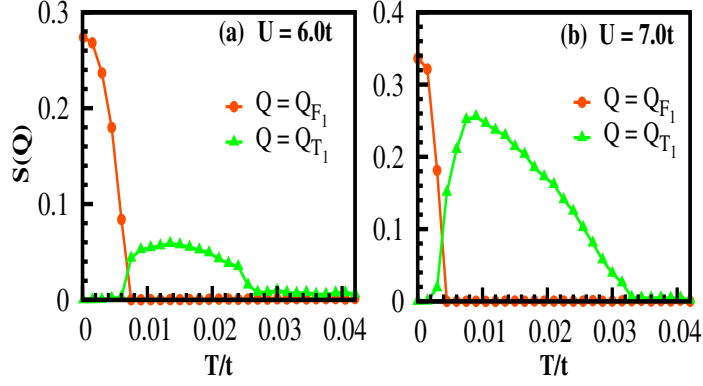


Figure 4.4: Variation of structure factor peak amplitude at the flux wavevector $\vec{Q}_{F_1} = (\pi, 0)$ and the triangular arrangement wavevector $\vec{Q}_{T_1} = (\pi/3, 2\pi/3)$ with temperature.

(iv) In the asymptotically large coupling regime, $U \gtrsim 8t$, the same sequence of flux and 120 degree correlations are obtained with increasing temperature, but the characteristic T scales fall with increasing U/t .

The top panel in Fig.4.3 shows the phase diagram based on the $S(\vec{q})$. Fig.4.4 shows the T dependence of the structure factor peak, highlighting the multiple thermal crossovers observed within our MC. Here $S(\vec{Q}_{F_1})$ corresponds to the structure factor for flux like order, whereas $S(\vec{Q}_{T_1})$ corresponds to the structure factor for ‘120 degree’ like order.

4.2.3 Local moment distribution

Fig.4.5(a) shows the behaviour of the mean local moment magnitude m_{avg} with interaction strength. In the ground state, there is no local-moment for $U \leq U_{c1} \sim 3t$. There is a small average moment for $U_{c1} \leq U < U_{c2} \sim 5.3t$. The average moment increases with interaction strength in the $[U_{c1}, U_{c2}]$ window but for $U = U_{c2}$ there is a jump in the average moment value. The average moment again increases slowly for $U > U_{c2}$ and saturates to $m_{avg} = 1.0$ as $U/t \rightarrow \infty$.

With increase in temperature there are both orientational and magnitude fluctuations in the moments. Though the average moment remains unchanged in the strong interaction side, it shows significant changes in the weak interaction side due to the small amplitude stiffness.

Fig.4.5(b) shows the $P(m)$ for the ground state. This evolves from a broad distribution in the spin glass window to essentially a delta function in the Mott phase. To get a feel for the thermal fluctuations at different interaction strengths

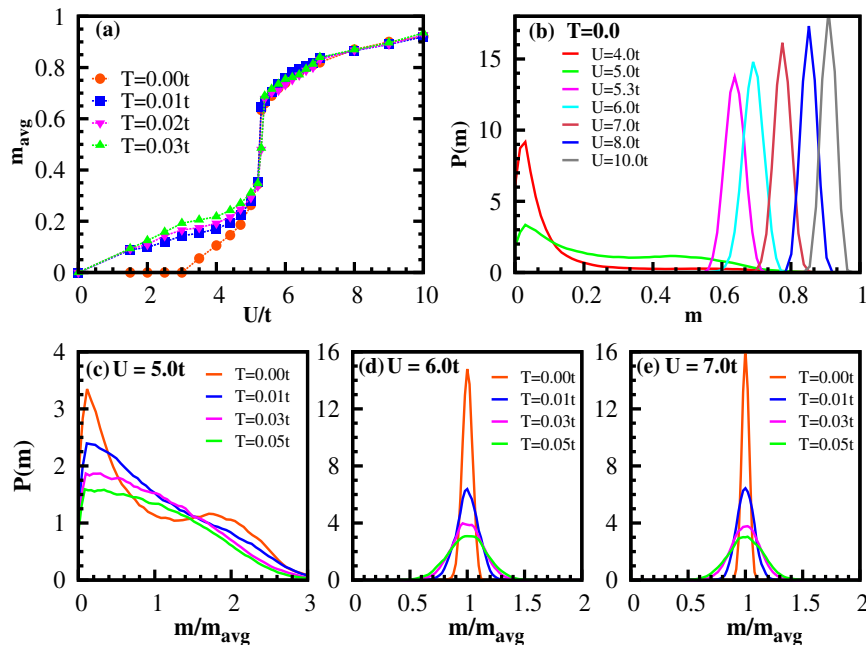


Figure 4.5: (a) Temperature dependence of average local moment m_{avg} with U/t . (b) $P(m)$ in the ground state for varying U/t . (c)-(e) Temperature dependence of $P(m)$ for $U/t = 5.0, 6.0, 7.0$.

we have plotted the $P(m)$ vs m/m_{avg} for $U = 5t, 6t, 7t$ and different temperatures (Fig.4.5(c)-(e)). At $U = 5t$ the distribution is already broad at $T = 0$ due to the amplitude inhomogeneity in the glassy state. The low T for which the data is shown does not lead to significant change. At $U = 6t, 7t$ the $T = 0$ result is essentially a delta function and it broadens slightly on raising temperature. On the strong coupling, Mott, side the dominant fluctuations are in the orientation of the moments, not their magnitude.

4.2.4 Insulator-metal transition

The first guess about the metallic or insulating behaviour of the electrons can be made from the single particle density of states $N(\omega)$. Fig.4.6 shows the density of states for different U/t and temperatures. For $U/t = 5.0$ the ground state has small m_{avg} , ≈ 0.1 , and spatially disordered local moments. These local-moments are not large enough to open a gap at the Fermi energy. They broaden the flat tight-binding band, generating finite DOS at the Fermi energy. The system would be metallic in this regime. For $U/t = 6.0$ the local-moments are sizable, $m_{avg} \approx 0.7$, large enough to open a gap in the DOS. Thus the system is insulating in this regime. With further increase in U/t , m_{avg} increase monotonically saturating to $m_{avg} \approx 1.0$.

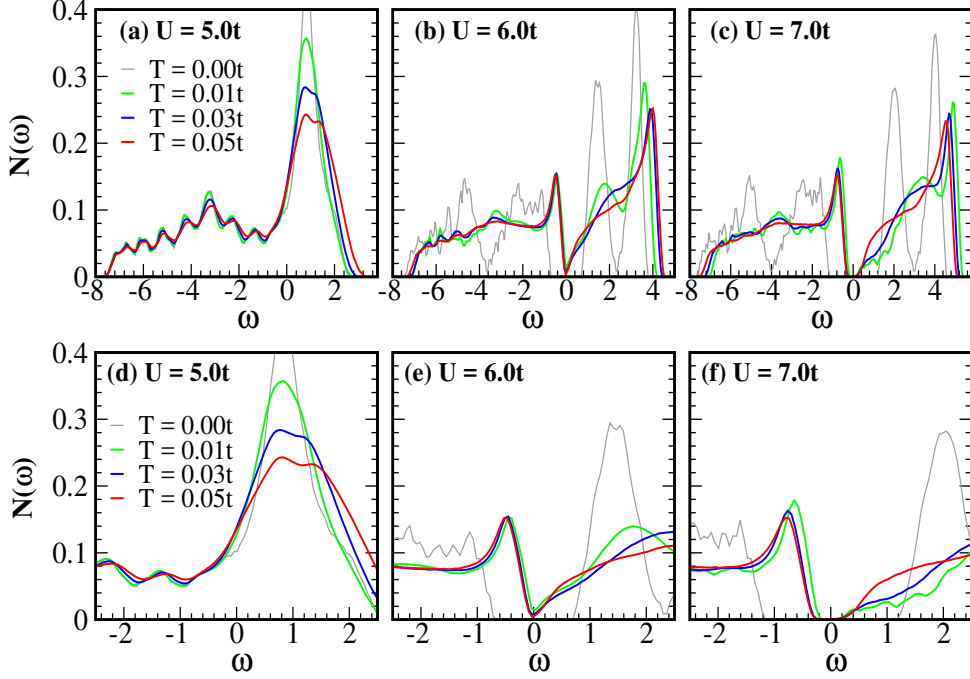


Figure 4.6: Electronic density of states (DOS) for $U/t = 5.0, 6.0, 7.0$ and varying temperature. The upper row shows the DOS over a wide frequency window to emphasize its global features while the lower row shows the DOS over a much smaller frequency window centred on the Fermi level.

With increase in temperature the local moments fluctuate, both in amplitude and orientation. At weak coupling, $U < U_{c2}$, the small fluctuating moments broaden the DOS feature around $\omega = 0$ maintaining the metallic nature. In the strong coupling side, $U/t > 7.0$, the sizable moments maintain a gap in the DOS despite strong angular fluctuations. At intermediate coupling, $5.0 < U/t < 6.4$, the DOS shows a dip at $\omega = 0$ without any clear gap. We call this ‘pseudogap’ (PG) phase. The PG feature survives upto very large temperature.

The metallic or insulating character should actually be inferred from a conductivity calculation. At large U/t the presence of a gap is enough to ensure that the system would be insulating, without having to compute the conductivity. On the small U/t side however, the situation is more complicated since we have a disordered situation in 2D. Since the disorder is weak and of a magnetic nature (rather than a scalar potential) we guess that spin flip scattering would sustain a metallic state.

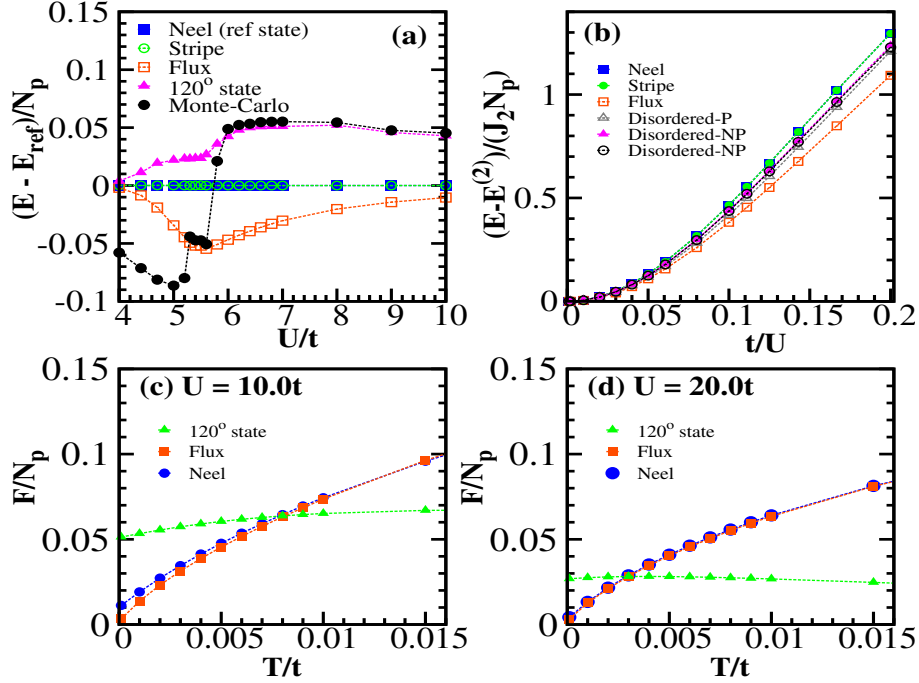


Figure 4.7: (a) Ground state energies of variational Neel, stripe, flux, the 120 degree state, and the state obtained from Monte-carlo cooling. Energy of the Neel state is taken as the reference energy. (b) Energy due to the quartic hopping processes (leading t^4/U^3 corrections). The energy change of the Neel, 120 degree state, and disordered zero-plaquette-spin configurations (planar and non-planar) are higher than the flux phase (they all have the same energy in the Heisenberg limit). (c)-(d) Free energy due to low-lying excitations on the variational Neel, flux, 120 degree triangle states at two values of U/t . The methodology is explained in the text. Notice that the free energy of the 120 degree state falls below that of the flux phase at a temperature that reduces with increasing U/t . N_p is the number of plaquettes on the lattice.

4.3 Discussion

4.3.1 Origin of the magnetic phases

Let us describe the variational scheme that we have used to complement the Monte Carlo and then move on to the analysis of the magnetic phases observed in Fig.4.2. We set up trial states using spiral spin configurations, $\vec{m}_i = m_0(\cos(\vec{Q} \cdot \vec{R}_i), \sin(\vec{Q} \cdot \vec{R}_i), 0)$, with uniform magnitude m_0 and wave-vector \vec{Q} as variational parameters, and minimised the energy of H_{eff} at half-filling. This differs slightly from the real situation where the \vec{m}_i 's have some amplitude inhomogeneity. We also included several 'non spiral' configurations, notably the flux, that satisfy the local constraint of vanishing plaquette spin.

Comparing the minimum energy obtained via variational calculation with that from the MC cooling run, see Fig.4.7(a), confirms that the *flux* state is the ground state for $U \geq U_{c2}$. However the inhomogeneous small moment ‘spin glass’ phase obtained by our Monte-Carlo cooling indeed turns out to be the lowest energy state for $U_{c1} < U < U_{c2}$, lower than the trial periodic configurations.

How do we understand the magnetic phases? It is helpful to consider three separate regimes: (i) The $U/t \gg 1$ window where only the leading exchange term $J_2 \sim t^2/U$ is relevant, and the moment size $m_{avg} \sim 1$. (ii) Intermediate U/t , down to $U \sim U_{c2}$, where the moment size is still large but higher order spin-spin couplings, in particular $J_4 \propto t^4/U^3$, is significant. Finally (iii) the ‘weak coupling’ end, $U \sim 3t$, where the moment is small and it is more appropriate to expand about the band limit rather than the Mott state. Let us consider the ground state and thermal effects in succession.

4.3.1.1 Ground state

In the strong coupling limit, we can write an effective magnetic Hamiltonian on this lattice by tracing out the fermions order by order in t/U (see appendix A). This gives us

$$H_{eff}\{\mathbf{m}\} = E^{(2)}\{\mathbf{m}\} + E^{(4)}\{\mathbf{m}\} + \dots$$

$$E^{(2)}\{\mathbf{m}\} = J_2 \sum_{\boxtimes} \sum_{\langle i,j \rangle} (\mathbf{m}_i \cdot \mathbf{m}_j - 1)$$

$$E^{(4)}\{\mathbf{m}\} = E_{\boxtimes}^{(4)}\{\mathbf{m}\} + E_{coup}^{(4)}\{\mathbf{m}\}$$

$$\begin{aligned} E_{\boxtimes}^{(4)}\{\mathbf{m}\} = & J_4 \sum_{\boxtimes} [\sum_{\langle i,j \rangle} \{ \frac{5}{2} (\mathbf{m}_i \cdot \mathbf{m}_j)^2 - 13 \mathbf{m}_i \cdot \mathbf{m}_j - 1 \} \\ & + \sum_{\langle i,j,k \rangle} \{ 5 (\mathbf{m}_i \cdot \mathbf{m}_j) (\mathbf{m}_j \cdot \mathbf{m}_k) \} \\ & + \sum_{\langle i,j,k,l \rangle} \{ 5 (\mathbf{m}_i \cdot \mathbf{m}_j) (\mathbf{m}_k \cdot \mathbf{m}_l) + 5 (\mathbf{m}_i \cdot \mathbf{m}_l) (\mathbf{m}_j \cdot \mathbf{m}_k) + 5 (\mathbf{m}_i \cdot \mathbf{m}_k) (\mathbf{m}_j \cdot \mathbf{m}_l) \}] \end{aligned}$$

$$E_{coup}^{(4)}\{\mathbf{m}\} \sim J_4' \sum_{i \in \boxtimes_1, j \in \boxtimes_2} \mathbf{m}_i \cdot \mathbf{m}_j + J_4'' \sum_{i \in \boxtimes_1, j \in \boxtimes_2}^{k \in \boxtimes_1 \cap \boxtimes_2} (\mathbf{m}_i \cdot \mathbf{m}_k) (\mathbf{m}_j \cdot \mathbf{m}_k) \dots$$

where \boxtimes represents the crossed plaquette. $E^{(2)}\{\mathbf{m}\}$ corresponds to the second order perturbation energy with $J_2 = t^2/U$, and $E^{(4)}\{\mathbf{m}\}$ corresponds to the fourth order perturbation energy. $E_{\boxtimes}^{(4)}$ describes the 4th order terms within a crossed-plaquette,

while $E_{coup}^{(4)}$ describes the interplaquette terms with a common corner shared site. We have found $J_4 = \frac{t^4}{U^3}$ and $J'_4, J''_4 \sim O(\frac{t^4}{U^3})$.

In regime (i), one would drop the $E^{(4)}\{\mathbf{m}\}$ term and obtain a classical Heisenberg model. On the checkerboard lattice the Heisenberg interaction can be written as the sum of squares of the total spin on each plaquette, $\vec{S}_P = \sum_i \vec{m}_i$, where the sum is over spins in individual crossed plaquettes. This feature arises due to the ‘fully connected’ nature of the crossed plaquettes, which are essentially tetrahedra, and is true of the pyrochlore lattice as well. The minimum energy corresponds to all $\vec{S}_P = 0$ but there is a macroscopic degeneracy in the number of ways this can be satisfied. In such degenerate situations thermal fluctuations sometime select out collinear ordered configurations, due to the entropy gain [32]. For the checkerboard lattice it seems that free energy barriers are small and the thermal ‘order-by-disorder’ mechanism does not select out an ordered state. The classical Heisenberg limit, $U/t \rightarrow \infty$, is disordered at all temperatures as in the pyrochlore lattice [?]. For the Hubbard model the actual spins are $S = 1/2$ and not classical, and a $1/S$ expansion about the classical limit suggests that a ‘quantum order by disorder’ mechanism selects a valence bond solid (VBS) ground state [162–164].

In regime (ii) the contribution of $E^{(4)}\{\mathbf{m}\}$ becomes important. This can be seen as follows. Various configurations satisfying the local constraint, $\sum_{i \in \boxtimes} \mathbf{m}_i = 0$ have equal $E^{(2)}\{\mathbf{m}\}$. However the Hubbard energy for these different configurations are found to be different. Thus the crucial difference to the Hubbard energy is dominated by the $E^{(4)}\{\mathbf{m}\}$ contribution. We believe these multi-spin exchange interactions are responsible in modifying the magnetic ground state away from the Heisenberg limit. In figure 4.7.(b), we show this contribution as $(E - E^{(2)}\{\mathbf{m}\})/J_2 \approx (t/U)^2 f(\mathbf{m}_i, \mathbf{m}_j, \mathbf{m}_k, \mathbf{m}_l)$ with the expected quadratic behaviour as $t/U \rightarrow 0$ (or $U/t \rightarrow \infty$). It is also seen that the flux state has the largest lowering of energy to $\mathcal{O}(t^4/U^3)$. This trend persists down to $U \sim U_{c2}$. The strong coupling expansion in t/U ceases to be useful once the Mott gap closes.

(iii) At weaker coupling, $U \sim [3t, 5.3t]$, the system is gapless and the moments are small. The state as $U \rightarrow 3t$ is better understood as an instability in the tight binding band, controlled by the susceptibility $\chi_0(\vec{q})$. In non frustrated lattices this usually has a prominent peak at some $\vec{q} = \vec{Q}$, and the condition $1 - U\chi_0(\vec{Q}) = 0$, defines the onset of ordering at U_c . We have shown $\chi_0(\vec{q})$ for the checkerboard lattice (see figure 4.8). We observe that $\chi_0(\mathbf{q})$ has dominant weight over wide regions of \mathbf{q} space, rather than at specific a wavevector or few \mathbf{q} points. This suggests that as local moments are formed, they encounter competing interactions in real space

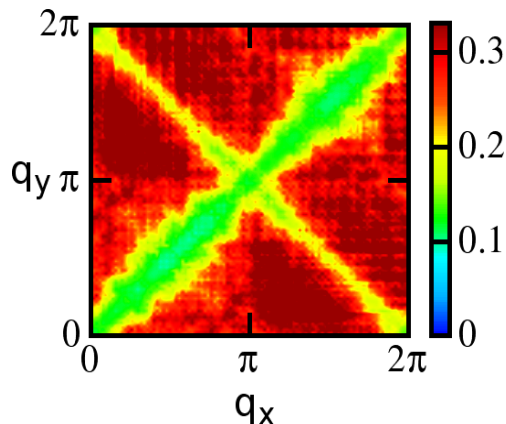


Figure 4.8: $\chi_0(\mathbf{q})$ on the checkerboard lattice at half-filling. It has dominant weight over different regions of \mathbf{q} space (seen as dark-red), indicating an instability towards a disordered magnetic state.

resulting in a disordered phase. This, within our scheme, appears to be a spin frozen state.

4.3.1.2 Finite temperature

The finite temperature state is dictated by the free-energy of the possible low energy ordered configurations. While the entropy difference around different ordered configurations is not large enough to stabilise long range order in the Heisenberg limit, we wanted to check how the situation is modified in the Hubbard model. We tried a rather crude free energy estimate to gain some insight since the explicit \vec{m}_i based model is not available at intermediate coupling.

We considered a homogeneous ordered state and chose a reference site \vec{R}_0 . We create a single spin ‘fluctuation’ on the ordered state by giving angular twists to \vec{m}_{R_0} without disturbing the other \vec{m}_i ’s. We calculate the energy cost for these fluctuations with respect to the ordered state by using the Hubbard model. This process was repeated for random twists distributed uniformly on the surface of a sphere and for different temperatures. An averaging over the reference site also had been taken into account. The density of states of these single spin excitation energies allows us to roughly estimate the free-energy. It is expected that the states with a high density of low energy excitations would be preferred since they have the largest entropy.

Our results Fig.4.7(c),(d) show that at intermediate temperature the checkerboard Hubbard model prefers a 120 degree correlated state (which does not satisfy the plaquette constraint) due to entropic reasons. The 120 degree state, however, has a higher internal energy than the flux state and loses out to it at a lower T .

We would like to point out the differences of our results in the present study, from the earlier studies [160] of the Mott transition on the checkerboard lattice. We address it in terms of the validity of our approximation in the $U - T$ plane based on $T = 0$ and finite T results.

- At $T = 0$, three features are noteworthy. (a) The U_c for the Mott transition: we obtain $U_c \sim 5.3t$, the only other value we know in the literature is $U_c \sim 6.7t$. These are in the same ballpark. (b) The large U state: we obtain a flux like state while another study [160] uses a more sophisticated approach to obtain a plaquette singlet state. Within our approach we believe the singlet state can be accessed only if we include quantum fluctuations of the \mathbf{m}_i 's. Both the plaquette singlet and the flux state lift the classical degeneracy of the Heisenberg limit but through different mechanisms. (c) The low U metallic spin glass would be susceptible to quantum fluctuations, since it is a gapless state, and the Hartree-Fock result is likely to be modified in a full theory.
- Finite T : While our $T = 0$ results have the limitation of being Hartree-Fock, increasing T brings into play the fluctuations that were suppressed at $T = 0$. In fact as T grows these classical fluctuations dominate over the quantum fluctuations and dictate the magnetic correlations and the electronic properties. To our knowledge, this aspect of checkerboard Mott physics has not been explored before.

4.3.2 Magnetic impact on electrons

Within our framework the electronic properties are dictated by the behaviour of the local moments, which in turn is decided by the electrons. We wish to establish a more quantitative connection between the magnetic order and the electronic DOS in some limiting cases.

For $T = 0$ and $U \leq U_{c1}$ there are no local moments and the system is described by the tight-binding model. On the checkerboard structure this leads to a flat band at the upper band edge. For $U_{c1} \leq U < U_{c2}$ small moments show up, modifying the tight-binding DOS by broadening the flat band. For $U \geq U_{c2}$ the moments are sizable and they open a gap in the DOS. The ‘flux’ like order has a unique 4-peak structure in the DOS with a wide gap around the Fermi level. The 120 degree ‘triangle’ phase shows pseudogap in the intermediate interaction window and has a gapped phase at strong interaction side. The specific behaviour of the DOS in these magnetic ordered states can be understood as follows.

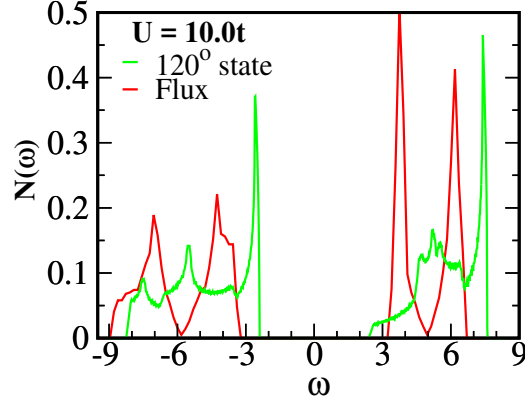


Figure 4.9: Electronic DOS in the ideal flux and 120 degree spin configurations. For the same U/t the 120 degree state has a smaller gap than the flux phase.

In the ‘flux’ phase, the local-moment at any lattice site \vec{R}_i can be parametrized as $\vec{m}_i = (m_{ix}, m_{iy}, 0)$ where

$$\begin{aligned} m_{ix} &= \frac{m}{2}(e^{iQ_{F1} \cdot \vec{R}_i} + e^{iQ_{F2} \cdot \vec{R}_i}) \\ m_{iy} &= \frac{\tilde{m}}{2}(e^{iQ_{F2} \cdot \vec{R}_i} - e^{iQ_{F1} \cdot \vec{R}_i}) \end{aligned}$$

This magnetic ordering leads to two distinct energy levels at $\pm \frac{U}{2}$, each with a two-fold degeneracy. As electrons move on this magnetic background, they further split to bands $\pm(U/2) \pm t\sqrt{2 + \cos 2k_x + \cos 2k_y}$. Thus the electron motion in the ‘flux’ phase gives rise to the unique 4-peak structure in the DOS. The minimum gap in the DOS for this state is $U - 4t$.

In the ‘120 degree’ phase, the local-moment at any lattice site \vec{R}_i can be parametrized as $\vec{m}_i = (m_{ix}, m_{iy}, 0)$ where $m_{ix} = m \cos(2Q_{T1} \cdot \vec{R}_i)$, $m_{iy} = m \sin(2Q_{T1} \cdot \vec{R}_i)$. This phase also has two-fold degenerate energy levels at $\pm \frac{U}{2}$. Itinerant electrons on this magnetic background lift the degeneracy by $t[-g(k_x, k_y) \pm h(k_x, k_y)]/4$ where

$$\begin{aligned} g(k_x, k_y) &= [4\cos(k_x - k_y) + \cos(k_x + k_y) + \sqrt{3}\sin(k_x + k_y)] \\ h^2(k_x, k_y) &= [26 + 8\cos(2k_x + 2k_y) - \cos(2k_x - 2k_y) - 8\cos(2k_x) \\ &\quad - 8\cos(2k_y) - 8\cos(k_x + k_y) + 16\cos(k_x - k_y) \\ &\quad + \sqrt{3}\sin(2k_x - 2k_y) - 8\sqrt{3}\sin(k_x + k_y) - 8\sqrt{3}\sin(2k_x)] \end{aligned}$$

Thus the motion of electrons in the ‘120 degree’ phase retains the upper and lower Hubbard band features without undergoing any further splitting of bands (unlike the ‘flux’ phase). The minimum gap in the DOS for this state is $U - t[(h + g)_{max} + (h -$

$g)_{max}]/4$. We observe that in the Brillouin zone $[(h + g)_{max} + (h - g)_{max}] > 16$. Thus the gap for the ideal ‘flux’ phase is always larger than the ideal ‘120 degree’ phase for same interaction strength Fig.4.9.

4.4 Conclusion

We have studied the single band Hubbard model at half-filling on the checkerboard lattice. The Hartree-Fock ground state is non magnetic upto an interaction strength U_{c1} , then a small moment spin glass upto U_{c2} , and a ‘flux’ ordered state beyond. The Mott transition, associated with a gap opening in the density of states, occurs at U_{c2} . The presence of order differentiates this lattice of corner shared ‘tetrahedra’ from its three dimensional counterpart, the pyrochlore lattice, which remains disordered at all interaction strengths. A static auxiliary field based Monte Carlo provides an estimate of the temperature window over which the magnetic correlations survive. Strikingly, we observe that the flux order is replaced by a ‘120 degree’ correlated spin arrangement at intermediate temperature before all order is lost. We provide an entropic argument for this effect.

Our results reveal a wide variety of magnetic and spectral regimes on this lattice, summarised below.

- *Strong coupling:* Deep in the Mott phase the Hubbard model selects out a flux like state from the infinitely degenerate manifold of the checkerboard Heisenberg model. This persists as the low temperature state down to $U \sim 5.3t$. Increasing temperature promotes a 120 degree spin arrangement, before the final loss of order.
- *Weak coupling:* Small *disordered* moments persist below the insulator-metal transition (at $U \sim 5.3t$) down to $U \sim 3t$.
- *Electronic state:* The electrons are gapped in the flux phase, but the crossover to the 120 degree state leads to a reduction of the gap. As U/t reduces, the 120 degree phase becomes pseudogapped.

MOTT PHYSICS IN THE PYROCHLORE MOLYBDATES

5.1 Introduction

As we have seen in earlier chapters, the metal-insulator transition on a frustrated lattice occurs in the background of short-range magnetic correlation and the deep Mott insulating state is often a spin-liquid. It would be vital to have experimental realisations to test out the predictions of theory. While there is significant effort in analysing the quasi 2D κ -BEDT organics [88–91] in terms of the triangular lattice, 3D realisations of ‘Hubbard physics’ on a frustrated structure are rare. Materials like the manganites [93] do involve strong correlation effects (and much else) but are on a bipartite structure - with relatively simple magnetic order. In this situation the discovery of the rare-earth (R) based pyrochlores, the molybdates [1, 2, 86, 94–96], and the iridates [8–10, 97], provide a breakthrough.

Both the molybdates and iridates show a metal-insulator transition as the rare-earth ionic radius, r_R , is reduced [8, 9, 95, 96]. There are, however, key differences in terms of (i) the degrees of freedom and couplings, and (ii) the magnetic state that emerges in these two families. This chapter focuses on the molybdates, the next one discusses the iridates.

The active degrees of freedom in the molybdates, $R_2Mo_2O_7$, include one electron per Mo in a twofold degenerate orbital, Hund’s coupled to a $S = 1/2$ moment on the same ion. The electrons have onsite Hubbard repulsion (U) between them while the local moments have a nearest neighbour antiferromagnetic coupling, J_{AF} . The Hund’s coupling drives double exchange (DE) ferromagnetism, opposed by AF su-

perexchange, while Hubbard repulsion promotes a Mott insulating state. Reducing r_R reduces the hopping - weakening DE and also enhancing the effect of Hubbard repulsion, while increasing pressure is supposed to (mainly) affect the antiferromagnetic coupling [96]. There are several major questions left unresolved by existing theoretical work:

- At ambient pressure the metal-insulator and magnetic ‘transition’ are simultaneous, is that true with increasing pressure as well?
- Is there an ‘universal’ quantity that dictates the MIT trajectory over a large pressure window?
- What is the fate of the coupled spin-orbital state for changing pressure and rare earth radius?
- What is the low energy spectral behaviour in the vicinity of the MIT as the pressure is varied?
- What is the quasiparticle character close to the Mott transition?
- Can we obtain realistic thermal scales for the magnetic transitions?

We employ our real space approach, equivalent to unrestricted Hartree-Fock at zero temperature, using a static auxiliary orbital field to handle the Hubbard interaction. We solve the resulting ‘electron - local moment - orbital moment’ problem via Monte Carlo based simulated annealing.

In next section we describe the model and different observables used for this study. Then we explore the parameter space of the model problem, probing the ground state and thermal properties over a wide parameter window. In the last section we choose parameters suggested by first-principle studies on the molybdate family and compare our results in quantitative detail to experiments.

5.2 Model for the molybdates

The rare earth based pyrochlore molybdates ($R_2Mo_2O_7$) structure consists of two interpenetrating pyrochlore lattices, one formed by Mo cations and the other by R. For our studies, we ignore the orbitals on R and oxygen, focusing instead on the orbitals on Mo. The Mo atom has octahedral oxygen coordination (MoO_6), and the resulting crystal field splits the fivefold degenerate Mo 4d states into doubly

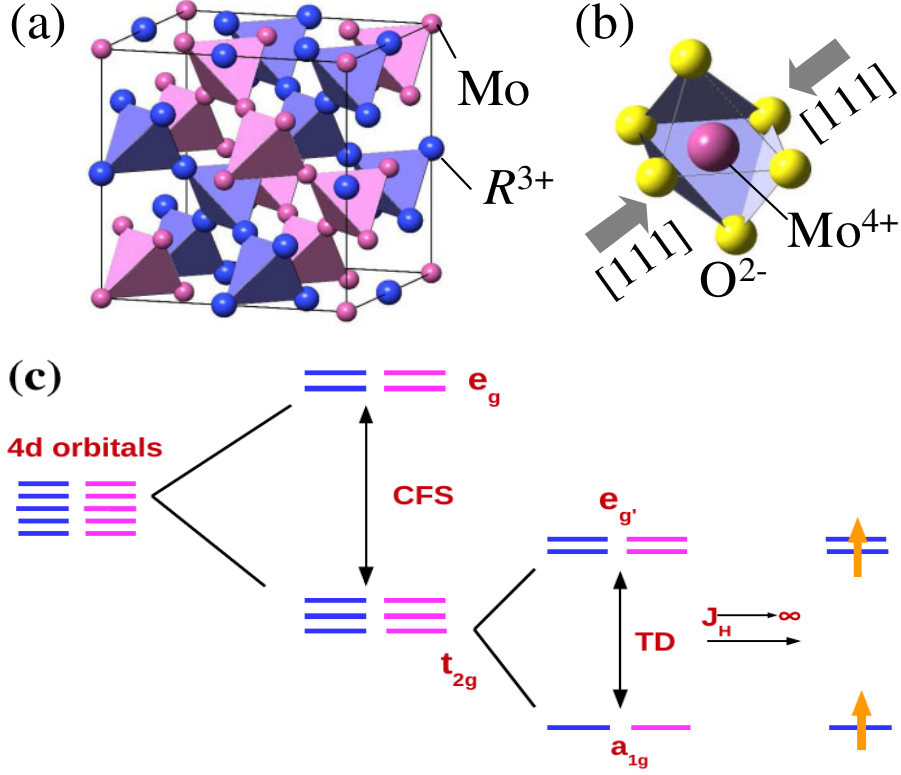


Figure 5.1: ((a)-(b) taken from [4]) (a) Rare earth molybdates with interpenetrating pyrochlore sublattices. (b) The MoO₆ octahedron with trigonal distortion along the [111] direction. (c) Mo 4d level splitting under crystal field effect (represent by CFS) and trigonal distortion(TD) in the molybdates. (see text for details)

degenerate e_g and triply degenerate t_{2g} manifolds. A compressive trigonal distortion of the octahedron along the [111] direction splits the t_{2g} further into a nondegenerate a_{1g} and a doubly degenerate e'_g . The hopping matrix elements between Mo orbitals at different sites is dictated by the intervening oxygen. The Mo cation is nominally tetravalent and has two electrons on an average. The deeper a_{1g} state behaves like a local moment, and the single electron in the two e'_g orbitals is the ‘itinerant’ degree of freedom [112]. The e_g state remains unoccupied.

There are additional small scales, related to bond distortions, *etc*, that are responsible for the spin freezing phenomena [165, 166]. We ignore them for the time being. Also, the moments on R can be relevant when studying effects like spin chirality induced anomalous Hall effect [6, 7, 168–170]. We do not include these moments in our model in the present study. Based on the degrees of freedom of the Mo in the molybdates, an appropriate model [19] is given by

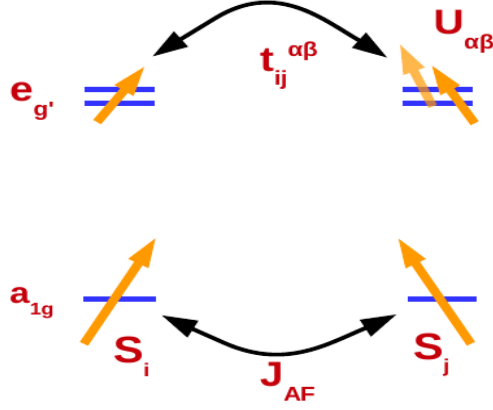


Figure 5.2: Schematic of relevant interactions and hopping processes in the molybdates.

$$\begin{aligned}
H = & \sum_{\langle ij \rangle, \alpha\beta, \sigma} t_{ij}^{\alpha\beta} c_{i\alpha\sigma}^\dagger c_{j\beta\sigma} - J_H \sum_{i, \alpha} \mathbf{S}_i \cdot c_{i\alpha\sigma}^\dagger \vec{\sigma}_{\sigma\sigma'} c_{i\alpha\sigma'} \\
& + J_{AF} \sum_{\langle ij \rangle} \mathbf{S}_i \cdot \mathbf{S}_j + \sum_{i, \alpha\beta\alpha'\beta'}^{\sigma, \sigma'} U_{\alpha\beta}^{\alpha'\beta'} c_{i\alpha\sigma}^\dagger c_{i\beta\sigma'}^\dagger c_{i\beta\sigma'} c_{i\alpha\sigma}
\end{aligned}$$

The first term is the kinetic energy, involving nearest neighbour intra and inter-orbital e'_g hopping. The second term is the Hund's coupling between the a_{1g} local moment \mathbf{S}_i and the e'_g electrons, J_{AF} is the AF superexchange coupling between local moments at neighbouring sites on the pyrochlore lattice, and the U represent onsite e'_g Coulomb matrix elements.

To simplify the computational problem we treat the localised spins \mathbf{S}_i as classical unit vectors, absorbing the size S in the magnetic couplings. We will comment on the limitations of this approximation later. Also, to reduce the size of the Hilbert space we assume that $J_H/t \gg 1$, where t is the typical hopping scale, so that only the locally 'spin aligned' fermion state is retained. In this local basis the hopping matrix elements are dictated by the orientation of the \mathbf{S}_i on neighbouring sites. This leads to the simpler model:

$$H = \sum_{\langle ij \rangle, \alpha\beta} \tilde{t}_{ij}^{\alpha\beta} \tilde{c}_{i\alpha}^\dagger \tilde{c}_{j\beta} + J_{AF} \sum_{\langle ij \rangle} \mathbf{S}_i \cdot \mathbf{S}_j + U \sum_i^{\alpha \neq \beta} n_{i\alpha} n_{i\beta}$$

where the fermions are now 'spinless'. $U > 0$ is the inter-orbital Hubbard repulsion. The effective hopping is determined by the orientation of the localised spins $\mathbf{S}_i =$

$(\sin\theta_i\cos\phi_i, \sin\theta_i\sin\phi_i, \cos\theta_i)$, as $\tilde{t}_{ij}^{\alpha\beta} = [\cos\frac{\theta_i}{2}\cos\frac{\theta_j}{2} + \sin\frac{\theta_i}{2}\sin\frac{\theta_j}{2}e^{-i(\phi_i-\phi_j)}]t^{\alpha\beta}$, with $t^{11} = t^{22} = t$ and $t^{12} = t^{21} = t'$. We set $t' = 1.5t$ as is appropriate for these kinds of orbitals [112].

The first two terms represent fermions in a classical spin background and the resulting magnetic phase competition has been studied on a pyrochlore [113]. While these results are interesting they miss out on the large correlation scale, U , that drives the Mott transition. One option is to treat the model within dynamical mean field theory (DMFT) [71], but then the spatial character crucial to the pyrochlore lattice is lost. To explore the Mott transition in a non trivial spatial background we will follow the SPA approach. This will not only capture the ground state but also the behaviour at finite temperature. Below we describe the simulated annealing scheme for arriving at the ground state.

5.2.1 Method

We handle the model in real space as follows: We use a Hubbard-Stratonovich (HS) transformation that decouples $Un_{i\alpha}n_{i\beta}$ in terms of an auxiliary orbital variable $\mathbf{\Gamma}_i(\tau)$, coupling to the electronic orbital moment $\mathbf{O}_i = \sum_{\mu\nu} c_{i\mu}^\dagger \vec{\sigma}_{\mu\nu} c_{i\nu}$, and a scalar field $\Phi_i(\tau)$ coupling to the electronic density n_i at each site.

Following the static path approximation (SPA), described in chapter.2, we have,

$$H_{eff}\{\mathbf{\Gamma}_i, \mathbf{S}_i\} = -\frac{1}{\beta}\log\text{Tr}e^{-\beta H_{el}} + H_{AF} + \frac{U}{4}\sum_i \mathbf{\Gamma}_i^2$$

$$H_{el} = \sum_{ij}^{\alpha\beta} \tilde{t}_{ij}^{\alpha\beta} c_{i\alpha}^\dagger c_{j\beta} - \tilde{\mu}\sum_i n_i - \frac{U}{2}\sum_i \mathbf{\Gamma}_i \cdot \mathbf{O}_i$$

with $\tilde{\mu} = \mu - U/2$ and H_{AF} the Heisenberg term. The localised spin and orbital moment configurations follow the distribution

$$P\{\mathbf{S}_i, \mathbf{\Gamma}_i\} \propto \text{Tr}_{cc^\dagger} e^{-\beta H_{eff}}$$

We obtain a solution of this model numerically via a Monte Carlo by generating the equilibrium configuration for the $\{\mathbf{S}_i, \mathbf{\Gamma}_i\}$ through iterative diagonalisation of H_{el} . We start with reasonable high temperature, $T \sim t$, higher than any transition temperature in the problem, and reduce it to $T \sim 0$ to access ground state properties.

5.2.2 Observables

From the equilibrium configurations obtained at the end of annealing we calculate the following averaged quantities (angular brackets represent thermal average over MC configurations): (i) Magnetic and orbital structure factors are:

$$S_{mag}(\mathbf{q}) = \frac{1}{N^2} \sum_{ij} \langle \mathbf{S}_i \cdot \mathbf{S}_j \rangle e^{i\mathbf{q} \cdot (\mathbf{r}_i - \mathbf{r}_j)}$$

$$S_{orb}(\mathbf{q}) = \frac{1}{N^2} \sum_{ij} \langle \mathbf{\Gamma}_i \cdot \mathbf{\Gamma}_j \rangle e^{i\mathbf{q} \cdot (\mathbf{r}_i - \mathbf{r}_j)}$$

(ii) The size distribution of the orbital field is computed as

$$P(\Gamma) = \frac{1}{N} \sum_i \langle \delta(\Gamma - |\mathbf{\Gamma}_i|) \rangle$$

(iii) The optical conductivity is:

$$\sigma_{xx}(\omega) = \frac{\sigma_0}{N} \left\langle \sum_{n,m} \frac{f(\epsilon_n) - f(\epsilon_m)}{\epsilon_m - \epsilon_n} |J_x^{nm}|^2 \delta(\omega - E_{mn}) \right\rangle$$

where J_x^{nm} is $\langle n | J_x | m \rangle$ and the current operator is given by

$$J_x = -i \sum_{i,\alpha\beta} \left[(\tilde{t}_{i,i+\hat{x}}^{\alpha\beta} c_{i,\alpha}^\dagger c_{i+\hat{x},\beta} - \text{hc}) \right]$$

$E_{mn} = \epsilon_m - \epsilon_n$, $f(\epsilon_n)$ is the Fermi function, ϵ_n and $|n\rangle$ are the single particle eigenvalues and eigenstates of H_{el} respectively. The conductivity is in units of $\sigma_0 = e^2/(\hbar a_0)$, where a_0 is the lattice constant. (iv) The d.c. conductivity is obtained as a low frequency average of the optical conductivity over a window $\Omega = 0.05t$.

$$\sigma_{dc} = \frac{1}{\Omega} \int_0^\Omega d\omega \sigma_{xx}(\omega)$$

and the resistivity $\rho = 1/\sigma_{dc}$.

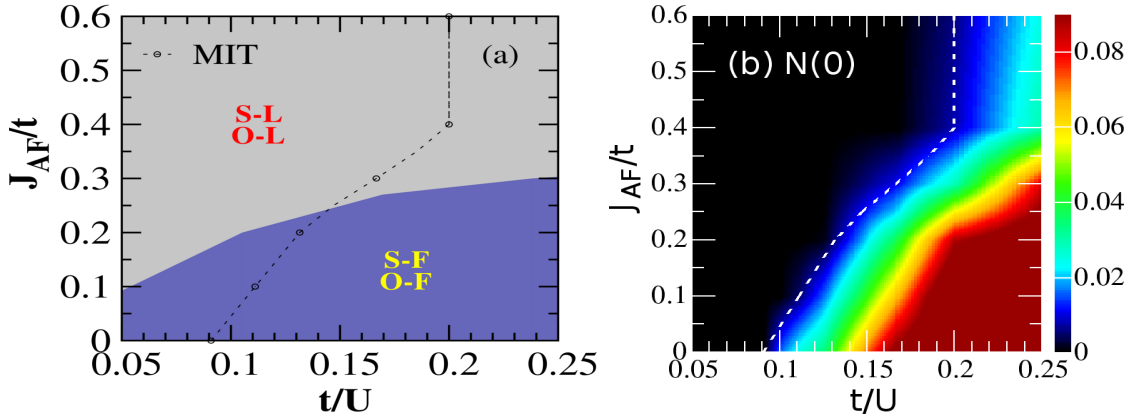


Figure 5.3: (a) Ground state phase diagram showing the metal-insulator transition (MIT) boundary in the t/U , and J_{AF}/t plane. We label the various magnetic phases as spin-ferromagnet (S-F) and spin liquid (S-L). The two orbital phases are labeled as orbital-ferromagnet (O-F) and orbital liquid (O-L). The detailed characterization of these phases is mentioned in the text. Panel (b) shows the density of states at the Fermi level, $N(0)$, for varying t/U and J_{AF}/t . The vanishing $N(0)$ corresponds to the MIT (cross checked also with transport).

5.3 Model Hamiltonian study

5.3.1 Ground state results

5.3.1.1 Phase diagram

Fig.5.3(a) shows the ground state phase diagram of the model for varying U/t and J_{AF}/t , while Fig.5.3(b) shows the density of states at the Fermi level, $N(0)$, over the same parameter space.

Notation: We characterise phases in terms of their spin and orbital character, S-L is spin-liquid and S-F is a spin ferromagnet. Similarly, O-L is orbital-liquid, *etc.* These phases also need to be specified in terms of their transport character. To avoid a cluttered picture we have simply shown the insulator-metal boundary in the $t/U - J_{AF}/t$ plane, the metal/insulator aspect can be inferred from it. The metal-insulator transition can be located from the vanishing of $N(0)$, and also from a calculation of the d.c conductivity.

When $J_{AF} = 0$ there is a metal-insulator transition at $U_c \sim 11t$ from a ferromagnetic metal to a *ferromagnetic insulator*. When the superexchange is moderate, $J_{AF} \sim 0.2t$, there is strong competition between ferromagnetism (S-F, mediated by double-exchange) and antiferromagnetic tendency. As a result there is a crossover from S-F to spin disordered (S-L) behaviour with increasing U/t roughly around

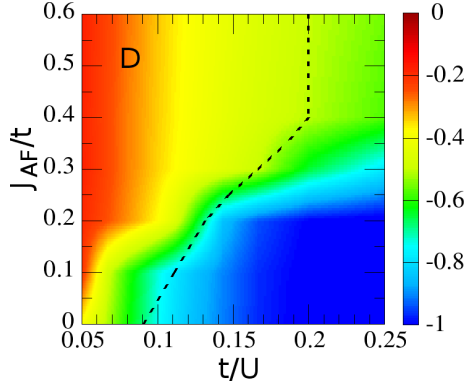


Figure 5.4: The effective ferromagnetic exchange, D , at $T = 0$ for varying t/U and J_{AF}/t . The calculation and significance of this quantity is explained in the text. The MIT boundary is shown by dotted lines and coincides with change from large to small values of D .

the MIT, although weak ferromagnetism survives in the insulator. For strong superexchange, $J_{AF} \gtrsim 0.5t$, the antiferromagnetic tendency suppresses ferromagnetism completely and, as we will show, there is no magnetisation at any U/t . We have a spin liquid state at all U/t . In this large J_{AF} limit, a relatively weak Hubbard repulsion, $U \sim 5t$, is enough to drive the metal-insulator transition.

To get a feel for the changing magnetic state and the shifting MI transition point, it is useful to examine an approximate effective ‘spin only’ model. Consider the electronic kinetic energy, on the ij bond, in a spin configuration $\{\mathbf{S}_i\}$. It is the product of an electronic average and a modulated hopping both of which depend on $\{\mathbf{S}_i\}$. The dependence of the spin overlap factor is explicit, it is simply: $\sqrt{(1 + \mathbf{S}_i \cdot \mathbf{S}_j)/2}$. The electronic average does not have an obvious expression in terms of the spins but, as a starting approximation, we can replace $\langle c_{i\alpha}^\dagger c_{j\beta} \rangle$ by its thermal average [171]. The thermal average, please note, is not a spin configuration dependent quantity.

Under this assumption for the kinetic energy the total energy involving the magnetic variables can be written as

$$\begin{aligned}
 H_{eff}\{\mathbf{S}\} &\approx \sum_{ij} D_{ij} \sqrt{(1 + \mathbf{S}_i \cdot \mathbf{S}_j)/2} + J_{AF} \sum_{\langle ij \rangle} \mathbf{S}_i \cdot \mathbf{S}_j \\
 D_{ij} &= \sum_{\alpha\beta} t_{ij}^{\alpha\beta} \langle c_{i\alpha}^\dagger c_{j\beta} + h.c \rangle
 \end{aligned}$$

The role of the Hubbard interaction, acting through the orbital moment, is implicit in the model above. The D_{ij} are supposed to be computed in backgrounds that include the $\mathbf{\Gamma}_i$ as well as the AF coupling. Since the dependence of D_{ij} on

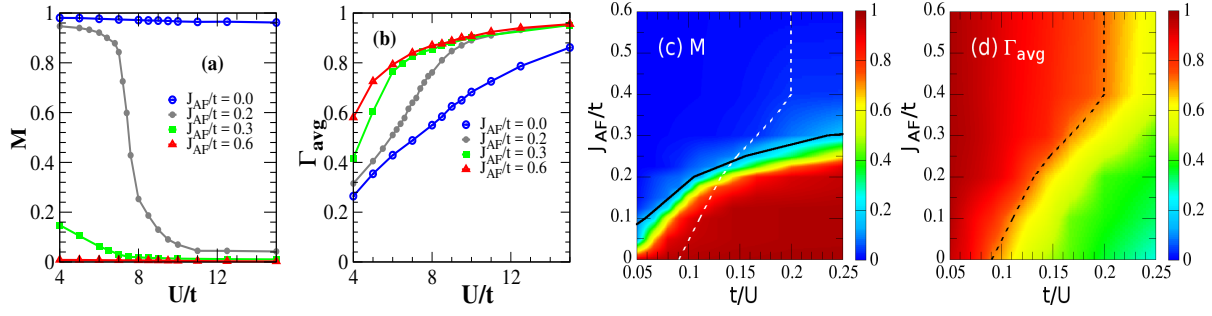


Figure 5.5: Magnetisation (M) and average orbital moment (Γ_{avg}) in the ground state. (a) U/t dependence of M for several J_{AF} . At $J_{AF} = 0$ the system has $M = 1$ at all U , irrespective of metal/insulator character. For $J_{AF} \gtrsim 0.5t$, $M \sim 0$ for the entire U window probed. At intermediate J_{AF} the magnetisation has a rapid crossover around a scale $U_{mag}(J_{AF})$ that is close to but not quite the metal-insulator transition point $U_c(J_{AF})$. (b) Shows the system averaged magnitude of the orbital moment $\Gamma_{avg} = 1/N \sum_i |\Gamma_i|$. For $U/t \rightarrow \infty$, the orbital moment $\rightarrow 1$, as one expects in the atomic limit. The approach to this asymptote is faster at larger J_{AF} . The $U \rightarrow 0$ behaviour is dictated by the bandstructure, and change in the magnetic state with J_{AF} . (c)-(d) Overall variation of M and Γ_{avg} in the J_{AF}/t and t/U plane. The dashed line is the MIT boundary separating the metallic and insulating regimes.

the magnetic and orbital state is not known the model above does not have much predictive value. However, the thermally (and system) averaged D_{ij} , which we call just D , can serve to identify the origin of the changing magnetic character. It can also be related to direct measurables, *e.g.* (i) the spin stiffness (spin wave velocity), since the D and J_{AF} dictate this quantity, and (ii) the integrated optical weight, via the f -sum rule

$$\sum_{ij} D_{ij} \sqrt{(1 + \mathbf{S}_i \cdot \mathbf{S}_j)/2} \propto \int_0^\infty \sigma(\omega) d\omega \equiv n_{eff}$$

where n_{eff} , the integrated optical weight, is related to the effective carrier density. This can be roughly simplified to $D\sqrt{1 + m^2} \propto n_{eff}$, where we have approximated the spin average by m^2 . The physics content of this is simple - reducing magnetisation reduces the hopping (D) and the combination determines n_{eff} .

The metal-insulator transition line: The role of J_{AF} is to generate magnetic phase competition and reduce the ferromagnetic tendency by suppressing the kinetic energy. To set a convenient reference, the effective bond resolved kinetic energy, D , at $J_{AF} = 0$ and $U \rightarrow 0$ is $\sim -t$. That allows us to set up three regimes.

(a). When $J_{AF} \ll D$, we essentially have a weakly renormalised FM ground state and U_c is only modestly suppressed with respect to the $J_{AF} = 0$ value. For us this

happens when $J_{AF} \lesssim 0.1t$. (b). In the interval $0.1t < J_{AF} < 0.4t$ the U_c changes quickly, at $J_{AF} = 0.4t$ it is roughly half the value at $J_{AF} = 0$. (c). For $J_{AF} \gtrsim 0.4t$ the U_c does not reduce any further since the magnetic ground state is completely disordered and the magnetisation cannot be suppressed any further. This shows up as the vertical asymptote of the MIT line in Fig. 5.3.

The ferromagnet to ‘spin liquid’ transition: The ferromagnet to spin liquid ‘transition’ occurs along a line that we call $U_{mag}(J_{AF})$. There is some ambiguity in locating this line since within our parameter space the magnetisation is always finite, if small. We set $M = 0.05$ as the S-F to S-L transition. Just as U_c is dictated roughly by the competition between U and D , U_{mag} is decided by the competition between J_{AF} and D .

Orbital character: The various orbital (O) phases obtained in our study are based on the orbital structure factor $S_{orb}(\mathbf{q})$ calculation. For the orbital-ferromagnet phase $S_{orb}(\mathbf{q})$ shows a peak at $\mathbf{q} = (0, 0, 0)$ while for the orbital liquid phase it doesn’t show any peak at any \mathbf{q} .

5.3.1.2 The magnetic state

A detailed understanding of the magnetic state is provided by the magnetic structure factor $S_{mag}(\mathbf{q})$ computed in the equilibrium state. It highlights not only long range order, in terms of prominent peaks in \mathbf{q} space, but also possible correlations in the disordered state when there is no long range order.

Fig.5.6 shows $S_{mag}(\mathbf{q})$ for three different superexchange couplings and for three U ’s in each case. The U ’s are chosen so that they capture the metal, insulator, and crossover regime for all three values of J_{AF} .

For $J_{AF} = 0$ there is no magnetic phase competition. At $U = 4t$, $S_{mag}(\mathbf{q})$ has dominant weight at $\mathbf{q} = (0, 0, 0)$ describing the ferromagnetic order promoted by double-exchange. The magnetisation is $\gtrsim 0.95$ (limited by our annealing process) and the structure factor peak is $\sim 0.9 \sim M^2$. As the row shows, this result does not depend on U , suggesting that even deep in the Mott insulator one would obtain a saturated ferromagnetic state. The T_c ’s would of course differ, as we discuss later, since the stiffness of the FM state depends on the kinetic energy - which is U dependent.

For $J_{AF} = 0.2t$, $S_{mag}(\mathbf{q})$ has a large weight at $\mathbf{q} = (0, 0, 0)$ at $U = 4t$, as in the first row, but at $U = 7t$ the peak, although still at $(0, 0, 0)$, has diminished weight, ~ 0.6 . The metal-insulator transition occurs around $U \sim 8t$ and by the time $U = 10t$ (last row) S_{mag} does not have any prominent peaks at any \mathbf{q} . The superexchange

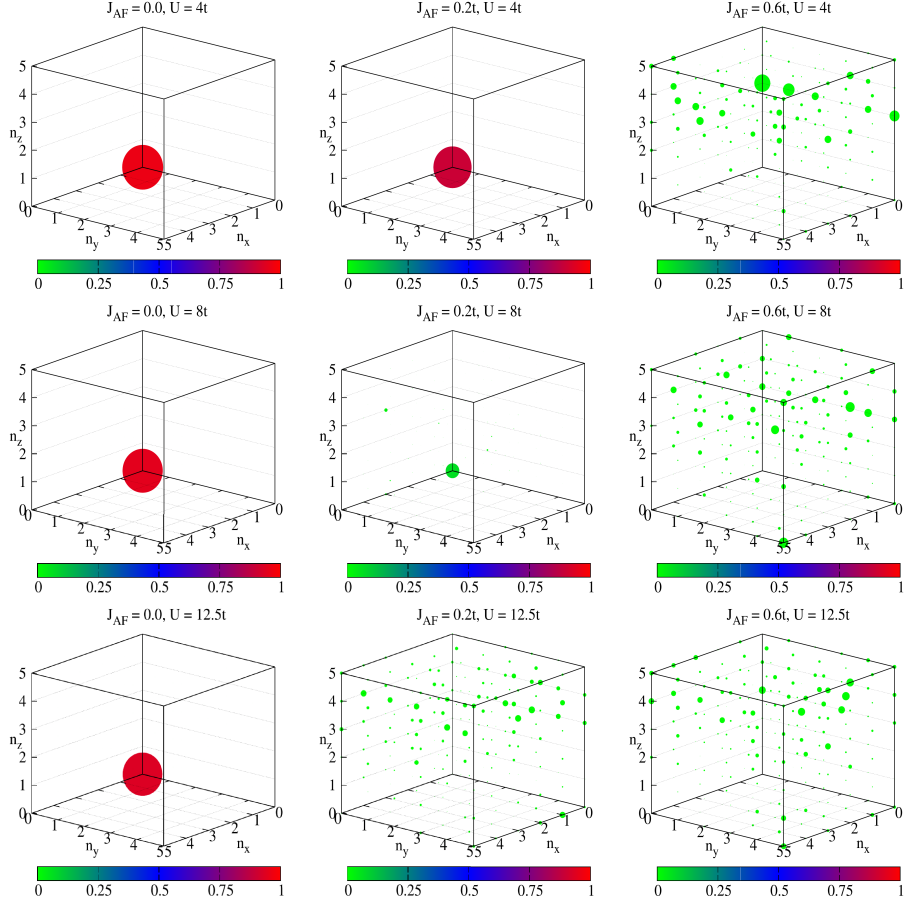


Figure 5.6: Spin structure factor $S_{mag}(\mathbf{q})$ at $T = 0$ for $U/t = 4, 8$ and 12.5 for each of $J_{AF}/t = 0$ (left column), 0.2 (middle column) and 0.6 (right column). We use the notation $\mathbf{q} = \frac{2\pi}{L}(n_x, n_y, n_z)$, where n_i 's are integers and $0 \leq n_i < L$. In our calculation $L = 6$. The size of a dot signifies relative weight at a given \mathbf{q} while its colour represents the actual magnitude of $S_{mag}(\mathbf{q})$. The presence of dominant weight at some \mathbf{q} , in these cases $\mathbf{q} = (0, 0, 0)$ indicates magnetic order phase, while the 'random' but correlated patterns indicate a spin liquid.

coupling overcomes the kinetic energy gain from DE but the pyrochlore structure prevents AF ordering.

For $J_{AF} = 0.6t$, $S_{mag}(\mathbf{q})$ the weight is spread over all \mathbf{q} but in a correlated manner, indicative of a spin liquid phase.

5.3.1.3 The orbital state

To have an idea of the underlying orbital state, we calculate the orbital structure factor $S_{orb}(\mathbf{q})$. Fig.5.8 shows the structure factor for the three superexchange couplings. For $J_{AF} = 0$ we see $S_{orb}(\mathbf{q})$ has dominant weight at $\mathbf{q} = (0, 0, 0)$ describing

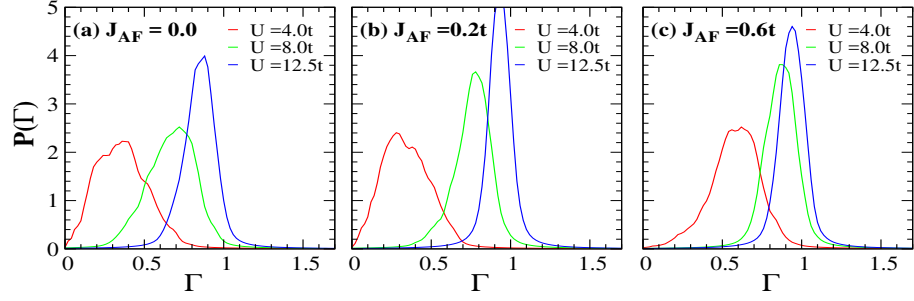


Figure 5.7: Ground state size distribution of the orbital field $P(\Gamma)$ for $J_{AF} = 0, 0.2t$ and $0.6t$ for indicated U values.

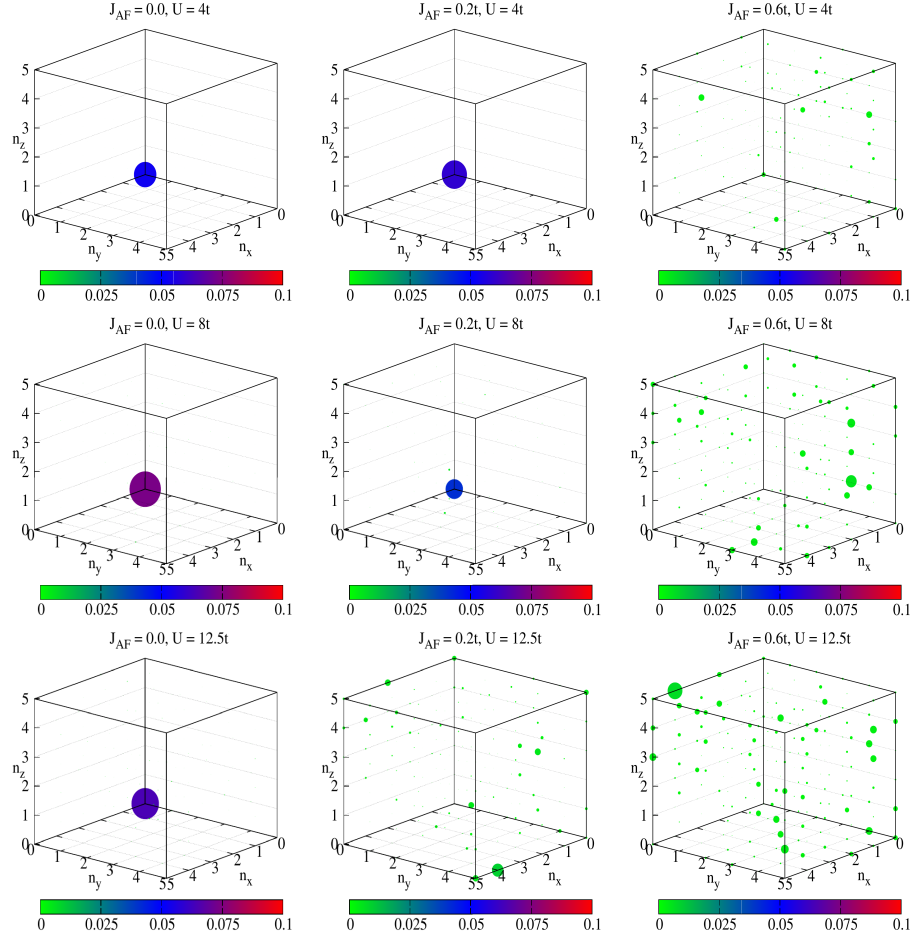


Figure 5.8: Orbital structure factor at $T = 0$ for $U/t = 4, 8$ and 12.5 for each of $J_{AF}/t = 0$ (left column), 0.2 (middle column) and 0.6 (right column). We use the same convention as described in Fig. 5.6. The size of a dot signifies relative weight at a given \mathbf{q} while its colour represents the actual magnitude of $S_{orb}(\mathbf{q})$. The presence of dominant weight at some \mathbf{q} , indicates an orbital ordered phase, otherwise a disordered phase.

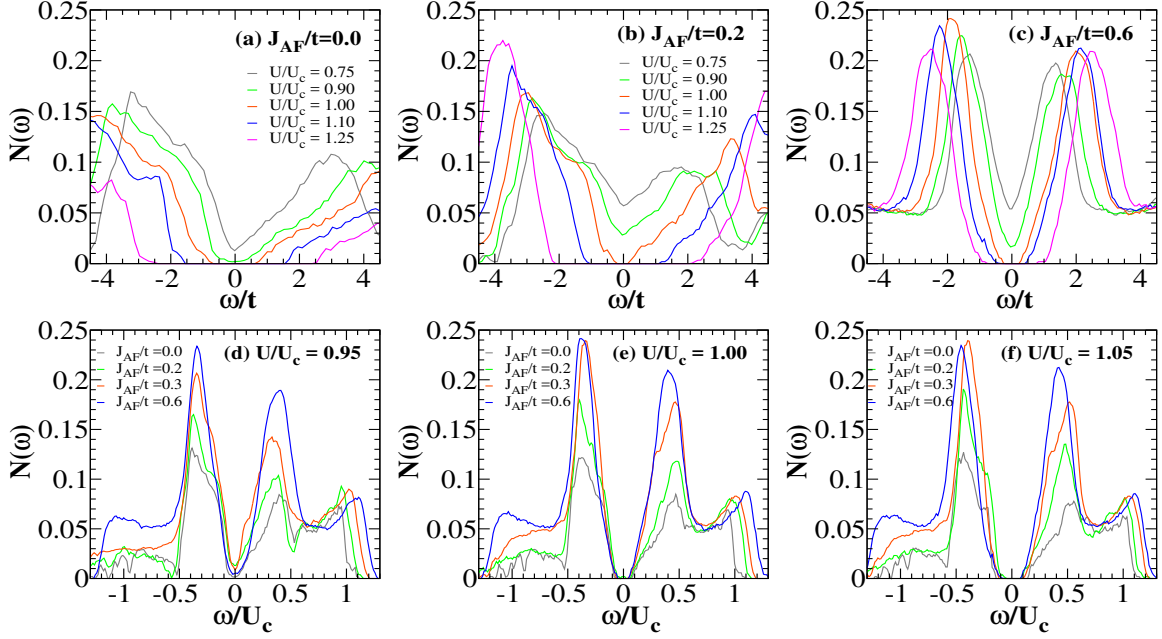


Figure 5.9: (a)-(c) Density of states for $J_{AF}/t = 0, 0.2, 0.3, 0.6$ for different $U/U_c(J_{AF})$. (d)-(f) Density of states for varying J_{AF} at three fixed values of $U/U_c(J_{AF})$. This is to probe if the DOS has an ‘universal’ character near the MIT, depending only on U/U_c , or depends explicitly on J_{AF} as well. The frequency scale is normalised by the respective U_c .

the ferro-orbital (O-F) ordering. For $J_{AF} = 0.2t$, $S_{orb}(\mathbf{q})$ has dominant weight at $\mathbf{q} = (0, 0, 0)$ for $U = 4t$ and $7t$ (O-F ordering), and an orbital liquid state for $U = 10t$. For $J_{AF} = 0.6t$, $S_{orb}(\mathbf{q})$ has weight spread over all \mathbf{q} indicating an orbital liquid state.

5.3.1.4 Density of states

Fig.5.9 shows the ground state density of states (DOS) for various interaction strengths for the three regimes of superexchange interaction of our phase-diagram. We can see that for $U < U_c$, the DOS has a finite weight at the Fermi energy, and for $U \geq U_c$, the DOS has a gap in the spectrum. As $U \rightarrow U_c$, the DOS develops a prominent dip at the Fermi energy, a signature of the pseudogap (PG) phase. We can understand this in the following way. The band ($U = 0$) limit of this model is a metal, with finite DOS and a peak at the Fermi level. Inclusion of the inter-orbital interaction (U) leads to the emergence of orbital moments $\mathbf{\Gamma}_i$, with its size determined by U . For $U < U_c$, we have $|\mathbf{\Gamma}_i| \ll \Gamma_{sat} = 1$. The presence of these orbital moments reduce the DOS at the Fermi level. As $U \rightarrow U_c$, $|\mathbf{\Gamma}_i|$ increases monotonically and for $U \gg U_c$ it saturates to the atomic value $|\mathbf{\Gamma}_i| = 1$. The presence of large orbital moments for $U \geq U_c$ leads to the opening of a gap in the DOS. From our calculation, we estimate

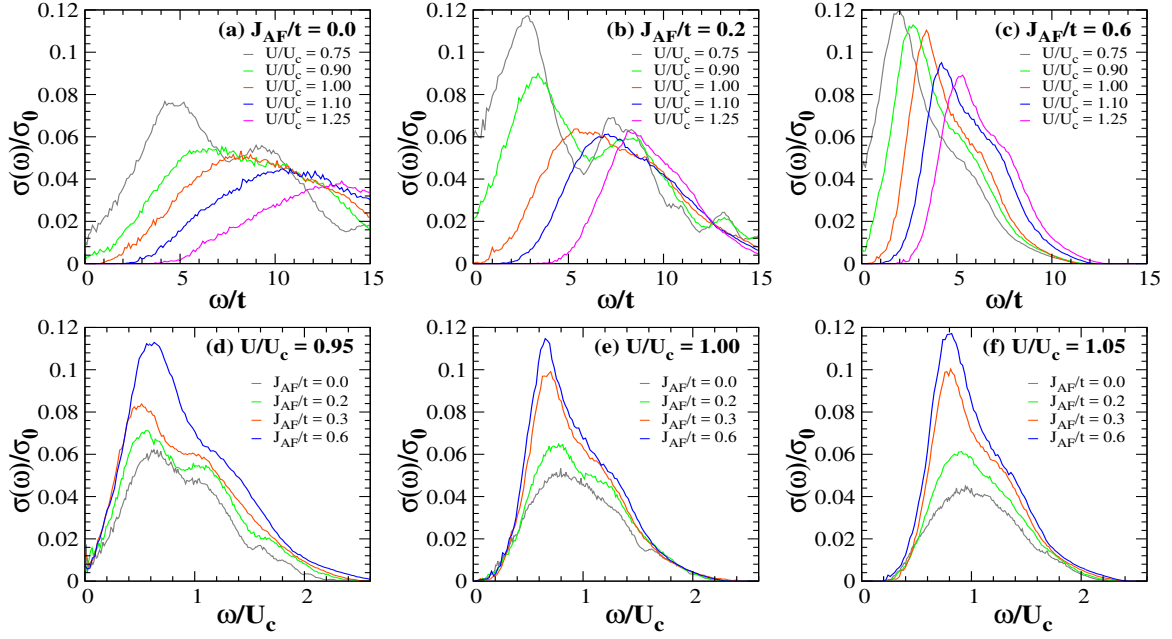


Figure 5.10: (a)-(c) Ground state optical conductivity for $J_{AF} = 0, 0.2t$ and $0.6t$ for different U/U_c . (d)-(f) Ground state optical conductivity for $U/U_c = 0.95, 1.0$ and 1.05 , on a normalised frequency scale, for the indicated J_{AF} values.

that for $J_{AF} = 0$, $U_c = 11.0t$, for $J_{AF} = 0.2t$, $U_c = 7.6t$ and for $J_{AF} = 0.6t$, $U_c = 5.0t$. The superexchange interaction favours the Mott-insulating phase.

The lower set of panels in Fig.5.9 show the DOS near the MIT for fixed ratios of $U/U_c(J_{AF})$. Within each panel the J_{AF} is varied to probe if the spectral behaviour changes with changing AF coupling, after factoring out the effect of U_c change by normalising the frequency axis by U_c . Our primary observation is that increasing J_{AF} leads to enhanced low energy DOS for a fixed ratio U/U_c . We attribute this to the increased spin and orbital disorder in the larger J_{AF} situation - leading to an increasing ‘Anderson-Mott’ character of the metal-insulator transition.

5.3.1.5 Optics and transport

Fig.5.10 shows the optical conductivity, $\sigma(\omega)$, in the ground state for various interaction strengths and three regimes of superexchange interaction of our phase-diagram.

The band ($U = 0$) limit of the model has finite DOS at the Fermi level. As a result $\sigma(\omega)$ shows a Drude peak in this limit. Inter-orbital interaction (U) leads to the emergence of orbital moments Γ_i . For $U < U_c$, we have $|\Gamma_i| \ll \Gamma_{sat} = 1$. Increasing size of these orbital moments leads to a suppressed Drude response, and $\sigma(\omega)$ peak shifts to finite frequency.

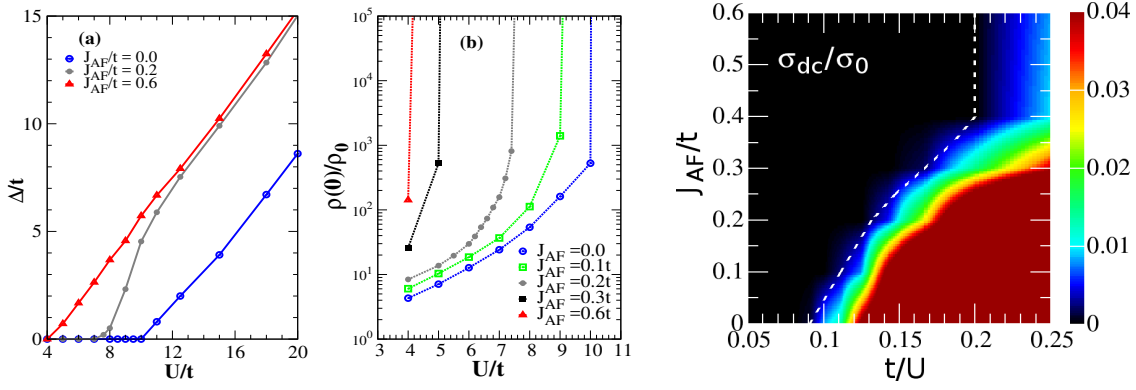


Figure 5.11: (a) Variation of optical gap (Δ/t) with U/t for different J_{AF}/t values. Panel (b) shows the variation of residual resistivity $\rho(T = 0)$ with U/t for different J_{AF}/t values. The normalising scale is $\rho_0 = \hbar/e^2$. (Right panel) Ground state d.c. conductivity, σ_{dc} , for varying t/U and J_{AF}/t . The normalising scale is $\sigma_0 = e^2/\hbar$. The MIT boundary can be thought of as the vanishing of σ_{dc} , with increasing U/t values.

$|\Gamma_i|$ increases monotonically with increasing U and for $U \gg U_c$ it saturates to the atomic value $|\Gamma_i| = 1$. Beyond U_c there is an optical gap in $\sigma(\omega)$. From our calculation, we find that the U_c 's for different superexchange scales are consistent with those obtained from the DOS results.

The lower set of panels in Fig.5.10 show the optical conductivity near the MIT for fixed ratios of $U/U_c(J_{AF})$. Within each panel the J_{AF} is varied to probe if $\sigma(\omega)$ changes with changing AF coupling, after factoring out the effect of U_c change by normalising the frequency axis by U_c . Our primary observation is the increase in the low frequency spectral weight at a fixed U/U_c as J_{AF} , and the associated background disorder, increases.

We show the optical gap Δ in Fig.5.11(a). It is clearly seen that $\Delta = 0$ for $U < U_c$ and it increases monotonically for $U \geq U_c$. Fig.5.11(b) shows the variation of residual dc resistivity, $\rho(T = 0)$ with U/t for different superexchange values. The finite $\rho(0)$ for $U < U_c$ can be understood by the scattering of electrons from the (small) orbital moments. For $U \geq U_c$, the (large) orbital moments lead to an opening of a Mott-gap which manifests as $\rho(0) \rightarrow \infty$. These behaviours are seen in figure 5.11.

Fig.5.11(right panel) shows the dc conductivity σ_{dc} from our calculation for various interaction strengths and superexchange values of our phase-diagram. We observe σ_{dc} vanishing as $U \geq U_c$. This also allows us to roughly estimate the MIT boundary.

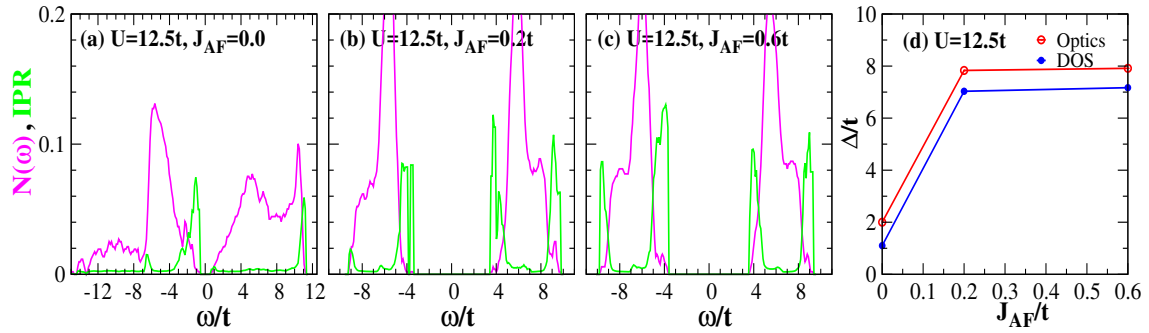


Figure 5.12: (a)-(c) Variation in DOS and IPR with increasing superexchange strength for fixed $U/t = 12.5$. (d) Comparison of the optical gap (obtained from the zero temperature optical conductivity) with the spectral gap (obtained from the DOS) with changing superexchange values for fixed $U/t = 12.5$.

5.3.1.6 Discussion

Our DOS and optics results indicate an increasing ‘Anderson-Mott’ character of the metal-insulator transition with increasing superexchange. To understand it further we have computed the inverse participation ratio (IPR) as,

$$IPR = \sum_i |\psi_i|^4$$

where ψ_i is the amplitude of the normalised wave function. When the electron is fully localised at a given site, we have $IPR = 1$ and when its completely delocalised, $IPR = 0$. However, on a finite size lattice, a fully delocalised state has $IPR = 1/V$, where V is the system size (volume in 3D). Therefore any localised state on a finite lattice has $IPR > 1/V$.

Following this procedure, we calculate the total number of localised states at $J_{AF}/t = 0, 0.2$ and 0.6 . For this we consider a state as localised if its $IPR > \frac{1}{4L^3}$ ($V = 4L^3$ for a pyrochlore lattice). We also calculate the fraction of localised states, which is the ratio of the number of localised states and the total number of states. We now discuss the variation of IPR as J_{AF}/t changes.

Fig.5.12 shows the DOS and IPR at fixed $U/t = 12.5$ for different SE scales. It can be seen that the optical and spectral gaps are not equal. From the IPR results, we establish that in the ground state, the fraction of localised states is 0.17 for $J_{AF} = 0$, 0.24 for $J_{AF} = 0.2t$, and 0.29 for $J_{AF} = 0.6t$. This clearly indicate that the fraction of localised states (at the band edges) increase with the SE strength. Our results show increasing localisation as the strength of superexchange is enhanced.

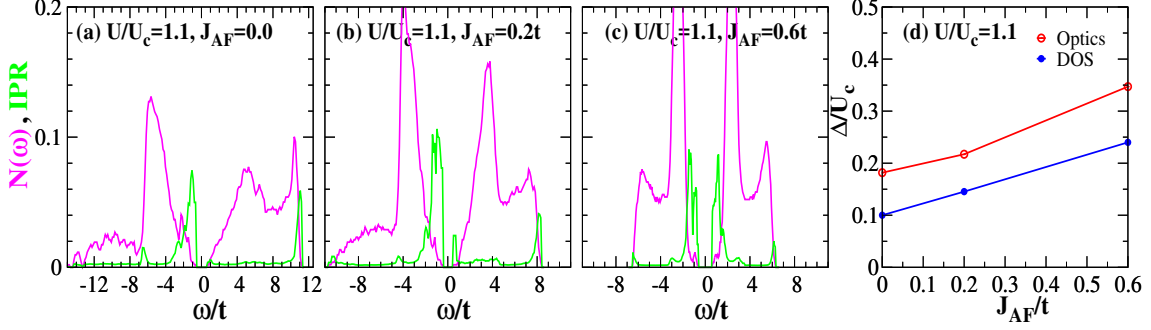


Figure 5.13: (a)-(c) Variation in DOS and IPR with increasing SE for fixed $U/U_c = 1.1$. (d) Comparison of the rescaled optical and spectral gap (Δ/U_c) with changing SE values for $U/U_c = 1.1$.

To explore further if the localisation effects change with changing SE, after factoring out the effects of U_c , we calculate the DOS and IPR for fixed $U/U_c(J_{AF}) = 1.1$ and different SE scales (see figure 5.13). We also show the rescaled optical and spectral gaps which show increasing behaviour with increasing SE. Our IPR results also indicate that in the ground state, for $U/U_c(J_{AF}) = 1.1$, the fraction of localised states is 0.17 for $J_{AF} = 0$, 0.21 for $J_{AF} = 0.2t$, and 0.26 for $J_{AF} = 0.6t$. Based on these results we believe that with increasing the strength of superexchange, the localisation effects are enhanced.

The ‘Anderson’ aspect of molybdate metal-insulator transition is associated with the difference one observes between the DOS gap and the optical gap and its interpretation in terms of ‘localised’ single particle states. The key effect is that the single particle states are localised due to self generated disorder, despite the absence of any extrinsic disorder. Note that interaction effects are crucial in our problem in driving the metal-insulator transition. We cannot have a purely non interacting ‘Anderson transition’ without extrinsic disorder.

In the presence of quantum fluctuations the single particle states here would face dephasing and it is not clear whether the ‘localisation’ aspect at $T = 0$ will survive. However at high temperature, this might still be an useful way to think about the problem and describe the difference between the single particle and optical spectra.

5.3.2 Finite temperature results

5.3.2.1 Overall thermal phase diagram

Fig.5.14 shows the overall thermal phase diagram of our calculation for varying Hubbard repulsion (U/t), superexchange interaction (J_{AF}/t), and temperature (T/t).

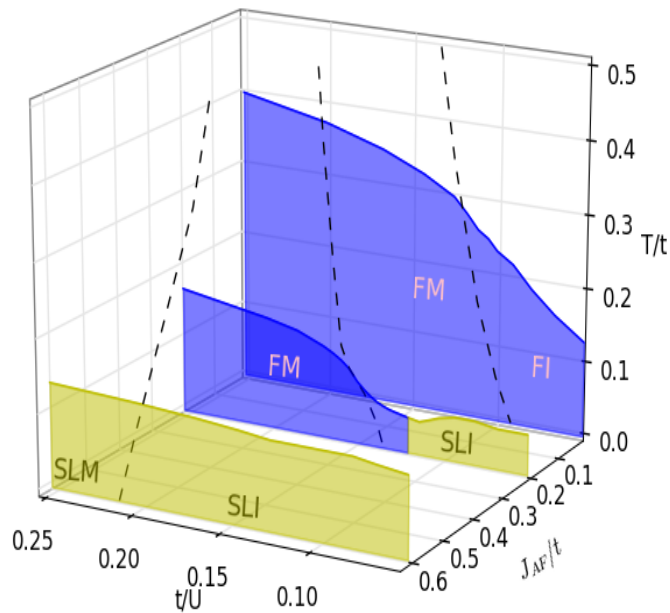


Figure 5.14: Overall thermal phase diagram of the two orbital Hubbard model with competing double exchange and superexchange interactions in the t/U , J_{AF}/t and T/t parameter space. Here we focus on the fate of the ferromagnetic phase in the shown parameter space.

The fate of the ferromagnetic window in this parameter space can be clearly seen in the figure. We note the following features – In the absence of superexchange ($J_{AF}/t = 0$), the underlying magnetic state is ferromagnetic at all U/t values below the critical temperature. The presence of finite superexchange interaction ($J_{AF}/t = 0.2$) leads to a competition between the double exchange dominated ferromagnetic state and superexchange promoted spin-liquid on the pyrochlore geometry, in addition to the finite temperature paramagnet. The competition results in the shrinking of the ferromagnet window in the parameter space. As superexchange interaction dominates further ($J_{AF}/t > 0.3$), we observe that the underlying magnetic state is no more ferromagnetic, rather a spin-liquid at low temperature, and a paramagnet at high temperature.

At low temperature and with increased superexchange, the ferromagnetic state loses out to a disordered phase. This disordered phase, however, has some prominent features in the magnetic structure factor (visible as inhomogeneities of the structure factor weight distribution as opposed to a fully homogeneous distribution for a paramagnet). We identify the temperature scale, which separates this spin-liquid and paramagnet as T_{SL} . Our ‘spin’ structure factor calculations have shown

that with increasing superexchange, the scale T_{SL} increases noticeably. However, the variation of T_{SL} with U/t is rather small.

Apart from the magnetic behaviour, it is also important to note that with increasing superexchange interaction strength, the metallic window also gets narrowed, and the Mott-insulating regime shows up in an extended regime of the parameter space.

The crucial ingredients of the minimal model for the rare earth molybdates are Hubbard repulsion, double exchange, and superexchange on the pyrochlore lattice. To describe the finite temperature physics of this model, we proceed as follows. We divide the whole parameter regime based on the the strength of the superexchange interaction. We first describe the regime without superexchange ($J_{AF} = 0$), followed by moderate ($J_{AF} = 0.2t$), and then strong ($J_{AF} = 0.6t$) superexchange scales. We will now discuss the results in detail for each of these regimes.

5.3.2.2 Double exchange and Hubbard repulsion

Fig.5.15(a) shows the phase diagram for varying t/U and T/t in terms of the magnetic, transport, and spectral properties that emerge from our calculation when $J_{AF} = 0$. We observe the following features –

- The ground state is a ferromagnet promoted by double exchange interaction at all U/t . With increasing temperature, the ferromagnetic state loses out to a paramagnetic phase governed by thermal fluctuations.
- With increasing U , the average local orbital moment increases. This reduces the average kinetic energy and as a result the system shows Mott insulating behaviour.
- The weak-coupling side ($U < U_c$) is a metal with finite density of states (DOS) at the Fermi-level. The strong-coupling side ($U > U_c$) has a Mott-gap in the DOS. In the Mott-transition neighbourhood, the Mott gap quickly converts to a pseudogap (PG) with increasing T , leading to the widening of the PG region (not shown in figure).

Fig.5.15(b) shows the average magnetisation M for varying t/U and T/t . At $T = 0$ the system has $M = M_{sat} = 1$ at all U values, irrespective of metallic or insulating character. With increasing T the magnetisation reduces due to angular fluctuation of the moments and we can infer a T_c .

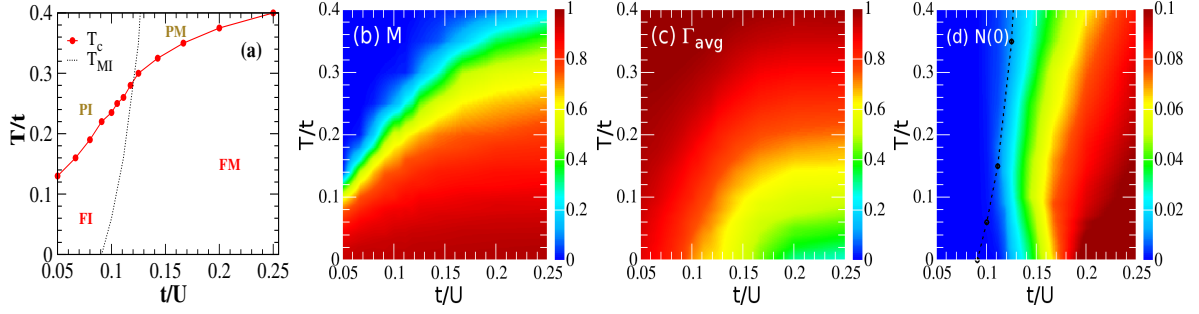


Figure 5.15: $J_{AF} = 0$ (a) Phase diagram for varying t/U and T/t . The solid line corresponds to the ferromagnetic to paramagnetic phase transition and the dotted line corresponds to the metal to Mott-insulator transition (MIT). The various phases shown in the phase diagram are, ferromagnetic metal (FM), ferromagnetic insulator (FI), paramagnetic metal (PM) and paramagnetic insulator (PI). The detailed characterization of these phases is mentioned in the text. Panel (b) and (c) show average magnetisation M and average orbital moment Γ_{avg} for varying t/U and T/t . Panel (d) shows the density of states at the Fermi level, $N(0)$, for varying t/U and T/t . The vanishing $N(0)$ corresponds to the MIT.

Fig.5.15(c) shows the average magnitude of the orbital moment Γ_{avg} for varying t/U and T/t . At $T = 0$, as $U/t \rightarrow \infty$, $\Gamma_{avg} \rightarrow 1$, as one expects in the atomic limit. Γ_{avg} reduces with decreasing U such that $\Gamma_{avg} \rightarrow 0$ as $U/t \rightarrow 0$. For $T/t > 0$, thermal fluctuations lead to quick growth of Γ_{avg} in the metallic side.

Fig.5.15(d) shows the DOS at the Fermi level, $N(0)$, for varying t/U and T/t . On the metallic side ($U < U_c$), we see the DOS reducing gradually with increasing temperature. This can be ascribed to the increase of Γ_{avg} due to thermal fluctuations, pushing weight away from the Fermi level. On the insulating side ($U \geq U_c$), the Mott gap persists till the highest probed temperature. This is because, in the insulating side, all sites have a large Γ_i . In the MIT neighbourhood we observe a non monotonic behaviour. The non monotonicity is mainly due to the presence of a wide pseudogap window, the appearance of which can be attributed to the emergence of thermally induced orbital moments. These moments, are not large enough to open up a gap in the spectrum. However, these are sizable enough to deplete the DOS at Fermi level. Further with the hopping mediated ‘self-generated’ short-range correlations, these moments develop a dip at the Fermi level - signature of the pseudogap window.

The magnetic state: For a detailed understanding of the magnetic state, we calculate the magnetic structure factor, $S_{mag}(\mathbf{q})$, computed in the optimised background. It highlights not only long range order, in terms of prominent peaks in \mathbf{q} space, but also possible correlations in the disordered state when there is no long range order.

Fig.5.16 shows $S_{mag}(\mathbf{q})$ for three different U values in our phase diagram, for three

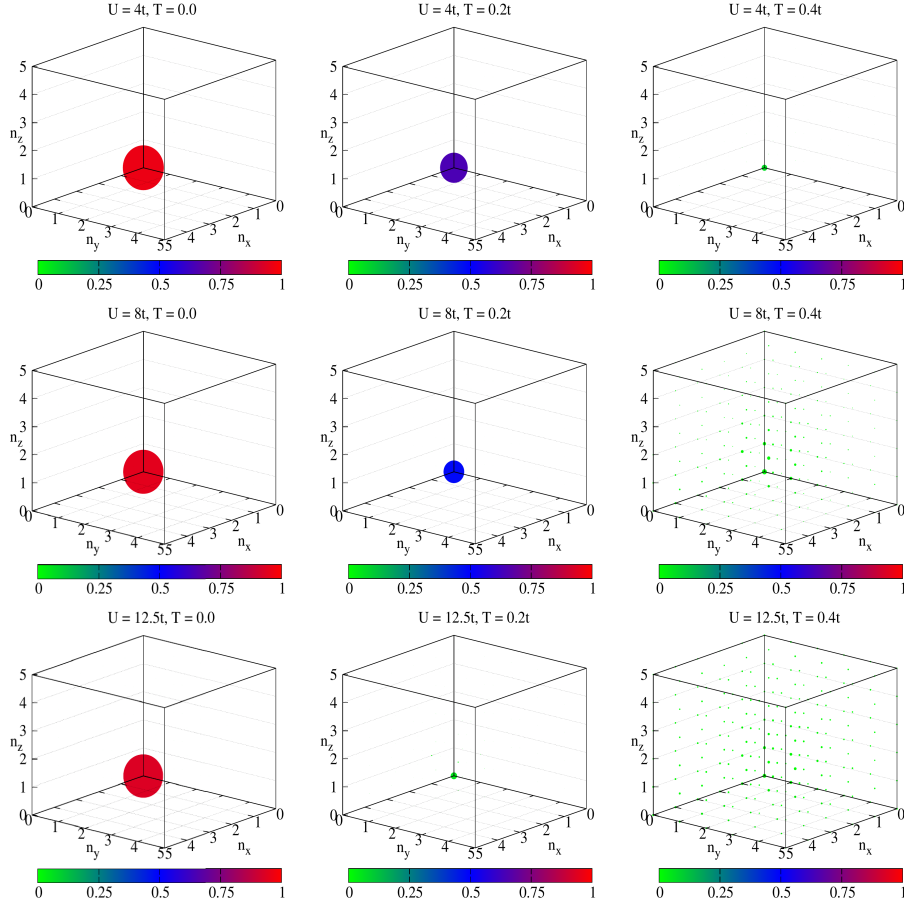


Figure 5.16: Spin structure factor $S_{mag}(\mathbf{q})$ at $T = 0$ for $U/t = 4, 8$ and 12.5 for $T = 0$ (left column), $0.2t$ (middle column) and $0.4t$ (right column). We use the notation $\mathbf{q} = \frac{2\pi}{L}(n_x, n_y, n_z)$. The size of a dot signifies relative weight at a given \mathbf{q} while its colour represents the actual magnitude of $S_{mag}(\mathbf{q})$. The presence of dominant weight at some \mathbf{q} , (in these cases $\mathbf{q} = (0, 0, 0)$) indicates presence of a magnetic ordered phase, while the ‘random’ but correlated patterns indicate a spin liquid.

representative temperature regimes in each case. We observe that at $T = 0$, $S_{mag}(\mathbf{q})$ has a peak (dominant weight) at $\mathbf{q} = (0, 0, 0)$ at all U values. This corresponds to a ferromagnetic ground state. With increase in temperature, thermal fluctuations randomise the spin orientations. As a result the $S_{mag}(\mathbf{q})$ weight at $\mathbf{q} = (0, 0, 0)$ reduces. With further rise in temperature, the ferromagnetic phase loses out to a paramagnetic state. This can be seen in the $S_{mag}(\mathbf{q})$ in the form that the $S_{mag}(\mathbf{q})$ weight gets distributed homogeneously among the \mathbf{q} ’s. The ferromagnetic critical temperature, T_c , is estimated by tracking $S_{mag}(0, 0, 0)$ weight with temperature.

The orbital state: Fig.5.17 shows the the amplitude distribution of the orbital moments, $P(\Gamma)$ for different temperature and interaction values. Panel (a) shows $P(\Gamma)$ for $U/t = 4$. $P(\Gamma)$ shows a single narrow peak structure, highlighting an

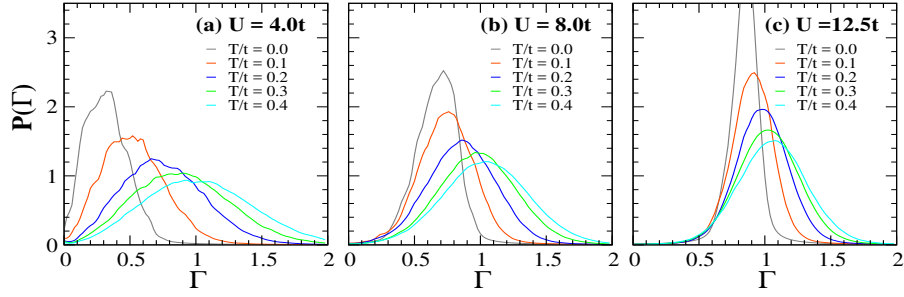


Figure 5.17: Size distribution of the orbital field $P(\Gamma)$ for indicated U/t and T/t values.

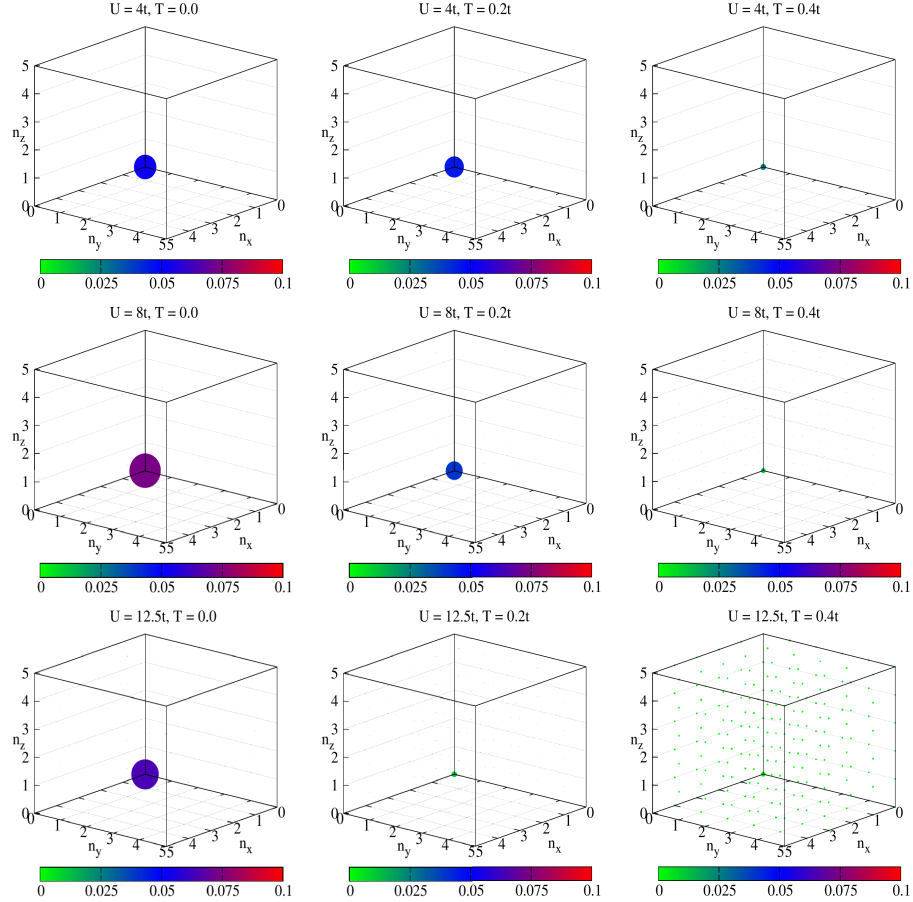


Figure 5.18: Orbital structure factor for $U/t = 4, 8$ and 12.5 at $T = 0$ (left column), $0.2t$ (middle column) and $0.4t$ (right column). We use the notation $\mathbf{q} = \frac{2\pi}{L}(n_x, n_y, n_z)$. The size of a dot signifies relative weight at a given \mathbf{q} while its colour represents the actual magnitude of $S_{orb}(\mathbf{q})$. The presence of dominant weight at some \mathbf{q} , indicates an orbital ordered phase, otherwise a disordered phase.

amplitude homogeneous state. With rise in temperature, the single peak feature of $P(\Gamma)$ retained. However the narrow peak becomes broad and the peak position

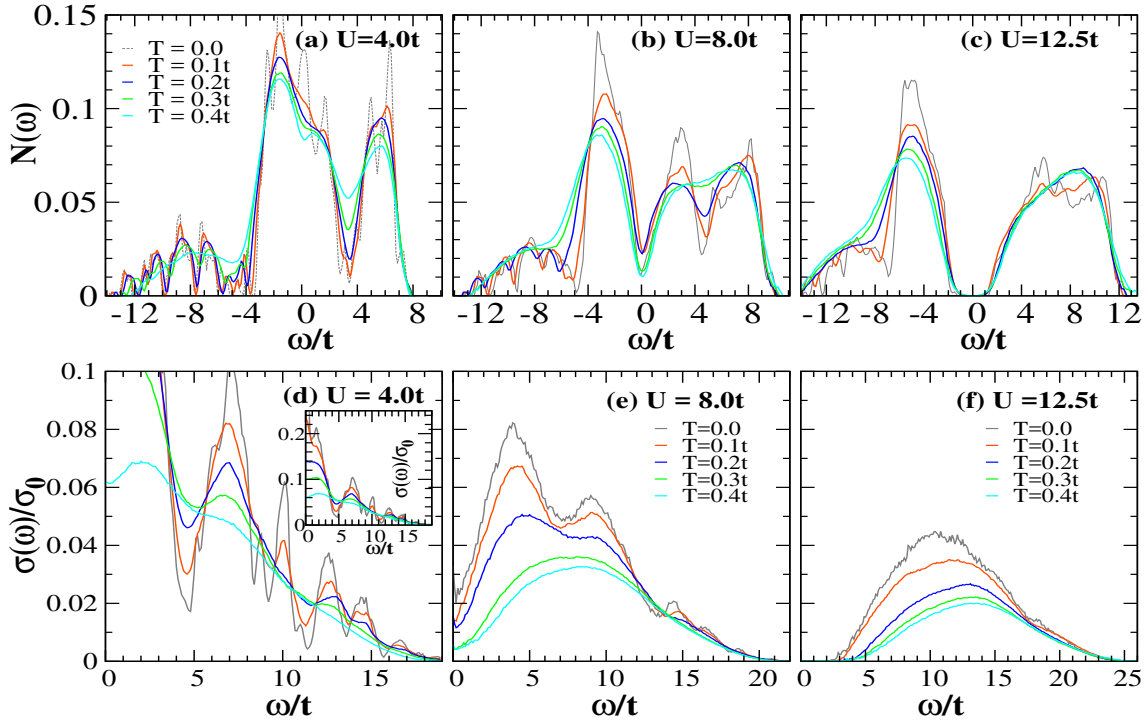


Figure 5.19: (a)-(c) Variation of density of states (DOS) for $U/t = 4, 8$ and 12.5 for indicated temperatures. (d)-(f) Variation of optical conductivity for $U/t = 4, 8$ and 12.5 for indicated temperatures.

shifts towards large Γ values. Panel (b) and (c) show $P(\Gamma)$ for $U/t = 8$ and 12.5 . We observe similar behaviour as in panel (a), but with important difference that the peaks are more narrow with increasing U/t values. This can be understood by the fact that the fluctuations of Γ_{avg} about the mean, are weaker in the insulating regime than in the metallic regime.

To understand the orbital state further, we calculate the orbital structure factor, $S_{orb}(\mathbf{q})$ in the optimised background. Fig.5.18 shows the \mathbf{q} dependence of the orbital structure factor $S_{orb}(\mathbf{q})$ for varying T/t and U/t values. We observe that at $T = 0$, $S_{orb}(\mathbf{q})$ has a peak (dominant weight) at $\mathbf{q} = (0, 0, 0)$ at all U values. This corresponds to a ferromagnetic ground state. However it can be seen that the $S_{orb}(0, 0, 0)$ weight increases initially with increasing U and after reaching a maximum (for $U/t = 10$), it decreases with further increasing U/t . With increase in temperature, thermal fluctuations lead to the orientational randomness of the orbital moments. As a result the $S_{orb}(\mathbf{q})$ weight at $\mathbf{q} = (0, 0, 0)$ reduces. With further rise in temperature, we find that the weight in $S_{orb}(\mathbf{q})$ gets distributed homogeneously among the \mathbf{q} 's. This can be understood as that the ferromagnet transiting to a paramagnet.

Density of states: Fig.5.19. (top row) shows the thermal evolution of the density of states (DOS) in three interaction regimes of our phase-diagram. We observe following features – (i) For $U < U_c$ the ground state has small orbital moments. The DOS is gapless and the weight at the Fermi level decreases monotonically with increasing T (see Fig.5.19.(a)). (ii) For $U \geq U_c$ the ground state has a hard gap in the DOS. With increase in temperature, the angular fluctuations of the orbital moments result in a slight reduction of the Mott-gap, and an increase in the low energy DOS (see Fig.5.19.(c)). The Mott-gap survives till very high temperature, $T \sim \Gamma_{avg}U$. (iii) In the neighbourhood of MIT boundary, for $U \sim U_c$, the DOS shows a sharp dip, a characteristic of a pseudogap (PG) phase. This dip fills up initially with increasing T , but deepens further with increasing temperature (see Fig.5.19.(b)).

Optics and transport: Fig.5.19.(bottom row) shows the optical conductivity from our calculation as we cross the Mott transition. The important points are as follows: (i) $\sigma(\omega)$ for $U < U_c$ is a metal. It shows a Drude peak at $T = 0$, and the Drude weight reduces with increasing temperature (see Fig.5.19.(d)). (ii) For $U > U_c$ the system has a clear Mott gap $\Delta(T)$ in the DOS. Thus, $\sigma(\omega) = 0$ for $\omega < \omega_c \sim \Delta(T)$. With increasing temperature the gap $\Delta(T)$ reduces, resulting in small, but increasing low frequency weight of $\sigma(\omega)$ and the $\sigma(\omega)$ peak position shifts to higher frequency (see Fig.5.19.(f)). (iii) For $U \leq U_c$, $\sigma(\omega)$ shows finite Drude weight, a response with the $\sigma(\omega)$ peak at a small finite frequency. The Drude weight reduces, while the $\sigma(\omega)$ peak slowly shifts to higher frequency with increasing T (see Fig.5.19.(e)). We would like to mention that as $U \rightarrow U_c$, $\sigma(\omega = 0) \rightarrow 0$. However, with increasing temperature the low frequency weight in $\sigma(\omega)$ increases initially and then decreases in accord with the behaviour of the DOS in this regime.

Fig.5.20 shows the d.c. resistivity $\rho(T)$ for different U/t . Following features are noteworthy. (i) For $U < U_c$, the residual resistivity $\rho(0)$ colour is finite with $d\rho/dT > 0$ over the entire T range. The resistivity can be understood in terms of the scattering of electrons from the small orbital moments. This is the metallic regime. (ii) For $U \geq U_c$ the system has a clear Mott gap at $T = 0$ with $\rho(0) \rightarrow \infty$. In this regime $d\rho/dT < 0$ over the entire temperature window we have explored. This is the Mott-insulating regime. (iii) In the neighbourhood of U_c , i.e. $|U - U_c| \ll U_c$, $\rho(T)$ shows a non-monotonic behaviour. We observe $d\rho/dT > 0$ in the low temperature limit, crossing over to $d\rho/dT < 0$ with increasing T . The temperature at which $d\rho/dT$ changes its sign is indicated as the T_{MIT} .

We observe T_{MIT} decreasing with increasing U (see Fig.5.15.(a)). This behaviour

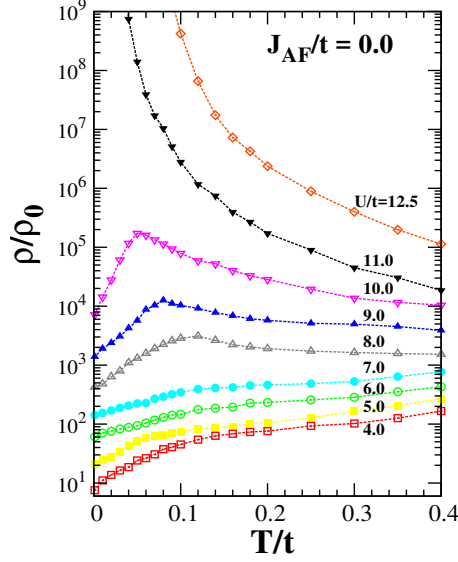


Figure 5.20: Variation of resistivity $\rho(T)$ with temperature for different U/t values. The normalising scale is $\rho_0 = (\hbar a_0)/e^2$, where a_0 is the lattice spacing.

can be understood as the scattering of electrons from the background fluctuating orbital moments. As U increases, $\Gamma_{avg}(U)$ also increases, resulting in the increased scattering of the electrons and a depleting DOS at the Fermi level.

The key features of this regime are. (i) The ground state is always a spin-ferromagnet due to the absence of the competing superexchange. (ii) The Mott transition is the result of stronger Hubbard repulsion, and manifests in the form of large orbital moments at each site of the lattice. These moments essentially dictate the spectral and transport properties.

5.3.2.3 Double exchange, superexchange and Hubbard repulsion

Fig.5.21(a) shows the phase diagram for varying t/U and T/t from our calculation for $J_{AF}/t = 0.2$. This is the most interesting regime, and is believed to be relevant for describing the Mott physics of the rare earth molybdates [112]. We observe the following features –

- The ground state is decided by the competition between double exchange and superexchange interactions. It is a ferromagnet when double exchange dominates. With increasing U , the kinetic energy and hence the double exchange reduces. When the antiferromagnetic superexchange prevails over the double exchange, the resulting ground state turns out to be a spin-liquid due to the frustrated pyrochlore geometry.

- With increasing temperature, the ferromagnetic or spin-liquid states loose out to the paramagnetic phase dominated by thermal fluctuations. With increasing U , the average local orbital moment's magnitude increases. This reduces the average kinetic energy and as a result, the system shows Mott insulating behaviour.
- The weak-coupling side ($U < U_c$) is a metal with finite density of states (DOS) at the Fermi-level. The strong-coupling side ($U > U_c$) has a Mott-gap in the DOS. In the Mott-transition neighbourhood, the Mott gap quickly converts to a pseudogap (PG) with increasing T , leading to the widening of the PG region (not shown in figure).

Fig.5.21(b) shows the average magnetisation M for varying t/U and T/t values. At $T = 0$ the system has $M = 1$ for $U < U_c$. With increasing U , the effect of double exchange reduces and superexchange takes over. This leads to reduction of M values. For $T/t > 0$, thermal fluctuations reduce M further, resulting in $M < 0.1$ for $T > T_c$.

Fig.5.21(c) shows the average magnitude of the orbital moment Γ_{avg} for varying t/U and T/t . At $T = 0$, as $U/t \rightarrow \infty$, $\Gamma_{avg} \rightarrow 1$, as one expects in the atomic limit. Γ_{avg} reduces with decreasing U such that $\Gamma_{avg} \rightarrow 0$ as $U/t \rightarrow 0$. For $T/t > 0$, thermal fluctuations lead to quick growth of Γ_{avg} in the metallic side.

Fig.5.21(d) shows the DOS at the Fermi level, $N(0)$, for varying t/U and T/t . On the metallic side ($U < U_c$), we see the DOS reducing gradually with increasing temperature. This can be ascribed to the increase of Γ_{avg} due to thermal fluctuations. On the Mott insulating side ($U \geq U_c$), we observe, the DOS slowly increasing with temperature, which can be understood as the gradual filling of the Mott gap. In the MIT neighbourhood we observe a non monotonic behaviour.

The magnetic state: Fig.5.22 shows $S_{mag}(\mathbf{q})$ for different U values in our phase diagram, for three representative temperature regimes in each case. We observe that at $T = 0$, $S_{mag}(\mathbf{q})$ has a peak (dominant weight) at $\mathbf{q} = (0, 0, 0)$ for $U/t < 10$. This corresponds to a ferromagnetic ground state. For $U/t \geq 10$, $S_{mag}(\mathbf{q})$ doesn't show a peak (dominant weight) at a given \mathbf{q} , rather, the dominant $S_{mag}(\mathbf{q})$ weight is distributed among several \mathbf{q} 's, suggesting that the underlying state is a spin-liquid. Increased temperature leads to further randomness in the spin orientation and disordered behaviour. As a result the $S_{mag}(\mathbf{q})$ weight at $\mathbf{q} = (0, 0, 0)$ reduces. With further rise in temperature, the ferromagnet and spin-liquid phases loose out to a paramagnetic state. This can be seen in the $S_{mag}(\mathbf{q})$ in the form that the $S_{mag}(\mathbf{q})$

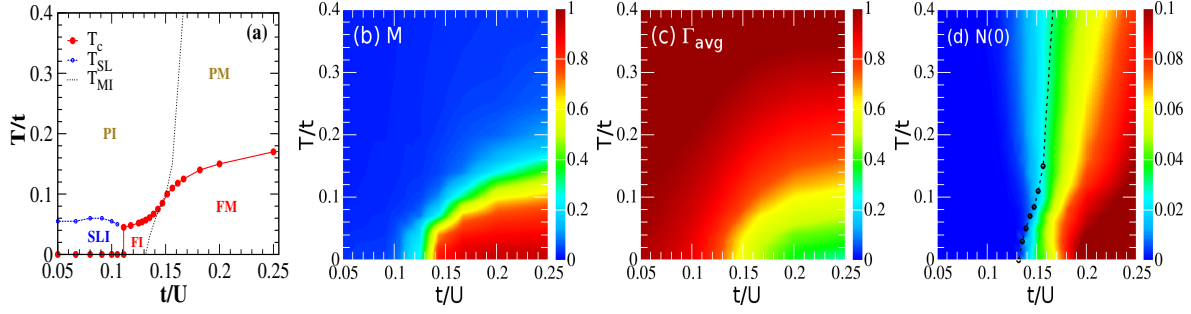


Figure 5.21: $J_{AF} = 0.2t$ (a) Phase diagram for varying t/U and T/t . The various phases shown in the phase diagram are, ferromagnetic metal (FM), ferromagnetic insulator (FI), paramagnetic metal (PM), spin-liquid insulator (SLI) and paramagnetic insulator (PI). The detailed characterisation of these phases is mentioned in the text. The T_{MI} line corresponds to the metal to Mott-insulator transition and the T_c line corresponds to a transition from the ferromagnetic ordered state to a paramagnetic phase. As can be seen, a small window of ferromagnetic phase survives also in the insulating side. The disordered phase in the insulating side is a spin-liquid with short-range correlations at low temperature (see figure 5.22). The T_{SL} line corresponds to a thermal transition from spin-liquid state to paramagnetic phase. Panel (b) and (c) show average magnetisation M and average orbital moment Γ_{avg} for varying t/U and T/t . Panel (d) shows the density of states at the Fermi level, $N(0)$, for varying t/U and T/t . The vanishing $N(0)$ corresponds to the MIT.

weight gets distributed homogeneously among the \mathbf{q} 's. The ferromagnetic critical temperature, T_c , is estimated by tracking $S_{mag}(0, 0, 0)$ weight with temperature.

The orbital state: Fig.5.23 shows the the amplitude distribution of the orbital moments, $P(\Gamma)$ for different temperature and interaction regimes. Panel (a) shows $P(\Gamma)$ for $U/t = 4$. $P(\Gamma)$ shows a single narrow peak structure, highlighting an amplitude homogeneous state. With rise in temperature, the single peak feature of $P(\Gamma)$ retained. However the narrow peak becomes broad and the peak position shifts towards large Γ values. Panel (b) and (c) show $P(\Gamma)$ for $U/t = 8$ and 12.5 . We observe similar behaviour as in panel (a), but with important difference that the peaks are more narrow with increasing U/t values. This can be understood by the fact that the fluctuations of Γ_{avg} about the mean, are weaker on the insulating regime than on the metallic regime.

Fig.5.24 shows the \mathbf{q} dependence of the orbital structure factor $S_{orb}(\mathbf{q})$ for varying T and U . We observe that at $T = 0$, $S_{orb}(\mathbf{q})$ has a peak (dominant weight) at $\mathbf{q} = (0, 0, 0)$ for $U/t < 10$. This corresponds to a ferromagnetic ground state. For $U/t \geq 10$, $S_{orb}(\mathbf{q})$ shows dominant weight is distributed among several \mathbf{q} 's, suggesting that the underlying orbital state is a spin-liquid. The $S_{orb}(0, 0, 0)$ weight decreases

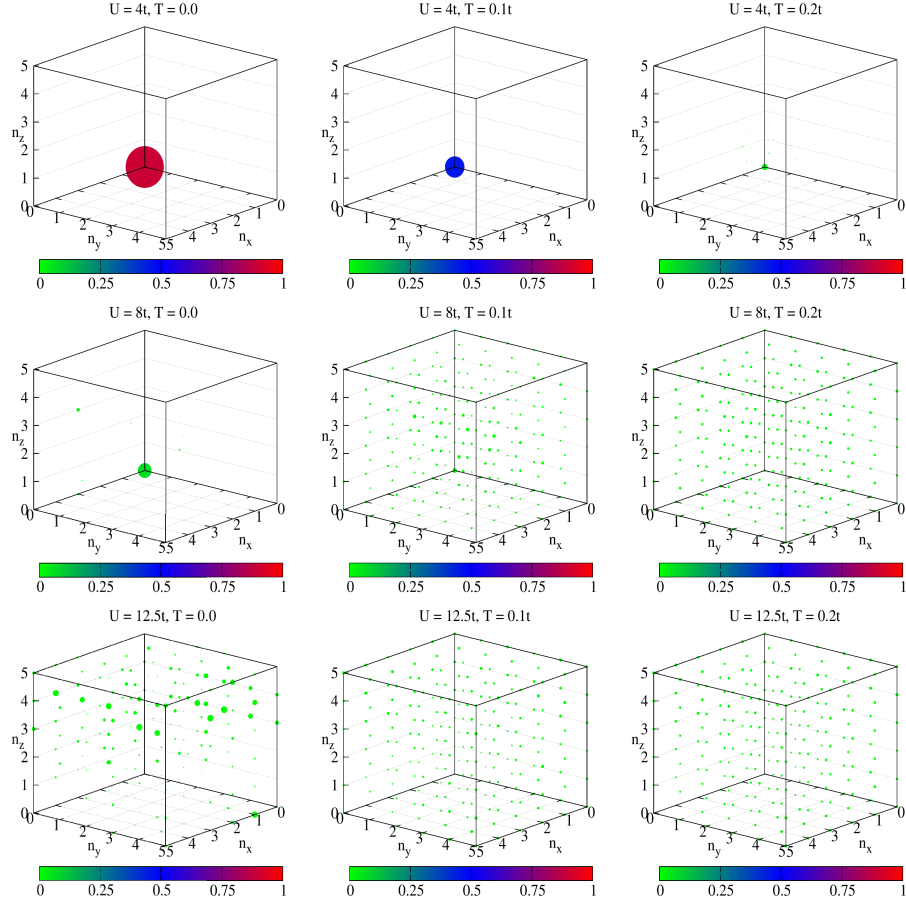


Figure 5.22: Spin structure factor $S_{mag}(\mathbf{q})$ at $T = 0$ for $U/t = 4, 8$ and 12.5 for $T = 0$ (left column), $0.1t$ (middle column) and $0.2t$ (right column). We use the notation $\mathbf{q} = \frac{2\pi}{L}(n_x, n_y, n_z)$. The size of a dot signifies relative weight at a given \mathbf{q} while its colour represents the actual magnitude of $S_{mag}(\mathbf{q})$. The presence of dominant weight at some \mathbf{q} , ($\mathbf{q} = (0, 0, 0)$ in this case) indicates magnetic order phase, while the ‘random’ but correlated patterns indicate a spin liquid.

with increasing U . With increase in temperature, thermal fluctuations promote further disordered behaviour. As a result the $S_{orb}(\mathbf{q})$ weight at $\mathbf{q} = (0, 0, 0)$ reduces. With further rise in temperature, we observe that the $S_{orb}(\mathbf{q})$ weight gets distributed homogeneously among the \mathbf{q} ’s. This can be understood as that the ferromagnetic phase losing out to a paramagnetic phase.

Density of states: Fig.5.25.(top row) shows the thermal evolution of the density of states (DOS) in three interaction regimes of our phase-diagram. We observe following features – (i) For $U < U_c$ the ground state has small orbital moments. The DOS is gapless and the weight at the Fermi level decreases monotonically with increasing T (see Fig.5.25.(a)). (ii) For $U \geq U_c$ the ground state has a hard gap in the DOS. With increase in temperature, the angular fluctuations of the orbital moments result

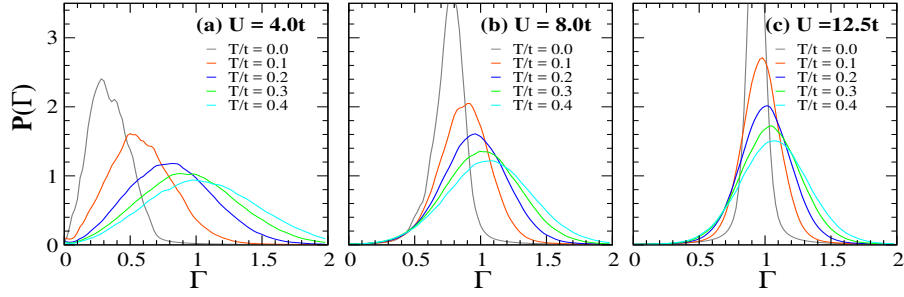


Figure 5.23: Size distribution of the orbital field $P(\Gamma)$ for indicated U/t and T/t values.

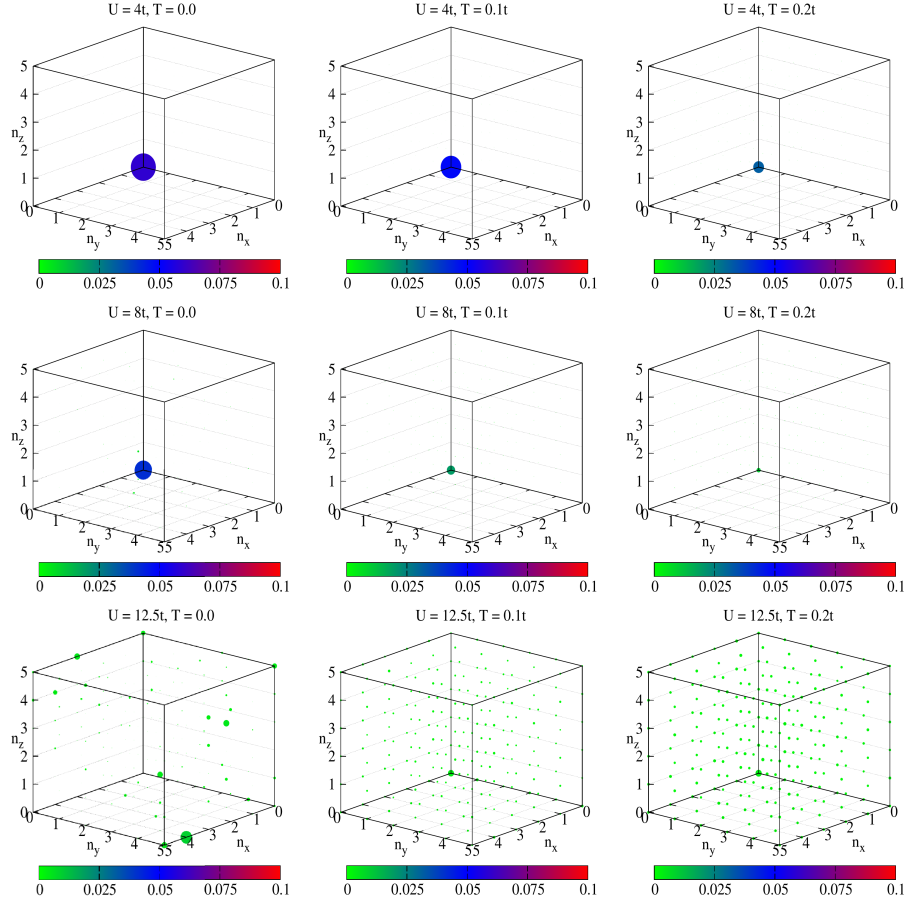


Figure 5.24: Orbital structure factor for $U/t = 4, 8$ and 12.5 at $T = 0$ (left column), $0.1t$ (middle column) and $0.2t$ (right column). We use the notation $\mathbf{q} = \frac{2\pi}{L}(n_x, n_y, n_z)$. The size of a dot signifies relative weight at a given \mathbf{q} while its colour represents the actual magnitude of $S_{orb}(\mathbf{q})$. The presence of dominant weight at some \mathbf{q} , indicates an orbital ordered phase, otherwise a disordered phase.

in a slight reduction of the Mott-gap, and an increase in the low energy DOS (see Fig.5.25.(c)). The Mott-gap survives till very high temperature, $T \sim \Gamma_{avg}U$. (iii)

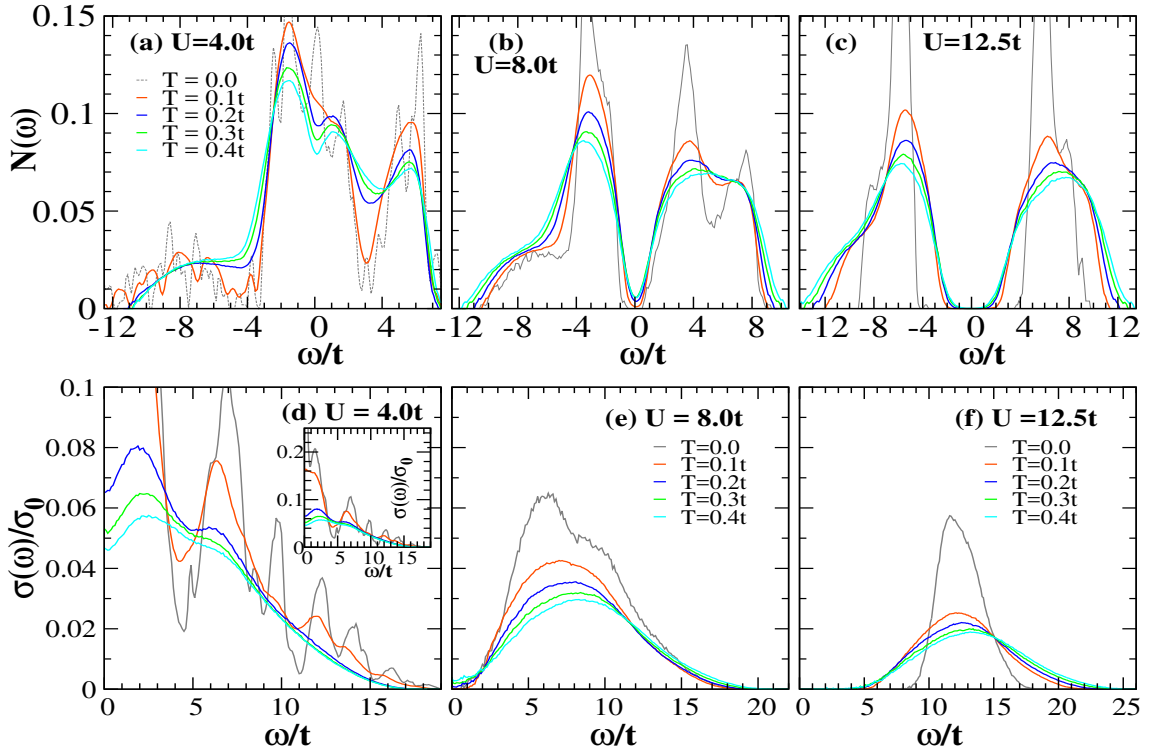


Figure 5.25: (a)-(c) Variation of density of states (DOS) for $U/t = 4, 8$ and 12.5 for indicated temperatures. (d)-(f) Variation of optical conductivity for $U/t = 4, 8$ and 12.5 for indicated temperatures.

In the neighbourhood of MIT boundary, for $U \sim U_c$, the DOS shows a sharp dip, a characteristic of a pseudogap (PG) phase. This dip fills up initially with increasing T , but deepens further with increasing temperature (see Fig.5.25.(b)).

Optics and transport: Fig.5.25.(bottom row) shows the optical conductivity from our calculation as we cross the Mott transition. The important points are as follows: (i) $\sigma(\omega)$ for $U < U_c$ is a metal. It shows a Drude peak at $T = 0$, and the Drude weight reduces with increasing temperature (see Fig.5.25.(d)). (ii) For $U > U_c$ the system has a clear Mott gap $\Delta(T)$ in the DOS. Thus, $\sigma(\omega) = 0$ for $\omega < \omega_c \sim \Delta(T)$. With increasing temperature the gap $\Delta(T)$ reduces, resulting in small, but increasing low frequency weight of $\sigma(\omega)$ and the $\sigma(\omega)$ peak position shifts to higher frequency (see Fig.5.25.(f)). (iii) For $U \leq U_c$, $\sigma(\omega)$ shows finite Drude weight, a response with the $\sigma(\omega)$ peak at a small finite frequency. The Drude weight reduces, while the $\sigma(\omega)$ peak slowly shifts to higher frequency with increasing T (see Fig.5.25.(e)). We would like to mention that as $U \rightarrow U_c$, $\sigma(\omega = 0) \rightarrow 0$. However, with increasing temperature the zero frequency $\sigma(\omega)$ weight increases initially and then decreases in accord with the behaviour of the DOS in this regime.

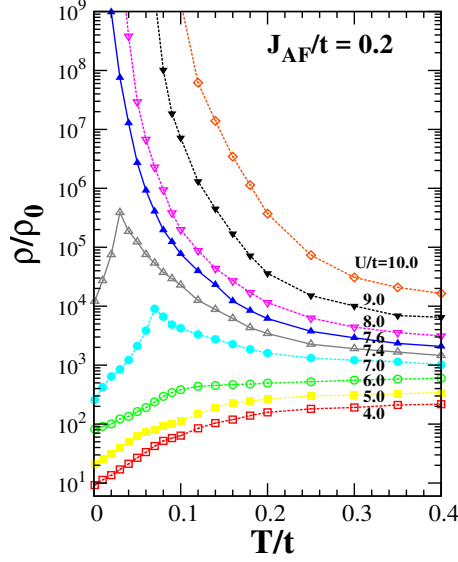


Figure 5.26: Variation of resistivity $\rho(T)$ with temperature for different U/t values. The normalising scale is $\rho_0 = \hbar/e^2$.

Fig.5.26 shows the d.c. resistivity $\rho(T)$ for different U/t . Following features are noteworthy. (i) For $U < U_c$, the residual resistivity $\rho(0)$ is finite with $d\rho/dT > 0$ over the entire T range. The resistivity can be understood in terms of the scattering of electrons from the small orbital moments. This is the metallic regime. (ii) For $U \geq U_c$ the system has a clear Mott gap at $T = 0$ with $\rho(0) \rightarrow \infty$. In this regime $d\rho/dT < 0$ over the entire temperature window we have explored. This is the Mott-insulating regime. (iii) In the neighbourhood of U_c , i.e., $|U - U_c| \ll U_c$, $\rho(T)$ shows a non-monotonic behaviour. We observe $d\rho/dT > 0$ in the low temperature limit, crossing over to $d\rho/dT < 0$ with increasing T . The temperature at which $d\rho/dT$ changes its sign is indicated as the T_{MIT} . We observe T_{MIT} decreasing with increasing U (see Fig.5.21.(a)). This behaviour can be understood as the scattering of electrons from the background fluctuating orbital moments. As U increases, $\Gamma_{avg}(U)$ also increases, resulting in the increased scattering of the electrons and a depleting DOS at the Fermi level.

The key features of this regime are. (i) A competition between double exchange and superexchange decides the underlying magnetic state. (ii) Though metal insulator transition occurs due to stronger Hubbard repulsion in this regime, the presence of finite superexchange, which, if dominates over the double exchange, leads to an ‘Anderson’ (disorder) aspect to this MIT. (iii) Metal-insulator transition and the magnetic transitions are not simultaneous.

5.3.2.4 Strong superexchange and Hubbard repulsion

Fig.5.27(a) shows the phase diagram for varying t/U and T/t at $J_{AF}/t = 0.6$, in terms of the magnetic, transport, and spectral properties that emerge from our calculation. We observe the following features –

- The ground state is a spin-liquid promoted by the antiferromagnetic superexchange interaction on the frustrated pyrochlore lattice. Spin structure factor calculation indicates that this phase has short-range correlations. With increasing temperature, this state loses out to a paramagnetic phase governed by thermal fluctuations.
- With increasing U/t , the average local orbital moment's magnitude increases. This reduces the average kinetic energy and as a result, the system shows Mott insulating behaviour.
- The weak-coupling side ($U < U_c$) is a metal with finite density of states (DOS) at the Fermi-level. The strong-coupling side ($U > U_c$) has a Mott-gap in the DOS. In the Mott-transition neighbourhood, the Mott gap quickly converts to a pseudogap (PG) with increasing T/t , leading to the widening of the PG region (not shown in figure).

Fig.5.27(b) shows the average magnetisation M for varying t/U and T/t values. We find that the system has $M \ll M_{sat} = 1$ even at $T = 0$ at all U values. At finite temperature, we observe that thermal fluctuations tend to enhance M further. However, in this strong superexchange regime $M \ll M_{sat}$ at all temperature values.

Fig.5.27(c) shows the average magnitude of the orbital moment Γ_{avg} for varying t/U and T/t . At $T = 0$, as $U/t \rightarrow \infty$, $\Gamma_{avg} \rightarrow 1$, as one expects in the atomic limit. Γ_{avg} reduces with decreasing U such that $\Gamma_{avg} \rightarrow 0$ as $U/t \rightarrow 0$. At finite temperature, thermal fluctuations lead to quick growth of Γ_{avg} in the metallic regime.

Fig.5.27(d) shows the DOS at the Fermi level, $N(0)$, for varying t/U and T/t . On the metallic side ($U < U_c$), we see the DOS reducing gradually with increasing temperature. This can be ascribed to the increase of Γ_{avg} due to thermal fluctuations. On the Mott insulating side ($U \geq U_c$), we observe, the DOS slowly increasing with temperature, which can be understood as the gradual filling of the Mott gap.

The magnetic state: Fig.5.28 shows $S_{mag}(\mathbf{q})$ for three different U values in our phase diagram, for three representative temperature regimes in each case. We observe that at $T = 0$, $S_{mag}(\mathbf{q})$ has no dominant weight at any given \mathbf{q} values, rather its distributed among several \mathbf{q} 's for all U/t values. This shows that the ground state

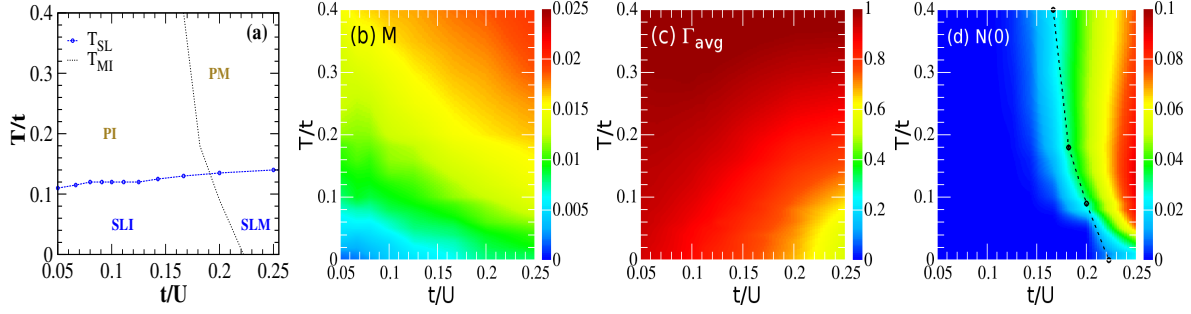


Figure 5.27: $J_{AF} = 0.6t$ (a) Phase diagram for varying t/U and T/t . The various phases shown in the phase diagram are, spin-liquid metal (SLM), paramagnetic metal (PM), spin-liquid insulator (SLI) and paramagnetic insulator (PI). The detailed characterisation of these phases is mentioned in the text. The T_{MI} line corresponds to the metal to Mott-insulator transition (MIT) and the T_{SL} line corresponds to the thermal transition from spin-liquid state to paramagnetic phase. The scale, T_{SL} , separates the disordered phase with short-range correlations (spin-liquid phase) from the randomly disordered paramagnet. This difference can be seen in Fig.5.28. Panel (b) and (c) show average magnetisation M and average orbital moment Γ_{avg} for varying t/U and T/t . Panel (d) shows the density of states at the Fermi level, $N(0)$, for varying t/U and T/t . The vanishing $N(0)$ corresponds to the MIT.

is a spin-liquid. With increasing temperature, thermal fluctuations randomise the magnetic phase further. As a result the $S_{mag}(\mathbf{q})$ weight gets distributed uniformly among the \mathbf{q} values, a signature of a paramagnetic phase. Our calculation shows this spin-liquid to paramagnet thermal transition is independent of the metallic or insulating behaviour and occurs for $T/t > 0.1$.

The orbital state: Fig.5.29 shows the amplitude distribution of the orbital moments, $P(\Gamma)$ for different temperature and interaction regimes. Panel (a) shows $P(\Gamma)$ for $U/t = 4$. $P(\Gamma)$ shows a single narrow peak structure, highlighting an amplitude homogeneous state. With rise in temperature, the single peak feature of $P(\Gamma)$ retained. However the narrow peak becomes broad and the peak position shifts towards large Γ values. Panel (b) and (c) show $P(\Gamma)$ for $U/t = 8$ and 12.5 . We observe similar behaviour as in panel (a), but with important difference that the peaks are more narrow with increasing U/t values. This can be understood by the fact that the fluctuations of Γ_{avg} about the mean, are weaker on the insulating regime than on the metallic regime.

Fig.5.30 shows the \mathbf{q} dependence of the orbital structure factor $S_{orb}(\mathbf{q})$ for varying T/t and U/t values. We observe that at $T = 0$, $S_{orb}(\mathbf{q})$ has no peak (dominant weight) at any given \mathbf{q} values, rather it is distributed among several \mathbf{q} 's, suggesting that the ground state is an orbital spin-liquid. Thermal fluctuations play detrimental role

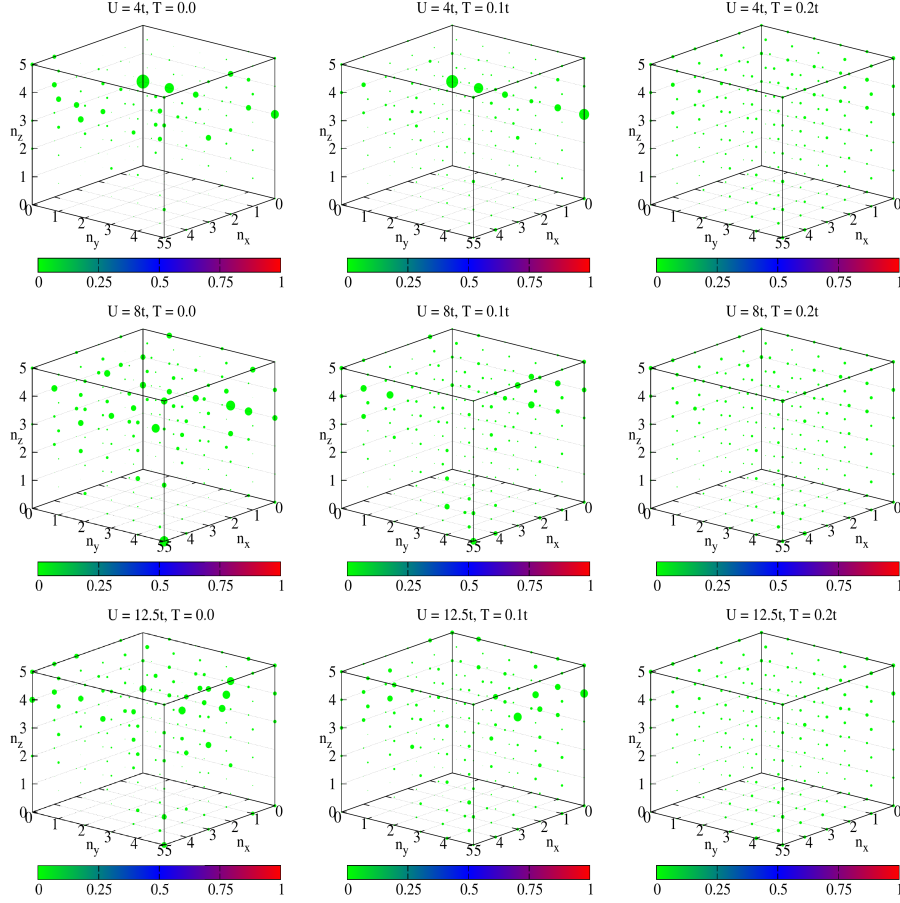


Figure 5.28: Spin structure factor $S_{mag}(\mathbf{q})$ at $T = 0$ for $U/t = 4, 8$ and 12.5 for $T = 0$ (left column), $0.1t$ (middle column) and $0.2t$ (right column). We use the notation $\mathbf{q} = \frac{2\pi}{L}(n_x, n_y, n_z)$. The size of a dot signifies relative weight at a given \mathbf{q} while its colour represents the actual magnitude of $S_{mag}(\mathbf{q})$. The presence of dominant weight at some \mathbf{q} , indicates magnetic ordering, while a ‘random’ but correlated patterns indicate the presence of a spin-liquid phase.

in further randomising this behaviour with increasing temperature. As a result an orbital paramagnetic phase shows up. This can be seen as the $S_{orb}(\mathbf{q})$ weights get distributed uniformly among the \mathbf{q} values.

Density of states: Fig.5.31.(top row) shows the thermal evolution of the density of states (DOS) in three interaction regimes of our phase-diagram. We observe following features – (i) For $U \ll U_c$ the ground state has small orbital moments. The DOS is gapless and the weight at the Fermi level decreases monotonically with increasing T . As $U \rightarrow U_c$ we see a sharp dip in the DOS, highlighting the presence of a pseudogap phase. This dip fills up initially with increasing T , but deepens further with increasing temperature (see Fig.5.31.(a)). (ii) For $U \geq U_c$, the DOS shows a Mott-gap in the spectrum at $T = 0$. With increasing temperature, thermal

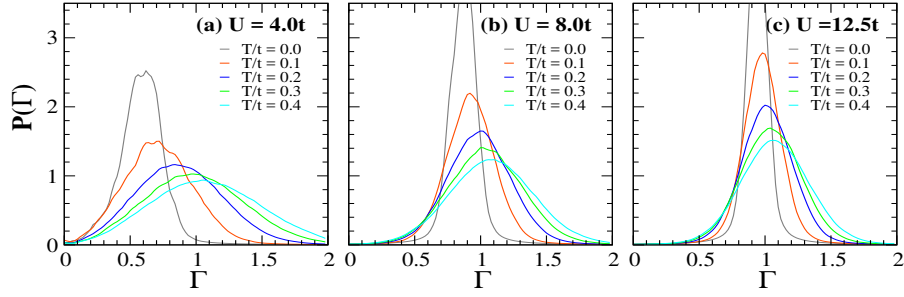


Figure 5.29: Size distribution of the orbital field $P(\Gamma)$ for indicated U/t and T/t values.

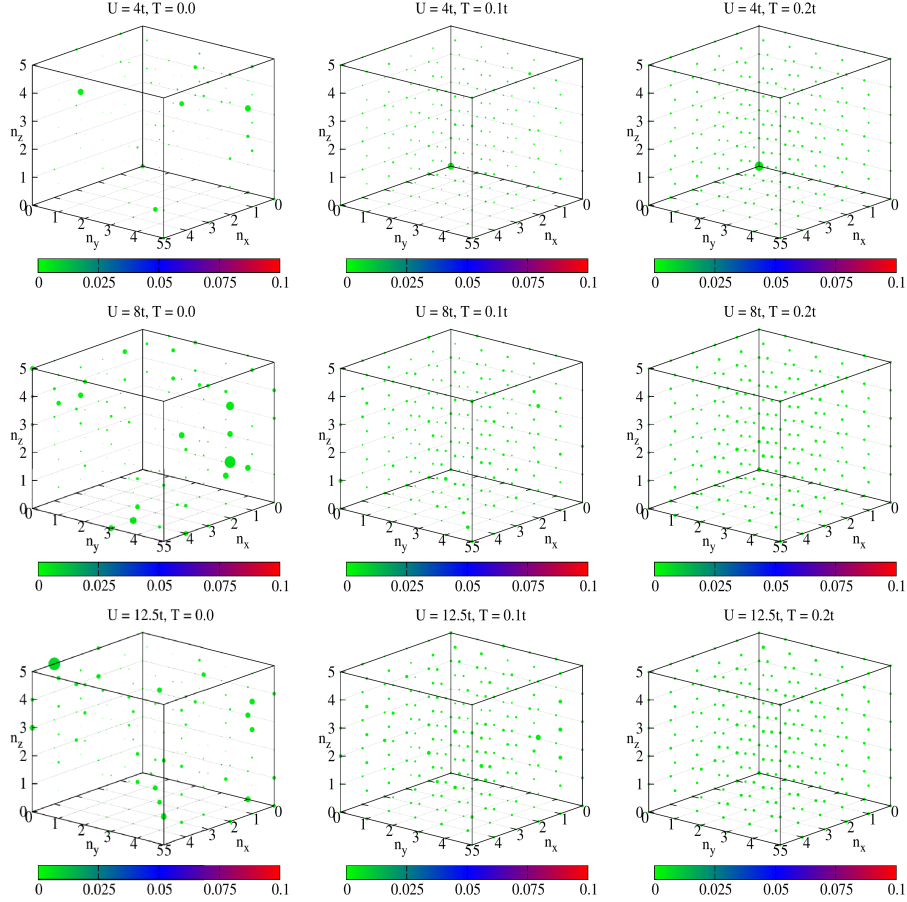


Figure 5.30: Orbital structure factor for $U/t = 4, 8$ and 12.5 at $T = 0$ (left column), $0.1t$ (middle column) and $0.2t$ (right column). We use the notation $\mathbf{q} = \frac{2\pi}{L}(n_x, n_y, n_z)$. The size of a dot signifies relative weight at a given \mathbf{q} while its colour represents the actual magnitude of $S_{orb}(\mathbf{q})$. The absence of dominant weight at some \mathbf{q} values, indicates an orbital disordered phase.

fluctuations manifest as amplitude fluctuations of the orbital moments. As a result, the Mott-gap reduces, and at high enough temperature it turns into a pseudogap

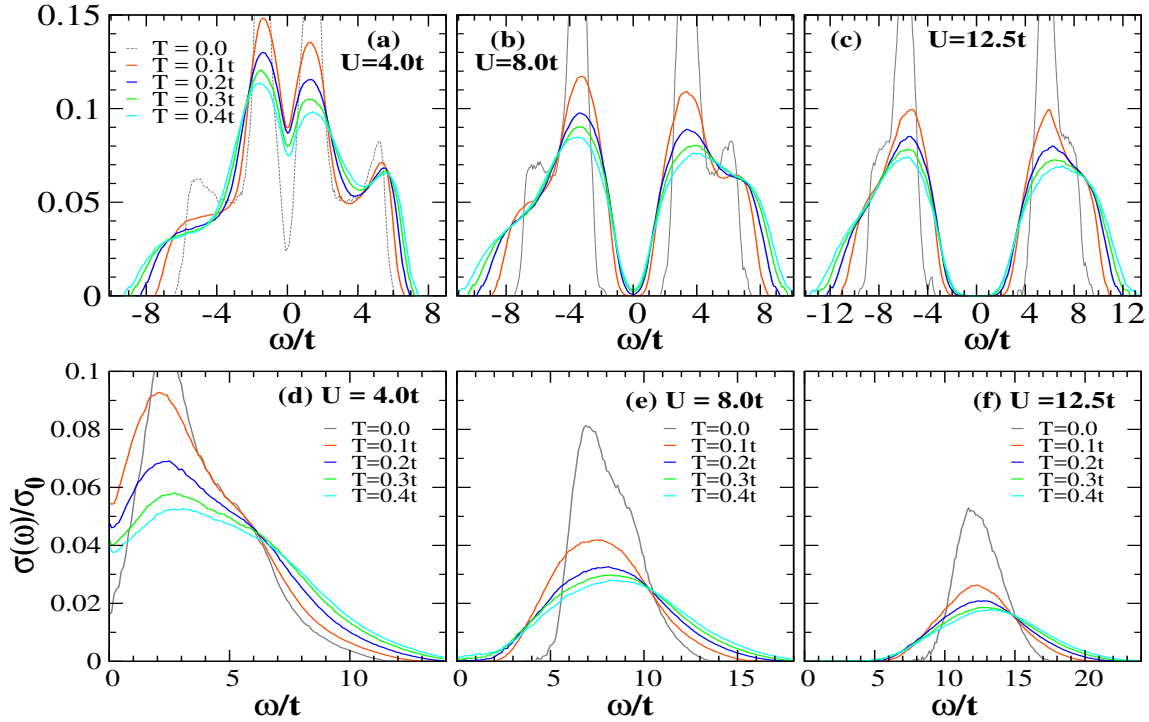


Figure 5.31: (a)-(c) Variation of density of states (DOS) for $U/t = 4, 8$ and 12.5 for indicated temperatures. (d)-(f) Variation of optical conductivity for $U/t = 4, 8$ and 12.5 for indicated temperatures.

phase (see Fig.5.31.(b)). (iii) For $U \gg U_c$ the ground state has a hard gap in the DOS. With increase in temperature, the angular fluctuations of the orbital moments result in a slight reduction of the Mott-gap (see Fig.5.31.(c)). However, the Mott-gap survives till very high temperature, $T \sim \Gamma_{avg}U$.

Optics and transport: Fig.5.31.(bottom row) shows the optical conductivity from our calculation as we cross the Mott transition. The important points are as follows: (i) $\sigma(\omega)$ for $U \ll U_c$ shows a Drude peak at $T = 0$, suggesting metallic behaviour. The Drude weight reduces with increasing temperature. As $U \rightarrow U_c$, $\sigma(\omega)$ shows finite Drude weight, with the $\sigma(\omega)$ peak at a small finite frequency. With increasing T , the Drude weight reduces further, and the $\sigma(\omega)$ peak slowly shifts to higher frequency (see Fig.5.31.(d)). (ii) For $U \geq U_c$, $\sigma(\omega)$ shows a small, but finite optical gap. However, with increasing temperature, the optical gap reduces gradually, and the low frequency optical weight increases monotonically (see Fig.5.31.(e)). (iii) For $U \gg U_c$ the system has a clear Mott gap $\Delta(T)$ in the DOS. Thus, $\sigma(\omega) = 0$ for $\omega < \omega_c \sim \Delta(T)$. With increasing temperature the gap $\Delta(T)$ reduces, resulting in small, but increasing low frequency weight of $\sigma(\omega)$ and the $\sigma(\omega)$ peak position shifts to higher frequency (see Fig.5.31.(f)).

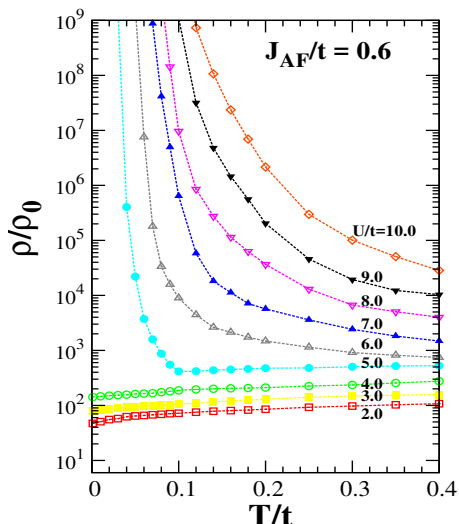


Figure 5.32: Variation of resistivity $\rho(T)$ with temperature for different U/t values. The normalising scale is $\rho_0 = \hbar/e^2$.

Fig.5.32 shows the d.c. resistivity $\rho(T)$ for different U/t . Following features are noteworthy. (i) For $U < U_c$, the residual resistivity $\rho(0)$ is finite with $d\rho/dT > 0$ over the entire T range. The resistivity in this regime is a result of the scattering of electrons from the small orbital moments. This is the metallic regime. (ii) For $U > U_c$ the system has a clear Mott gap at $T = 0$ with $\rho(0) \rightarrow \infty$. In this regime $d\rho/dT < 0$ over the entire temperature window we have explored. This is the Mott-insulating regime. (iii) In the neighbourhood of U_c , *i.e.*, $|U - U_c| \ll U_c$, $\rho(T)$ shows a non-monotonic behaviour. We observe $d\rho/dT < 0$ in the low temperature limit, crossing over to $d\rho/dT > 0$ with increasing T . The temperature at which $d\rho/dT$ changes its sign is indicated as the T_{MIT} . We observe T_{MIT} increasing with increasing U/t (see Fig.5.27.(a)).

The key features of this regime are. (i) The underlying magnetic state is always a spin-liquid due to the dominance of superexchange interaction. (ii) Strong superexchange and Hubbard repulsion lead to the metal-insulator transition.

5.3.3 Summary of the model study

In the previous sections we have studied the two orbital Hubbard model with the electrons additionally strongly coupled to a background local moment - and the moments interacting antiferromagnetically amongst themselves. This Hubbard-double exchange-superexchange scenario, on the pyrochlore lattice, is the minimal model for the rare earth molybdates. We mapped out the ground state phase diagram via

Physical properties	DE dominated	Phase competing	SE dominated
Magnetic ground state	Ferromagnetic	FM for $U < U_{mag}$, spin-liquid for $U > U_{mag}$	Spin-liquid
Ferromagnetic T_c	Large	Moderate for $U < U_{mag}$, zero for $U > U_{mag}$	Zero
Residual resistivity	Small	Small	Large
Localisation effect	Weak	Moderate	Strong

Table 5.1: Changing physical properties, as one moves from DE dominated to phase competing to the SE dominated regimes.

a simulated annealing based unrestricted Hartree-Fock calculation and established the metal-insulator and ferromagnet-spin liquid transition boundaries.

In Table.5.1, we summarise the results of our study in terms of changing physical properties, as one moves from DE dominated to phase competing to the SE dominated regimes.

5.4 Comparing to molybdate experiments

The rare earth molybdate family $R_2Mo_2O_7$ exhibits ground states that vary from a ferromagnetic metal (FM) to a spin glass metal (SG-M) and then a spin glass insulator (SG-I) as the rare earth radius r_R is reduced [172]. Materials with $R = Nd$ and Sm are metallic, $R = Tb, Dy, Ho, Er,$ and Y are insulating, and $R=Gd$ is on the verge of the metal-insulator transition (MIT) [102, 103, 173, 174]. The unusual features in transport include very large residual resistivity, $\sim 10 m\Omega cm$ close to the metal-insulator transition [102], prominent anomalous Hall effect in metallic samples, *e.g.* $Nd_2Mo_2O_7$ [6, 7, 168–170], and magnetic field driven metallisation in the weakly insulating samples, *e.g.* $Gd_2Mo_2O_7$ [5].

The molybdates involve orbitally degenerate electrons Hund’s coupled to local moments. The large Hund’s coupling promotes ferromagnetism, the superexchange between the local moments prefers antiferromagnetism, and Hubbard repulsion tries to open a Mott gap. The phase competition is tuned by the rare earth ionic radius, decreasing which leads to change from a ferromagnetic metal to a spin disordered highly resistive ground state, and ultimately an ‘Anderson-Mott’ insulator.

The molybdates offer additional twists to the Mott problem: (i) the Mott transition in these materials occur in the background of overall *ferromagnetic* correlation [86, 173, 174], and (ii) the zero temperature resistivity seems to grow continuously with the control parameter [102] rather than have an abrupt zero to infinity transition.

These features owe their origin to the additional degrees of freedom, and couplings, involved in these materials. Here, we attempt a quantitative theory of the molybdates by studying their minimal model on the pyrochlore geometry. We establish a thermal phase diagram that closely corresponds to the experiments, predict the hitherto unexplored orbital correlations, quantify and explain the origin of the anomalous resistivity, and present dynamical properties across the MIT.

5.4.1 Parameter calibration

Following *ab initio* estimates [112, 175], we use parameters appropriate to the molybdates, as $t = 0.1$ eV and $J_{AF} = 0.02$ eV. The calibration of U/t in terms of r_R is based on the optical gap (see Fig.5.33). For $T \sim 0$, the optical gap Δ is determined by linearly extrapolating the decreasing edge of the optical conductivity spectra in the low energy regime. Fig.5.33.(a) shows the comparison of experimental gap [103] $\Delta_{expt} = \Delta(r_R)$ and theoretical gap $\Delta_{th} = \Delta(U/t)$ (see Fig.5.33.(b)) at low tempera-

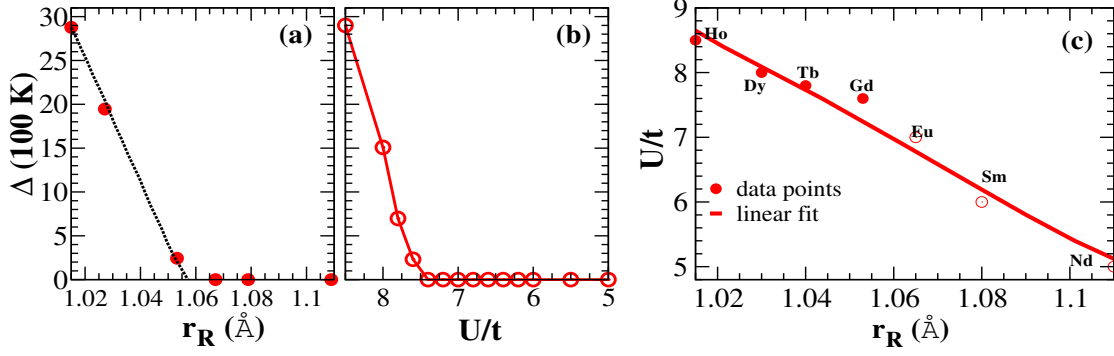


Figure 5.33: Optical gap (Δ) extracted from the low temperature optical conductivity: (a) experiment [103] $\Delta_{expt} = \Delta(r_R)$ and (b) theory $\Delta_{th} = \Delta(U/t)$. (c) $\Delta(r_R) \sim \Delta(U/t)$ gives us the values of U/t appropriate for the molybdates.

ture. We ‘calibrate’ the U/t of our model in terms of r_R based on $\Delta(r_R) \sim \Delta(U/t)$ in the insulating regime (finite optical gap). We try a linear fitting of this data and extrapolate it to lower U/t values, to have an estimate of the U/t in terms of r_R in the metallic regime (zero optical gap). Our calibration (see Fig.5.33.(c)) suggests that for the rare-earth molybdates the appropriate U/t value varies from $\sim 5 - 9$ as R varies from Nd to Ho.

We discuss our results for the chosen t , J_{AF} , and U/t , using absolute scales, and compare with available experimental data [102, 167].

5.4.2 Results

Phase diagram: Fig.5.34.(a) shows the experimental phase diagram. At large r_R , where the U/t ratio is relatively small, the ground state is a ferromagnetic metal with a moment $\sim 1.4\mu_B$ per Mo [7, 167]. The magnetisation seems to diminish slowly as r_R reduces (panel 5.34.(c)), and then rapidly around the metal-insulator transition, $r_R^c \sim 1.06\text{Å}$, but a small value survives into the weak insulating regime [167]. The FM T_c is $\sim 80\text{K}$ for large r_R and drops sharply near r_R^c . The state for $r_R \lesssim r_R^c$ is a spin glass, with $T_{SG} \sim 20\text{K}$.

Panel 5.34.(b) shows our result over the window $U/t \sim 5 - 10$. For our parameter calibration the metal-insulator transition (MIT) at $T = 0$ occurs at $U_c \sim 7.6t$, and we present our results in terms of U_c/U . At the right end, where $U \sim 0.7U_c$, the ground state is metallic, double exchange (DE) dominated, and an almost saturated ferromagnet. This is also a weakly ‘ferro orbital’ state. With increasing U the orbital moment grows and leads to a splitting of the e'_g band.

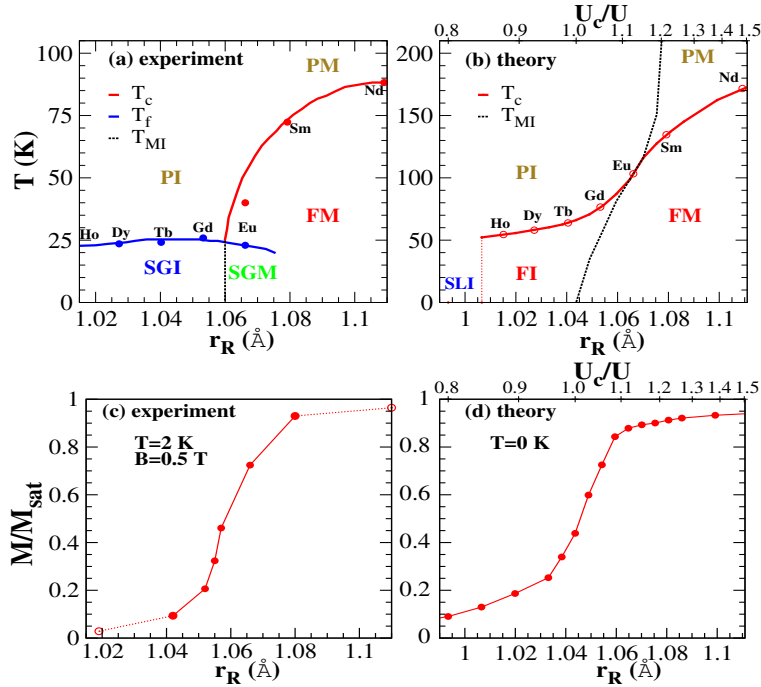


Figure 5.34: (a)-(b) Phase diagram of the molybdates- experiment [6, 172] and theory. The experimental ground state changes from ferromagnetic metal (FM) to spin-glass metal (SGM) and then spin-glass insulator (SGI) with reducing r_R . Within theory the FM transforms to a ‘spin liquid’ rather than a spin-glass. (c)-(d) Show the ferromagnetic moment at low T as the system is taken through the MIT. Within both experiment [167], (c), and theory, (d), a small moment survives in the insulator. In (b) we have cut off T_c at the point where the $T = 0$ magnetisation drops below 10%.

Temperature scales: We have used a model with Hund’s coupling $J_H \gg t$ for convenience, and obtain $T_c \sim 160\text{K}$ for Nd. In reality $J_H \sim 5t$ [112], and as earlier results show [176] this would reduce T_c by $\sim 50\%$ to about 80K (see Discussion), close to the actual value for Nd. Within our scheme we do not find any spin freezing, so no T_{SG} . Our magnetic state for $U \gtrsim U_c$ is a spin liquid (SL), rather than a spin glass, with weak ferromagnetism. We comment on the spin freezing issue later. Panels 5.34.(c) and 5.34.(d) show the low T magnetisation in the molybdates and in our scheme. The dependence is very similar and a small magnetisation survives beyond the MIT.

Resistivity: We demarcate the finite T metal-insulator boundary based on the temperature derivative of resistivity $d\rho/dT$: ‘metal’ if $d\rho/dT > 0$, ‘insulator’ if $d\rho/dT < 0$. We compute $\rho(T)$ via the low-energy limit of the optical conductivity. Fig.5.35.(a) shows experimental resistivity [102] while 5.35.(b) shows the theory result for parameter values set by the calibration.

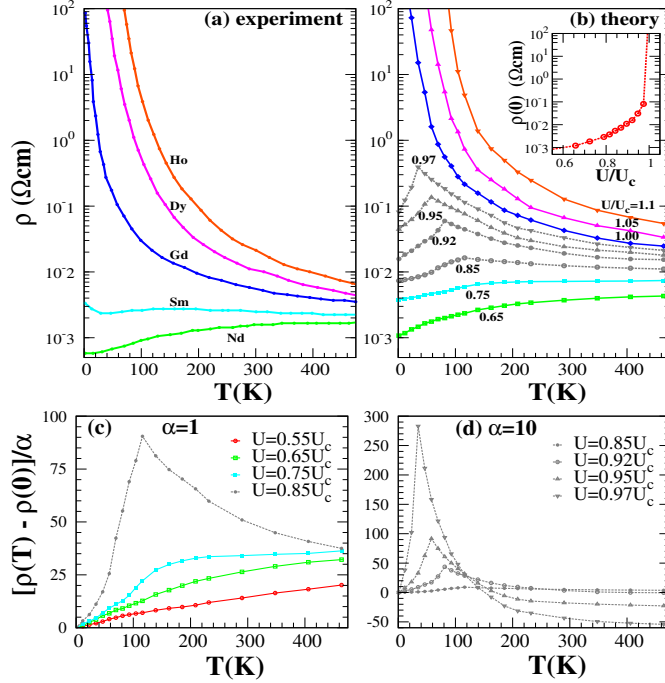


Figure 5.35: (a) Resistivity of the molybdates for varying rare earth [102]. (b) Resistivity computed within our scheme. The coloured plots are counterparts of the experimental data, while the dotted lines predict possible behaviour if intermediate compositions were to be synthesised. Inset to (b) shows the growth of the ‘residual’ resistivity, $\rho(0)$. (c)-(d) Show theory results for $\rho(T) - \rho(0)$ on a linear scale, to highlight the temperature driven metal to insulator crossover.

Even the limited R variation in the experiments can be thought to represent three ‘regimes’. (i) For R=Nd, the ‘high T_c ’ FM, $\rho(T)$ has traditional metallic behaviour, $\rho(0) < 1 \text{ m}\Omega\text{cm}$ and $d\rho/dT > 0$ all the way to 400K. (ii) For R=Gd, Dy, Ho, the system is insulating at all T , with $\rho(0) \rightarrow \infty$. The behaviour is clearly activated for Dy and Ho while Gd seems to be weakly insulating. (iii) R=Sm (and Eu, not shown) represents the most interesting case, with $\rho(0) \sim 3 \text{ m}\Omega\text{cm}$ and a non monotonic T dependence [102, 103]. Any theory would have to capture the obvious regimes (i) and (ii) and also the peculiar large $\rho(0)$ and non monotonicity in (iii).

Our results, panel 5.35.(b), show the following: (i) For $U \ll U_c$, the itinerant e'_g electrons see a DE dominated ferromagnetic background, as well as an orbital-ferro state. The $T = 0$ state is ideally clean, and finite T resistivity from spin and orbital fluctuations generate an approximate linear T behaviour (see 5.35.(c)). (ii) For $U \gg U_c$, there is a distinct gap Δ with $\rho(T) \sim \rho_0 e^{\Delta/T}$ as $T \rightarrow 0$ and $d\rho/dT < 0$ over the entire temperature range. (iii) For $U \lesssim U_c$, the residual resistivity $\rho(0)$ is finite. This arises from a combination of depleting DOS at the Fermi level (due to

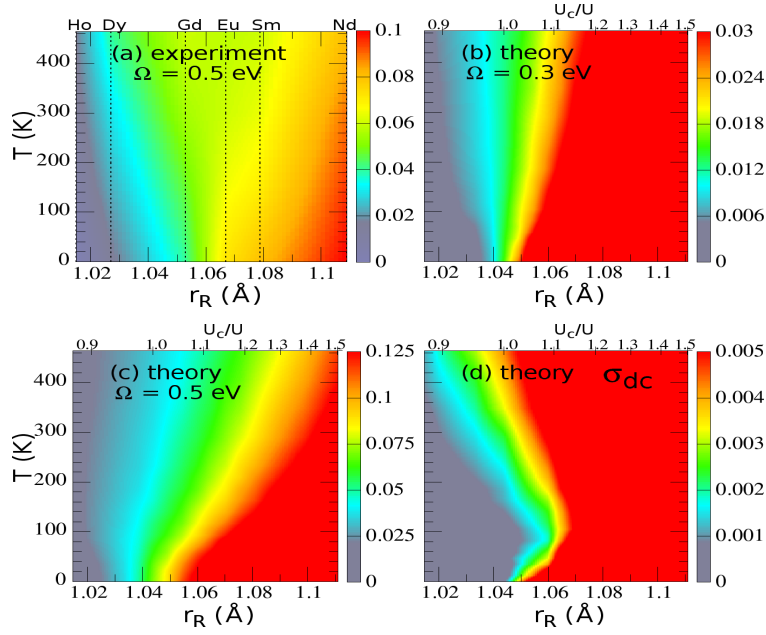


Figure 5.36: (a)-(c) Low energy optical spectral weight, $n_{eff} \propto \int_0^\Omega \sigma(\omega) d\omega$. (a) Experimental result for $\Omega = 0.5$ eV [102], (b) theory result for $\Omega = 0.3$ eV, (c) theory result for $\Omega = 0.5$ eV. (d) The d.c conductivity within theory.

the increasing orbital moment), and the magnetic disorder due to weakening DE. The behaviour of $\rho(0)$ is shown in the inset to panel 5.35.(b). Increasing T does lead to a linear behaviour, with a large slope, but the resistivity peaks at a scale $T_{peak}(U)$ and falls thereafter. Panels 5.35.(c)-(d) highlight this trend. As $U \rightarrow U_c$, $T_{peak} \rightarrow 0$, finally merging with the insulating behaviour in (ii).

Optical spectral weight: Fig.5.36.(a) shows the experimentally estimated optical spectral weight $n_{eff}(\Omega) = (2m_0/\pi e^2) \int_0^\Omega \sigma(\omega) d\omega$ for different R and varying temperature at $\Omega = 0.5$ eV [102]. It shows the expected trend of n_{eff} growing with T in the insulating, low r_R , side as the Mott gap is slowly filled, and reducing on the metallic side as weight gets transferred to high energy as coherence is lost.

We calculated the same quantity for different cutoff frequencies, Ω , as $n_{eff}(\Omega) = \int_0^\Omega \sigma(\omega) d\omega$. Fig.5.36.(b)-(c) show our result for $\Omega = 0.3$ eV and 0.5 eV respectively. Panel 5.36.(d) shows just σ_{dc} to contrast the features in optical weight to the non monotonicity of the d.c conductivity itself.

Our result at $\Omega = 0.3$ eV, roughly 2/3 the experimental cutoff, has the same features as the experimental data. At $\Omega = 0.5$ eV, however, our data reveal a weak non monotonicity in the T dependence when $U \gtrsim U_c$. This arises because $\sigma(\omega)$ gains weight at low frequency, as in panel (b), but *loses more* around $\omega \sim 0.5$ eV. The success in capturing the d.c resistivity, Fig.5.35, does not translate to similar success

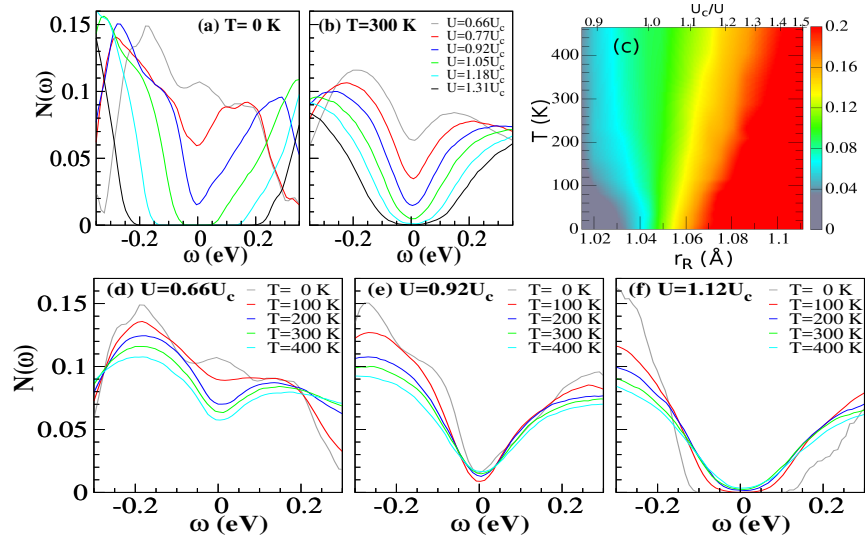


Figure 5.37: (a)-(b) Variation of DOS with U at $T = 0\text{K}$ and 300K . (c) Integrated DOS, over $\omega = \pm 0.15\text{eV}$, for varying U and T . (d)-(f) Temperature dependence of DOS at $U = 0.65U_c$, $0.9U_c$ and $1.1U_c$, respectively. (d) is a gapless metal, (e) shows a pseudogapped state, while (f) shows the T dependence in a gapped Mott insulator.

in the capturing the high energy optical conductivity. It is possible that some of the simplifying assumptions regarding band-structure and coupling constants, *i.e* J_H , affect this result.

The non monotonicity in our $\Omega = 0.5\text{ eV}$ spectral weight (Fig.5.36.(c)) is distinct from the d.c conductivity behaviour shown in Fig.5.36.(d). Fig.5.35.(b) shows that bad $T = 0$ metals, for $U \lesssim U_c$, become more resistive with increasing T and beyond a T_{peak} become less resistive again. We suggest that a detailed conductivity map, on materials like $\text{Gd}_{2-x}\text{Sm}_x\text{Mo}_2\text{O}_7$ or $\text{Gd}_{2-x}\text{Eu}_x\text{Mo}_2\text{O}_7$ could reveal this non monotonicity.

Density of states: We computed the single particle density of states (DOS), $N(\omega)$, for the interaction and temperature window studied. Fig.5.37.(a) shows the dependence of $N(\omega)$ on U/U_c as the system is driven across the Mott transition at $T = 0$. The DOS has its tight binding form upto $U \sim 0.7U_c$ beyond which the presence of the orbital moment shows a visible depletion in the DOS around $\omega = 0$. This dip becomes a gap for $U \geq U_c$, which grows in the insulating phase. At $T = 300\text{K}$, Fig.5.37.(b), the systems with $U < U_c$ lose weight near $\omega = 0$, while those with $U > U_c$ gain weight. Panel 5.37.(c) quantifies these trends by calculating $\int_{-\Omega'}^{\Omega'} N(\omega)d\omega$, where $\Omega' = 0.15\text{ eV}$ (to make a comparison with Fig.5.36.(b)). We suggest that the optical behaviour observed experimentally has an analog in the single particle spectral weight transfer as well.

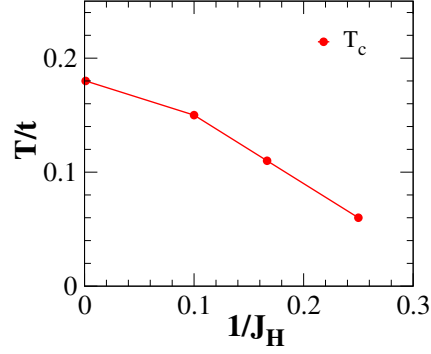


Figure 5.38: Variation of the ferromagnetic T_c with Hund's coupling J_H [176]. This result on the single orbital model indicates that the T_c reduces to about half when J_H is lowered to $\sim 5t$ from infinity.

Panels 5.37.(d)-(f) show the thermal evolution of the DOS at three representative U/U_c . (i) In 5.37.(d) $U \sim 0.6U_c$, the ground state is a nearly saturated ferromagnet with a small orbital moments Γ_i 's and has finite DOS at $\omega = 0$. Thermal growth and fluctuations of the Γ_i 's decrease the DOS at $\omega = 0$ resulting in a small dip at high temperature. (ii) For $U = 1.1U_c$, panel 5.37.(f), there is significant spin disorder in the ground state (the ferromagnetic moment is ~ 0.1) and the Γ_i 's are large, ~ 1 , at all sites. A remnant of the atomic gap $\sim U|\Gamma|$, survives despite the presence of hopping. The DOS shows a Mott gap. With increase in temperature, the angular fluctuations of the Γ_i 's result in a slight smearing of the gap edge and increase in 'low energy' weight. (iii) For $U = 0.9U_c$, panel 5.37.(e), the magnetic state has magnetisation, $M \sim 0.5$ and the Γ_i 's are moderately large. As a result there is only a loss in weight around $\omega = 0$ but no hard gap. This is a pseudogap state.

5.4.3 Discussion

(1). *Effect of finite Hund's coupling:* To simplify the study of our starting model, we have considered the Hund's coupling (J_H) as infinite. This allows us to retain only one spin species of electrons in the two orbitals at a site. In reality, however, J_H is finite for all materials. As we decrease J_H from infinite, we observe the lowering of the ferromagnetic T_c . We show the dependence of T_c with J_H in Fig.5.38.

(2) *Mechanism behind the molybdate metal-insulator transition:* (i) Increasing U increases the splitting $\Delta \sim |\Gamma|U$ between the electronic levels on Mo. This becoming comparable to the bandwidth would lead to a Mott transition (the correlation aspect). (ii) With increasing U , the growing orbital moment suppresses the electron

kinetic energy. This weakens DE. The competing AF superexchange reduces the magnetisation and increases the extent of spin disorder in the ground state. We call this the ‘Anderson’ (disorder) aspect of the problem. It depends crucially on the presence of J_{AF} . U_c is determined by a combination of the Mott and Anderson effects opening a gap in the electronic spectrum. Since magnetic disorder plays a role in the MIT, one can affect the transition by applying a magnetic field [5].

5.4.4 Conclusion

We discussed a quantitative approach to the Mott transition in the pyrochlore molybdates using a real space framework, retaining the double exchange, superexchange and correlation effects. We showed the results for the chosen t , J_{AF} , and U/t , using absolute scales, and compared with available experimental data [102,167]. After making parameter choices suggested by *ab initio* estimates [112,175] our main results are as follows.

(i) We obtain a phase diagram with ferromagnetic metal and spin disordered metal and insulator phases. However, our disordered state is a ‘spin liquid’ in contrast to the experimental spin glass. (ii) The FM T_c is in the experimental ballpark if we make room for a simple renormalisation of the Hund’s coupling. (iii) Our transport results bears almost quantitative correspondence with experiments [102,103], explain the high residual resistivity in terms of spin and orbital disorder scattering, and predict a highly non monotonic temperature dependence for samples of the form $\text{Gd}_{2-x}\text{Sm}_x\text{Mo}_2\text{O}_7$. (iv) The temperature and correlation dependence of our intermediate frequency optical spectral weight is very similar to the experiments [102,103] but changing the cutoff frequency reveals peculiarities, also reflected in the single particle weight.

There are several molybdate effects that we have not touched upon in this chapter, but they can also be readily explored. These include (i) the experimental $P - r_R$ phase diagram, (ii) the field driven IMT in $\text{Gd}_2\text{Mo}_2\text{O}_7$ [5], (iii) anomalous Hall effect (AHE) observed in $\text{Nd}_2\text{Mo}_2\text{O}_7$ [6,7,168–170], and (iv) spin glass freezing, which requires some degree of quenched disorder [165] (or bond distortions [166,177–179]).

MOTT PHYSICS IN THE PYROCHLORE IRIDATES

6.1 Introduction

The rare-earth pyrochlore iridates $R_2\text{Ir}_2\text{O}_7$ involve an interplay of Coulomb interaction and spin-orbit coupling on a frustrated geometry. Despite the pyrochlore structure these materials show non-trivial magnetic ordering. A detailed understanding of the properties of these compounds, particularly at finite temperature, remains wanting. This chapter describes our work on the iridate Mott transition using the SPA as a tool. To start with we review the experimental situation, and the existing theory, on these compounds.

Experiment: The iridates show a metal-insulator transition (MIT) [180, 181] with reduction of the rare-earth ionic radius (r_R). The Pr based iridate shows metallic behaviour down to the lowest observed temperature without any magnetic order [182]. Other iridates, with smaller r_R , show a magnetically ordered insulating phase at low temperature, and a non-magnetic insulating state at high temperature [183]. The low temperature magnetic phase is speculated to be an antiferromagnet with ‘all-in-all-out’ (AIAO) ordering [184, 185].

The r_R driven low temperature MIT is accompanied by a magnetic transition from a paramagnetic metal to an antiferromagnetic AIAO insulator (see figure 1.18). Iridates also show MIT on applying pressure [186–188] and an external magnetic field [189] showing unusually resistive ground states. As shown in figure 6.1, with applying pressure the resistivity decreases significantly. Similarly, with increasing field strength, the resistivity is strongly suppressed (see figure 6.2) giving rise to a

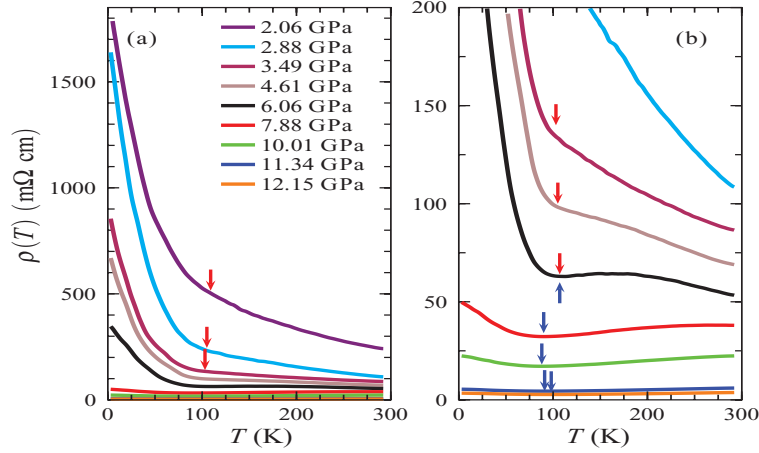


Figure 6.1: (Taken from [187]) Temperature dependence of resistivity under application of pressure in $\text{Eu}_2\text{Ir}_2\text{O}_7$. With increasing the pressure, the insulator become a metal by undergoing a metal-insulator transition.

large magnetoresistance. This field driven metallisation is possibly due to a change in the underlying magnetic behaviour with the application of the external magnetic field. There are reports of spin chirality driven anomalous Hall effect (AHE) in $\text{Pr}_2\text{Ir}_2\text{O}_7$ [182, 190].

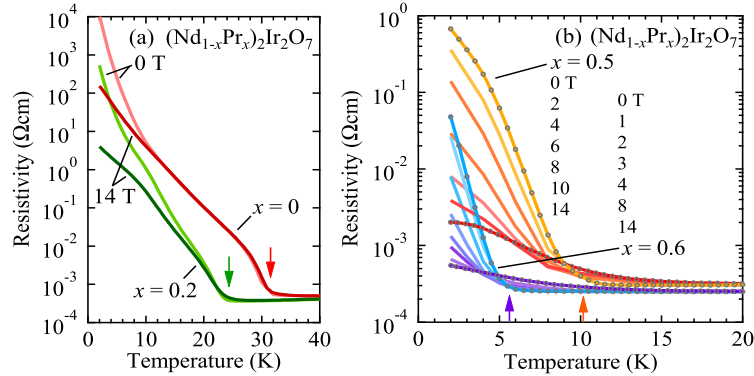


Figure 6.2: (Taken from [189]) Variation of resistivity as a function of temperature under the application of an external magnetic field. By increasing the field strength, the insulator begins to metallise.

Theory: The iridates have been studied theoretically using various tools:

- An *ab initio* calculation using a combination of local density approximation (LDA) and Hubbard U predicted the existence of a Weyl semimetal and an antiferromagnetic AIAO phase [191] (see figure 6.3).
- Model studies of the single band Hubbard model with spin-orbit coupling (SOC) reveal the following (see figure 1.20): (i) In the absence of U the ground

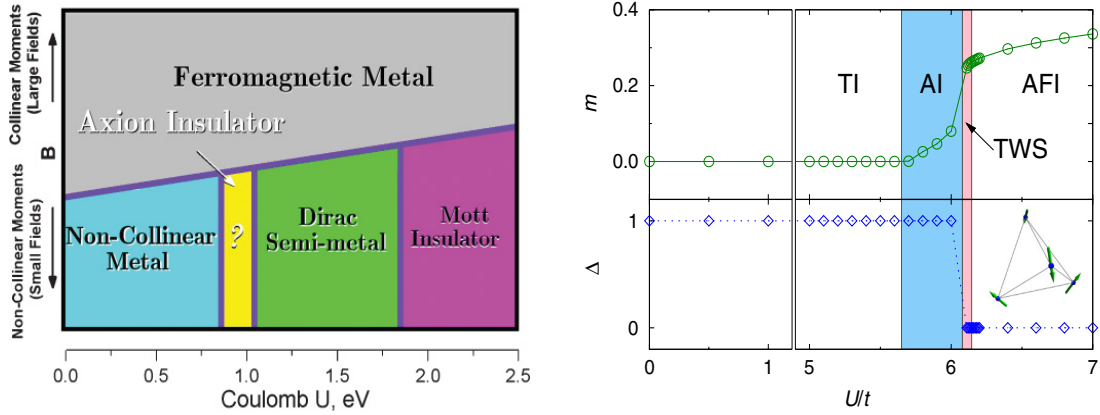


Figure 6.3: (Obtained from [191] and [116]) (Left) Sketch of the predicted phase diagram for pyrochlore iridates based on a first principle ‘LDA+U’ study [191]. (Right) Phase diagram based on the variation of magnetization (m) and topological index (Δ) with U [116]. An interaction-driven topological transition accompanies an abrupt change in m . At intermediate U , a topologically nontrivial insulator with a finite m indicates an axion insulator (AI). As U increases, a topological Weyl semimetal appears after the magnetisation jump. At large U , the system is a topologically trivial AIAO insulator.

state is a semimetal or topological insulator depending on the ratio of spin-orbit coupling and hopping amplitude [114], the picture remaining unchanged for weak U . (ii) For strong interactions, the system becomes an AIAO magnetic insulator [114]. Hartree-Fock mean-field theory (MFT) shows that a topological Weyl semimetal (TWS) phase shows up [115] near the magnetic transition.

- A cluster dynamical mean-field theory (CDMFT) calculation confirms the scenario above, and in addition finds an axion-insulator phase near the MIT point [116] (see figure 6.3).
- A more elaborate LDA+CDMFT study shows a first order MIT from a paramagnetic metal to an antiferromagnetic AIAO ordered insulating phase by taking into consideration a three-band description of the iridates [117] (see figure 1.20).

Despite the progress achieved, some issues remain unresolved.

- The AIAO phase is obtained by neglecting all other ordering (or disordered) possibilities. For a frustrated lattice one should try an unconstrained optimisation without biasing towards any order.
- An estimate of the T_N for the AIAO phase within Hartree-Fock theory yields a

scale that increases with increasing U/t . In reality T_N increases with reducing r_R , reaches a maximum for $R = Y$ and then falls on further reducing r_R . This non monotonicity is not captured by Hartree-Fock theory.

- LDA+CDMFT captures the correct qualitative feature but the neglect of spatial fluctuations leads to a T_N that is ~ 3 -times the experimental value.

A better theory would be (i) unbiased in the magnetic optimisation, (ii) work all the way from weak to strong coupling, and (iii) retain the crucial low energy modes in the problem. In order to address these issues we study the single band Hubbard model with SOC, at half filling, on a pyrochlore lattice using the real space SPA based Monte Carlo. We present results on the phase diagram, detailed magnetic correlations, and the single particle and optical spectral features.

6.2 Model for the iridates

In the iridate $R_2Ir_2O_7$ the R (rare-earth or Y) and Ir ions live on two interpenetrating pyrochlore lattices. The physics is mainly dictated by the 5d electrons of Ir, which have strong spin-orbit coupling and moderate Hubbard repulsion (due to the large spatial extent of the 5d orbitals). The Ir atom has octahedral oxygen coordination (IrO_6), and the resulting crystal field splits the fivefold degenerate Ir 5d states into doubly degenerate e_g and triply degenerate t_{2g} manifolds (see figure 6.4). As a result, the $L = 2$ orbital angular momentum of the d orbitals is projected down to an effective angular momentum $l = 1$ (with a minus sign) in the t_{2g} manifold. SOC splits the t_{2g} orbitals with spin into a $j = 1/2$ doublet and $j = 3/2$ quadruplet.

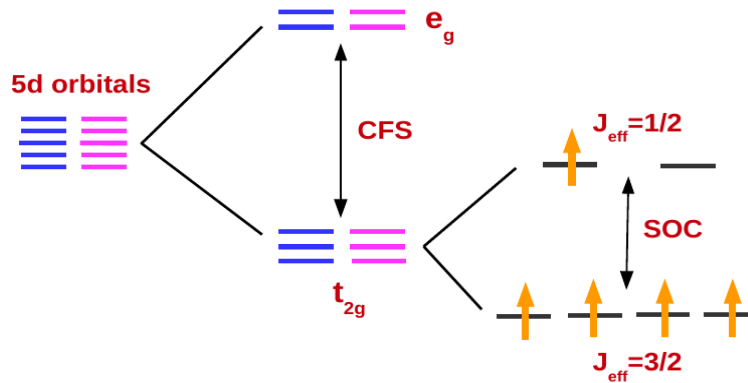


Figure 6.4: 5d level splitting in the pyrochlore iridates. CFS refers to the crystal field splitting due to octahedral oxygen coordination (see text for details).

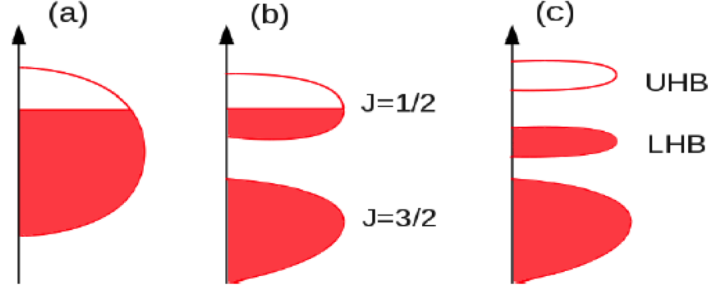


Figure 6.5: (Taken from [192]) Schematics of the Mott transition in the iridates. In the absence of SOC and U , the system would behave as a metal, as represented in (a). SOC leads to a band splitting, but still a metallic system, as represented in (b). The presence of moderate Hubbard U in addition to the SOC could lead to a Mott insulating state, represented in (c).

Strong SOC, thus, not only lifts the orbital degeneracy of 5d electrons, but also reduces the bandwidth.

The SOC leads to an effective single band description in terms of pseudo-spin $j_{eff} = 1/2$ states. These states are given by

$$\begin{aligned}
 |J_{eff} = 1/2, +1/2\rangle &= \frac{1}{\sqrt{3}}(|xy, \uparrow\rangle + |yz, \downarrow\rangle + i|zx, \downarrow\rangle) \\
 |J_{eff} = 1/2, -1/2\rangle &= \frac{1}{\sqrt{3}}(|xy, \downarrow\rangle - |yz, \uparrow\rangle - i|zx, \uparrow\rangle)
 \end{aligned}$$

Fig.6.5 demonstrates how the effect of SOC and electron-electron interaction results in the Mott-insulating state in the iridates. Thus, it is expected that by tuning SOC and electron-electron interaction (Hubbard U) the Mott transition physics can be understood in the pyrochlore iridate family.

We study the single band Hubbard model, in the $J_{eff} = 1/2$ pseudospin space, with nearest neighbour hopping, on the pyrochlore lattice:

$$\begin{aligned}
 H &= H_0 + U \sum_i n_{i\uparrow} n_{i\downarrow} - \mu \sum_i n_i \\
 H_0 &= \sum_{ij, \sigma} t_{ij} c_{i\sigma}^\dagger c_{j\sigma} - \lambda \sum_{\langle ij \rangle \sigma \sigma'} c_{i\sigma}^\dagger i \mathbf{d}_{ij} \cdot \vec{\sigma} c_{j\sigma'}
 \end{aligned}$$

Here, $U > 0$ is the Hubbard repulsion and λ is the SOC. The chemical potential μ is varied to maintain the density at $n = 1$ as the interaction and temperature T are varied. The $t_{ij} = -t$ for nearest neighbour hopping on the pyrochlore lattice and we

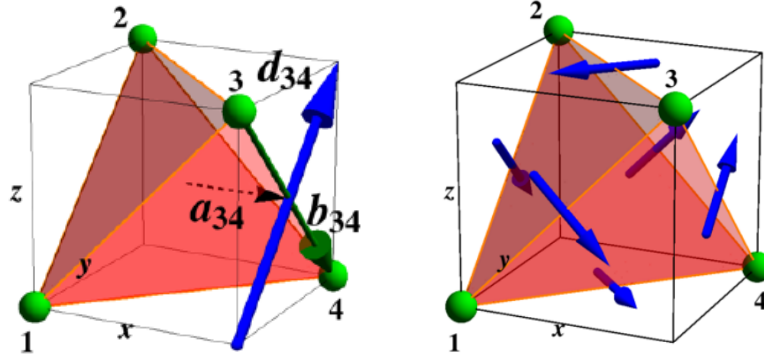


Figure 6.6: (Taken from [114, 115]) Calculation of the nearest-neighbour Dzyaloshinski-Moriya vectors on the pyrochlore lattice.

will set $t = 1$. The vectors \mathbf{d}_{ij} are parallel to the nearest neighbour Dzyaloshinski-Moriya (DM) vectors on the pyrochlore lattice. We calculate them as $\mathbf{d}_{ij} = 2\mathbf{a}_{ij} \times \mathbf{b}_{ij}$ where $\mathbf{a}_{ij} = \frac{1}{2}(\mathbf{b}_i + \mathbf{b}_j) - \mathbf{x}_c$ and $\mathbf{b}_{ij} = \mathbf{b}_j - \mathbf{b}_i$ with $\mathbf{b}_1 = (0, 0, 0)$, $\mathbf{b}_2 = (0, 1, 1)$, $\mathbf{b}_3 = (1, 0, 1)$, $\mathbf{b}_4 = (1, 1, 0)$ and $\mathbf{x}_c = \frac{1}{2}(1, 1, 1)$.

6.2.1 Method

We use a Hubbard-Stratonovich (HS) transformation [14] that introduces a three dimensional vector field $\mathbf{m}_i(\tau)$ and a scalar field $\phi_i(\tau)$ at each site to decouple the interaction. Following the static path approximation (SPA), described in chapter 2, we have,

$$H_{eff}\{\mathbf{m}_i\} = -\frac{1}{\beta} \log \text{Tr} e^{-\beta H_{el}} + \frac{U}{4} \sum_i \mathbf{m}_i^2$$

$$H_{el} = H_0 - \tilde{\mu} \sum_i n_i - \frac{U}{2} \sum_i \mathbf{m}_i \cdot \vec{\sigma}_i$$

where $\tilde{\mu} = \mu - \frac{U}{2}$. H_{eff} can be seen as comprising of an electronic Hamiltonian, H_{el} and the classical ‘stiffness’ $H_{cl} = \frac{U}{4} \sum_i \mathbf{m}_i^2$. Within this approach the problem is mapped on to electrons coupled to the field \mathbf{m}_i , which itself follows a distribution function $P\{\mathbf{m}_i\}$.

$$P\{\mathbf{m}_i\} \propto \text{Tr}_{cc^\dagger} e^{-\beta H_{eff}} \quad (6.1)$$

Within SPA, H_{eff} and $P\{\mathbf{m}_i\}$ define a coupled fermion-local moment problem. We obtain a solution of this model numerically via a Monte Carlo by generating the

equilibrium configuration for the $\{\mathbf{m}_i\}$ through iterative diagonalisation of H_{el} . We begin the Monte Carlo with reasonable high temperature, $T \sim t$, higher than any transition temperature in the problem, and reduce it in discrete steps to reach $T \sim 0$, thereby accessing the ground state properties. Results of this study are conducted for pyrochlore lattices of size $6^3 \times 4$ atoms and using a cluster with $3^3 \times 4$ atoms.

6.2.2 Observables

Electronic properties are calculated by diagonalising H_{el} on the full lattice for equilibrium $\{\mathbf{m}_i\}$ configurations. From the equilibrium configurations obtained at the end of Monte Carlo annealing, we calculate the following averaged quantities (angular brackets represent thermal average over 100 Monte Carlo configurations): (i) Magnetic structure factor:

$$S(\mathbf{q}) = \frac{1}{N^2} \sum_{ij} \langle \mathbf{m}_i \cdot \mathbf{m}_j \rangle e^{i\mathbf{q} \cdot (\mathbf{r}_i - \mathbf{r}_j)}$$

(ii) The size distribution of the moment is computed as

$$P(m) = \frac{1}{N} \sum_i \langle \delta(m - |\mathbf{m}_i|) \rangle$$

(iii) The optical conductivity is:

$$\sigma_{xx}(\omega) = \frac{\sigma_0}{N} \left\langle \sum_{n,m} \frac{f(\epsilon_n) - f(\epsilon_m)}{\epsilon_m - \epsilon_n} |J_x^{nm}|^2 \delta(\omega - E_{mn}) \right\rangle$$

where J_x^{nm} is $\langle n | J_x | m \rangle$ and the current operator is given by

$$J_x = -i \sum_{i,\sigma\sigma'} \left[(t_{i,i+\hat{x}}^{\sigma\sigma'} c_{i,\sigma}^\dagger c_{i+\hat{x},\sigma'} - \text{hc}) \right]$$

$E_{mn} = \epsilon_m - \epsilon_n$, $f(\epsilon_n)$ is the Fermi function, ϵ_n and $|n\rangle$ are the single particle eigenvalues and eigenstates of H_{el} respectively. The conductivity is in units of $\sigma_0 = e^2/(\hbar a_0)$, where a_0 is the lattice constant. (iv) The d.c. conductivity is obtained as a low frequency average of the optical conductivity over a window $\Omega = 0.05t$.

$$\sigma_{dc} = \frac{1}{\Omega} \int_0^\Omega d\omega \sigma_{xx}(\omega)$$

and the resistivity $\rho = 1/\sigma_{dc}$.

6.3 Model Hamiltonian study

6.3.1 Ground state results

In the absence of electron-electron interaction, H_0 corresponds to a generic time-reversal invariant hopping hamiltonian with a single Kramer's doublet at each site of the pyrochlore lattice. In this limit H_0 can be diagonalised in momentum space, yielding:

$$H_0 = \sum_{a,b,\vec{k}} c_{a\vec{k}}^\dagger H_{ab}(\vec{k}) c_{b\vec{k}}$$

$$H_{ab}(\vec{k}) = -2(t + i\lambda \vec{d}_{ab} \cdot \vec{\sigma}) \cos(\vec{k} \cdot \vec{b}_{ab})$$

The indices a,b are the sublattice indices of the pyrochlore tetrahedron. At the Γ point, the eigenspectrum has a 2-4-2 degeneracy with $\epsilon_1 = -2t - 8\lambda$ (degeneracy=2), $\epsilon_2 = -2t + 4\lambda$ (degeneracy=4), and $\epsilon_3 = 6t$ (degeneracy=2). At half-filling only 4 levels get filled in the tetrahedron. In the regime $-2 \leq \lambda/t \leq 0$, it can be seen that there are states available at the Fermi-energy for half-filling. Outside this regime the Fermi-energy lies in the gap for half-filling.

Further detailed calculation of band-structure and topological index [193] shows that the variation of SOC (λ/t) leads to a phase transition from a semi-metal to a strong topological insulator (STI), as shown in Fig.6.7.

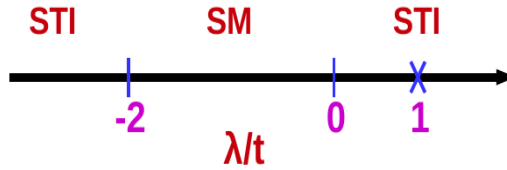


Figure 6.7: Phase diagram of the tight binding model (appropriate for the iridates) in the non-interacting limit. By tuning λ/t we see a phase transition between a semi-metal (SM) and a strong topological insulator (STI). The $\lambda = t$ point corresponds to gap closing in the spectrum.

In the presence of interaction, the ground state phase diagram shows semimetal, metal and Mott insulating phases. In Fig.6.8, we plot the average spin-orbital moment value m_{avg} and the gap (Δ/t) in the spectrum, to identify these phases.

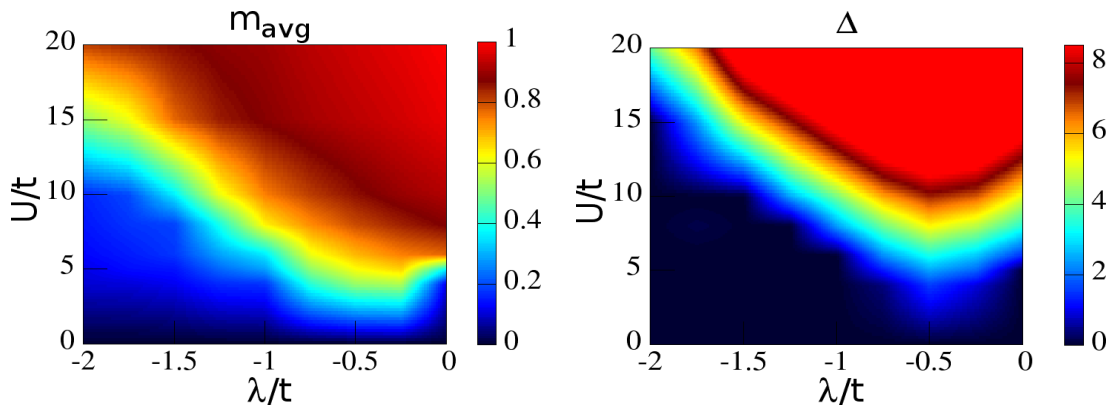


Figure 6.8: Behaviour of m_{avg} (left) and Δ/t (right) for varying U/t and λ/t .

6.3.2 Finite temperature

6.3.2.1 Thermal phase diagram

For our study, we choose $\lambda = -1.5t$ as suggested by a density functional theory calculation [196]. Fig.6.9 shows the $U - T$ phase diagram in terms of the magnetic, transport, and spectral properties we have observed.

The following features emerge: The ground state is a tight-binding semi-metal for $U < 9t$, a paramagnetic metal for $9t < U < U_c \sim 10.5t$, and an insulating all-in-all-out (AIAO) ordered state for $U \geq U_c$. With increasing temperature, we observe a transition from the AIAO ordered phase to the paramagnetic phase at a critical temperature T_c . This T_c increase with U/t , reaches a maximum at $U \sim 14t$, and then decreases again on further increasing U/t .

At finite T , thermal fluctuations of local moments on the weak-coupling side ($U < U_c$) gives rise to finite density of states (DOS) and a metallic phase. On the strong-coupling side ($U > U_c$) the angular fluctuations of the local moments result in a slight reduction of the Mott-gap with temperature. In the vicinity of the Mott-transition the Mott gap quickly converts to a PG with increasing T , leading to the widening of the PG region shown in Fig.6.9. We demarcate the finite T metal-insulator boundary in terms of the temperature derivative $d\rho/dT$. A state is metallic if $d\rho/dT > 0$ and insulating if $d\rho/dT < 0$. The detailed spectral features and resistivity are discussed later.

We can broadly classify our phase diagram into following three different regimes: $U < U_c$, $U > U_c$, and $U \sim U_c$. In the following, we show the magnetic, spectral, and transport behaviour of our study in these three regimes.

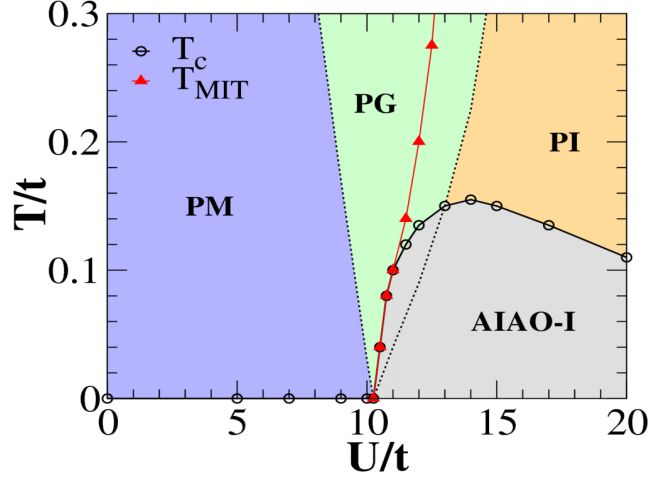


Figure 6.9: Phase diagram for varying U/t and T/t . $\lambda = -1.5t$. The ground state is a semi-metal for $U < 5t$, and becomes a metal at finite temperature due to the emergence of thermally generated weak, random moments. At low temperature we obtain a paramagnetic metal (PM) and an insulator with ‘all-in-all-out’ order (AIAO-I) for $U \geq U_c$. With increase in temperature we see a transition from the AIAO-I to a paramagnetic insulator (PI). PG refers to a pseudogap state. The metal-insulator transition line separates regions with opposite signs of $d\rho/dT$.

6.3.2.2 Magnetic order

Fig.6.10 shows the \mathbf{q} dependence of the magnetic structure factor at different T values, for the representative interaction regimes of our phase diagram. (i) The top panel refers to $U = 9t$ (generic for $U < U_c$, regime-I of our model). We observe that at $T = 0$, $S(\mathbf{q})$ has no ordering peak at any \mathbf{q} 's. The magnetic ground state is disordered in this regime due to the frustrated pyrochlore lattice structure. With increasing temperature the disordered phase shows a crossover to a fully random paramagnetic phase. (ii) The middle panel refers to $U = 11t$ (generic for $U \sim U_c$, regime-II of our model). We see that at $T = 0$, $S(\mathbf{q})$ has dominant weight at $\mathbf{q} = (\pi, \pi, 0)$, $(\pi, 0, \pi)$ and $(0, \pi, \pi)$. The orientation of the moments in the pyrochlore tetrahedral geometry in real space shows this ordering to be the all-in-all-out ordering on the pyrochlore lattice. With increasing T we see $S(\mathbf{q})$ showing no ordering peak at any \mathbf{q} 's for $T \geq 0.1t$. This can be understood as the magnetic transition to a paramagnetic phase. (iii) The lower panel refers to $U = 15t$ (generic for $U \geq U_c$, regime-III of our model). We see that at $T = 0$, $S(\mathbf{q})$ has dominant weight at $\mathbf{q} = (\pi, \pi, 0)$, $(\pi, 0, \pi)$ and $(0, \pi, \pi)$. corresponding to the all-in-all-out order on the pyrochlore lattice. With increasing T we see the $S(\mathbf{q})$ at these wavevectors reducing and for $T \sim 0.2t$ the AIAO transits to a paramagnet.

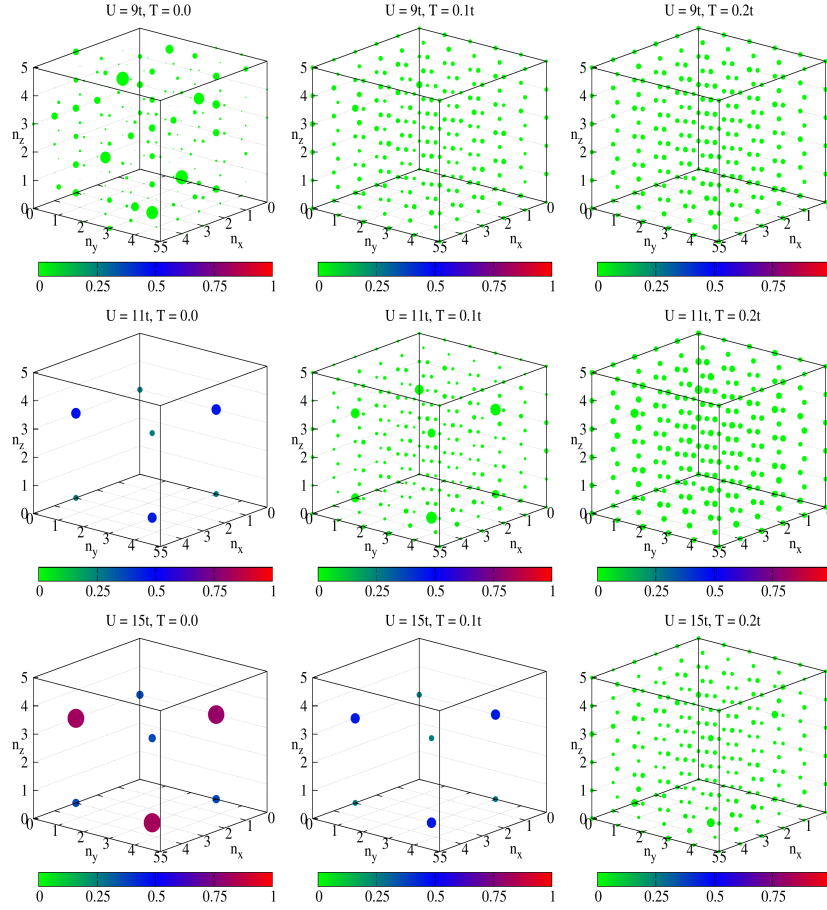


Figure 6.10: The full ‘magnetic’ structure factor $S(\mathbf{q})$ for $U = 9t, 11t,$ and $15t$ (along column) and $T = 0, 0.1t, 0.2t$ (along row). $\lambda = -1.5t$. We use the notation $\mathbf{q} = \frac{2\pi}{L}(n_x, n_y, n_z)$, n ’s are integers. The size of a dot signifies relative weight at a given \mathbf{q} while its colour represents the actual magnitude of $S(\mathbf{q})$.

For a detailed understanding of the thermal magnetic phase transition, we look into the T dependence of the structure factor peak at $\mathbf{q} = (\pi, \pi, 0), (\pi, 0, \pi)$ and $(0, \pi, \pi)$. Fig.6.11(a) shows this behaviour for $\mathbf{q} = (\pi, \pi, 0)$. We can see that $S(\mathbf{q})$ shows a rapid growth with decreasing temperature for $U \geq U_c$ indicating the onset of the AIAO magnetic order. It is important to note that the thermal transition is *discontinuous (first order)* for $U_c \leq U < 12.5t$, whereas it is *continuous (second order)* for $U \geq 12.5t$.

6.3.2.3 Local moment distribution

Fig.6.11(b) shows m_{avg} for varying U/t and T/t in our calculation. At $T = 0$, as $U/t \rightarrow \infty$, $m_{avg} \rightarrow 1$, as one expects in the atomic limit. m_{avg} reduces with

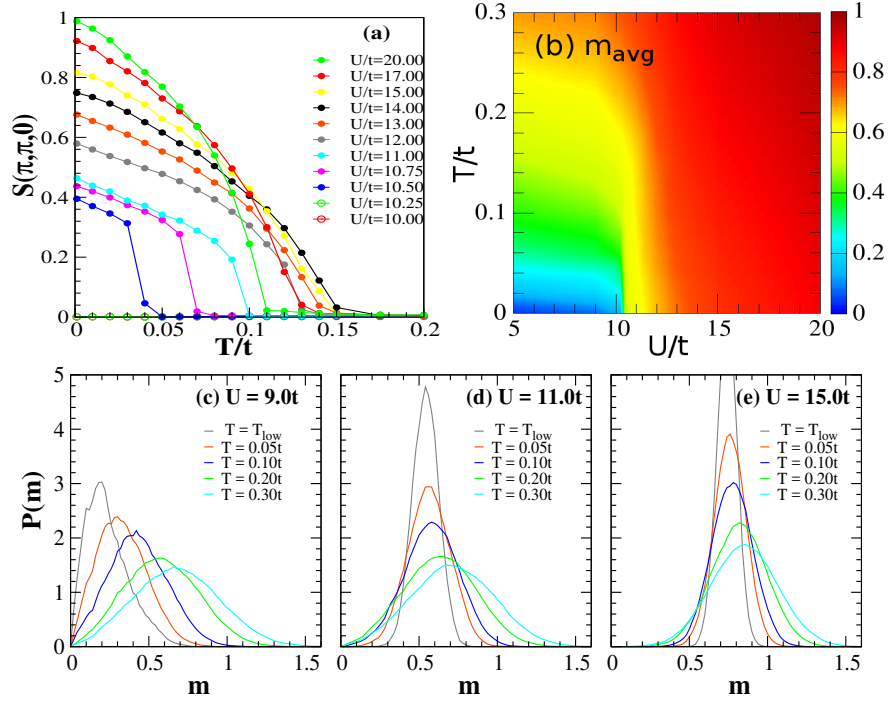


Figure 6.11: $\lambda = -1.5t$. (a) Variation of the structure factor peak at $\mathbf{q} = (\pi, \pi, 0)$ with U/t and temperature. (b) Behaviour of m_{avg} in the U/t and T/t plane. (c)-(e) Temperature dependence of $P(m)$ for $U = 9t$, $11t$ and $15t$.

decreasing U/t such that $m_{avg} \rightarrow 0$ as $U \ll U_c$. For $T/t > 0$, thermal fluctuations lead to quick growth of m_{avg} in the metallic side, whereas m_{avg} increase slowly in the Mott insulating side.

Fig.6.11(c)-(e) show the $P(m)$ for different temperature and interaction values of our study. Panel (c) shows $P(m)$ for $U = 9t$. $P(m)$ shows a single narrow peak structure, highlighting an amplitude homogeneous state. With rise in temperature, the single peak feature of $P(m)$ retained. However, the narrow peak becomes broad and the peak position shifts towards large m values. Panel (d) and (e) show $P(m)$ for $U = 11t$ and $15t$. We observe similar behaviour as in panel (c), but with important difference that the peaks are more narrower with increasing U/t values. This happens because fluctuations of m_{avg} about the mean are weaker in the insulating regime than in the metallic regime.

6.3.2.4 Transport and optics

Fig.6.12 shows the d.c. resistivity $\rho(T)$ for different U/t . Following are the noteworthy features. (i) For $U < U_c$, the residual resistivity $\rho(0)$ is finite with $d\rho/dT > 0$ over

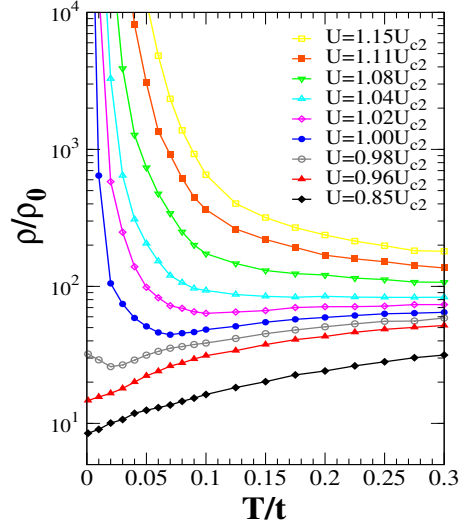


Figure 6.12: Temperature dependence of the resistivity for different U/t values near the Mott transition. The normalising scale is $\rho_0 = (\hbar a_0)/e^2$.

the entire T range. This resistivity can be understood in terms of the scattering of electrons from the background small disordered local moments. This is the metallic regime. (ii) For $U \gg U_c$ the system has a clear Mott gap at $T = 0$ with $\rho(0) \rightarrow \infty$. In this regime $d\rho/dT < 0$ over the entire temperature window we have explored. This is the Mott-insulating regime. (iii) In the regime $U \geq U_c$, but $|U - U_c| \ll U_c$, we have $\rho(T)$ showing non-monotonic behaviour. We observe $d\rho/dT > 0$ in the high temperature limit, crossing over to $d\rho/dT < 0$ with decreasing T . The temperature at which $d\rho/dT$ changes its sign is indicated as T_{MIT} in our phase diagram 6.9.

Fig.6.13(a)-(c) show the optical conductivity from our calculation as we cross the Mott transition. The relevant features are: (i) $\sigma(\omega)$ at $T = 0$ for $U < U_c$ shows finite Drude weight, but with a peak at finite frequency. With increasing temperature, the peak location shifts slowly to higher frequency (see Fig.6.13(a)). (ii) For $U \gg U_c$ the system has a clear optical gap $\Delta(T)$ such that $\sigma(\omega) = 0$ for $\omega < \omega_c \sim \Delta(T)$. With increasing temperature the gap $\Delta(T)$ reduces, resulting in small, but increasing low frequency weight of $\sigma(\omega)$ and the $\sigma(\omega)$ peak position shifts to higher frequency (see Fig.6.13(c)). (iii) For $U \sim U_c$, $\sigma(\omega)$ shows no Drude weight at $T = 0$. With increasing T , there is quick increase of Drude weight initially, which then reduces gradually, and the $\sigma(\omega)$ peak slowly moving to higher frequency (see Fig.6.13(b)).

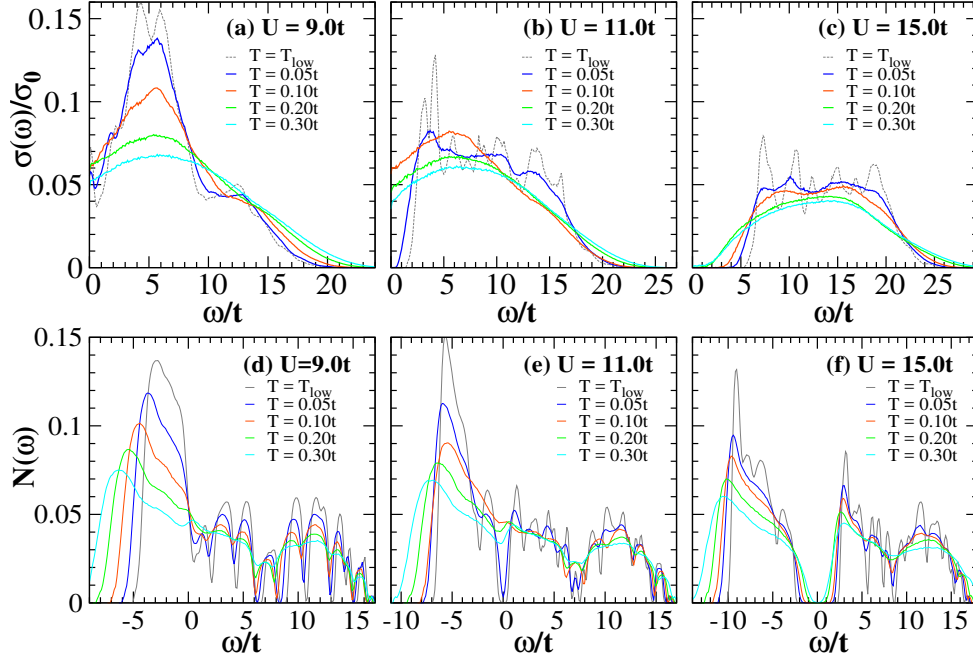


Figure 6.13: (a)-(c) Optical conductivity for $U = 9t$, $11t$ and $15t$ for indicated temperatures. (d)-(f) Behaviour of DOS at different temperatures for $U = 9t$, $11t$ and $15t$.

6.3.2.5 Density of states

Fig.6.13(d)-(f) show the thermal evolution of density of states (DOS) at different interaction regimes of our study. We observe following features – (i) For $U < U_c$ the ground state has small local moments. The DOS is gapless and the weight at the Fermi level decreases monotonically with increasing T (see Fig.6.13(d)). (ii) For $U \geq U_c$ the ground state has a finite gap in the DOS. With increase in temperature, the angular fluctuations of the local moments result in a slight reduction of the Mott-gap, and an increase in the low energy DOS as can be seen in Fig.6.13(f). The Mott-gap survives till very high temperature, $T \sim m_{avg}U$. (iii) In the neighbourhood of MIT boundary, for $U \sim U_c$, the DOS shows a sharp dip, a characteristic of a pseudogap (PG) phase. This dip fills up quickly with increasing T , but deepens further with increasing temperature (see Fig.6.13(e)).

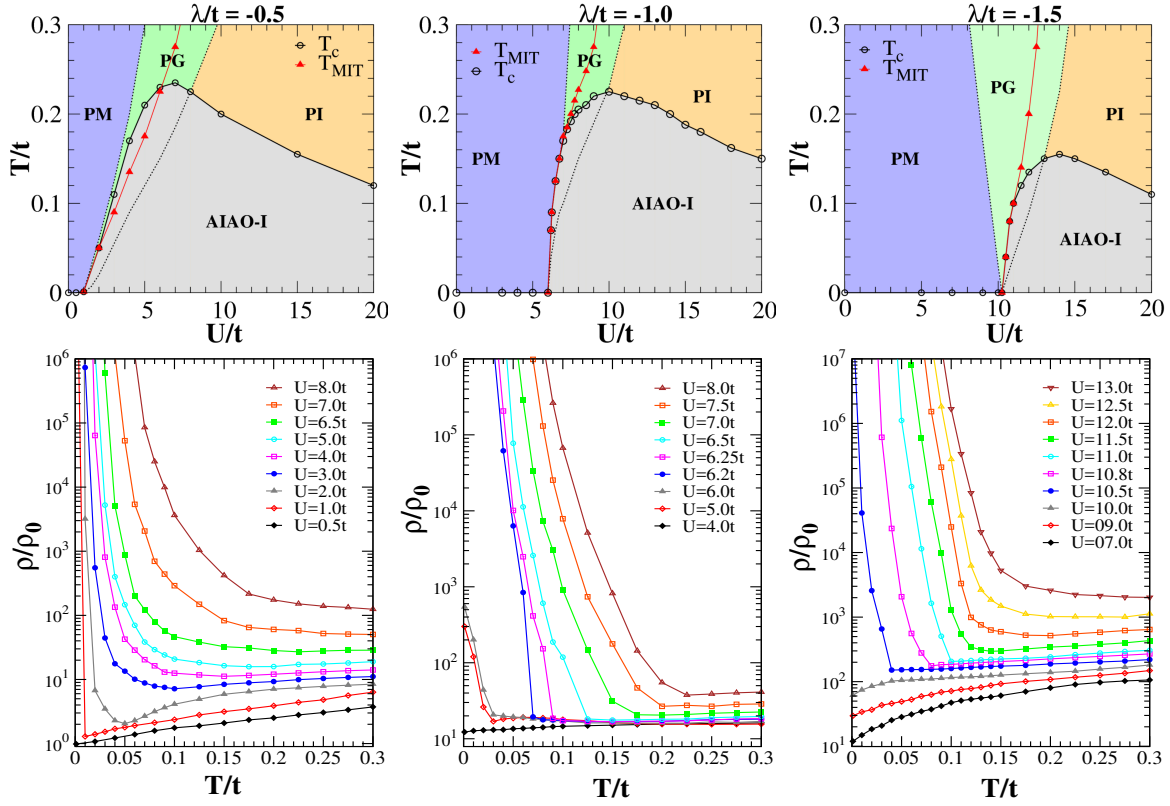


Figure 6.14: The effect of SOC on the phase diagram and transport properties. With increasing SOC, the U_c increases, resulting in a wider metallic window. However, the maximum T_c scale of the AIAO phase decreases with increasing SOC.

6.3.3 Discussion

6.3.3.1 Effective magnetic model

The origin of the AIAO magnetic ordering can be understood by working out the effective magnetic Hamiltonian by tracing out the fermions deep in the strong coupling limit (see appendix A). In the limit $U \gg \lambda, t$, we have:

$$H_{eff}\{\mathbf{m}\} = \sum_{ij} [J(\mathbf{m}_i \cdot \mathbf{m}_j - 1) + \mathbf{D}_{ij} \cdot (\mathbf{m}_i \times \mathbf{m}_j) + m_i^\alpha \Gamma_{ij}^{\alpha\beta} m_j^\beta] \quad (6.2)$$

where, $J = \frac{t^2 + 2\lambda^2}{U}$, $\vec{D}_{ij} = \frac{2\lambda t}{U} \vec{d}_{ij}$, and $\Gamma_{ij}^{\alpha\beta} = \frac{2\lambda^2}{U} (d_{ij}^\alpha d_{ij}^\beta - \delta^{\alpha\beta} |d_{ij}^\alpha|^2)$. It has been shown [194] for $\lambda/t < 0$, $\vec{D}_{ij} \propto \vec{d}_{ji}$, leading to a direct DM interaction and the AIAO magnetic ordering. It is this DM interaction which is responsible for selecting out the AIAO state from the infinitely degenerate pyrochlore Heisenberg ground state manifold.

6.3.4 Conclusion

Based on our study of the Hubbard model with SOC on the pyrochlore lattice, we conclude that (i) The low temperature state is a paramagnetic metal at weak interaction, but a Mott insulator with all-in-all-out order at intermediate and strong interaction. (ii) There is a narrow pseudogap window near the insulator-metal boundary. (iii) The resistivity and low energy density of states show non monotonic temperature dependence near the MIT. The pyrochlore lattice in the absence of SOC, doesn't show any magnetic order, as described in detail in chapter 3. With inclusion of SOC, we find that U_c reduces as $\lambda \sim 0.5t$, and giving rise to an AIAO ordered phase. Further increasing the SOC increases the U_c .

6.4 Comparing to iridate experiments

The real iridates are a complex material. The hybridization between the $j_{eff} = 1/2$ and the $j_{eff} = 3/2$ manifolds is not negligible, thus requiring a multiband model. Also next nearest neighbour hoppings may be relevant. The low temperature magnetic behaviour could depend on the magnetic character of the rare-earth atom. However, as a starting approximation, we attempted a comparison of our single band study with experimental results.

For the iridates the typical t_{2g} band width in the LDA band structure is ~ 2 eV [195] and the typical values of U for Ir^{4+} is ~ 2.7 eV [196]. With the choice of NN hopping scale, $t \sim 0.25$ eV [196], and for the choice of SOC $\lambda \sim 0.375$ eV, we have $U_c \sim 2.65$ eV in close agreement with a previous study [117]. Within our calculation, the maximum of $T_c \sim 375$ K corresponds to $U \sim 3.5$ eV. We have explored the physics of this model for other SOC values. Our results suggest increasing the SOC parameter would lead to an increase of U_c , but would suppress the maximum T_c further.

However, if we take into account only the $j_{eff} = 1/2$ bandwidth ~ 1 eV (appropriate for our study), then we have a reasonable choice of $t \sim 0.125$ eV [117]. As a results, our max $T_c \sim 200$ K, pretty close to the real iridates, and also a great improvement compared to the CDMFT study. Below we discuss our results for the chosen $t = 125$ meV, $\lambda = -1.5t$, and U/t , using absolute scales, and compare with available experimental data [9, 105].

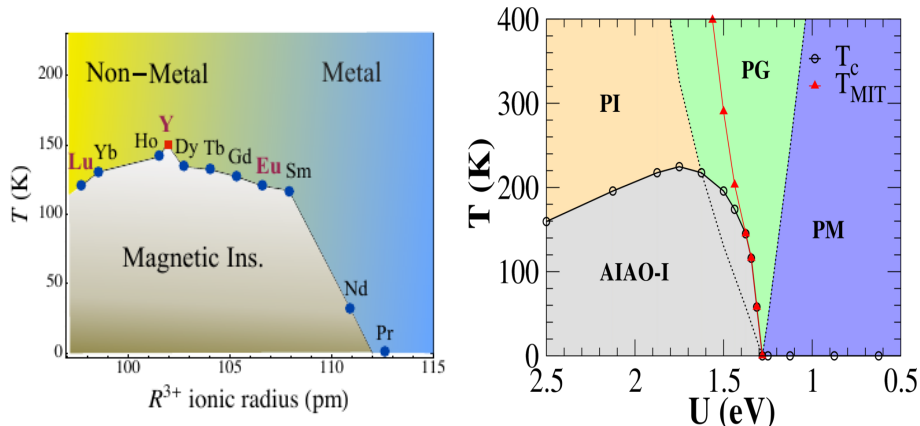


Figure 6.15: Comparison of the phase diagrams between experiment [105] (left) and our results (right). Similarities: Both phase diagrams show a Mott insulating phase with long-range antiferromagnetic order and a paramagnetic metallic phase. The magnetic transition coincides with the MIT. Near the MIT boundary, the insulating phase becomes a metal with increased temperature, by losing magnetic order. In the Mott insulating regime, the critical temperature, T_c , of the antiferromagnetic order initially increases with interaction scale (or decreasing ionic radius in the experiment), reaches a maximum and then decreases with further increasing with interaction scale (or decreasing ionic radius in the experiment). Differences: The maximum T_c scale observed in the experiments is ≈ 150 K, whereas our theory shows a maximum T_c scale to be ≈ 225 K. A change by a small fraction in the ionic radius describes the various iridate phases in the experiment. However, to obtain these phases, we require a large fractional change in the coulomb interaction in our theory study.

Phase diagram: Fig.6.15.(a) shows the experimental phase diagram. At large r_R (R^{3+} ionic radius), the ground state is a paramagnetic metal. With reducing r_R the system undergoes a magnetic transition, to an antiferromagnetic all-in-all-out (AIAO) phase, (confirmed via other experimental measurements). The AIAO ordered phase shows an insulating behaviour. Thus the magnetic transition coincides with the metal-insulator transition. Also as shown in the figure, the antiferromagnetic transition temperature first increases with reducing r_R , reaches a maximum ($T_N^{max} \approx 150$ K) for $R = Y$ ($r_R \approx 102$ pm), and then decreases with further reducing the r_R .

A careful comparison of experiment with theory requires calibration of U/t and λ/t in terms of r_R . Though this is a task we would pursue in future, here we assume an appropriate interaction regime and make an attempt to explain the behaviour of the iridate phase diagram. Panel 6.15.(b) shows our theory phase diagram over the window $U \sim 0.5 - 2.5$ eV. We believe this interaction range correctly describes

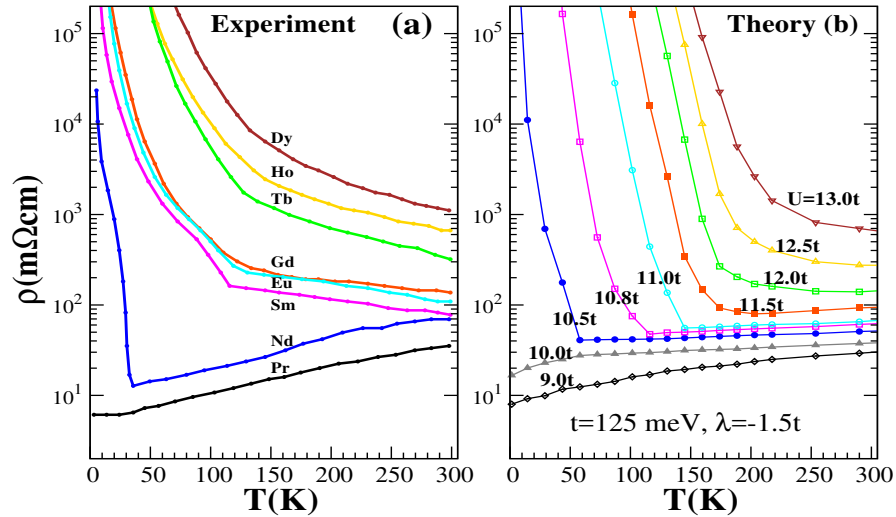


Figure 6.16: Comparison of the resistivity in the iridates. Left: experiment (taken from [9]), Right: theory.

the metal-insulator transition as observed in the iridates. Our calculation shows $U_c \approx 1.3 \text{ eV}$.

Temperature scales: Our structure factor calculations suggest the insulating state below the antiferromagnetic transition temperature is a long-ranged AIAO phase. It correctly captures the trend in the variation of the T_N with increasing U/t . The LDA+CDMFT study [117] has captured this physics correctly. However, due to ignoring the long-range spatial fluctuations, the maximum T_N scale it gives is roughly 3-times that of the experimentally observed maximum T_N values [105]. However, in our study, we retain the crucial low temperature thermal and spatial fluctuations. As a result, the maximum T_N scale ($T_N^{max} \approx 225 \text{ K}$) we obtain by following the SPA approach is roughly 1.5-times that of the experimentally observed maximum T_N values.

Resistivity: We demarcate the finite T metal-insulator boundary based on the temperature derivative of resistivity $d\rho/dT$: ‘metal’ if $d\rho/dT > 0$, ‘insulator’ if $d\rho/dT < 0$. We compute $\rho(T)$ via the low-energy limit of the optical conductivity. Fig.6.16.(a) shows experimental resistivity [9] while 6.16.(b) shows the theory results.

Experiments show that the rare-earth variation in the iridates represent following three ‘regimes’ (see Fig.6.16.(a)). (i) For $R=\text{Pr}$, $\rho(T)$ has traditional metallic behaviour, $\rho(0) < 1 \text{ m}\Omega\text{cm}$ and $d\rho/dT > 0$ all the way to 300K. (ii) For $R=\text{Sm, Eu, Gd, Tb, Ho, Dy}$, the system is insulating at all T , with $\rho(0) \rightarrow \infty$ as $T \rightarrow 0$. The behaviour is clearly activated for Tb, Ho and Dy, while Sm, Eu and Gd seems to be weakly insulating. In all these insulating samples, $d\rho/dT$ changes its

value (without changing sign) as temperature passes through $T = T_N$. (iii) R=Nd represents the most interesting case, with $d\rho/dT > 0$ for $T > T_N$ and $d\rho/dT < 0$ for $T < T_N$. This signals the finite temperature metal-insulator transition in the Nd iridate.

Any theory would have to capture the obvious regimes (i) and (ii) and also the non monotonic behaviour as in (iii). Our results, panel 6.16.(b), show the following behaviour: (i) For $U < U_c$, the itinerant $J_{eff} = 1/2$ electrons see a paramagnetic background, with small spin-orbital moments. The finite T resistivity arises due to the scattering from the thermal fluctuations of local spin-orbital moments, giving an approximate linear T behaviour. (ii) For $U \gg U_c$, the $J_{eff} = 1/2$ electrons see a long-range AIAO ordered background for $T < T_N$. This magnetic order leads to a distinct gap Δ in the spectrum, such that $\rho(T) \sim \rho_0 e^{\Delta/T}$ as $T \rightarrow 0$ and $d\rho/dT < 0$. Though magnetic order disappears for $T > T_N$, thermal fluctuations of the local spin-orbital moments are sizable in this regime. The scattering of electrons from these fluctuating moments manifest as $d\rho/dT < 0$ over the entire temperature range. (iii) For $U \gtrsim U_c$, the $T < T_N$ insulating behaviour is due to the long-range AIAO magnetic ordering. However, the $T > T_N$ metallic behaviour can be the result of a net increasing density of states at the Fermi level (arising from the competition between an increasing spin-orbital moment and randomness in the magnetic degrees of freedom).

Concluding Remarks

In this thesis, we address the interplay of electron correlation and geometric frustration in the context of the Mott transition in pyrochlore based lattices. We formulate the single band Hubbard model on these lattices in terms of electrons coupled to auxiliary local magnetic moments, and treat the resulting ‘fermion-spin’ problem through a real-space Monte Carlo technique. While the ground states we obtain are equivalent to unrestricted Hartree-Fock, the presence of the crucial low energy fluctuations in our approach, and their coupling to the electrons, allows us to establish the temperature dependence of transport and spectral features across the Mott transition.

We not only focus on model problems, but also on real life pyrochlore materials (the rare earth molybdates and iridates) by appropriately choosing the parameters of the theory. The main findings (chapter-wise) of the thesis are –

Chapter-3 of this thesis studies the Mott transition in the half-filled Hubbard model on a pyrochlore lattice. The geometric frustration and the corresponding large magnetic degeneracy prevents the occurrence of any magnetic order in the deep Mott state. This continues all the way to the insulator-metal transition. Beyond the insulator-metal transition there is a window with a pseudogap in the density of states, disordered local moments, and a large residual resistivity. At even weaker interaction one recovers the non magnetic band semimetal. Thermal fluctuations destroy the ‘spin liquid’ correlations in the insulating state, converting the system to an uncorrelated paramagnet. The low energy electronic density of states and the resistivity show a monotonic temperature dependence deep in the metallic and insulating phases, but a non monotonic character near the insulator-metal transition.

Chapter-4 of the thesis describes the single band Hubbard model at half-filling on the checkerboard lattice. The Hartree-Fock ground state is non magnetic upto an interaction strength U_{c1} , then a small moment spin glass upto U_{c2} , and a ‘flux’ ordered state beyond. The Mott transition, associated with a gap opening in the density of states, occurs at U_{c2} . The presence of order differentiates this lattice of corner shared ‘tetrahedra’ from its three dimensional counterpart, the pyrochlore lattice, which remains disordered at all interaction strengths. We observe that the flux order is replaced by a ‘120 degree’ correlated spin arrangement at intermediate temperature before all order is lost.

Chapter-5 of the thesis discusses the two orbital Hubbard model with the electrons additionally strongly coupled to a background local moment and the moments interacting antiferromagnetically amongst themselves. This Hubbard-double exchange-superexchange scenario, on the pyrochlore lattice, is the minimal model for the rare earth molybdates. We mapped out the ground state phase diagram via a simulated annealing based unrestricted Hartree-Fock calculation and established the metal-insulator and ferromagnet-spin liquid transition boundaries.

Chapter-6 of this thesis focuses on the model appropriate for the pyrochlore iridates. This model has spin-orbit coupling (SOC) as a crucial ingredient in addition to the electron correlation. Weak SOC lowers the U_c , thereby favouring the Mott state and gives rise to the all-in-all-out (AIAO) ordered phase; a moderate SOC increases the U_c , and reducing the T_c . Strong SOC results in large anisotropic interactions and may suppress the AIAO phase altogether.

Questions that need to be tackled in future work.

- What is the effect of quantum fluctuations on the underlying magnetic state at low temperatures on the pyrochlore lattice?
- A detailed analysis of the magnetic correlations on the pyrochlore lattice near the MIT is required.
- Detailed study of anomalous Hall effect, field-driven MIT etc. in the pyrochlore molybdates and iridates is highly desired.

APPENDIX **A**

EFFECTIVE SPIN MODELS VIA PERTURBATION EXPANSION

Here we describe how to obtain the effective spin hamiltonians by setting up a perturbation calculation at some limit of the coupled ‘spin-fermion’ problem.

As described in chapter 2, we have,

$$Z = \int \mathcal{D}\Gamma e^{-S_{eff}\{\Gamma\}}$$

$$S_{eff}\{\Gamma\} = \ln \text{Det}[\mathcal{G}^{-1}\{\Gamma\}] + \sum_i \int_0^\beta d\tau \frac{\Gamma_i^2(\tau)}{U}$$

where \mathcal{G} is the electron Green’s function in a $\{\Gamma\}$ background.

We can write,

$$\mathcal{G}^{-1}\{\Gamma\} \sim \partial_\tau + T - V$$

where $T = \sum_{ij}^{\alpha\beta} t_{ij}^{\alpha\beta} c_{i\alpha}^\dagger c_{j\beta}$ is the hopping term and $V = \sum_i \Gamma_i \cdot \sigma_i$ is the coupling term.

Rewriting $\Gamma_i(\tau)$ in terms of its Matsubara Fourier modes, $\Gamma_i(i\omega_n)$, we have

$$\{\Gamma\} S_{eff} = -Tr \ln[-i\omega_n + T - V] + \sum_{i,n} \frac{\Gamma_i(i\omega_n)\Gamma_i(-i\omega_n)}{U} \quad (\text{A.1})$$

A.1 Weak coupling

In this limit $U \ll t$. The hopping term is the reference point in this limit and the coupling term is treated as a perturbation. Going to the momentum space, we have

$$\begin{aligned} T &= \sum_k \epsilon_k c_k^\dagger c_k \\ V &= \sum_{k,k'} c_{k\alpha}^\dagger (\mathbf{\Gamma}_{k-k'} \cdot \sigma_{\alpha\beta}) c_{k'\beta} = V_{k,k'} \end{aligned}$$

We can write equation (A.1) as,

$$\begin{aligned} S_{eff}\{\mathbf{\Gamma}\} &= -Tr \ln[(-i\omega_n + \epsilon_k)\delta_{k,k'} - V_{k,k'}] + \sum_{k,n} \frac{|\mathbf{\Gamma}_k(i\omega_n)|^2}{U} \\ &= -Tr \ln[(-i\omega_n + \epsilon_k)(1 + (i\omega_n - \epsilon_k)^{-1}V_{k,k'})] + \sum_{k,n} \frac{|\mathbf{\Gamma}_k(i\omega_n)|^2}{U} \end{aligned}$$

The free fermion Green's function is $G_0(k) = (i\omega_n - \epsilon_k)^{-1}$. Thus we can write,

$$\begin{aligned} S_{eff}\{\mathbf{\Gamma}\} &= -Tr \ln[G_0^{-1}(k)(1 + G_0(k)V_{k,k'})] + \sum_{k,n} \frac{|\mathbf{\Gamma}_k(i\omega_n)|^2}{U} \\ &= -Tr \ln[G_0^{-1}(k)] - Tr \ln[1 + G_0(k)V_{k,k'}] + \sum_{k,n} \frac{|\mathbf{\Gamma}_k(i\omega_n)|^2}{U} \\ &= \mathcal{F}_0 + \Delta\mathcal{F} + \sum_{k,n} \frac{|\mathbf{\Gamma}_k(i\omega_n)|^2}{U} \end{aligned} \tag{A.2}$$

In equation (A.2), \mathcal{F}_0 represents the free energy of the non-interacting fermions and $\Delta\mathcal{F}$ is the change in the free energy of the fermions due to the background bosonic field $\{\mathbf{\Gamma}\}$. $\Delta\mathcal{F}$ can be further simplified as

$$\begin{aligned} \Delta\mathcal{F} &= -Tr \ln[1 + G_0V] \\ &= -Tr[-G_0V - \frac{1}{2}(G_0V)^2 - \frac{1}{3}(G_0V)^3 + \dots] \end{aligned} \tag{A.3}$$

Equation (A.3) can be understood as the change in the free energy of the fermions due to repeated scattering from the background $\{\mathbf{\Gamma}\}$ field. The total change in the free energy can be identified as $\Delta\mathcal{F} = \Delta\mathcal{F}^{(1)} + \Delta\mathcal{F}^{(2)} + \Delta\mathcal{F}^{(3)} + \dots$ where

$$\begin{aligned}
\Delta\mathcal{F}^{(1)} &= -Tr[-G_0V] \\
\Delta\mathcal{F}^{(2)} &= -Tr[-\frac{1}{2}(G_0V)^2] \\
\Delta\mathcal{F}^{(3)} &= -Tr[-\frac{1}{3}(G_0V)^3] \\
&\dots \\
\Delta\mathcal{F}^{(n)} &= -Tr[-\frac{1}{n}(G_0V)^n]
\end{aligned}$$

A.2 Strong coupling

In this limit $U \gg t$. The coupling term is the reference point in this limit and the hopping term is treated as a perturbation. We retain only the zero Matsubara mode of the $\{\mathbf{\Gamma}\}$ field. This leads a Hamiltonian formulation of the problem. The coupling term can be diagonalised in a local basis as

$$V = \Gamma \sum_i (\gamma_{i,\sigma}^\dagger \gamma_{i,\sigma} - \gamma_{i,-\sigma}^\dagger \gamma_{i,-\sigma})$$

In this basis, the hopping term can be rewritten as

$$T = \sum_{ij} \tilde{t}_{ij}^{\alpha\beta} \gamma_{i\alpha}^\dagger \gamma_{j\beta} = \tilde{T}_{ij}$$

We can write equation (A.1) as,

$$\begin{aligned}
S_{eff}\{\mathbf{\Gamma}\} &= -Tr \ln[(-i\omega_n + \Gamma)\delta_{i,j} + \tilde{T}_{ij}] + \sum_i \frac{|\mathbf{\Gamma}_i(0)|^2}{U} \\
&= -Tr \ln[(-i\omega_n + \Gamma)(1 + (i\omega_n - \Gamma)^{-1}\tilde{T}_{ij})] + \sum_i \frac{|\mathbf{\Gamma}_i(0)|^2}{U}
\end{aligned}$$

The local Green's function is $G_0^{ii} = (i\omega_n - \Gamma)^{-1}$. Thus we can write,

$$\begin{aligned}
S_{eff}\{\mathbf{\Gamma}\} &= -Tr \ln[(G_0^{ii})^{-1}(1 + G_0^{ii}\tilde{T}_{ij})] + \sum_i \frac{|\mathbf{\Gamma}_i(0)|^2}{U} \\
&= -Tr \ln[(G_0^{ii})^{-1}] - Tr \ln[1 + G_0^{ii}\tilde{T}_{ij}] + \sum_i \frac{|\mathbf{\Gamma}_i(0)|^2}{U}
\end{aligned}$$

$$= \mathcal{F}_0 + \Delta\mathcal{F} + \sum_i \frac{|\mathbf{\Gamma}_i(0)|^2}{U} \quad (\text{A.4})$$

In equation (A.4), \mathcal{F}_0 represents the free energy of local problem, and $\Delta\mathcal{F}$ is the change in the free energy of the local background due to the motion of fermions on this background. $\Delta\mathcal{F}$ can be further simplified as

$$\begin{aligned} \Delta\mathcal{F} &= -Tr \ln[1 + G_0\tilde{T}] \\ &= -Tr[-G_0\tilde{T} - \frac{1}{2}(G_0\tilde{T})^2 - \frac{1}{3}(G_0\tilde{T})^3 + \dots] \end{aligned} \quad (\text{A.5})$$

The total change in the free energy is $\Delta\mathcal{F} = \Delta\mathcal{F}^{(1)} + \Delta\mathcal{F}^{(2)} + \Delta\mathcal{F}^{(3)} + \dots$ where

$$\begin{aligned} \Delta\mathcal{F}^{(1)} &= -Tr[-G_0\tilde{T}] \\ \Delta\mathcal{F}^{(2)} &= -Tr[-\frac{1}{2}(G_0\tilde{T})^2] \\ \Delta\mathcal{F}^{(3)} &= -Tr[-\frac{1}{3}(G_0\tilde{T})^3] \\ &\dots \\ \Delta\mathcal{F}^{(n)} &= -Tr[-\frac{1}{n}(G_0\tilde{T})^n] \end{aligned}$$

A.2.1 Some Results

We choose $V = -\frac{U}{2} \sum_i \mathbf{\Gamma}_i \cdot \sigma$ and $T = -t \sum_{\langle ij \rangle, \sigma} c_{i\sigma}^\dagger c_{j\sigma}$.

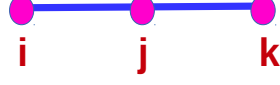
1. *Two sites :*



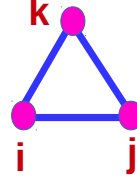
$$\begin{aligned} \Delta\mathcal{F}^{(1)} &= -Tr[-G_0\tilde{T}] = 0 \\ \Delta\mathcal{F}^{(2)} &= -Tr[-\frac{1}{2}(G_0\tilde{T})^2] = \frac{t^2}{U}(\mathbf{\Gamma}_i \cdot \mathbf{\Gamma}_j - 1) \\ \Delta\mathcal{F}^{(3)} &= -Tr[-\frac{1}{3}(G_0\tilde{T})^3] = 0 \\ \Delta\mathcal{F}^{(4)} &= -Tr[-\frac{1}{4}(G_0\tilde{T})^4] = \frac{1}{4} \frac{t^4}{U^3} [10(\mathbf{\Gamma}_i \cdot \mathbf{\Gamma}_j)^2 - 4\mathbf{\Gamma}_i \cdot \mathbf{\Gamma}_j - 6] \end{aligned}$$

2. *Three sites :*

Case - I



Case - II



(a) Case-I

$$\begin{aligned}\Delta\mathcal{F}^{(1)} &= -Tr[-G_0\tilde{T}] = 0 \\ \Delta\mathcal{F}^{(2)} &= -Tr[-\frac{1}{2}(G_0\tilde{T})^2] = \frac{t^2}{U}[(\mathbf{\Gamma}_i \cdot \mathbf{\Gamma}_j - 1) + (\mathbf{\Gamma}_j \cdot \mathbf{\Gamma}_k - 1)] \\ \Delta\mathcal{F}^{(3)} &= -Tr[-\frac{1}{3}(G_0\tilde{T})^3] = 0\end{aligned}$$

(b) Case-II

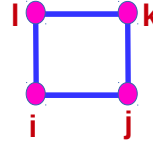
$$\begin{aligned}\Delta\mathcal{F}^{(1)} &= -Tr[-G_0\tilde{T}] = 0 \\ \Delta\mathcal{F}^{(2)} &= -Tr[-\frac{1}{2}(G_0\tilde{T})^2] = \frac{t^2}{U}[(\mathbf{\Gamma}_i \cdot \mathbf{\Gamma}_j - 1) + (\mathbf{\Gamma}_j \cdot \mathbf{\Gamma}_k - 1) + (\mathbf{\Gamma}_k \cdot \mathbf{\Gamma}_i - 1)] \\ \Delta\mathcal{F}^{(3)} &= -Tr[-\frac{1}{3}(G_0\tilde{T})^3] = 0\end{aligned}$$

3. *Four sites :*

Case - I



Case - II



(a) Case-I

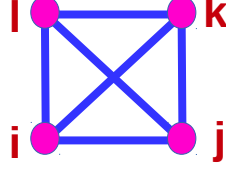
$$\begin{aligned}\Delta\mathcal{F}^{(1)} &= -Tr[-G_0\tilde{T}] = 0 \\ \Delta\mathcal{F}^{(2)} &= -Tr[-\frac{1}{2}(G_0\tilde{T})^2] = \frac{t^2}{U}[(\mathbf{\Gamma}_i \cdot \mathbf{\Gamma}_j - 1) + (\mathbf{\Gamma}_j \cdot \mathbf{\Gamma}_k - 1) + (\mathbf{\Gamma}_k \cdot \mathbf{\Gamma}_l - 1)] \\ \Delta\mathcal{F}^{(3)} &= -Tr[-\frac{1}{3}(G_0\tilde{T})^3] = 0\end{aligned}$$

$$\begin{aligned}
\Delta\mathcal{F}^{(4)} &= -Tr[-\frac{1}{4}(G_0\tilde{T})^4] \\
&= \frac{1}{4} \frac{t^4}{U^3} [10(\mathbf{\Gamma}_i \cdot \mathbf{\Gamma}_j)^2 - 4\mathbf{\Gamma}_i \cdot \mathbf{\Gamma}_j - 6 \\
&\quad + 10(\mathbf{\Gamma}_j \cdot \mathbf{\Gamma}_k)^2 - 4\mathbf{\Gamma}_j \cdot \mathbf{\Gamma}_k - 6 \\
&\quad + 10(\mathbf{\Gamma}_k \cdot \mathbf{\Gamma}_l)^2 - 4\mathbf{\Gamma}_k \cdot \mathbf{\Gamma}_l - 6 \\
&\quad + 20(\mathbf{\Gamma}_i \cdot \mathbf{\Gamma}_j)(\mathbf{\Gamma}_j \cdot \mathbf{\Gamma}_k) - 12(\mathbf{\Gamma}_i \cdot \mathbf{\Gamma}_k) \\
&\quad + 20(\mathbf{\Gamma}_j \cdot \mathbf{\Gamma}_k)(\mathbf{\Gamma}_k \cdot \mathbf{\Gamma}_l) - 12(\mathbf{\Gamma}_j \cdot \mathbf{\Gamma}_l)]
\end{aligned}$$

(b) Case-II

$$\begin{aligned}
\Delta\mathcal{F}^{(1)} &= -Tr[-G_0\tilde{T}] = 0 \\
\Delta\mathcal{F}^{(2)} &= -Tr[-\frac{1}{2}(G_0\tilde{T})^2] = \frac{t^2}{U} \sum_{\langle i,j \rangle} [(\mathbf{\Gamma}_i \cdot \mathbf{\Gamma}_j - 1)] \\
\Delta\mathcal{F}^{(3)} &= -Tr[-\frac{1}{3}(G_0\tilde{T})^3] = 0 \\
\Delta\mathcal{F}^{(4)} &= -Tr[-\frac{1}{4}(G_0\tilde{T})^4] \\
&= \frac{1}{4} \frac{t^4}{U^3} [10(\mathbf{\Gamma}_i \cdot \mathbf{\Gamma}_j)^2 - 4\mathbf{\Gamma}_i \cdot \mathbf{\Gamma}_j - 6 \\
&\quad + 10(\mathbf{\Gamma}_j \cdot \mathbf{\Gamma}_k)^2 - 4\mathbf{\Gamma}_j \cdot \mathbf{\Gamma}_k - 6 \\
&\quad + 10(\mathbf{\Gamma}_k \cdot \mathbf{\Gamma}_l)^2 - 4\mathbf{\Gamma}_k \cdot \mathbf{\Gamma}_l - 6 \\
&\quad + 10(\mathbf{\Gamma}_l \cdot \mathbf{\Gamma}_i)^2 - 4\mathbf{\Gamma}_l \cdot \mathbf{\Gamma}_i - 6 \\
&\quad + 20(\mathbf{\Gamma}_i \cdot \mathbf{\Gamma}_j)(\mathbf{\Gamma}_j \cdot \mathbf{\Gamma}_k) - 12(\mathbf{\Gamma}_i \cdot \mathbf{\Gamma}_k) \\
&\quad + 20(\mathbf{\Gamma}_j \cdot \mathbf{\Gamma}_k)(\mathbf{\Gamma}_k \cdot \mathbf{\Gamma}_l) - 12(\mathbf{\Gamma}_j \cdot \mathbf{\Gamma}_l) \\
&\quad + 20(\mathbf{\Gamma}_k \cdot \mathbf{\Gamma}_l)(\mathbf{\Gamma}_l \cdot \mathbf{\Gamma}_i) - 12(\mathbf{\Gamma}_k \cdot \mathbf{\Gamma}_i) \\
&\quad + 20(\mathbf{\Gamma}_l \cdot \mathbf{\Gamma}_i)(\mathbf{\Gamma}_i \cdot \mathbf{\Gamma}_j) - 12(\mathbf{\Gamma}_l \cdot \mathbf{\Gamma}_j) \\
&\quad + 20(\mathbf{\Gamma}_i \cdot \mathbf{\Gamma}_j)(\mathbf{\Gamma}_k \cdot \mathbf{\Gamma}_l) + 20(\mathbf{\Gamma}_i \cdot \mathbf{\Gamma}_l)(\mathbf{\Gamma}_j \cdot \mathbf{\Gamma}_k) - 20(\mathbf{\Gamma}_i \cdot \mathbf{\Gamma}_k)(\mathbf{\Gamma}_j \cdot \mathbf{\Gamma}_l)] \\
&= \frac{1}{4} \frac{t^4}{U^3} [\sum_{\langle i,j \rangle} \{10(\mathbf{\Gamma}_i \cdot \mathbf{\Gamma}_j)^2 - 4\mathbf{\Gamma}_i \cdot \mathbf{\Gamma}_j - 6\} \\
&\quad + \sum_{\langle i,j,k \rangle} \{20(\mathbf{\Gamma}_i \cdot \mathbf{\Gamma}_j)(\mathbf{\Gamma}_j \cdot \mathbf{\Gamma}_k) - 12(\mathbf{\Gamma}_i \cdot \mathbf{\Gamma}_k)\} \\
&\quad + \sum_{\langle i,j,k,l \rangle} \{20(\mathbf{\Gamma}_i \cdot \mathbf{\Gamma}_j)(\mathbf{\Gamma}_k \cdot \mathbf{\Gamma}_l) + 20(\mathbf{\Gamma}_i \cdot \mathbf{\Gamma}_l)(\mathbf{\Gamma}_j \cdot \mathbf{\Gamma}_k) - 20(\mathbf{\Gamma}_i \cdot \mathbf{\Gamma}_k)(\mathbf{\Gamma}_j \cdot \mathbf{\Gamma}_l)\}]
\end{aligned}$$

4. *Single tetrahedron :*



$$\begin{aligned}
 \Delta\mathcal{F}^{(2)} &= -Tr[-\frac{1}{2}(G_0\tilde{T})^2] = \frac{t^2}{U} \sum_{\langle i,j \rangle} [(\Gamma_i \cdot \Gamma_j - 1)] \\
 \Delta\mathcal{F}^{(4)} &= -Tr[-\frac{1}{4}(G_0\tilde{T})^4] \\
 &= \frac{1}{4} \frac{t^4}{U^3} [10(\Gamma_i \cdot \Gamma_j)^2 - 56\Gamma_i \cdot \Gamma_j - 4 \\
 &\quad + 10(\Gamma_j \cdot \Gamma_k)^2 - 56\Gamma_j \cdot \Gamma_k - 4 \\
 &\quad + 10(\Gamma_k \cdot \Gamma_l)^2 - 56\Gamma_k \cdot \Gamma_l - 4 \\
 &\quad + 10(\Gamma_l \cdot \Gamma_i)^2 - 56\Gamma_l \cdot \Gamma_i - 4 \\
 &\quad + 10(\Gamma_i \cdot \Gamma_k)^2 - 56\Gamma_i \cdot \Gamma_k - 4 \\
 &\quad + 10(\Gamma_j \cdot \Gamma_l)^2 - 56\Gamma_j \cdot \Gamma_l - 4 \\
 &\quad + 20(\Gamma_i \cdot \Gamma_j)(\Gamma_j \cdot \Gamma_k) + 20(\Gamma_i \cdot \Gamma_j)(\Gamma_j \cdot \Gamma_l) + 20(\Gamma_k \cdot \Gamma_j)(\Gamma_j \cdot \Gamma_l) \\
 &\quad + 20(\Gamma_j \cdot \Gamma_k)(\Gamma_k \cdot \Gamma_l) + 20(\Gamma_j \cdot \Gamma_k)(\Gamma_k \cdot \Gamma_i) + 20(\Gamma_i \cdot \Gamma_k)(\Gamma_k \cdot \Gamma_l) \\
 &\quad + 20(\Gamma_k \cdot \Gamma_l)(\Gamma_l \cdot \Gamma_i) + 20(\Gamma_k \cdot \Gamma_l)(\Gamma_l \cdot \Gamma_j) + 20(\Gamma_j \cdot \Gamma_l)(\Gamma_l \cdot \Gamma_i) \\
 &\quad + 20(\Gamma_l \cdot \Gamma_i)(\Gamma_i \cdot \Gamma_j) + 20(\Gamma_l \cdot \Gamma_i)(\Gamma_i \cdot \Gamma_k) + 20(\Gamma_j \cdot \Gamma_i)(\Gamma_i \cdot \Gamma_k) \\
 &\quad + 20(\Gamma_i \cdot \Gamma_j)(\Gamma_k \cdot \Gamma_l) + 20(\Gamma_i \cdot \Gamma_l)(\Gamma_j \cdot \Gamma_k) + 20(\Gamma_i \cdot \Gamma_k)(\Gamma_j \cdot \Gamma_l)] \\
 &= \frac{1}{4} \frac{t^4}{U^3} [\sum_{\langle i,j \rangle} \{10(\Gamma_i \cdot \Gamma_j)^2 - 56\Gamma_i \cdot \Gamma_j - 4\} \\
 &\quad + \sum_{\langle i,j,k \rangle} \{20(\Gamma_i \cdot \Gamma_j)(\Gamma_j \cdot \Gamma_k)\} \\
 &\quad + \sum_{\langle i,j,k,l \rangle} \{20(\Gamma_i \cdot \Gamma_j)(\Gamma_k \cdot \Gamma_l) + 20(\Gamma_i \cdot \Gamma_l)(\Gamma_j \cdot \Gamma_k) + 20(\Gamma_i \cdot \Gamma_k)(\Gamma_j \cdot \Gamma_l)\}]
 \end{aligned}$$

Let $\mathbf{P} = \Gamma_i + \Gamma_j + \Gamma_k + \Gamma_l$. Then we have on a tetrahedron,

$$\Delta\mathcal{F}^{(2)} = \frac{t^2}{U} \sum_{\langle i,j \rangle} [(\Gamma_i \cdot \Gamma_j - 1)] = \frac{1}{2} |\mathbf{P}|^2 - 8$$

$$\Delta\mathcal{F}^{(4)} = \frac{1}{4} \frac{t^4}{U^3} [\frac{5}{2} |\mathbf{P}|^4 - 48 |\mathbf{P}|^2 + 128]$$

A.2.2 Effective spin model for the pyrochlore molybdates

For the molybdates, we have, $J_H/t \gg 1$.

$$V = -\frac{U}{2} \sum_i \Gamma_i \cdot \sigma$$

and

$$T = \sum_{\langle ij \rangle, \alpha\beta} t_{ij}^{\alpha\beta} c_{i\alpha}^\dagger c_{j\beta}$$

$t_{ij}^{\alpha\beta}$ is determined by the orientation of the localised spins $\mathbf{S}_i = (\sin\theta_i \cos\phi_i, \sin\theta_i \sin\phi_i, \cos\theta_i)$, as $t_{ij}^{\alpha\beta} = [\cos\frac{\theta_i}{2} \cos\frac{\theta_j}{2} + \sin\frac{\theta_i}{2} \sin\frac{\theta_j}{2} e^{-i(\phi_i - \phi_j)}] t^{\alpha\beta}$,

In the limit $U \gg t$, following the strong coupling approach, we have,

$$\begin{aligned} H_{eff}\{\mathbf{S}, \Gamma\} &= J_{AF} \sum_{\langle ij \rangle} \mathbf{S}_i \cdot \mathbf{S}_j + \Delta\mathcal{F}^{(2)} \\ &= J_{AF} \sum_{\langle ij \rangle} \mathbf{S}_i \cdot \mathbf{S}_j + \sum_{\langle i,j \rangle} \frac{(1 + \mathbf{S}_i \cdot \mathbf{S}_j)}{2} \left[\frac{t_{\alpha\alpha}^2}{U} (\Gamma_i \cdot \Gamma_j - 1) + \frac{t_{\alpha\beta}^2}{U} (\Gamma_{ix} \Gamma_{jx} - \Gamma_{iy} \Gamma_{jy} - \Gamma_{iz} \Gamma_{jz} - 1) \right] \end{aligned}$$

A.2.3 Effective spin model for the pyrochlore iridates

For the iridates, we have,

$$V = -\frac{U}{2} \sum_i \mathbf{m}_i \cdot \sigma$$

and

$$T = -t \sum_{ij, \sigma} c_{i\sigma}^\dagger c_{j\sigma} - \lambda \sum_{\langle ij \rangle \sigma \sigma'} c_{i\sigma}^\dagger i \mathbf{d}_{ij} \cdot \vec{\sigma} c_{j\sigma'}$$

where the vectors \mathbf{d}_{ij} are parallel to the nearest neighbour Dzyaloshinski-Moriya (DM) vectors on the pyrochlore lattice. We calculate them as $\mathbf{d}_{ij} = 2\mathbf{a}_{ij} \times \mathbf{b}_{ij}$ where $\mathbf{a}_{ij} = \frac{1}{2}(\mathbf{b}_i + \mathbf{b}_j) - \mathbf{x}_c$ and $\mathbf{b}_{ij} = \mathbf{b}_j - \mathbf{b}_i$ with $\mathbf{b}_1 = (0, 0, 0)$, $\mathbf{b}_2 = (0, 1, 1)$, $\mathbf{b}_3 = (1, 0, 1)$, $\mathbf{b}_4 = (1, 1, 0)$ and $\mathbf{x}_c = \frac{1}{2}(1, 1, 1)$.

In the limit $U \gg t, \lambda$, following the same approach, we have,

$$\begin{aligned} \Delta\mathcal{F}^{(2)} &= -Tr[-\frac{1}{2}(G_0 \tilde{T})^2] \\ &= \sum_{\langle i,j \rangle} \left[\frac{t^2 + 2\lambda^2}{U} (\mathbf{m}_i \cdot \mathbf{m}_j - 1) + \frac{2\lambda t}{U} \mathbf{d}_{ij} \cdot (\mathbf{m}_i \times \mathbf{m}_j) + m_i^\alpha \Gamma_{ij}^{\alpha\beta} m_j^\beta \right] \end{aligned}$$

where $\Gamma_{ij}^{\alpha\beta} = \frac{2\lambda^2}{U} (d_{ij}^\alpha d_{ij}^\beta - \delta^{\alpha\beta} |\mathbf{d}_{ij}|^2)$

BIBLIOGRAPHY

- [1] B. D. Gaulin, J. N. Reimers, T. E. Mason, J. E. Greedan, and Z. Tun, Phys. Rev. Lett. **69**, 3244 (1992).
- [2] Y. Taguchi and Y. Tokura, Phys. Rev. B **60**, 10280 (1999).
- [3] I. Kezsmarki, *et al.*, Phys. Rev. B **73**, 125122 (2006).
- [4] S. Iguchi, *et al.*, Phys. Rev. Lett. **102**, 136407 (2009).
- [5] N. Hanasaki, *et al.*, Phys. Rev. Lett. **96**, 116403 (2006).
- [6] T. Katsufuji, H. Y. Hwang, and S-W. Cheong, Phys. Rev. Lett. **84**, 1998 (2000).
- [7] K. Ueda, *et al.*, Phys. Rev. Lett. **108**, 156601 (2012).
- [8] D. Yanagishima and Y. Maeno, J. Phys. Soc. Jpn. **70**, 2880 (2001).
- [9] K. Matsuhira, M. Wakeshima, Y. Hinatsu, and S. Takagi, J. Phys. Soc. J. **80**, 094701 (2011).
- [10] F. F. Tafti, J. J. Ishikawa, A. McCollam, S. Nakatsuji, and S. R. Julian, Phys. Rev. B **85**, 205104 (2012).
- [11] K. Ueda, *et al.*, Phys. Rev. Lett. **109**, 136402 (2012).
- [12] Y. Machida, *et al.*, Phys. Rev. Lett. **98**, 057203 (2007).
- [13] S. Nakatsuji, *et al.*, Phys. Rev. Lett. **96**, 087204 (2006).
- [14] J. Hubbard, Phys. Rev. Lett. **3**, 77 (1959).
- [15] S. Kumar and P. Majumdar, Eur. Phys. J. B, **50**, 571 (2006).

- [16] J. N. Reimers, Phys. Rev. B **45**, 7287 (1992).
- [17] M. P. Zinkin, M. J. Harris, and T. Zeiske, Phys. Rev. B **56**, 11786 (1997).
- [18] R. Moessner and J. T. Chalker, Phys. Rev. B **58**, 12049 (1998).
- [19] Y. Motome and N. Furukawa, J. Phys.: Conf. Ser. **320**, 12060 (2011).
- [20] B. J. Kim, *et al.*, Phys. Rev. Lett. **101**, 076402 (2008).
- [21] A. P. Ramirez, Annu. Rev. Mat. Sci. **24**, 453 (1994).
- [22] R. Moessner, Can. J. Phys. **79**, 1283 (2001).
- [23] H. T. Diep, *Frustrated spin systems*, World Scientific (2005)
- [24] C. Lacroix, P. Mendels, and F. Mila, *Introduction to Frustrated Magnetism : Materials, Experiments, Theory*, Springer (2010).
- [25] P. Chandra, B. Doucot, Phys. Rev. B **38**, 9335 (1988).
- [26] H. Ueda, *et al.*, J. Mag. Mag. Mat. **310**, 1275 (2007).
- [27] S. Kondo, C. Urano, Y. Kurihara, M. Nohara, H. Takagi, J. Phys. Soc. Jpn. **69**, 139 (2000).
- [28] S.-H. Lee, C. Broholm, T.H. Kim, W. Ratcliff, S.-W. Cheong, Phys. Rev. Lett. **84**, 3718 (2000).
- [29] H. Ueda, H. Aruga-Katori, H. Mitamura, T. Goto, and H. Takagi, Phys. Rev. Lett. **94**, 047202 (2005).
- [30] H. Ueda, H. Mitamura, and Y. Ueda, Phys. Rev. B **73**, 094415 (2006).
- [31] Y. Okamoto, M. Nohara, H. Aruga-Katori, H. Takagi, Phys. Rev. Lett. **99**, 137207 (2007).
- [32] J. Villain, Z. Phys. B **33**, 31 (1979).
- [33] A. P. Ramirez, *et al.*, Nature **399**, 333 (1999).
- [34] R. Moessner and J. T. Chalker, Phys. Rev. Lett. **80**, 2929 (1998).
- [35] G. Chern and R. Moessner, Phys. Rev. Lett. **110**, 077201 (2013)
- [36] A. V. Chubukov, Phys. Rev. Lett. **69**, 000832 (1992).

- [37] C. L. Henley, Phys. Rev. Lett. **96**, 047201 (2006).
- [38] G. H. Wannier, Phys. Rev. **79**, 357 (1950).
- [39] Y. Yafet and C. Kittel, Phys. Rev. **87**, 290 (1952).
- [40] R. R. P. Singh and D. A. Huse, Phys. Rev. Lett. **68**, 1766 (1992), B. Bernu, P. Lecheminant, C. Lhuillier, and L. Pierre, Phys. Rev. B **50**, 10048 (1994), L. Capriotti, A. E. Trumper, and S. Sorella, Phys. Rev. Lett. **82**, 3899 (1999),
- [41] p. W. Anderson, Phys. Rev. **102**, 1008 (1956).
- [42] J. B. Fouet, M. Mambrini, P. Sindzingre, and C. Lhuillier, Phys. Rev. B **67**, 54411 (2003).
- [43] D. A. Huse and A. D. Rutenberg, Phys. Rev. B **45**, 7536(R) (1992).
- [44] A. B. Harris, C. Kallin, and A. J. Berlinsky, Phys. Rev. B **45**, 2899 (1992).
- [45] C. Zeng and V. Elser Phys. Rev. B **42**, 8436 (1990), J. T. Chalker and J. F. G. Eastmond, Phys. Rev. B **46**, 14201 (1992).
- [46] M. K. Phani, J. L. Lebowitz, and M. H. Kalos, Phys. Rev. B **21**, 4027 (1980).
- [47] T. Oguchi, H. Nishimori, and Y. Taguchi, J. Phys. Soc. Jpn. **54**, 4494 (1985).
- [48] T. Yildirim, A. B. Harris, and E. F. Shender, Phys. Rev. B **58**, 3144 (1998).
- [49] B. Canals and C. Lacroix, Phys. Rev. Lett. **80**, 2933 (1998).
- [50] N. W. Ashcroft and N. D. Mermin, *Solid State Physics* (1976).
- [51] J. H. de Boer and E. J. W. Verway, Proc. Phys. Soc. London Sec. **49**, 59 (1937).
- [52] J. C. Slater, Phys. Rev. **82**, 538 (1951).
- [53] N. F. Mott, Proc. Phys. Soc. London Sec. **62**, 416 (1949).
- [54] P. W. Anderson, Phys. Rev. **115**, 2 (1959).
- [55] J. Hubbard Proc. R. Soc. London Ser. **A276**, 238 (1963).
- [56] M. C. Gutzwiller, Phys. Rev. Lett. **10**, 159 (1963).
- [57] J. Kanamori, Prog. Theor. Phys. **30**, 275 (1963).

- [58] J. Hubbard Proc. R. Soc. London Ser. **A277**, 237 (1963).
- [59] J. Hubbard Proc. R. Soc. London Ser. **A281**, 401 (1963).
- [60] J. Hubbard Proc. R. Soc. London Ser. **A285**, 542 (1963).
- [61] J. Hubbard Proc. R. Soc. London Ser. **A296**, 42 (1963).
- [62] J. Hubbard Proc. R. Soc. London Ser. **A296**, 100 (1963).
- [63] D. B. McWhan, T. M. Rice, and J. P. Remeika, Phys. Rev. Lett. **23**, 1384 (1969); D. B. McWhan, A. Menth, J. P. Remeika, W. F. Brinkman, and T. M. Rice, Phys. Rev. B **7**, 1920 (1973).
- [64] A. Perucchi, L. Baldassarre, P. Postorino, and S. Lupi, J. Phys.: Condens. Matter **21**, 323202 (2009).
- [65] H. Kuwamoto, J. M. Honig, and J. Appel, Phys. Rev. B **22**, 2626 (1980).
- [66] E. Dagotto, Rev. Mod. Phys. **66**, 763 (1994),
- [67] A. Damascelli, Z. Hussain, and Z. Shen, Rev. Mod. Phys. **75**, 473 (2003).
- [68] P. A. Lee, N. Nagaosa, and X. Wen, Rev. Mod. Phys. **78**, 17 (2006).
- [69] DFG FG 538 - “Doping Dependence of Phase transitions and Ordering Phenomena in Cuprate Superconductors”. http://for538.wmi.badw.de/projects/P4_crystal_growth/index.htm
- [70] H. Takagi, *et al.*, Phys. Rev. Lett., **69**, 2975 (1992).
- [71] A. Georges, G. Kotliar, W. Krauth and M. J. Rozenberg, Rev. Mod. Phys. **68**, 13 (1996).
- [72] N. F. Mott, *Metal-Insulator Transitions*, Taylor and Francis (1990).
- [73] M. Imada, A. Fujimori and Y. Tokura, Rev. Mod. Phys. **70** 1039 (1998)
- [74] J. N. Reimers, Phys. Rev. B **45**, 7287 (1992).
- [75] P. Limelette, *et al.*, Phys. Rev. Lett., **91**, 016401 (2003).
- [76] O. Parcollet, G. Biroli, and G. Kotliar, Phys. Rev. Lett., **92**, 226402 (2004).
- [77] P. Sahebsara and D. Senechal, Phys. Rev. Lett., **100**, 136402 (2008).

- [78] R. T. Clay, H. Li, and S. Mazumdar, Phys. Rev. Lett., **101**, 166403 (2008).
- [79] T. Watanabe, H. Yokoyama, Y. Tanaka, and J. Inoue, Phys. Rev. B, **77**, 214505 (2008).
- [80] R. Tiwari and P. Majumdar Europhys. Lett. **108**, 27007 (2014).
- [81] T. Ohashi, N. Kawakami, and H. Tsunetsugu, Phys. Rev. Lett. **97**, 066401 (2006).
- [82] T. Ohashi, T. Momoi, H. Tsunetsugu, and N. Kawakami, Prog. Ther. Phys. Suppl. **176**, 97 (2008).
- [83] A. Camjayi, *et al.*, Phys. Rev. Lett., **113**, 086404 (2014).
- [84] M. A. Timirgazin, P. A. Igoshev, A. K. Arzhnikov, and V. Yu. Irkhin, J. Phys.: Condens. Matter **28**, 505601 (2016).
- [85] S. Fujimoto, Phys. Rev. B **64**, 085102 (2001).
- [86] J. S. Gardner, M. J. P. Gingras, and J. E. Greedan, Rev. Mod. Phys. **82**, 53 (2010).
- [87] N. Swain, R. Tiwari, and P. Majumdar, Phys. Rev. B **94**, 155119 (2016).
- [88] Y. Shimizu, K. Miyagawa, K. Kanoda, M. Maesato and G. Saito, Phys. Rev. Lett. **91**, 107001 (2003).
- [89] M. Yamashita, *et al.* Nature Phys. **5**, 44 (2009).
- [90] K. Kanoda and R. Kato, Annu. Rev. Condens. Matter Phys. **2**, 167 (2011).
- [91] B. J. Powell and R. H. McKenzie, Rep. Prog. Phys. **74**, 056501 (2011).
- [92] Y. Tokura, (ed.), *Colossal Magnetoresistive Oxides*, CRC Press, (2000).
- [93] M. B. Salamon and M. Jaime, Rev. Mod. Phys. **73**, 583 (2001).
- [94] M. J. P. Gingras, C. V. Stager, N. P. Raju, B. D. Gaulin, and J. E. Greedan, Phys. Rev. Lett. **78**, 947 (1997).
- [95] I. Kezsmarki, *et al.*, Phys. Rev. B **73**, 125122 (2006).
- [96] S. Iguchi, *et al.*, Phys. Rev. Lett. **102**, 136407 (2009).

- [97] F. F. Tafti, J. J. Ishikawa, A. McCollam, S. Nakatsuji, and S. R. Julian, Phys. Rev. B **85**, 205104 (2012).
- [98] https://tspace.library.utoronto.ca/bitstream/1807/35847/6/Witczak-Krempa_William_201306_PhD_thesis.pdf
- [99] J. E. Greedan, J. N. Reimers, C. V. Stager, and S. L. Penny, Phys. Rev. B **43**, 5682 (1991).
- [100] J. S. Gardner, *et al.*, Phys. Rev. Lett. **83**, 211 (1999).
- [101] S. R. Dunsiger, *et al.*, Phys. Rev. B **54**, 9019 (1996).
- [102] I. Kezsmarki, *et al.*, Phys. Rev. Lett. **93**, 266401 (2004).
- [103] I. Kezsmarki, *et al.*, Phys. Rev. B **73**, 125122 (2006).
- [104] J. S. Kang, *et al.*, Phys. Rev. B **65**, 224422 (2002).
- [105] W. Witczak-Krempa, G. Chen, Y. B. Kim and L. Balents, Ann. Rev. Cond. Mat. Phys. **5**, 57 (2014).
- [106] K. Tomiyasu, *et al.*, J. Phys. Soc. Jpn. **81**, 034709 (2012).
- [107] S. Zhao, *et al.*, Phys. Rev. B **83**, 180402(R) (2011).
- [108] S. M. Disseler, *et al.*, Phys. Rev. B **86**, 014428 (2012).
- [109] K. Ueda, J. Fujioka, and Y. Tokura, Phys. Rev. B **93**, 245120 (2016).
- [110] K. Ueda, J. Fujioka, C. Terakura, and Y. Tokura, Phys. Rev. B **92**, 121110(R) (2015).
- [111] Z. Tian, *et al.*, Nature Physics **12**, 134 (2016).
- [112] I. V. Solovyeu, Phys. Rev. B **67**, 174406 (2003).
- [113] Y. Motome and N. Furukawa, Phys. Rev. Lett. **104**, 106407 (2010), Phys. Rev. B **82**, 060407(R) (2010).
- [114] W. Witczak-Krempa, and Y. B. Kim, Phys. Rev. B **85**, 045124 (2012).
- [115] W. Witczak-Krempa, A. Go, and Y. B. Kim, Phys. Rev. B **87**, 155101 (2013).

- [116] A. Go, W. Witczak-Krempa, G. S. Jeon, K. Park, and Y. B. Kim Phys. Rev. Lett. **109**, 066401 (2012).
- [117] H. Shinaoka, S. Hoshino, M. Troyer, and P. Werner Phys. Rev. Lett. **115**, 156401 (2015).
- [118] J. Hubbard, Proc. Roy. Soc. (London) **A281**, 401, (1964).
- [119] D. Bareswyl, *et. al.*, *The Mathematics and Physics of the Hubbard model*, Plenum Press, New York (1995).
- [120] W. Metzner and D. Vollhardt, Phys. Rev. Lett. **62**, 324 (1989).
- [121] J. Hubbard, Phys. Rev. B **19**, 2626 (1979).
- [122] H. J. Schulz, Phys. Rev. Lett. **65**, 2462 (1990).
- [123] P. Arve, G. Bertsch, B. Lauritzen, and G. Puddu, Ann. Phys. **183**, 309 (1988).
- [124] B. Lauritzen, P. Arve, and G. F. Bertsch, Phys. Rev. B **61**, 2835 (1988).
- [125] M. Mayr, G. Alvarez, C. Sen, and E. Dagotto, Phys. Rev. Lett. **94**, 217001 (2005).
- [126] Y. Dubi, Y. Meir, and Y. Avishai, Nature, **449**, 876 (2007).
- [127] R. Tiwari and P. Majumdar, Europhys. Lett. **108**, 27007 (2014).
- [128] N. Swain and P. Majumdar, J. Phys.: Condens. Matter **29**, 08560 (2017).
- [129] M. P. Zinkin, M. J. Harris, and T. Zeiske, Phys. Rev. B **56**, 11786 (1997).
- [130] C. L. Henley, Phys. Rev. B **71**, 014424 (2005).
- [131] S. V. Isakov, K. Gregor, R. Moessner, and S. L. Sondhi, Phys. Rev. Lett. **93**, 167204 (2004).
- [132] U. Hizi and C. L. Henley, Phys. Rev. B **73**, 054403 (2006).
- [133] U. Hizi and C. L. Henley, Phys. Rev. B **80**, 014407 (2009).
- [134] M. Hermele, M. P. A. Fisher, and L. Balents Phys. Rev. B **69**, 064404 (2004).
- [135] B. Normand and Z. Nussinov, Phys. Rev. Lett. **112**, 207202 (2014).
- [136] D. Tsuneishi and H. Kawamura, J. Phys. Condens. Matter **19**, 145273 (2007).

- [137] G.-W. Chern, R. Moessner, and O. Tchernyshyov Phys. Rev. B **78**, 144418 (2008).
- [138] T. Okubo, T. H. Nguyen, and H. Kawamura Phys. Rev. B **84**, 144432 (2011).
- [139] B. Javanparast, Z. Hao, M. Enjalran, and M. J. P. Gingras Phys. Rev. Lett. **114**, 130601 (2015).
- [140] S. Fujimoto, Phys. Rev. B **64**, 085102 (2001), Phys. Rev. B **67**, 235102 (2003).
- [141] Y. Akagi, M. Udagawa, and Y. Motome, Phys. Rev. Lett. **108**, 096401 (2012).
- [142] G.-W. Chern, Phys. Rev. Lett. **105**, 226403 (2010).
- [143] P. H. Conlon and J. T. Chalker, Phys. Rev. B **81**, 224413 (2010).
- [144] A. P. Ramirez, Annu. Rev. Mater. Sci. **24**, 453 (1994).
- [145] N. P. Ong and R. J. Cava, Science, **305**, 52 (2004).
- [146] L. Balents, Nature (London), **464**, 199 (2010).
- [147] D. J. Thouless Proc. Phys. Soc. **86**, 893 (1965).
- [148] M. Roger, J. H. Hetherington, and J. M. Delrieu, Rev. Mod. Phys. **55**, 1 (1983).
- [149] R. Tiwari and P. Majumdar arXiv:1302.2922v1 (2013).
- [150] E. H. Lieb and P. Schupp, Phys. Rev. Lett. **83**, 5362 (1999).
- [151] S. E. Palmer and J. T. Chalker, Phys. Rev. B **64**, 94412 (2001).
- [152] E. Berg, E. Altman, and A. Auerbach, Phys. Rev. Lett. **90**, 147204 (2003).
- [153] R. Moessner, O. Tchernyshyov, and S. Sondhi, Journal of Statistical Physics **116**, 755 (2004).
- [154] W. Brenig and M. Grzeschik, Phys. Rev. B **69**(R), 064420 (2004).
- [155] J. S. Bernier, C. H. Chung, Y. B. Kim, and S. Sachdev, Phys. Rev. B **69**, 214427 (2004).
- [156] N. Shannon, G. Misguich, and K. Penc, Phys. Rev. B **69**, 220403 (2004).
- [157] O. A. Starykh, A. Furusaki, and L. Balents, Phys. Rev. B **72**, 094416 (2005).

- [158] Z. Nussinov, C. D. Batista, B. Normand, and S. A. Trugman, Phys. Rev. B **75**, 094411 (2007).
- [159] S. Fujimoto, Phys. Rev. B. **67**, 235102 (2003).
- [160] T. Yoshioka, A. Koga, and N. Kawakami, J. Phys. Soc. Jpn. **77**, 104702 (2008).
- [161] K. Binder and A. P. Young, Rev. Mod. Phys. **58**, 801 (1986).
- [162] B. Canals, Phys. Rev. B **65**, 184408 (2002).
- [163] O. Tchernyshyov, O. A. Starykh, R. Moessner, and A. G. Abanov, Phys. Rev. B **68**, 144422 (2003).
- [164] U. Hizi and C. L. Henley, Phys. Rev. B **73**, 054403 (2006).
- [165] T. E. Saunders and J. T. Chalker, Phys. Rev. Lett. **98**, 157201 (2007).
- [166] H. Shinaoka, Y. Tomita, and Y. Motome, Phys. Rev. Lett. **107**, 047204 (2011), Phys. Rev. B **90**, 165119 (2014).
- [167] N. Hanasaki, *et al.*, Phys. Rev. Lett. **99**, 086401 (2007).
- [168] Y. Taguchi, *et al.*, Phys. Rev. Lett. **90**, 257202 (2003).
- [169] S. Iguchi, N. Hanasaki, and Y. Tokura, Phys. Rev. Lett. **99**, 077202 (2007).
- [170] K. Ueda, *et al.*, Phys. Rev. Lett. **108**, 156601 (2012).
- [171] S. Kumar and P. Majumdar, Eur. Phys. J. B, **46**, 315 (2005).
- [172] S. Iguchi, *et al.*, Phys. Rev. Lett. **102**, 136407 (2009).
- [173] J. E. Greedan, *et al.*, J. Solid State Chem. **68**, 300 (1987).
- [174] K. Miyoshi, *et al.*, J. Magn. Magn. Mater. **226**, 898 (2001).
- [175] H. Shinaoka, Y. Motome, T. Miyake, and S. Ishibashi, Phys. Rev. B **88**, 174422 (2013).
- [176] K. Pradhan and P. Majumdar, Europhys. Lett. **85**, 37007 (2009).
- [177] A. Keren and J. S. Gardner, Phys. Rev. Lett. **87**, 177201 (2001).
- [178] E. Sagi, O. Ofer, A. Keren, and J.S. Gardner, Phys. Rev. Lett. **94**, 237202 (2005).

- [179] J. E. Greedan, *et al.*, Phys. Rev. B **79**, 014427 (2009).
- [180] D. Yanagishima and Y. Maeno, J. Phys. Soc. Jpn. **70**, 2880 (2001).
- [181] K. Matsuhira, M. Wakeshima, Y. Hinatsu, and S. Takagi, J. Phys. Soc. J. **80**, 094701 (2011).
- [182] S. Nakatsuji, *et al.*, Phys. Rev. Lett. **96**, 087204 (2006).
- [183] N. Taira, M. Wakeshima, and Y. Hinatsu, J. Phys.: Condens. Matter **13**, 5527 (2001).
- [184] K. Tomiyasu, *et al.*, J. Phys. Soc. Jpn. **81**, 034709 (2012).
- [185] H. Sagayama, *et al.*, Phys. Rev. B **87**, 100403 (2013).
- [186] M. Sakata, *et al.*, Phys. Rev. B **83**, 041102 (2011).
- [187] F. F. Tafti, J. J. Ishikawa, A. McCollam, S. Nakatsuji, and S. R. Julian, Phys. Rev. B **85**, 205104 (2012).
- [188] K. Ueda, *et al.*, Phys. Rev. Lett. **109**, 136402 (2012).
- [189] K. Ueda, J. Fujioka, C. Terakura, and Y. Tokura, Phys. Rev. B **92**, 121110 (2015).
- [190] Y. Machida, *et al.*, Phys. Rev. Lett. **98**, 057203 (2007).
- [191] X. Wan, A. M. Turner, A. Vishwanath, and S. Y. Savrasov, Phys. Rev. B **83**, 205101 (2011).
- [192] “Complex oxides”. http://trivediresearch.org.ohio-state.edu/?page_id=43
- [193] M. Kurita, Y. Yamaji, and M. Imada, J. Phys. Soc. Jpn. **80**, 044708 (2011).
- [194] W. Witczak-Krempa and Y. B. Kim, Phys. Rev. B **85**, 045124 (2012). Eric Kin-Ho Lee, S. Bhattacharjee, and Y. B. Kim Phys. Rev. B **87**, 214416 (2013).
- [195] R. Singh, V. Medicherla, K. Maiti, and E. Sampathkumaran, Phys. Rev. B **77**, 201102 (2008).
- [196] Y. Yamaji, Y. Nomura, M. Kurita, R. Arita, and M. Imada, Phys. Rev. Lett. **113**, 107201 (2014).